

Determining the Role of the Calcium Sensing Receptor in Vascular Smooth Muscle Cells via Targeted Gene Deletion



Mag. Martin Schepelmann

PhD Thesis 2014

Summary

The extracellular-Ca²⁺ sensing receptor (CaSR) is a G protein-coupled receptor which is essential for Ca²⁺ homeostasis in the body. The best studied function of the CaSR lies in the parathyroid gland, where hypercalcaemia activates the receptor which in consequence inhibits parathyroid hormone secretion. However, for other tissues like the vasculature the physiological and pathophysiological roles of the CaSR are a lot less well defined.

The CaSR is expressed in all layers of blood vessels, the endothelium, the vascular smooth muscle cells (VSMC) and the tunica adventitia. Previous studies have suggested roles for the vascular CaSR in protection against vascular calcification and in blood pressure regulation. In the course of my thesis, I have investigated the specific roles of the vascular CaSR by characterising the phenotype of a transgenic mouse model of targeted CaSR deletion from VSMC (SM22 α -Cre x LoxP-CaSR). In characterising this mouse model, I have made three principal discoveries:

- 1) The VSMC CaSR protects against vascular calcification induced by high Ca²⁺ and Pi *in vitro*. No calcification was discovered in mice lacking the VSMC CaSR *in vivo*, suggesting that this protective effect of the CaSR might only assert itself in pathological disease.
- 2) The VSMC CaSR contributes to blood pressure regulation. Mice lacking the VSMC CaSR exhibit hypotension which is due to impaired vascular contractility and therefore reduced total peripheral resistance. I propose a role for the VSMC CaSR as auto- / paracrine amplifier of VSMC contraction. Furthermore, knock-out mice exhibit bradycardia and sporadic cardiac remodelling.
- 3) Mice lacking the VSMC CaSR exhibit profound changes in mineral ion metabolism, together with severe hypercalcaemia, hypercalciuria, hyperphosphaturia and increased 1,25-(OH)₂-Vitamin D₃ and phosphaturic FGF23 levels, and decreased bone mineral density, consistent with a phenotype resembling primary hyperparathyroidism. The mechanisms behind this influence remain yet to be fully understood.

Acknowledgements

First, I want to thank the European Union for funding my position via our “Multifaceted CaSR” Marie Curie Initial Training Network as well as Cardiff University for providing a great and comfortable working environment.

I want to thank my supervisors, Professor Daniela Riccardi and Professor Paul Kemp, who made it possible for me to work in their laboratory. From day one, you always had an open ear for me and helped and encouraged me with my work and my stay here in Cardiff. Very special thanks go towards my direct colleagues and members of “team vascular” who were working with me on my project in Cardiff and who I now regard as some of my closest friends: Sarah Brennan, Tom Davies, Polina “Polly” Yarova, Irene Lopez and Joao Graca! Thank you all so much, I could not have done it without your help, friendship and kindness! The amazing team spirit and atmosphere of “everyone pulling together” was it that made my work here in Cardiff so enjoyable.

I also want to thank all my colleagues here in Cardiff, who I now all consider dear friends, and who welcomed me into their midst and helped me in innumerable occasions. Thank you, Becky, Joao B, Alex, Belinda, Birgitta, Charlie, Dave, Laurie Lydia, Julia, Pawel, Rachel, Seva and Stuart! I am also immensely grateful to my friends and colleagues of the Marie Curie Initial Training network; we shared a lot of exciting, interesting and fun experiences! Thank you, Abhi, Ira, Paolo, Rita, Sama, Susanne, Ursula and Valerie! I also want to thank my friends in Austria who always made visits to home something to look forward to. A big “thank you” also goes to all of our collaborators who helped me with my work and contributed their expertise on uncountable occasions: Dr. Ann Canfield, Dr. Wenhan Chang, Professor Isabella Ellinger, Professor Rob Fenton, Dr. Enikö Kallay, Dr. Martin Krrsak, Dr. Vladimir Matchkov, Professor Peter Pietschmann, Dr. Sally Price, Mrs Annelisa Sadler, Mr Andrew Stewart and Dr. Donald Ward.

Finally, I want to thank my family, my father Wolfgang, my mother Enna and my sister Alexandra. I thank you for your belief in me, your unending support and love! I wish to dedicate this work to you.

Table of contents

Summary.....	iii
Acknowledgements	iv
Table of contents	v
List of abbreviations	xi
List of Figures.....	xiv
List of tables	xxi
Contributions	xxiii
1 Introduction	1
1.1 The extracellular Calcium-Sensing Receptor	1
1.1.1 General.....	1
1.1.2 Ligands of the CaSR.....	3
1.2 The role of the CaSR in Ca ²⁺ homeostasis.....	6
1.2.1 Ca ²⁺ homeostasis and the CaSR	6
1.2.2 Genetic and acquired conditions relating to the CaSR.....	9
1.3 Role of the CaSR in the vasculature	12
1.3.1 The vasculature and blood pressure regulation	12
1.3.2 Direct effects of the CaSR on vascular tone.....	17
1.3.3 <i>In vivo</i> effects of the CaSR on blood pressure	18
1.4 Role of the CaSR in vascular calcification	21
1.4.1 Vascular calcification	21
1.4.2 Protection against vascular calcification by the CaSR.....	24
1.4.3 Clinical use of calcimimetics.....	26
1.5 Models of CaSR deletion.....	27
1.5.1 Models of constitutive CaSR deletion.....	27
1.5.2 Models of targeted CaSR deletion via the Cre-LoxP system	28
1.5.3 The SM22 α -Cre x LoxP-CaSR mouse.....	28

1.6	Scope and objectives of the thesis	32
2	Materials and Methods	33
2.1	Chemicals and substances.....	33
2.2	Experimental animals	33
2.3	Genotyping of SM22 α -Cre x loxP-CaSR mice.....	35
2.4	<i>In vitro</i> assays	37
2.4.1	Culture media	37
2.4.2	HEK-CaSR cells	37
2.4.3	pH assays	38
2.4.4	Primary VSMC culture from explants.....	38
2.4.5	Acute isolation of VSMC	40
2.4.6	Double immunostaining of VSMC and HEK-CaSR cells.....	40
2.4.7	Staining of apoptotic cells (TUNEL assay).....	41
2.4.8	Quantitative immunofluorescence	42
2.4.9	VSMC numbers / proliferation.....	46
2.5	Histomorphometry and immunofluorescence studies.....	47
2.5.1	Organ fixation and sectioning	47
2.5.2	Immunofluorescence staining of tissues.....	47
2.6	Calcification assays.....	48
2.6.1	<i>In vitro</i> VSMC calcification	48
2.6.2	Staining for calcification on blood vessel sections.....	48
2.6.3	<i>Ex vivo</i> calcification of aortic explants.....	48
2.7	Cardiovascular analysis	49
2.7.1	Blood pressure measurement by tail cuff	49
2.7.2	Blood pressure measurement by radiotelemetry	50
2.7.3	Cardiac magnetic resonance imaging (MRI).....	54
2.8	Metabolism, clinical chemistry and bone	59

2.8.1	Metabolic cage studies.....	59
2.8.2	Clinical chemistry.....	59
2.8.3	Bone morphology	61
2.9	Statistical analysis.....	61
3	Method development and optimisation	62
3.1	Introduction.....	62
3.2	Results.....	64
3.2.1	Influence of addition of different concentrations of Ca ²⁺ and Pi on the pH of the culture medium	64
3.2.2	<i>In vitro</i> VSMC calcification protocol development	66
3.2.3	Immunofluorescence staining optimisation.....	68
3.3	Discussion.....	73
3.4	Conclusions.....	73
4	General phenotype of the CaSR-LoxP x SM22 α -Cre mouse.....	74
4.1	Introduction.....	74
4.2	Results.....	75
4.2.1	Genotyping and cursory phenotypic differences.....	75
4.2.2	Body weight.....	76
4.2.3	Reproductive capabilities	77
4.2.4	Expression of the CaSR in the vasculature.....	78
4.3	Discussion.....	81
4.4	Conclusions.....	81
5	Effect of CaSR deletion on cultured VSMC	82
5.1	Introduction.....	82
5.2	Results.....	83
5.2.1	CaSR expression in VSMC	83
5.2.2	VSMC proliferation.....	88

5.3	Discussion.....	91
5.3.1	CaSR expression in VSMC	91
5.3.2	Regulation of VSMC proliferation by the CaSR.....	93
5.4	Conclusions.....	94
6	Effect of CaSR deletion on vascular calcification.....	95
6.1	Introduction.....	95
6.2	Results.....	96
6.2.1	<i>In vivo</i> blood vessel calcification.....	96
6.2.2	<i>In vitro</i> VSMC calcification	97
6.3	<i>Ex vivo</i> calcification of aortic explants	101
6.4	Discussion.....	102
6.4.1	<i>In vitro</i> calcification.....	102
6.4.2	<i>In vivo</i> calcification	103
6.5	Conclusions.....	105
7	Effect of VSMC targeted CaSR deletion on the cardiovascular function.....	106
7.1	Introduction.....	106
7.2	Results.....	108
7.2.1	Blood pressure measurements by tail cuff.....	108
7.2.2	Blood pressure measurements by radiotelemetry.....	114
7.2.3	Cardiac cine-MRI	126
7.3	Discussion.....	141
7.3.1	Blood pressure measured by tail cuff	141
7.3.2	Baseline blood pressure measured by radiotelemetry	142
7.3.3	Role of the heart and arterial compliance.....	143
7.3.4	Role of TPR.....	146
7.3.5	Systemic influences	146
7.3.6	Effect of salt loading on blood pressure	147

7.3.7	Effect of NO synthesis inhibition on blood pressure.....	148
7.3.8	Direct influence of the vascular CaSR on vascular tone	149
7.3.9	Cardiac remodelling	157
7.4	Conclusions.....	162
8	Effect of VSMC specific CaSR deletion on metabolism and mineral ion homeostasis.	163
8.1	Introduction.....	163
8.2	Results.....	166
8.2.1	Metabolic cage studies.....	166
8.2.2	Clinical chemistry.....	170
8.2.3	Bone.....	178
8.3	Discussion.....	180
8.3.1	Food and water metabolism.....	180
8.3.2	Effect of L-NAME on plasma chemistry	181
8.3.3	KO mice are hypercalcaemic, hypercalciuric and hyperphosphaturic	182
8.3.4	Link between VSMC CaSR and changes in mineral ion metabolism.....	189
8.3.5	Bone.....	191
8.3.6	Future directions	191
8.4	Conclusions.....	192
9	Thesis conclusions and future directions.....	193
9.1	Protective effect of the VSMC CaSR against calcification	193
9.2	The VSMC CaSR is involved in blood pressure regulation	193
9.3	The VSMC CaSR is involved in mineral ion homeostasis.....	194
10	References	197
11	Appendix A	226
12	Appendix B.....	240
12.1	VSMC apoptosis	240

12.2	Radiotelemetry experiments - Variable time point comparisons based on rolling minimum and maximum detection.....	246
12.3	Cardiac cine MRI - 18 month old animals.....	255
13	Curriculum vitae.....	262

List of abbreviations

μ CT	micro X-ray computed tomography
1,25-D ₃	1,25-(OH) ₂ -Vitamin D ₃ (Calcitriol)
ACE	Angiotensin converting enzyme
ADH	Autosomal dominant hypocalcaemia
ADIS	Agonist driven insertion signalling
ALP	Alkaline phosphatase
ANOVA	Analysis of variance
AT	Angiotensin receptor
AU	Arbitrary units
BGP	Beta-glycero-phosphate
BMD	Bone mineral density
BMP1	Bone morphogenic protein 1
bp	base pairs
BSA	Bovine serum albumin
BV	Bone Volume
Ca ²⁺ _i	Intracellular Ca ²⁺
Ca ²⁺ _o	Extracellular Ca ²⁺
CaSR	Extracellular calcium-sensing receptor
CD	Connectivity density
CKD	chronic kidney disease
CO	Cardiac output
Cre	cyclization recombinase
Ct.	Cortical
DICOM	Digital Imaging and Communications in Medicine
DKK1	Dickkopf-related protein 1
DMEM	Dulbecco's modified eagle medium
DNA	Deoxyribonucleic acid
dNTP	deoxy-nucleotide triphosphate
DR	Daniela Riccardi
DRI	Diastolic remodelling index
EC ₅₀	Half maximal effective concentration (= potency)
ECG	Electrocardiography
EDD	End-diastolic diameter
EDL	End-diastolic length
EDTA	Ethylenediaminetetraacetic acid
EDV	End-diastolic volume
EF	Ejection fraction
EMRIC	Experimental MRI Centre
eNOS	Endothelial nitric oxide synthase

ESD	End-systolic diameter
ESL	End-systolic length
ESRD	End-stage renal disease
ESRD	End-stage renal disease
ESV	End-systolic volume
FBS	Foetal bovine serum
FGF23	Fibroblast growth factor 23
FHH	Familial Hypocalciuric Hypercalcaemia
GABA	γ -amino-butyric acid
Gcm2	Glial cells missing-2
GFR	Glomerular filtration rate
GPCR	G-protein coupled receptor
HAEC	Human aortic endothelial cells
HEK	Human embryonic kidney (cells)
HEPES	4-(2-hydroxyethyl)-1-piperazineethanesulfonic acid
HET	(from) heterozygous (mice), = SM22 α -Cre ⁺ x LoxP-CaSR ^{+/-}
HUVEC	Human umbilical vein endothelial cells
ICP-MS	Inductively-coupled plasma mass spectrometry
IK _{Ca}	intermediate conductance Ca ²⁺ -sensitive K ⁺ channel
KO	(from) knock out (mice), = SM22 α -Cre ⁺ x LoxP-CaSR ^{+/+}
L-NAME	L-nitro-arginine-methyl ester
LoxP	locus of X-over P1
LV	Left ventricle / left ventricular
LVM	Left ventricular mass
mGluR	metabotropic glutamate receptor
MGP	Matrix-Gla-Protein
MRI	Magnetic resonance imaging
MS	Martin Schepelmann
N	number
NO	Nitric oxide
NSHPT	Neonatal Severe Hyperparathyroidism
OCT	Optimal cutting temperature (embedding compound for cryosections)
OPG	Osteoprotegerin
PBS	Phosphate-buffered saline
PCR	Polymerase chain reaction
PER	Peak ejection rate
PFA	Paraformaldehyde
PFR	Peak fill rate
Pi	Inorganic phosphate
PPi	Pyrophosphate
PTH	Parathyroid hormone

RAAS	Renin angiotensin aldosterone system
rem	remodelled
rh	relative humidity
RNA	Ribonucleic acid
ROI	Region of interest
RT-qPCR	quantitative (real time) RT-PCR
RUNX2	Runt-related transcription factor 2
RV	Right ventricle / right ventricular
SB	Sarah Brennan
SDS	Sodium dodecyl sulphate
Six2	Sine oculis homeobox homolog 2
SM22 α	Smooth muscle protein of 22 kDa isoform α
SMI	Structure model index
SNAP	S-Nitroso-N-acetylpenicillamine
SOST	Sclerostin
Sp	Spacing
SRI	Systolic remodelling index
SV	Stroke volume
Tb.	Trabecular
TBW	Total body weight
TF	TissueFAXS®
TPR	Total peripheral resistance
TQ	TissueQuest®
TUNEL	Terminal deoxynucleotidyl transferase dUTP nick end-labelling
TV	Total Volume
VSMC	Vascular smooth muscle cells
WT	(from) wild type (mice), = SM22 α -Cre ⁻ x LoxP-CaSR ^{+/+}

List of Figures

Figure 1: Topology of the human CaSR.....	2
Figure 2: Ca ²⁺ dose dependent suppression of PTH release.....	3
Figure 3: Blood Ca ²⁺ set point for PTH secretion	5
Figure 4: Ca ²⁺ and Pi homeostasis.....	6
Figure 5: Histology of blood vessels.....	13
Figure 6: The renin-angiotensin-aldosterone system (RAAS)	15
Figure 7: Simplified overview of factors contributing to blood pressure homeostasis.....	16
Figure 8: Overview of osteogenic VSMC transdifferentiation and calcification.....	23
Figure 9: Generation of explant-derived aortic VSMC.....	39
Figure 10: Examples for incorrect and correct segmentation of nuclei for cell detection in quantitative immunofluorescence measurements.....	43
Figure 11: Example of ring masks for quantification of SM22 α and CaSR staining intensities.	44
Figure 12: Example of a nuclear mask for detection of apoptotic cells visualized using TUNEL staining.....	44
Figure 13: Example scattergram from TissueQuest® showing mean green fluorescence intensity (SM22 α) on the x axis (GFP – Mean Intensity) and mean red fluorescence intensity (CaSR) on the y axis (Texa – Mean Intensity).	45
Figure 14: Mouse restrainers.....	49
Figure 15: Implantation of radiotelemetry probes.....	50
Figure 16: Timeline of telemetry experiments.....	51
Figure 17: Example for use of a rolling average over.....	52
Figure 18: Fixed 3 hour intervals selected for comparison of telemetry derived parameters in active vs. resting state of the mice.....	53
Figure 19: Short and long axes of the heart.....	54
Figure 20: ECG-gated cardiac MRI.....	55
Figure 21: Workflow of the manual MRI analysis.....	57
Figure 22: Influence of external pH on EC ₅₀ for CaSR activation by Ca ²⁺ and Mg ²⁺	62
Figure 23: Influence of addition of different concentration of Pi or CaCl ₂ on medium pH.....	65
Figure 24: Optimization of <i>in vitro</i> mouse primary VSMC calcification assay.....	66
Figure 25: Test of anti CaSR antibodies on HEK293 cells stably transfected with human CaSR (HEK-CaSR).....	69

Figure 26: Antibody staining trial on control kidney sections.	70
Figure 27: Quenching of high autofluorescence in the kidney using Sudan Black B.	71
Figure 28: Effect of autofluorescence quenching using 0.2 % Sudan Black B.....	72
Figure 29: Exemplary genotyping results from mice of genotypes used in this study.....	75
Figure 30: Photographs of exemplary WT, HET and KO mice.	76
Figure 31: Body weight of male and female WT, HET and KO mice.	77
Figure 32: Reproductive capabilities of WT, KO and HET mice.	77
Figure 33: Immunolocalization of the CaSR, pecam-1 and SM22 α in transverse sections of mesenteric arteries from control mice	79
Figure 34: Immunolocalization of the CaSR, Pecam-1 and SM22 α in transverse section of aortae from WT and KO mice.	80
Figure 35: Representative picture of VSMC cultured from aortic explants of C57/Bl6 mice.	83
Figure 36: Average percentage of VSMC in all analysed batches of VSMC grown from WT and KO aortae.	84
Figure 37: Immunolocalization of the CaSR in VSMC.	85
Figure 38: CaSR expression in cultured WT and KO VSMC.	86
Figure 39: Quantitative immunofluorescence analysis of CaSR expression levels in all cells present in VSMC preparations of passages 2-6 cultured from WT and KO aortae.	87
Figure 40: Quantitative immunofluorescence analysis of CaSR expression levels in the population of VSMC (staining positive for SM22 α) in VSMC preparations of passages 2-6 cultured from WT and KO aortae.	87
Figure 41: Number of VSMC from C57/BL6 control mice after 5 and 10 days of incubation in three different Ca ²⁺ concentrations.	88
Figure 42: Number of VSMC from WT and KO mice after 10 days of incubation in the presence of medium containing different Ca ²⁺ concentrations.	89
Figure 43: Replicate of the WT/KO VSMC proliferation experiment shown in Figure 42 by Dr. Thomas Davies.	89
Figure 44: Presumed cause for remaining CaSR immunostaining in VSMC from KO mice.	93
Figure 45: Alizarin Red S stainings of three thoracic aortae from 12 month old WT and KO animals.	96
Figure 46: Photographs of WT and KO mouse derived VSMC cultured in 24-well plates stained with alizarin red S after 10 day incubation in medium containing different Ca ²⁺ and Pi concentrations.	97

Figure 47: Representative phase-contrast microscopic images of WT and KO alizarin red S staining for VSMC incubated for 10 days with medium containing 2 mM Pi and 2 mM Ca ²⁺ ..	98
Figure 48: Densitometric quantification of alizarin red S staining of VSMC.....	98
Figure 49: Quantification of Ca ²⁺ deposition using cresolphthalein complexone assay.....	100
Figure 50: <i>Ex vivo</i> calcification of aortic explants from 6 month old male WT and KO mice	101
Figure 51: Diastolic, systolic and mean arterial pressure of 3–6 month old male WT and KO mice, measured by tail cuff.	110
Figure 52: Diastolic, systolic and mean arterial pressure of 10–14 month old male WT and KO mice as measured by tail cuff..	110
Figure 53: Diastolic, systolic and mean arterial pressure of 4 month old male WT and KO mice as measured by tail cuff.	111
Figure 54: Diastolic, systolic and mean arterial pressure of 9 month old male WT and KO mice as measured by tail cuff.	111
Figure 55: Diastolic, systolic and mean arterial pressure of 17 month old male WT and KO mice as measured by tail cuff.....	112
Figure 56: Combined normalised diastolic, systolic and mean arterial pressure of all age groups including the overestimated values of the 3-6 and 10-14 month age group measurements.	112
Figure 57: Combined normalised diastolic, systolic and mean arterial pressure of all age groups excluding the overestimated values of the 3-6 and 10-14 month age group measurements.	113
Figure 58: Average paw temperatures of 3–6 and 10–14 month old WT and KO mice.....	113
Figure 59: Systolic, diastolic and mean arterial pressure traces of WT and KO mice fed a standard diet or high salt diet as measured by radiotelemetry.....	116
Figure 60: Pulse height, heart rate and dp/dt traces of WT and KO mice fed a standard diet or high salt diet as measured by radiotelemetry.....	117
Figure 61: Systolic, diastolic and mean arterial pressure traces of WT and KO mice fed a standard diet or 0.5 mg / l L-NAME in the drinking water as measured by radiotelemetry. .	118
Figure 62: Pulse height, heart rate and dp/dt traces of WT and KO mice fed a standard diet or 0.5 mg / l L-NAME in the drinking water as measured by radiotelemetry.....	119

Figure 63: Systolic, diastolic and mean arterial pressure of WT and KO mice during their active and resting times of the day, fed on standard diet or high salt diet as measured by radiotelemetry.....	121
Figure 64: Pulse height, heart rate and dp/dt of WT and KO mice during their active and resting times of the day, fed on standard diet or high salt diet as measured by radiotelemetry..	122
Figure 65: Systolic, diastolic and mean arterial pressure of WT and KO mice during their active and resting times of the day, fed on standard diet or 0.5 mg / ml L-NAME as measured by radiotelemetry.....	124
Figure 66: Pulse height, heart rate and dp/dt of WT and KO mice during their active and resting times of the day, fed on standard diet or 0.5 mg / ml L-NAME as measured by radiotelemetry.....	125
Figure 67: Long axis cardiac MRI scans of hearts from 12 month old WT and KO mice during diastole and systole.	127
Figure 68: Short axis cardiac MRI scans of the third basal slice of hearts from 12 month old WT and KO mice showing diastole and systole.....	127
Figure 69: Measured and calculated left-ventricular cardiac parameters from short-axis cardiac cine-MRI scans of 12 month old WT and KO mice.	128
Figure 70: Calculated cardiac remodelling indices of from short-axis cardiac cine-MRI scans of 12 month old WT and KO mice.....	129
Figure 71: Measured heart dimensions from long-axis cardiac cine-MRI scans of 12 month old WT and KO mice.....	129
Figure 72: Parameters obtained from cardiac cine-MRI scans of 12 month old mice normalised to TBW. See Table 9 for abbreviations..	130
Figure 73: Long axis cardiac MRI scans of hearts from 14 month old WT and KO mice showing diastole and systole.	133
Figure 74: Short axis cardiac MRI scans of the third basal slice of hearts from 3 representative hearts from 14 month old WT and KO mice with visible remodelling (KO rem) showing diastole and systole.....	134
Figure 75: Short axis cardiac MRI scans of the second apical slice of 3 representative hearts from 14 month old WT and KO mice with visible remodelling (KO rem) showing diastole and systole. Green = epicardium, red = endocardium.....	134
Figure 76: 3D reconstruction of the manually segmented left ventricles of 3 representative hearts from 14 month old WT and KO mice with visible remodelling (KO rem).	135

Figure 77: Measured and calculated left-ventricular cardiac parameters from short-axis cardiac cine-MRI scans of 14 month old WT, KO mice without visible cardiac remodelling (KO (no rem)) and KO mice with visible remodelling (KO (rem))	136
Figure 78: Calculated cardiac remodelling indices of from short-axis cardiac cine-MRI scans of 14 month old WT, KO mice without visible cardiac remodelling (KO (no rem)) and KO mice with visible remodelling (KO (rem)).	137
Figure 79: Measured right ventricular cardiac parameters from short-axis cardiac cine-MRI scans of 14 month old WT, KO mice without visible cardiac remodelling (KO (no rem)) and KO mice with visible remodelling (KO (rem))	137
Figure 80: Measured heart dimensions from long-axis cardiac cine-MRI scans of 14 month old WT, KO mice without visible cardiac remodelling (KO (no rem)) and KO mice with visible remodelling (KO (rem)).	138
Figure 81: Parameters obtained from cardiac cine-MRI scans of 14 month old mice normalised to TBW	139
Figure 82: Possible mechanisms of direct interaction of the VSMC CaSR with contraction and dilation of VSMC.	150
Figure 83: Wire myography experiments performed by Dr. Polina Yarova and Dr. Thomas Davies (Davies 2013)	152
Figure 84: Simplified model of balanced CaSR action on VSMC and the endothelium.	153
Figure 85: Proposed mechanism of the CaSR in VSMC and endothelial cells.....	156
Figure 86: Metabolic cage studies of WT and KO mice.	166
Figure 87: Metabolic cage studies of 3 month old male WT and KO mice.	168
Figure 88: Metabolic cage studies of 3 month old male WT and KO mice	169
Figure 89: Electrolyte analysis of sera collected from 3 month old WT and KO mice.	171
Figure 90: Electrolyte analysis of sera collected from 18 month old WT and KO mice.	171
Figure 91: FGF23 levels of sera collected from 3 month old WT and KO mice.	172
Figure 92: FGF23 levels of sera collected from 18 month old mice.	172
Figure 93: PTH, 1,25-D3, renin, aldosterone and fetuin A levels of plasma collected from 3 month old male WT and KO mice	173
Figure 94: Electrolyte, creatinine, blood urea nitrogen and total protein levels of sera collected from male WT and KO mice following metabolic cage studies and 2 days of 0.5 mg / ml L-NAME (drinking water) administration.	174

Figure 95: Electrolyte concentrations of urine from 24 h collections using metabolic cages from 3 month old WT and KO mice on standard or high salt (containing 4 % (w/w) NaCl) diet.....	176
Figure 96: Clinical chemistry of urine from 24 h collections using metabolic cages from 3 month old WT and KO mice on standard or high salt (containing 4 % (w/w) NaCl) diet.....	177
Figure 97: Bone parameters of the trabecular bone of the distal femur of 3 month old WT and KO mice as determined by μ CT.....	178
Figure 98: Bone parameters of the cortical bone of tibio-fibular junction of the distal femur of 3 month old WT and KO mice as determined by μ CT.....	179
Figure 99: Possible mechanism of mineral ion homeostasis and related phenotypic phenomena in the SM22 α -Cre x LoxP-CaSR mouse.....	188
Figure 100: Quantitative fluorescence microscopy of TUNEL stained VSMC preparations showing TUNEL staining intensity and nuclei size	241
Figure 101: Quantitative fluorescence microscopy of TUNEL stained VSMC preparations showing percentage of apoptotic cells.....	242
Figure 102: Quantitative fluorescence microscopy of TUNEL stained VSMC preparations showing percentage of apoptotic cells of VSMC.....	243
Figure 103: Quantitative fluorescence microscopy of TUNEL stained VSMC preparations showing total cell density	244
Figure 104: Illustration of small differences in the circadian rhythms of the single mice on a segment of MAP curves from two different mice.....	247
Figure 105: Illustration of local minimum / maximum detection on a segment of a MAP curve (smoothed by rolling average over 4 hours) of a single mouse.....	247
Figure 106: Systolic, diastolic and mean arterial pressure of WT and KO mice during their active and resting times of the day, fed on standard diet or high salt diet as measured by radiotelemetry.....	248
Figure 107: Pulse height, heart rate and dp/dt of WT and KO mice during their active and resting times of the day, fed on standard diet or high salt diet as measured by radiotelemetry.....	249
Figure 108: Systolic, diastolic and mean arterial pressure of WT and KO mice during their active and resting times of the day, fed on standard diet or 0.5 mg / ml L-NAME as measured by radiotelemetry.....	251

Figure 109: Pulse height, heart rate and dp/dt of WT and KO mice during their active and resting times of the day, fed on standard diet or 0.5 mg / ml L-NAME as measured by radiotelemetry.....	252
Figure 110: Long axis cardiac MRI scans of hearts from 18 month old WT and KO mice showing diastole and systole.	256
Figure 111: Short axis cardiac MRI scans of the third basal slice of hearts from 18 month old WT and KO mice showing diastole and systole.....	256
Figure 112: Measured and calculated left-ventricular cardiac parameters from short-axis cardiac cine-MRI scans of 18 month old WT and KO mice.	257
Figure 113: Calculated cardiac remodelling indices of from short-axis cardiac cine-MRI scans of 18 month old WT and KO mice.	258
Figure 114: Approximated left ventricular EF from the third basal slice of short axis cine-MRI scans of 18 month old WT and KO mice.	258
Figure 115: Measured heart dimensions from long-axis cardiac cine-MRI scans of 18 month old WT and KO mice.....	259
Figure 116: Parameters obtained from cardiac cine-MRI scans of 18 month old mice normalised to TBW.	260

List of tables

Table 1: Studies performed on transgenic mouse models of CaSR deletion. Studies are ordered chronologically.....	30
Table 2: Control, WT, HET and KO genotype depending on Sm22 α -Cre and CaSR-LoxP expression.....	34
Table 3: Primer sequences and expected product sizes for genotyping of SM22 α -Cre x LoxP-CaSR mice.....	35
Table 4: Mastermix for SM22 α -Cre PCR.....	36
Table 5: Thermocycler program for SM22 α -Cre PCR.....	36
Table 6: Mastermix for CaSR-LoxP PCR.....	36
Table 7: Thermocycler program for CaSR-LoxP PCR.....	36
Table 8: Parameters obtained from radiotelemetry.....	51
Table 9: Parameters obtained from cardiac cine MRI analysis.....	58
Table 10: Bone structure parameters measured by μ CT.....	61
Table 11: List of tested anti-CaSR antibodies.....	68
Table 12: Summary of the observed phenotype of the SM22 α -Cre x LoxP-CaSR mouse in the course of this thesis.....	195
Table 13: Future experiments to further the understanding of the VSMC CaSR and the phenotype of the SM22 α -Cre x LoxP-CaSR mouse.....	196
Table 14: Weights of WT, HET and KO mice.....	226
Table 15: Results of quantitative immunofluorescence analysis of CaSR expression levels in VSMC preparations of passages 2-6 cultured from WT and KO aortae.....	227
Table 16: Results of VSMC proliferation studies.....	227
Table 17: Results of <i>ex vivo</i> aortic ring calcification experiments.....	228
Table 18: Blood pressure measurements via tail cuff.....	229
Table 19: Paw temperatures of 3-6 and 10-14 month old male mice.....	230
Table 20: Results of radiotelemetry experiments carried out on 3 month old WT and KO mice, standard diet (1) vs. high salt diet (4 % NaCl diet).....	231
Table 21: Results of radiotelemetry experiments carried out on 3 month old WT and KO mice, standard diet (2) vs. 0.5 mg / l L-NAME in drinking waters.....	232
Table 22: Results of cardiac MRI analysis of 12 month old animals.....	233
Table 23: Results of cardiac MRI analysis of 14 month old animals).....	234

Table 24: Results of cardiac MRI analysis of 14 month old animals normalised to total body weight.	235
Table 25: Results of metabolic cage studies of 12-18 month old WT and KO animals and 3 month old WT and KO animals on standard or high salt (containing 4 % NaCl) diet.....	236
Table 26: Clinical chemistry of WT and KO mouse serum and plasma.	237
Table 27: Clinical chemistry of WT and KO mouse urine.....	238
Table 28: Results of μ CT analysis of 3 month old WT and KO mice.	239
Table 29: Results of quantitative fluorescence microscopy of TUNEL stained VSMC preparations.	245
Table 30: Results of radiotelemetry experiments carried out on 3 month old WT and KO mice, standard diet (1) vs. high salt diet (4 % NaCl diet).....	253
Table 31: Results of radiotelemetry experiments carried out on 3 month old WT and KO mice, standard diet (2) vs.0.5 mg / l L-NAME in drinking water	254
Table 32: Results of cardiac MRI analysis of 18 month old animals.....	261

Contributions

The project was started by Dr. Thomas Davies, who described the basic phenotype, *ex vivo* wire myography results and *in vitro* data (Davies 2013). Because of the highly collaborative nature of this project, many experiments, especially of the *in vitro* characterisation, were performed by Dr. Davies and me in a joint manner. Furthermore, Dr Polina Iarova, Dr. Sarah Brennan and Mrs Irene Lopez of our laboratory, as well as various external collaborators, contributed to the project. All contributors or data obtained through external means are referenced in the text and with the respective figures. All data analysis and interpretation of results provided in the results chapters are my own.

1 Introduction

In the course of this introduction, I want to give brief overviews of the calcium-sensing receptor (CaSR), its main actions in mineral ion metabolism and CaSR associated disorders. Furthermore, I will describe the discovered roles of the CaSR its role in the vasculature and in vascular calcification, thereby explaining the rationale behind this thesis and finally introduce models of CaSR deletion which are used to study CaSR function *in vivo* to set the stage for the investigations undertaken in the course of my thesis.

1.1 The extracellular Calcium-Sensing Receptor

1.1.1 General

In 1993, Brown *et al.* discovered a previously unknown G protein-coupled receptor in bovine parathyroid glands (Brown *et al.* 1993). The main physiological ligand of this receptor is extracellular free ionised calcium (Ca^{2+}), which consequently led to its name, extracellular calcium-sensing receptor (CaSR). The main function of this CaSR was discovered to be the regulation of free plasma Ca^{2+} levels via suppression of parathyroid hormone (PTH) synthesis and secretion in the parathyroid gland (Brown *et al.* 1993). In the years following the cloning of this receptor, CaSR expression was found not only in the parathyroid glands, but also in a multitude of organs including kidney (Riccardi *et al.* 1998), bone and cartilage (Chang *et al.* 2008), placenta (Bradbury *et al.* 1998), intestine (Chattopadhyay *et al.* 1998), pancreas (Bruce *et al.* 1999; Rasschaert and Malaisse 1999), skin (Komuves *et al.* 2002), brain (Ruat *et al.* 1995), liver (Canaff *et al.* 2001) and the vasculature (Bukoski *et al.* 1997; Weston *et al.* 2005; Ziegelstein *et al.* 2006). However, in many of these organs the roles of this protein are not yet fully understood.

The CaSR is a member of family C of the G protein-coupled receptors (GPCRs). This family comprises three subfamilies of receptors with group 1 containing metabotropic glutamate receptors (mGluRs), group 2 containing the CaSR and vomeronasal organ receptors and group 3 comprising of the γ -amino-butyric acid receptor family B (GABA_B) receptor subfamily (Brown and MacLeod 2001). Receptors belonging to family C GPCRs share a common topology which consists of a very large extracellular domain which forms a so called Venus-fly trap domain, which is an evolutionary old protein feature is involved in invertebrate

ligand sensing (Felder et al. 1999) and which contains Ca^{2+} binding sites (Silve et al. 2005). The human CaSR consists of 1085 amino acids and is encoded by a gene organized in 7 exons, with exon 2-6 encoding the extracellular domain (613 amino acids) and exon 7 encoding the transmembrane and intracellular domains (250 and 222 amino acids respectively (Brown et al. 1993); Figure 1). The CaSR is expressed at the cell surface in the form of homodimers (Bai et al. 1998; Ward et al. 1998), held together via disulphide bonds at cysteine residues 129 and 131 (Ray et al. 1999) as well as non-covalent interactions (Zhang et al. 2001b). The CaSR sequence shows high homology across different species, e.g. $\sim 90\%$ for rat and mouse (Riccardi et al. 1995; Pi et al. 2000) compared to the initially identified bovine receptor, and it is highly evolutionary conserved across vertebrates in general (Herberger and Loretz 2013).

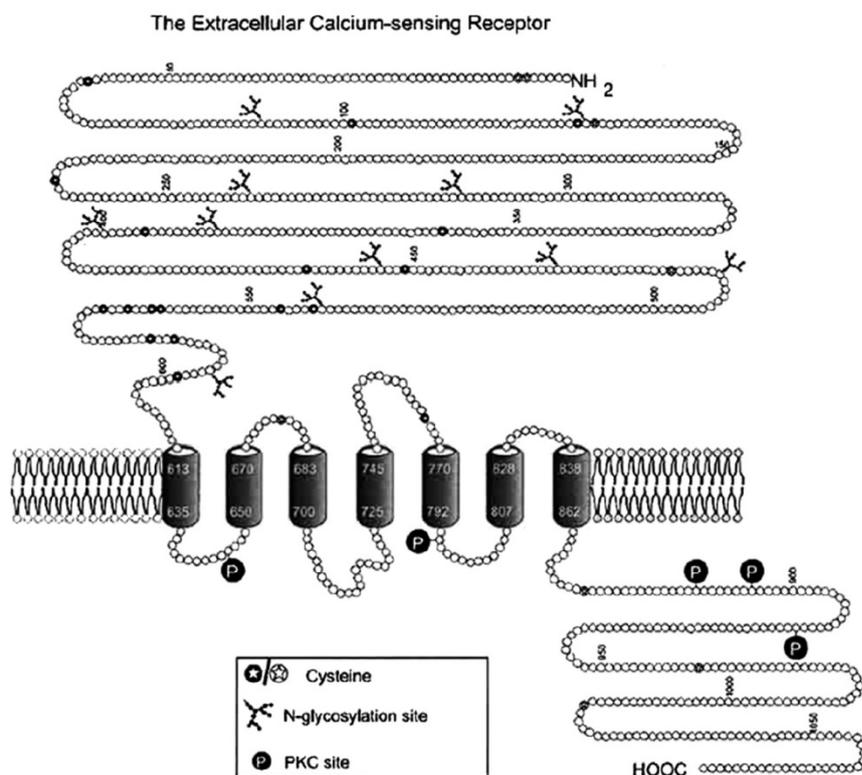


Figure 1: Topology of the human CaSR showing the large extracellular domain typical for family C type GPCRs. The rectangle indicates the plasma membrane region (Smajilovic and Tfelt-Hansen 2007). Image used under license from Oxford University Press.

1.1.2 Ligands of the CaSR

Compared to other GPCRs, the EC_{50} of the CaSR for Ca^{2+} in parathyroid cells is rather high (ca. 1.2 mM) (Brown and MacLeod 2001), but such a feature is compatible with the role for the receptor in the control free ionised blood plasma Ca^{2+} levels within a very narrow concentration frame (1.1 – 1.3 mM Ca^{2+}). This tight control is possible through a very high cooperativity of the receptor, which results in a very steep inverse dependence for PTH secretion of Ca^{2+} levels (Figure 2). It has been shown that this steep control of receptor activation is facilitated by a mechanism named agonist-driven insertion signalling (ADIS) which appears to be a unique feature of the CaSR. In ADIS, activation of the receptor leads to maturation and insertion of more receptors into the plasma membrane (Grant et al. 2011) from its main reservoir the endoplasmic reticulum (Cavanaugh et al. 2010).

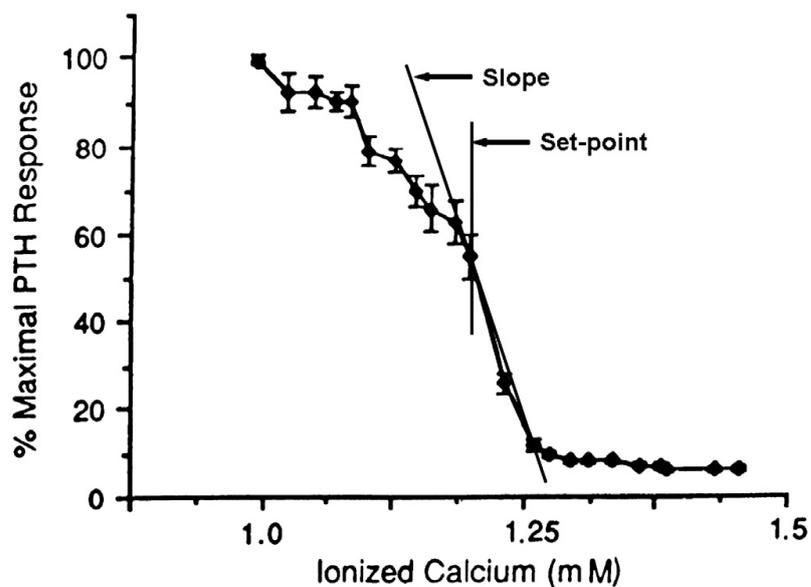


Figure 2: Ca^{2+} dose dependent suppression of PTH release. The “Set point” indicates the physiological free ionised blood plasma Ca^{2+} level. Zero to maximal effect (suppression of PTH secretion) is achieved over a very narrow concentration range, resulting in a steep PTH / Ca^{2+} relationship (Brown 2013). Image used under license from Elsevier.

CaSR activation can effect a variety of intracellular signalling cascades, largely involving activation of $G_{q/11}$, but also including $G_{i/o}$, $G_{12/13}$ and β -arrestin. The preference for one of these pathways has recently been shown to be influenced by the type of agonist activating the CaSR, orthosteric and allosteric alike (Davey et al. 2012; Thomsen et al. 2012). More

information on CaSR signalling which would go beyond the scope of this thesis can be found in the aforementioned literature as well as in many pertinent reviews (Brown and MacLeod 2001; Hofer and Brown 2003; Magno et al. 2011).

Orthosteric agonists achieve direct activation of the CaSR. As already indicated, in addition to Ca^{2+} , the CaSR also binds a variety of other ligands. Orthosteric and allosteric agonists, as well as antagonists have been identified.

Orthosteric agonists, which are able to activate the receptor directly in the absence of Ca^{2+} , include di- and trivalent cations (such as Ca^{2+} , Sr^{2+} , Mg^{2+} , Gd^{3+} or La^{3+}) (Brown and MacLeod 2001) polyamines (spermine, spermidine) (Quinn et al. 1997) and aminoglycoside antibiotics (e.g. neomycin, gentamicin) (McLarnon et al. 2002).

Amino acids like L-Phe, L-Trp, L-Tyr and L-His act as natural allosteric agonists of the CaSR (Conigrave et al. 2007). Synthetic allosteric agonists of the CaSR are the so called calcimimetics (including compounds such as Cinacalcet, Calindol or R-568). Cinacalcet has been approved as medication for treating severe hyperparathyroidism caused by chronic kidney disease (CKD), so called secondary hyperparathyroidism (see below) (Cunningham et al. 2011). However, cinacalcet also sees off-label use for therapy of primary hyperparathyroidism (e.g. by adenoma of the parathyroid gland) or phosphate wasting (Shoback et al. 2003; Brown 2010).

Calcilytics are allosteric antagonists of the CaSR show therapeutic potential, as exemplified by their possible use for the treatment of hypoparathyroidism (Saidak et al. 2009) or Alzheimer's disease (Armato et al. 2013). Because of their potential to evoke rapid fluctuations in PTH levels, some compounds of this class were initially developed for the treatment of osteoporosis (John et al. 2011). On the other hand, the profile of PTH release was recently found to be unfavourable for treatment of osteoporosis at least for the calcilytic ronacaleret (Caltabiano et al. 2013).

In contrast to the orthosteric agonists, these allosteric-acting compounds require the presence of an orthosteric ligand like Ca^{2+} to affect the receptor and thus can only modulate the potency of orthosteric compounds by shifting the half-maximal effective concentration (EC_{50}) for Ca^{2+} to the left (calcimimetics) or right (calcilytics). Figure 3 illustrates these effects. Interestingly, neither natural / nor synthetic endogenous orthosteric antagonists of the CaSR have been found (Saidak et al. 2009).

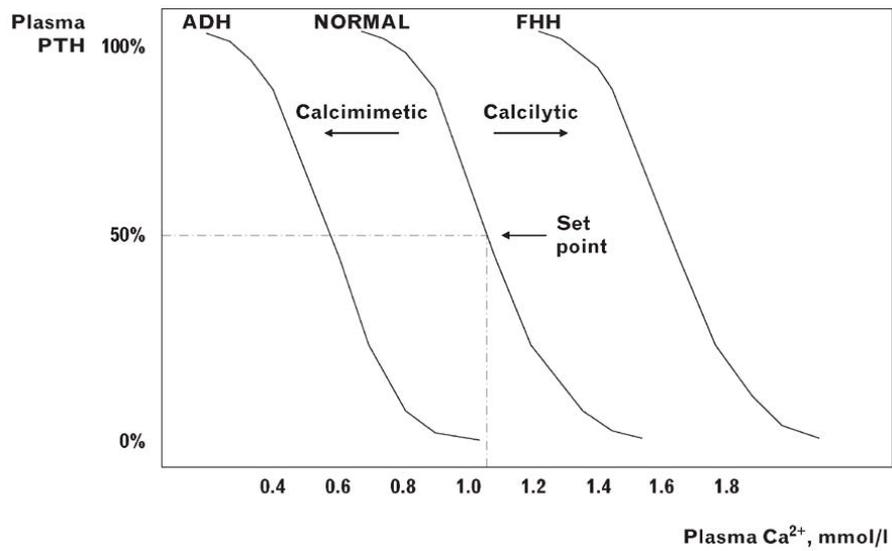


Figure 3: Blood Ca²⁺ set point for PTH secretion. Increasing blood Ca²⁺ concentrations reduce PTH secretion caused by the CaSR. The allosteric CaSR agonists calcimimetics, as well as activating mutations of the CaSR (autosomal dominant hypocalcaemia, ADH) cause left shifts of the curve, indicative of the greater activation of the CaSR in response to blood Ca²⁺, while the allosteric CaSR antagonists calcilytics as well as heterozygous inactivating mutations (familial hypercalcaemic hypercalciuria, FHH) cause rightward shifts, indicative of attenuated CaSR activation. (Christensen et al. 2011). Image used under license from Wolters Kluwer Health.

1.2 The role of the CaSR in Ca²⁺ homeostasis

1.2.1 Ca²⁺ homeostasis and the CaSR

Ca²⁺ homeostasis is a highly controlled process and involves a variety of hormones which are interconnected by multiple feedback loops. Figure 4 shows an overview of these complex interactions. The CaSR plays a major role in this homeostasis by directly or indirectly controlling the various factors that contribute to absorption, reabsorption, resorption and excretion of Ca²⁺ thus keeping blood Ca²⁺ levels in their physiological range, which is about 1.1 – 1.3 mM free ionised Ca²⁺. The largest reservoir for Ca²⁺ is the bone, which contains 85 % of the bodies Ca²⁺ in the form of hydroxyapatite (Ca₁₀(PO₄)₆(OH)₂) (Guyton and Hall 2006).

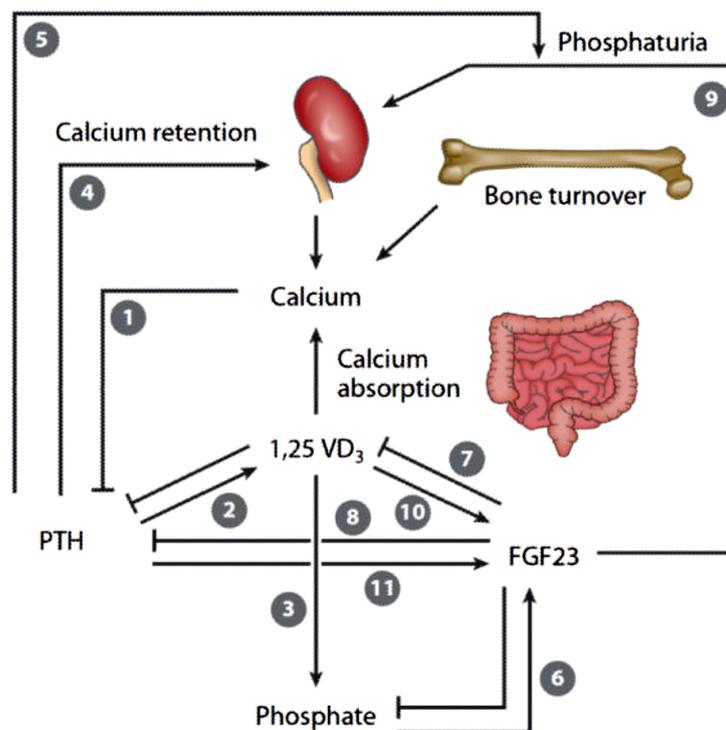


Figure 4: Ca²⁺ and Pi homeostasis. (1) Ca²⁺ suppresses PTH release via the CaSR. (2) PTH stimulates 1,25-D3 synthesis in the kidney which is in turn inhibiting PTH release via negative feedback. (3) 1,25-D3 stimulates Ca²⁺ and Pi (re-) absorption from kidney and intestine. (4) PTH also has a direct effect on the kidney where it increases Ca²⁺ reabsorption and (5) increases bone turnover which can act, dependent on the secretion kinetics, either act net anabolic (transient spikes) or catabolic (continuous elevation). (8) In bone, PTH also stimulates the production of FGF23, which decreases renal Pi reabsorption and leads to (9) phosphaturia via downregulation of NaPi2A and

NaPi2C Na⁺-Pi cotransporters (Gattineni et al. 2009). (7, 10) FGF23 has an inhibiting effect on 1,25-D3 production, which in turn upregulates FGF23 production. (11) FGF23 also inhibits PTH production, although this effect seems to be lost under uremic conditions (Canalejo et al. 2010). Modified after (Hu et al. 2013). Image used with permission from Annual Reviews.

1.2.1.1 Systemic effects of the CaSR

As mentioned, the most prominent and first discovered role of the CaSR is regulation of PTH production in the parathyroid gland (Brown et al. 1993). PTH is a key regulator of Ca²⁺ provision in case of hypocalcaemia sensed by the CaSR. The main function of PTH is to increase blood Ca²⁺ levels. PTH is secreted from chief cells of the parathyroid gland and acts on the kidney, by increasing renal Ca²⁺ reabsorption, by increasing Pi excretion, and by upregulating 1 α -hydroxylase thus increasing production of the hormone 1,25-(OH)₂-Vitamin D3 (calcitriol, 1,25-D3). Furthermore, PTH, as well as 1,25-D3, stimulate bone resorption by acting on osteoblasts upregulating receptor activator of nuclear factor κ B ligand (RANKL) production and thereby bone-resorption through osteoclasts (Brown 2013).

With regard to Figure 2 it was already mentioned that the CaSR keeps a tight control over PTH secretion with a very steep relation between Ca²⁺_o and PTH production. This control does not end at increased PTH secretion though. In case of high PTH demand, like in some of the disorders mentioned in section 1.2.2, continuous hypocalcaemia leads to upregulation of PTH gene expression and finally increased proliferation of parathyroid cells, leading to parathyroid hyperplasia (Naveh-Manly et al. 1995) which is associated with a loss of CaSR expression (Yano et al. 2000, 2003). Importantly, calcimimetics can upregulate CaSR expression in hyperplastic parathyroid glands, contributing to the therapeutic effect of enhanced CaSR activation in hyperparathyroidism (Mendoza et al. 2009).

Activation of the parathyroid CaSR not only reduces PTH secretion, but also enhances vitamin D receptor (VDR) expression (Rodriguez et al. 2007; Mendoza et al. 2009). 1,25-D3 acting on the parathyroid VDR inhibits PTH secretion, thus acting together with the CaSR to defend against hypercalcaemia. Finally 1,25-D3 also inhibits its own production via VDR, thus acting as a negative feedback loop.

1,25-D3 production by the rate-limiting enzyme 1- α -hydroxylase in the renal proximal tubules is stimulated by PTH and stimulates Ca²⁺ and Pi absorption from the gastrointestinal tract as well as reabsorption from the kidney (Guyton and Hall 2006). 1,25-D3, which is upregulated

by PTH, not only promotes increased Ca^{2+} but also Pi absorption. As a negative feedback mechanism, both 1,25-D3 as well as Pi stimulate upregulation of fibroblast growth factor 23 (FGF23).

FGF23 is a 251 amino acid factor (Yamashita et al. 2000) which is synthesized chiefly in osteocytes, and together with its co-factor Klotho, inhibits Pi reabsorption in the kidney by inhibiting insertion of phosphate transporters in the proximal tubule (Razzaque 2009) but also inhibits PTH release and 1,25-D3 synthesis (Krajisnik et al. 2007), thus contributing to maintaining blood Pi levels. This feedback mechanism is important, as increased 1,25-D3 stimulates both Ca^{2+} and Pi absorption. To avoid an inappropriate increase in the $\text{Ca}^{2+} \times \text{Pi}$ product, FGF23 in turn lowers Pi concentration by inhibiting Pi reabsorption (Quinn et al. 2013b). Finally, FGF23 also exerts an inhibiting influence on PTH as well as 1,25-D3 production, again closing a negative feedback loop, as reviewed in (Brown 2013)..

Apart from these systemic effects on Ca^{2+} homeostasis, the CaSR also has very specific local effects that contribute to maintenance of Ca^{2+} homeostasis, which include roles in the kidney and in bone.

1.2.1.2 Local effects of the CaSR

In the kidney, the CaSR acts independently of PTH to predominantly decrease blood Ca^{2+} levels by preventing further reabsorption of Ca^{2+} from the filtrate. The best documented action of the CaSR in the kidney is its action in the thick ascending limb, where Ca^{2+} (and Mg^{2+}) reabsorption passively follows a gradient in potential difference between positively charged luminal side and negatively charged intracellular side. Apical NKCC2 transports 1 Na^+ , 1 K^+ and 2 Cl^- into the cells of the thick ascending limb. K^+ is brought back into the lumen by ROMK K^+ channels. Na^+ and Cl^- are transported into the blood by the $3\text{Na}^+/2\text{K}^+$ -ATPase and Cl^- channels. Therefore, the effusing K^+ creates a potential difference which in turn leads to increased passive (paracellular) reabsorption of Ca^{2+} and Mg^{2+} . Fitting with its main function to control Ca^{2+} homeostasis in the blood, increased serum Ca^{2+} levels activate the CaSR on the basolateral side of the thick ascending limb which inhibits ROMK channels. Therefore, less K^+ can be recycled into the lumen, leading to a reduction in NKCC2 activity and potential difference and therefore reduced reabsorption of Ca^{2+} , Mg^{2+} and Na^+ from the urine back into the blood, as reviewed in (Riccardi and Brown 2010). PTH induced

transcellular Ca^{2+} reabsorption is also inhibited by the CaSR (Motoyama and Friedman 2002). Apart from these actions in the thick ascending limbs, the CaSR also has roles in other parts of the nephron. In the proximal tubule, the luminal CaSR suppresses the PTH-induced inhibition of phosphate reabsorption (Ba et al. 2003) and is probably involved in inhibition of 1,25-D3 synthesis (Bland et al. 1999). In the distal tubule, the CaSR probably promotes Ca^{2+} -channel dependent transcellular Ca^{2+} reabsorption, as compensation for reduced Ca^{2+} reabsorption in case of renal Na^+ wasting (Topala et al. 2009). Finally, in the collecting ducts, the CaSR is involved in the upregulation of the Na^+/H^+ pump in the collecting ducts, which acidifies the urine in case of hypercalciuria to prevent formation of kidney stones (Renkema et al. 2009).

It was already mentioned that CaSR regulated PTH induces bone resorption by stimulation of RANKL production on osteoblasts. However, the CaSR is also expressed in the bone where it regulates mineralisation, but these functions are still poorly understood. Using their mouse model of targeted gene deletion (see 1.5.2), Chang and colleagues demonstrated that the osteoblast CaSR is directly responsible for regulation of osteoblast function as well as indirectly by inhibiting RANKL production (Chang et al. 2008; Dvorak-Ewell et al. 2011).

1.2.2 Genetic and acquired conditions relating to the CaSR

Because of its prominent role in regulation of Ca^{2+} homeostasis, it should not come as a surprise that disorders in mineral ion metabolism frequently involve the CaSR. Genetic conditions relating to the CaSR include familial hypocalciuric hypercalcaemia (FHH), neonatal severe hyperparathyroidism (NSHPT) and autosomal dominant hypocalcaemia (ADH). Acquired conditions include primary and secondary hyperparathyroidism.

1.2.2.1 Familial hypocalciuric hypercalcaemia

FHH is caused by heterozygous autosomal dominant inactivating mutations of the CaSR, causing a rightwards shift in the set point for blood Ca^{2+} levels. This change in set point means that patients suffering from FHH have higher PTH levels and increased Ca^{2+} reabsorption by the kidney, resulting in hypercalcaemia and hypocalciuria, thus the name. However, this change in blood Ca^{2+} levels is very often asymptomatic (Pollak et al. 1996;

Ward et al. 2012). 1,25-D3 levels are often normal in FHH. Since parathyroidectomy normally does not resolve FHH, it is important to discriminate between primary hyperparathyroidism (see below) and FHH. The best diagnostic criterion for this (apart from the detection of a known CaSR mutation) is the hypocalciuria associated with the reduced CaSR activation in the kidney. Reviewed in (Egbuna and Brown 2008; Christensen et al. 2011).

1.2.2.2 Neonatal severe hyperparathyroidism

Similar to FHH, NSHPT is caused by inactivating mutations of the CaSR, but in contrast to the former, both CaSR alleles are affected in NSHPT. In contrast to the mostly benign form of FHH, the loss of a functional CaSR in NSHPT leads to a life threatening condition which is associated with extreme hyperparathyroidism, hypercalcaemia and elevated 1,25-D3 levels, polyuria, reduced blood pressure, dehydration and failure to thrive, possibly leading to premature death. In severe cases, parathyroidectomy is the only option for treatment. Reviewed in (Pollak et al. 1996; Egbuna and Brown 2008).

1.2.2.3 Autosomal dominant hypocalcaemia

In contrast to FHH and NSHPT where inactivating mutations of the CaSR were right-shifting the blood Ca^{2+} set-point, activating mutations of the CaSR cause a left-shift of this set-point, thus leading to pathologically enhanced suppression of PTH release by the CaSR. The clinical presentation of this disorder can range from asymptomatic to severe, with low PTH levels, hypocalcaemia and hypercalciuria. Because of the latter, curative intervention with Vitamin D therapy can lead to formation of kidney stones. Reviewed in (Pollak et al. 1994; Egbuna and Brown 2008).

1.2.2.4 Bartter-like syndrome

Bartter syndrome, classified in types I-V are characterised by defective electrolyte reabsorption in the TAL of the kidney. Types I-IV are not related to the CaSR but mutations in the genes for certain ion channels and transporters. Bartter syndrome type V, also called Bartter-like syndrome is caused by severe gain-of-function mutations of the CaSR (Hebert

2003). As described, activity of NKCC2 is indirectly controlled by the inhibiting action of the CaSR on ROMK channels. Activating mutations in the renal CaSR (Vargas-Poussou et al. 2002) therefore lead to increased inhibition of ROMK channels, reduced activity of NKCC2, loss of the potential gradient in the loop of Henle and therefore reduces Ca^{2+} and Mg^{2+} reabsorption. The net effect is therefore renal salt, potassium, Ca^{2+} and Mg^{2+} wasting, going along with insufficient urine concentration, activation of the RAAS, polyuria and dehydration. The main criteria to discriminate Bartter-like syndrome from “classical” Bartter syndrome caused by mutations of ion channels and transporters (e.g. NKCC2 for Bartter syndrome type I) is the associated hypocalcaemia. Reviewed in (Hebert 2003; Egbuna et al. 2009; Ward et al. 2012).

1.2.2.5 Primary hyperparathyroidism

In primary hyperparathyroidism, PTH secretion is elevated despite high circulating blood Ca^{2+} levels. As the disorder originates only from the parathyroid gland, urinary Ca^{2+} excretion is not affected and primary hyperparathyroidism is therefore associated with hypercalciuria (in contrast to FHH, where the loss-of-function mutation in the renal CaSR leads to hypocalciuria). Primary hyperparathyroidism can be associated with hypertension, cardiac remodelling or blood vessel stiffness, although the data on this are conflicting, as these changes do not affect all patients (Silverberg 2000; Walker et al. 2010). Primary hyperparathyroidism is normally caused by parathyroid adenoma, in which expression of the CaSR is lost. It has also been shown that reduction of CaSR expression in parathyroid chief cells is associated with increased proliferation of these cells, explaining the parathyroid hyperplasia associated with this disorder (Naveh-Many et al. 1995; Yano et al. 2003). Reviewed in (Habib and Camacho 2010; Ward et al. 2012).

1.2.2.6 Secondary hyperparathyroidism

Secondary hyperparathyroidism, as the name implies, is not principally caused by changes in the parathyroid gland, but is instead a feature developing during progression of CKD. In this disease state, the progressive loss of renal function leads to decreased 1,25-D3 production and Pi excretion. The reduced 1,25-D3 levels lead to reduced absorption and reabsorption of Ca^{2+} , culminating in hypocalcaemia. The reduced blood Ca^{2+} levels lead to reduced suppression of

PTH release via the CaSR. Continuous stimulation of the parathyroid gland leads to hyperplasia in which CaSR expression is diminished (Lee et al. 2013). Reduced 1,25-D3 levels, as a feature of secondary hyperparathyroidism, again decreases the direct inhibitory effect of 1,25-D3 on PTH secretion. Parathyroid hyperplasia, together with reduced CaSR expression then leads to severe hyperparathyroidism which initiates bone catabolism and together with the impaired renal function, leads to hypercalcaemia in combination with hyperphosphataemia. Reviewed in (Cunningham et al. 2011). This increase in blood Pi and Ca²⁺ levels then can then induce vascular calcification, as described below.

1.3 Role of the CaSR in the vasculature

1.3.1 The vasculature and blood pressure regulation

Mammalian blood vessels consist of three layers, from the lumen outwards, these layers are the tunica intima, which is composed of a single layer of endothelial cells and forms the barrier to the blood. The tunica intima is separated by the innermost (internal) elastic lamina from the tunica media, which is composed of a varying number alternating layers of vascular smooth muscle cells (VSMC), and elastic laminae, depending on the size of the blood vessel.

The main physiological role of VSMC is to provide the means for contraction and maintenance of the blood vessel tone and therefore regulating blood supply (and pressure) in the organs of the body (Guyton and Hall 2006). VSMC are of mesenchymal origin (Shroff et al. 2013) which is important in the context of their transdifferentiation into cell types of the same origin, specifically osteoblast-like cells (see below).

The outermost (external) elastic lamina finally marks the beginning of the tunica adventitia, which anchors the blood vessel to the surrounding tissue. The tunica adventitia is made up of connective tissue, fibroblasts, bordering fatty tissue and perivascular nerves (and in case of very large arteries such as the aorta also *vasa vasorum*, i.e. supporting blood vessels to supply oxygen to the thick layers of cells in these arteries). See Figure 5 for a microphotograph of a murine aorta.

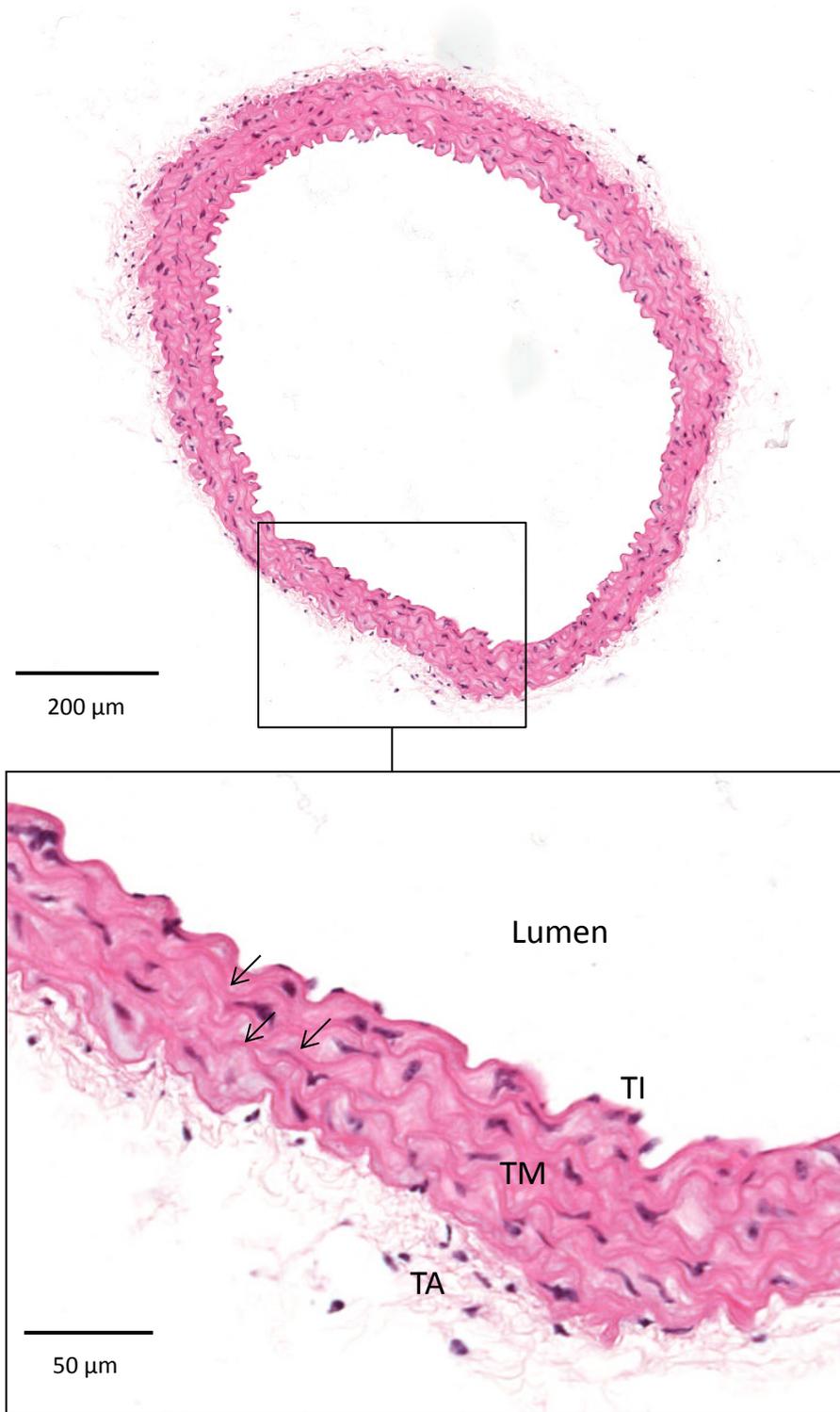


Figure 5: Histology of blood vessels. Microphotograph shows murine aorta cross-section in low (upper panel) and high (lower panel) magnification. Tunica adventitia (TA), tunica media (TM), tunica intima (TI), the lumen and elastic laminae (arrows) are indicated.

Arteries can be categorised into large conductance arteries, such as the aorta or the femoral artery, small resistance arteries, which are responsible for control of peripheral resistance and capillaries, where the gas exchange takes place and which form the last part of the blood vessel tree. Large conductance arteries act as a pressure reservoir by expanding during systole and contracting during diastole, keeping the blood flow constant during the cardiac cycle, the so called “Windkessel” effect (Belz 1995). A loss of elasticity, as associated with vascular calcification and arteriosclerosis, leads to increase stiffness of these large conductance arteries and a subsequent increase in pulse wave velocity and pulse height (PH, difference between systolic and diastolic blood pressure) with especially prominent increases in systolic blood pressure because the pressure reservoir effect is lost, as reviewed in (Amann and Ritz 1998; Dao et al. 2005). On the other hand, small resistance arteries serve as one of the main factors in blood pressure regulation by providing resistance (total peripheral resistance, TPR) against the blood flow.

Contraction of VSMC is regulated by the sympathetic nervous system through α 1-adrenergic receptors. Relaxation of VSMC is elicited indirectly by the action of endothelial cells by producing gaseous nitric oxide (NO), which acts in large conductance as well as small resistance arteries and the endothelial derived hyperpolarization (EDH) (Nagao et al. 1992), which is mostly active in the small resistance arteries (Shimokawa et al. 1996) and is a summary name for a variety of different factors including K^+ , reactive oxygen species or prostacyclin (Edwards et al. 2010) as well as charge transfer via myo-endothelial gap junctions (Sandow et al. 2002).

In addition to TPR, blood pressure is also dependent on blood volume, in that an increased blood volume, e.g. through osmotic causes like increased Na^+ ingestion, causes elevations in pressure while loss of blood volume, e.g. in hypovolemic shock goes along with reduced blood pressure. Blood volume and TPR are tightly controlled by the renin angiotensin aldosterone system (RAAS). In brief, the RAAS works by secretion of renin from the juxtaglomerular cells of the kidney following stimulation through various stimuli, the most important being reduction in urine compared to plasma osmolarity, and reduction in renal perfusion pressure. Renin cleaves angiotensinogen into angiotensin I which is metabolised in the lung by the angiotensin converting enzyme (ACE) into angiotensin II, the physiologically active form. Angiotensin II directly contracts resistance arteries thus increasing TPR and blood pressure by acting on AT1 receptors on VSMC effecting vasoconstriction through $G_{q/11}$ and intracellular (Ca^{2+}_i) signalling. Furthermore, angiotensin II induces production and

secretion of aldosterone, a mineralocorticoid hormone, which acts on the collecting duct of the kidney promoting upregulation of the Na^+/K^+ ATPase on the basolateral side of the collecting duct cells, as well as the amiloride sensitive Na^+ channel ENaC on the apical side, thus increasing reabsorption of water and Na^+ as well as excretion of K^+ . The net effect of RAAS activation is therefore an increase in blood pressure through increased TPR and blood volume (Guyton and Hall 2006; Kobori et al. 2007). See Figure 6 for a graphical representation of the RAAS.

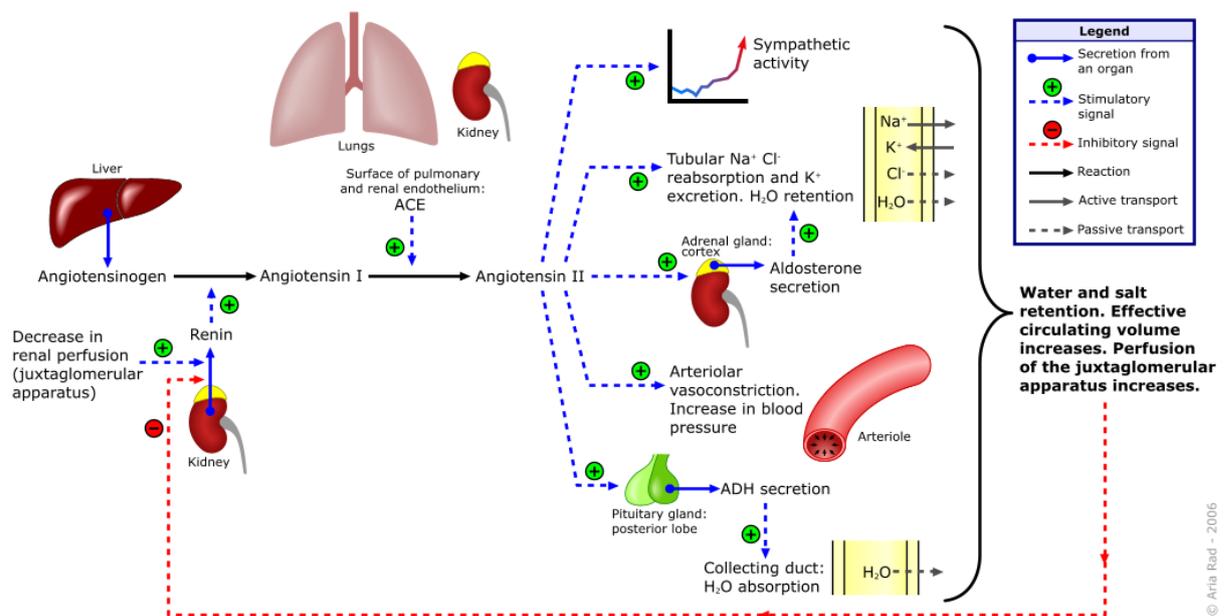


Figure 6: The renin-angiotensin-aldosterone system (RAAS). Renin which is secreted by the juxtaglomerular apparatus in response to decreased renal perfusion pressure and changes in filtrate osmolality cleaves liver-produced angiotensinogen into angiotensin I which in turn is cleaved into angiotensin II by the angiotensin converting enzyme (ACE). Angiotensin II then has a variety of effects, including increase of sympathetic activity, stimulation of aldosterone production and therefore tubular water and salt reabsorption, direct vasoconstrictive effects on blood vessels and antidiuretic hormone (ADH, vasopressin) secretion. The sum of these effects leads to an increase in blood pressure and circulating volume which in turn exhibits a negative feedback on the RAAS: Modified after A. Rad [licensed under GFDL (<http://www.gnu.org/copyleft/fdl.html>) or CC-BY-SA-3.0 (<http://creativecommons.org/licenses/by-sa/3.0/>)], via Wikimedia Commons.

Finally, blood pressure depends on heart rate or, more specifically, cardiac output (CO), which is defined as stroke volume x heart rate, thus indicating the amount of blood ejected by

the heart per time interval. Increases in CO increase predominantly systolic pressure (Klabunde 2005). Heart rate and blood pressure are closely regulated in physiology, with an increase in the one resulting in a compensating decrease in the other (baroreflex) thus keeping systemic blood pressure constant (Wang et al. 2004). Figure 7 shows an overview of factors contributing to blood pressure homeostasis.

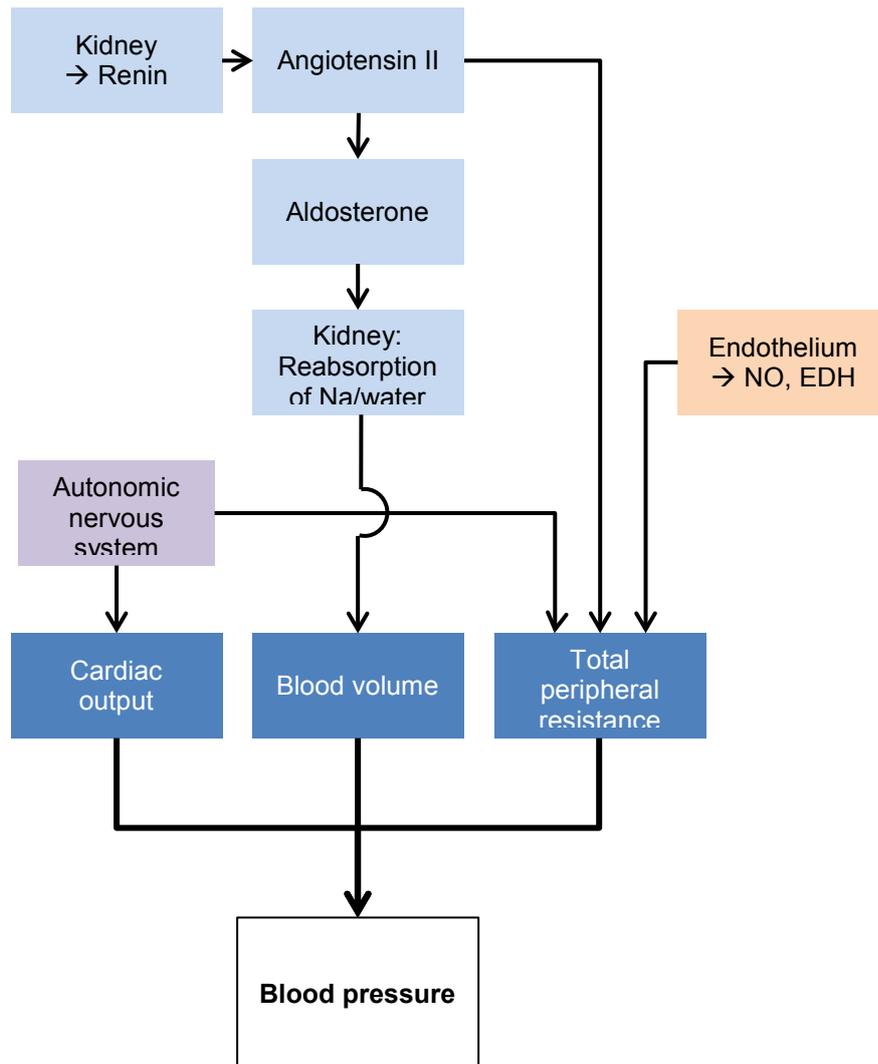


Figure 7: Simplified overview of factors contributing to blood pressure homeostasis. The autonomic nervous system (lilac) contributes to control of cardiac output and TPR via sympathetic and parasympathetic innervation. The RAAS (light blue) contributes to regulation of blood volume and TPR. Shear stress and other factors contribute to local autoregulation of TPR by the blood vessels themselves, e.g. by NO production or EDH (orange).

1.3.2 Direct effects of the CaSR on vascular tone

The CaSR has been found to be expressed in all three layers of blood vessels, the tunica intima, the tunica media as well as the tunica adventitia (Bukoski et al. 1997; Wonneberger et al. 2000; Ohanian et al. 2005; Weston et al. 2005). The functional role of the CaSR in these three layers of blood vessels has initially been related to vascular tone regulation.

The earliest discovery of CaSR in the vasculature was in 1997, when Bukoski et al. (Bukoski et al. 1997) found the CaSR to be expressed in the perivascular nerves of mesenteric arteries where it was believed to cause perivascular mediated vasodilation, a hypothesis which is now controversial (Weston et al. 2005).

CaSR in VSMC was identified first in the gerbilline spiral modiolar artery where CaSR activation was associated with a biphasic increase in Ca^{2+}_i induced vasoconstriction (Wonneberger et al. 2000). Ohanian and colleagues found the CaSR to be expressed in rat subcutaneous small arteries, where Ca^{2+}_o evoked a biphasic response of initial contraction in concentrations of up to 2 mM and dilation at higher concentrations (Ohanian et al. 2005). The CaSR has subsequently been found in cultured rat (Smajilovic et al. 2006), bovine and human VSMC, and in human (Alam et al. 2009) and murine aortae (Loot et al. 2013). Finally, the CaSR was found to be expressed in the vascular endothelium where activation of the receptor by the calcimimetic calindol produced endothelium-dependent relaxation of rat mesenteric arteries, which was mediated by VSMC hyperpolarization (Weston et al. 2005). In contrast to the described findings by Bukoski and colleagues (Bukoski et al. 1997), perivascular nerves did not seem to be involved in this effect. In the study by Weston *et al.* the authors concluded that this hyperpolarizing effect is the result of opening of the endothelial intermediate conductance Ca^{2+} sensitive K^+ channel (IK_{Ca}) by the CaSR, leading to endothelial hyperpolarisation which is transferred to the VSMC by gap-junctions or the increased interstitial K^+ concentrations resulting from IK_{Ca} activation (Weston et al. 2005). Another study performed on isolated human aortic endothelial cells (HAEC), provided evidence, through absence of the observed effects in CaSR siRNA treated cells, for a CaSR-dependent G_q modulated Ca^{2+}_i increase leading to stimulation of NO production (Ziegelstein et al. 2006), pointing towards an NO-mediated mode of VSMC relaxation for the endothelial CaSR. Similar observations were made in other studies, e.g. in a recent study on aortic rings of healthy and diabetic mice where the authors detected the CaSR in the endothelium as well as in VSMC (Loot et al. 2013). The endothelial CaSR evoked NO production and vasorelaxation

was reversible by calcilytics. The VSMC CaSR was described to have a potentiating effect on VSMC contraction induced by Ca^{2+}_i -dependent contracting agonists like the α_1 -adrenoreceptor agonist phenylephrine. In essence, Ca^{2+}_i removed from the VSMC into the interstitium activates the CaSR which in turn potentiates the initial contraction. Inexplicably, calcimimetics evoked a CaSR dependent, endothelium independent relaxation (Loot et al. 2013). One can speculate that this highly surprising result could be indicative of different signalling pathways by orthosteric and allosteric agonists (Davey et al. 2012) but further investigation in this phenomenon will clearly be necessary.

In addition, a recent study suggested that this endothelium-mediated effect on blood pressure regulation might not exclusively be CaSR regulated. On cultured HUVEC and HAEC, both the active R-enantiomer of the calcimimetic 568 (R-568) as well as the inactive S-enantiomer both evoked a response of increased Ca^{2+}_i mobilization and subsequent eNOS activation, in the absence or presence of the calcilytic calhex-231 (Bonomini et al. 2012). The authors speculate that GPRC6A, a structurally very similar “orphan” GPCR to CaSR which has been implicated in amino-acid as well as osteocalcin sensing (Clemmensen et al. 2014), could be the effector of the observed effect of R- and S-568 on eNOS activation in their study. It has to be noted however, that the concentrations of R- and S-568 used in these experiments were high (1–100 μM) which suggests that off-target effects of the compounds could have been responsible for the observed results. These target non-specific effects of (some) calcimimetics are related to their chemical structure, as they were originally derived from phenylalkylamines, inhibitors of L-type (voltage gated) Ca^{2+} channels (Nemeth et al. 1998). In another study calcimimetic-induced vasorelaxation has been attributed to the inhibition of Ca^{2+}_o influx into VSMC through inhibition of L-type Ca^{2+} channels, rather than activation of CaSR (or GPRC6A) (Thakore and Ho 2011).

These complex interactions and different observations of CaSR actions on endothelium and VSMC highlight the importance of our study of targeted gene deletion of the CaSR from VSMC.

1.3.3 *In vivo* effects of the CaSR on blood pressure

A calcium rich diet is generally recognized as reducing blood pressure (Ayachi 1979) while reduced Ca^{2+} intake is associated with an increase in blood pressure (McCarron et al. 1982).

The mechanism behind this blood pressure lowering effect of Ca^{2+} has been attributed to elevated diuresis (Ayachi 1979), reduction in sympathetic drive (Peuler et al. 1987) or direct dilatory effects on the vasculature thereby causing a reduction in TPR (Bukoski et al. 1997; Bukoski 2001). As implied by the multitude of *in vitro* results of the vascular CaSR on blood vessel contractility described above, some of these effects might be CaSR mediated.

Despite this possibly blood pressure lowering effect of a Ca^{2+} rich diet, patients suffering from hypercalcaemic hyperparathyroidism in CKD after renal transplantation are often hypertensive. Parathyroidectomy has been shown to reduce this hypertension in humans (Rostaing et al. 1997) and animals (Ogata et al. 2003). A similar reduction of blood pressure can be seen by calcimimetic treatment in humans (Zitt et al. 2011) as well as uremic animal models (Ogata et al. 2003; Odenwald et al. 2006). Indeed, calcimimetics have been shown to have a profound influence on blood pressure *in vivo*. In a study on healthy and uremic rats, R-568 showed a distinctive biphasic influence on blood pressure, leading to a short-term increase in blood pressure in both healthy and uremic animals which went back to normal in healthy animals but was succeeded by a pronounced antihypertensive long-term effect in uremic rats (Odenwald et al. 2006). A study by Fryer and colleagues suggested that this short-term increase in blood pressure might be attributed to reduced blood Ca^{2+} levels, leading to reduced activation of endothelial NO production (Fryer et al. 2007). Since Fryer and colleagues only studied the rats for 90 minutes following cinacalcet treatment, it is possible that they might have missed the beneficial long term blood pressure lowering effects of cinacalcet observed in the previously described studies.

Apart from the mentioned direct effects of the CaSR and calcimimetics on vascular tone, these blood pressure lowering effects on uremic animals could be related to other, more direct actions of the CaSR.

One of these could be the general protective effect the CaSR exerts against complications associated with CKD, such as arterial and cardiac remodelling (Ogata et al. 2003). Loss of blood vessel elasticity is associated with increased blood pressure (Dao et al. 2005). The CaSR has been implicated in protection against vascular calcification (see chapter 1.4) and one *modus operandi* of blood pressure reduction by calcimimetics could be via reduction, or prevention, of vascular remodelling. In their pertinent review on CaSR in blood pressure, Smajilovic and colleagues have however pointed out that this protection from calcification would be a very long-term effect which could hardly account for the blood pressure reducing

effects observed in studies over a course of days (Smajilovic et al. 2011). Indeed a large clinical trial, investigating the effects of cinacalcet on the prevention of cardiovascular diseases like myocardial infarction or heart failure failed to detect a protective influence of the calcimimetic on cardiovascular events. However, as described below, this study was riddled with major limitations, such as patients in the placebo group buying over-the-counter calcimimetics (Chertow et al. 2012).

Other possibilities of CaSR action on blood pressure regulation include interaction of the CaSR with sympathetic drive. An older study suggested an impaired sympathetic drive and baroreflex as the causes for Ca^{2+} induced hypotension (Peuler et al. 1987). Our own group have detected CaSR expression in sympathetic neurons (Vizard et al. 2008). The mechanisms of CaSR influence on sympathetic tone remain yet to be determined.

Other studies suggested that the blood pressure lowering action of calcimimetics might not at all be entirely CaSR mediated: intravenous administration of the calcimimetic R-568 and its non-CaSR selective enantiomer S-568 did not alter blood pressure in rats when applied in concentrations sufficient to induce suppression of PTH via CaSR activation. In higher concentrations, both R-568 and its non-CaSR sensitive enantiomer S-568 reduced blood pressure (Nakagawa et al. 2009), which might be attributed to non-specific effects on L-type Ca^{2+} channels (Smajilovic et al. 2007; Thakore and Ho 2011). These results were in line with the already described unspecific effects of R- and S-568 in HUVEC and HAEC *in vitro*, where both R- and S-568 enantiomers induced endothelial NO production (Bonomini et al. 2012). In support of the idea of non-CaSR mediated effects of calcimimetics on blood pressure reduction has been suggested in a recent study where R-568 was shown to inhibit the endothelin-converting-enzyme 1 in human endothelial cells (Martinez-Miguel et al. 2013).

Importantly, the CaSR has also been shown to be involved in renal renin production. Stimulation of the receptor with the calcimimetic cinacalcet directly inhibits renin production *in vivo* (Maillard et al. 2009; Atchison et al. 2010) and *in vitro* (Ortiz-Capisano et al. 2007) again emphasising the major role of the receptor in regulation of mineral ion homeostasis. However, the decrease in renin production did not go along with a decrease in blood pressure in rats treated with cinacalcet: low doses of the calcimimetic had no effect on blood pressure, while renin production was still reduced (Atchison et al. 2010). Another study found that the calcilytic NPS 2143 increased blood pressure in rats which was attenuated by losartan, an inhibitor of the angiotensin II AT1 receptor and potent anti-hypertensive drug, highlighting

the involvement of the CaSR, or allosteric modulators of the CaSR, in regulation of the RAAS (Rybczynska et al. 2010). In addition, Bartter V patients, in which there are activating CaSR mutations, exhibit hypokalaemia, hyperreninaemia and hyperaldosteronaemia (Vargas-Poussou et al. 2002).

1.4 Role of the CaSR in vascular calcification

1.4.1 Vascular calcification

It is important to differentiate between the different types of calcifications that can occur in blood vessels. When talking about vascular calcification, this generally means medial calcification (or Mönckeberg's sclerosis), which is predominantly associated with the mineral ion imbalance present in CKD, namely hyperphosphataemia and hypercalcaemia. Vascular calcification is the active process of mineral deposition in VSMC and is a major complication and one of the main causes of death in CKD and end-stage renal disease (ESRD) (Blacher et al. 2001; London et al. 2005). It has been shown that vascular calcification is directly associated with accelerated arterial aging and remodelling (Gauthier-Bastien et al. 2013; London et al. 2013) in CKD and ESRD patients and that Ca^{2+} load is a major factor in determining risk for aortic aging (London et al. 2008), resulting in blood vessel stiffening, subsequent rise in pulse wave velocity, hypertension and cardiac hypertrophy (Blacher et al. 1999). This should not be confused with calcific atherosclerosis, or intimal calcification, which is primarily caused by ossification of atherosclerotic plaques and is associated with inflammation, hypertension and dyslipidaemia and ischemic heart disease. Importantly, in contrast to atherosclerosis, vascular calcification is probably at least not initially associated with inflammation, although in advanced stages of CKD, atherosclerosis might occur together with medial calcification because of a high prevalence of risk factors for the former in such patients (Shroff et al. 2013). Finally, calcification of small peripheral arterioles, calcific uremic arteriolopathy, also called calciphylaxis, is a form of medial calcification which predominantly affects small arterioles, eventually causing occlusion and ischemia (Karwowski et al. 2012).

The arterial remodelling and calcification of blood vessels was shown to be caused by a transdifferentiation of medial VSMC into an osteoblast-like phenotype, going along with upregulation of typical bone-associated biomarkers such as alkaline phosphatase, osterix, or

runx-related transcription factor 2 (runx2) (Shanahan et al. 1999; Tyson et al. 2003). The importance of runx2 and osteogenic differentiation in the process of vascular calcification has recently been demonstrated by a mouse model of targeted deletion of runx2 from VSMC where the KO mice developed markedly less vascular calcification on a high fat diet than control mice (Sun et al. 2012). Indeed, the calcified deposits in calcified VSMC are chemically identical to the structure mineral of bone, namely hydroxyapatite (Duer et al. 2008).

It has been demonstrated that matrix vesicles originating from VSMC are initial sites of hydroxyapatite formation. These vesicles are a mechanism by which the cell rids itself from high Ca^{2+} levels and which under physiological conditions contain inhibitors of calcification such as fetuin A, pyrophosphate (PPi) and matrix gla protein (MGP) to prevent calcification. Fetuin A is produced in the liver accumulates at sites of calcification and binds Ca^{2+} and Pi complexes (Reynolds et al. 2005). PPi similarly is produced directly by VSMC and disrupts hydroxyapatite deposition, thus also protecting against vascular calcification (Prosdocimo et al. 2010). MGP protects against vascular calcification (Luo et al. 1997) by inhibiting crystal formation and scavenging bone morphogenic protein 2 (BMP-2), an inducer of osteogenic (trans)differentiation (Proudfoot and Shanahan 2006). In uraemia, these calcification inhibitors are depleted, leading to formation of hydroxyapatite in those vesicles (Reynolds et al. 2004; Reynolds et al. 2005). However, clinically, the levels of not all of these calcification inhibitors seem to be correlated with vascular stiffness in patients suffering from CKD. A relatively small correlation was only found for MGP but not fetuin A (Liabeuf et al. 2013). It is possible that the missing correlation of vascular calcification with circulating levels of fetuin A can be explained by the aforementioned accumulation of fetuin A at sites of calcification (Reynolds et al. 2005). Figure 7 provides a graphical overview of VSMC transdifferentiation into an osteogenic phenotype.

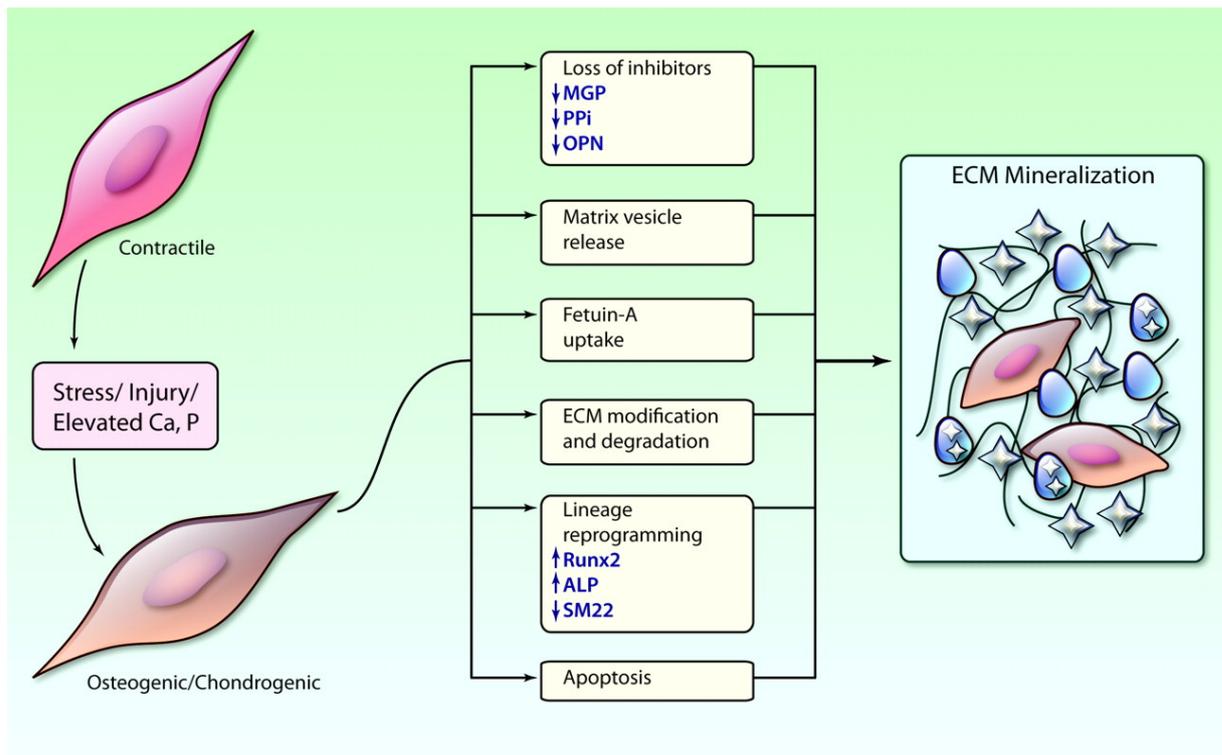


Figure 8: Overview of osteogenic VSMC transdifferentiation and calcification. Transdifferentiation of VSMC into an osteogenic phenotype goes along with a loss of calcification inhibitors and calcifying matrix vesicle release as well as changes in gene expression including upregulation of osteogenic marker genes like runx2 or alkaline phosphatase (ALP) and downregulation of smooth muscle markers like SM22. ECM = extracellular matrix (Shanahan et al. 2011). Image used under license from Wolters Kluwer Health.

Indeed, calcification of blood vessels is highly dependent on their environment. *Ex vivo* experiments on human blood vessels showed that, under the same conditions of high Ca^{2+}_o and Pi, blood vessels from dialysis patients exhibited a marked increase in calcification compared to blood vessels from healthy controls. This indicates that long term predisposition in an uremic environment is required for the onset of calcification and is believed to be associated with increased levels of apoptosis occurring in uremic blood vessels, which in turn form nucleation sites for beginning vascular calcification (Shroff et al. 2008).

The exact mechanism behind this phenotypic change and onset of vascular calcification is still unclear but seems to be a response to the altered environment of the cells in uremic conditions, that is elevated Pi and blood Ca^{2+}_o levels (Block et al. 1998). High Pi and Ca^{2+}_o levels were demonstrated to induce the upregulation of bone biomarkers in VSMC. Animal studies on uremic rats suggested that high phosphate levels induce the phenotypic

transdifferentiation of VSMC leading to vascular calcification (Pai et al. 2011). *In vitro* experiments also suggested that (passive) hydroxyapatite formation may precede the onset of vascular calcification and drives the transdifferentiation into an osteoblastic phenotype (Sage et al. 2011; Villa-Bellosta et al. 2011). It is very possibly that a combination of different effects occurs at the same time *in vivo*. The CaSR is believed to play a key role in preventing this transdifferentiation of VSMC into an osteoblastic phenotype which is described below.

As already hinted at, vascular calcification is very often associated with other cardiovascular complications such as hypertension and cardiac hypertrophy. Increased stiffness of large conductance arteries associated with vascular calcification results in a loss of the ability of the blood vessel to dilate in response to the systolic pressure, resulting in increased pulse wave velocity and pulse wave reflection leading to systolic hypertension. This results in an increase in cardiac afterload and consequently left ventricular hypertrophy (Blacher et al. 1999; Amann and Tyralla 2002; Dao et al. 2005).

1.4.2 Protection against vascular calcification by the CaSR

Recently, evidence has been accumulating that one of the roles of the vascular CaSR could be in the protection from vascular calcification.

Calcimimetics lower PTH – and consequentially extracellular Ca^{2+} levels – via activation of the CaSR in the parathyroid glands. In uremic animal models, administration of calcimimetics has been shown to be protective against vascular calcification and other complications. Consequently, an indirect protective effect of the CaSR against vascular calcification, mediated by normalising Ca^{2+} and phosphate homeostasis has been proposed (Ogata et al. 2003; de Francisco et al. 2006; Kawata et al. 2008).

However, the abundant expression of the CaSR in blood vessels suggests that the CaSR might also have a direct protective role on the vasculature itself, in addition to its indirect effects via the parathyroid glands. Our group has demonstrated that over-expression of a dominant negative mutation of CaSR (R392X) increases calcification of isolated VSMC *in vitro*, and that treatment of the VSMC with calcimimetics reduces vascular calcification (Alam et al. 2009). These findings have been confirmed by later studies (Mendoza et al. 2011; Ciceri et al. 2013).

However, direct stimulation of the CaSR by agonists alone cannot be the driving force behind the protective action of the CaSR as Ca^{2+} , the main agonist of the CaSR, is available in abundance in pathophysiological states or experimental conditions leading to vascular calcification, i.e. high Ca^{2+} levels. It is well established that *in vitro* calcified cultured VSMC as well as calcified arteries (Molostvov et al. 2007; Alam et al. 2009) lose CaSR expression, which points towards a different mechanism behind the protective effect of calcimimetic treatment against vascular calcification. This mechanism seems to be associated with prevention of CaSR downregulation. Indeed, in human VSMC increasing Ca^{2+} from 1.8 mM to 5 mM led to a reduction of CaSR expression. Under these conditions, calcimimetics increased CaSR surface and total expression levels in VSMC (Henaut et al. 2014). Similarly, calcification of cultured rat VSMC was reduced by the calcimimetic calindol (Ciceri et al. 2012b). The protective action of the CaSR against vascular calcification could therefore be interpreted as a direct effect of the calcimimetics on preventing CaSR downregulation and therefore the preservation of its function in blood vessels. This upregulating action of the calcimimetics on CaSR is well known also in other model systems of CaSR transfected human embryonic kidney (HEK) 293 cells (Davies et al. 2006; Cavanaugh et al. 2010) or *in vivo*, in the parathyroid gland (Mendoza et al. 2009).

The signalling pathways downstream of CaSR stimulation leading to this protective effect against VSMC calcification are still unclear. It is long since known that, when VSMC begin to mineralise, their phenotype changes from a smooth muscle to an osteoblastic one (Jakoby and Semenkovich 2000; Tyson et al. 2003), a process which goes along with increased arterial stiffness and blood pressure (Gauthier-Bastien et al. 2013). Calcimimetics, and therefore CaSR activation and upregulation, appear to delay this transdifferentiation, as shown in animal models of CKD where increased osteoblastic gene expression in aortic VSMC was inhibited by calcimimetic treatment while the endogenous calcification inhibitor matrix-gla-protein (MGP) was upregulated *in vivo* (Koleganova et al. 2009) as well as *in vitro* (Mendoza et al. 2011; Ciceri et al. 2013). Whether the two events appear sequentially remains to be investigated.

Taken together, these results from pre-clinical studies supported the idea that calcimimetics might prove beneficial at reducing vascular calcification in patients suffering from CKD both indirectly, by reducing circulating parathyroid hormone and therefore Ca^{2+} levels, but also directly, by targeting the vascular CaSR.

1.4.3 Clinical use of calcimimetics

Yet, clinical trials aimed at testing the efficacy of calcimimetic (Cinacalcet hydrochloride) treatment in preventing vascular calcification are ambiguous at best. In a retrospective study, patients treated with Cinacalcet exhibited significantly reduced risks of cardiovascular associated mortality (Block et al. 2010), although the mechanism behind this is still not understood. In contrast, a medium scale (360 patients) clinical trial (ADVANCE) to investigate the effects of cinacalcet + vitamin D on vascular calcification in patients undergoing haemodialysis suggested a slightly slower progression of vascular calcification (coronary artery calcification) in patients treated with cinacalcet + vitamin D compared to vitamin D alone (Raggi et al. 2011; Urena-Torres et al. 2013) but could not prove a significant benefit in patients treated with cinacalcet alone. The study had some significant design flaws, including an open-label design, lack of control of other medication of the patients and a follow up period of only 12 months. The latter issue has been addressed in the large scale, multicentre EVOLVE study (3883 patients) which recruited patients suffering from stage 5 chronic kidney disease with concomitant secondary hyperparathyroidism and undergoing dialysis (Chertow et al. 2007). The primary endpoints of this study were time until death or appearance of a severe cardiovascular event (such as, for instance, myocardial infarction or unstable angina pectoris). In this study cinacalcet treatment only showed a relative risk reduction of 7 % for these events, which was not significantly different from conventional treatment alone (Vitamin D, phosphate binders) (Chertow et al. 2012). Unfortunately, similarly to the ADVANCE study, the EVOLVE study was riddled by many shortcomings. A large difference in baseline characteristics, a high rate of treatment discontinuation in 1/3 of the patients recruited in the cinacalcet group and the availability and of self-medication with over the counter available cinacalcet in the placebo group probably played a large role in these questionable outcomes (Carney 2013).

These difficult to interpret clinical results highlight the importance to clarify the physiological role of the CaSR in the vasculature, and its putative protective role against vascular calcification. Producing a tissue-specific CaSR ablation from VSMC should enable us to evaluate the physiological significance of the VSMC CaSR in protection against vascular calcification. This was the rationale for the generation and phenotypic characterisation of the SM22 α -Cre x LoxP-CaSR mouse when devising this study.

1.5 Models of CaSR deletion

1.5.1 Models of constitutive CaSR deletion

Transgenic animals are the preferred model system to address the specific function of a protein in physiology and pathophysiology as they allow a holistic study of a genes function in the context of the whole organism (Austin et al. 2004), and indeed a great multitude of studies using transgenic models of CaSR deletion have been performed to determine the role of the receptor in various tissues and regulating systems. The first model of constitutive CaSR deletion was developed by Ho and colleagues in 1995, 2 years after the identification of the CaSR (Ho et al. 1995). The constitutive CaSR knock-out mouse (CaSR^{-/-}) shows a phenotype of severe hypercalcaemia, growth retardation and impaired bone structure and rarely lives longer than a few weeks resembling NSHPT, while the heterozygous CaSR knock-out mouse (CaSR^{+/-}) only shows a mild phenotype resembling FHH. To allow for investigation of CaSR function in adults, different mouse models for constitutive knock-out of the CaSR have been developed where the phenotype of the CaSR^{-/-} mouse was (partly) rescued: In Gcm2^{-/-}-CaSR^{-/-} mice, where the CaSR is knocked out in mice of a background of deleted glial cells missing-2 (Gcm2), a master regulator for parathyroid gland development (thus leading to parathyroid gland ablation), the severe phenotype of the CaSR^{-/-} mouse is rescued except for persisting hypocalciuria (Tu et al. 2003). A very similar rescue was observed when knock-out of the CaSR was combined with knock out of PTH gene. The resulting CaSR^{-/-}-PTH^{-/-} mice are not different in size and lifespan from control mice but have imbalanced Ca²⁺ levels in blood and urine due to the missing action of the CaSR in the kidney (Kos et al. 2003).

Finally, deletion of 1,25-D3 in with mice lacking the CaSR (1,25-D3^{-/-}-CaSR^{-/-}) improved lifespan, growth, bone status and serum Ca²⁺ levels compared to those observed in CaSR^{-/-} mice, but also exacerbated hypophosphataemia and hyperparathyroidism (Liu et al. 2011).

Table 1 shows an overview of all studies on CaSR function performed with transgenic models of CaSR deletion (including those of targeted gene deletion, see below).

Importantly, the constitutive CaSR^{-/-} mouse is not a complete knockout. When investigating specific effects of CaSR deletion in some tissues, an alternative splice variant of the CaSR, lacking the 77 amino acid exon 5 (which is targeted by the gene deletion strategy in the CaSR^{-/-} mouse) was discovered (Oda et al. 2000). In some tissues, this exon 5-less splice variant was non-functional (Oda et al. 2000) while it functionally replaced full-length CaSR function in

others (Rodriguez et al. 2005; Finney et al. 2011), making investigation of tissue specific effects of CaSR KO difficult.

1.5.2 Models of targeted CaSR deletion via the Cre-LoxP system

To overcome these problems and allow studying of CaSR roles in specific tissues, the Cre- (cyclization recombinase) LoxP (locus of X-over P1) system of targeted gene deletion was used to generate mice lacking the CaSR only in certain tissues (Chang et al. 2008).

The Cre-LoxP system facilitates deletion of specific genes from specific tissue by breeding two types of genetically modified mice: the first mouse carries LoxP-sites flanking a portion of a gene which is to be deleted in the final knock-out mouse model. The LoxP-sites are originally a feature of bacteriophage P1 consisting of 34 base pairs; bp (Sternberg and Hamilton 1981). This sequence is recognised by the 38 kDa enzyme Cre recombinase, which is introduced under the control of a tissue- and/or age-specific promoter into the second transgenic mouse (Orban et al. 1992) When these two mice are bred, the Cre-recombinase, which is only expressed in cells where the promoter which controls Cre expression is active, will cleave the gene flanked by the LoxP-sites, resulting in tissue, or rather promoter-specific deletion of the target gene.

Using this system, Chang et al. have developed a tissue selective CaSR knock-out mouse (CaSR-LoxP, Δ exon7) in which ablation of the CaSR from chondrocytes, osteoblasts and the parathyroid cells was successfully established by using three specific Cre driving promoters. Using these models, they showed that the osteoblastic, parathyroid and chondrocyte CaSR are essential for regulation of osteoblastic activity, with KO mice showing severe growth retardation and impaired bone structure (Chang et al. 2008). Recently, the same CaSR-LoxP mouse has also been used to generate an intestinal epithelium-specific CaSR knock-out mouse which presented a marked phenotype of altered colonic crypt structure and colonic epithelial cell hyperproliferation (Rey et al. 2012).

1.5.3 The SM22 α -Cre x LoxP-CaSR mouse

The aim of my study was to determine the role of the vascular CaSR. Targeted deletion of the CaSR from VSMC was achieved by breeding the CaSR-LoxP (Δ exon7) mouse with an

SM22 α (smooth muscle protein of 22 kDa isoform alpha (Lees-Miller et al. 1987)) promoter driven Cre mouse (Li et al. 1996b; Holtwick et al. 2002), thus creating the SM22 α -Cre x LoxP-CaSR mouse. Mice were bred by our Dr. Wenhan Chang as part of a collaborative study. Two heterozygous breeding pairs were sent to Cardiff for phenotypic characterisation.

The transgenic strategy used in the CaSR-LoxP mouse model consists of LoxP sites flanking exon 7 of the murine CaSR (CaSR-LoxP), leading to deletion of exon 7 and thus the production of a truncated (Δ exon7) CaSR protein in Cre expressing tissues. Exon 7 encodes the whole intracellular and transmembrane domain of the CaSR (REF here). The truncated product therefore consists of the extracellular domain only which, due to lack of its transmembrane domain, cannot anchor to plasmamembrane and is therefore trapped in the cell. Δ exon7-CaSR in human embryonic kidney (HEK) 293 cells show absence of CaSR activation when exposed to extracellular Ca²⁺ compared to HEK 293 transfected with the full length CaSR, proving that the truncated product is indeed non-functional. For PTH-Cre x LoxP-CaSR mice, a reduction of about 90 % in CaSR mRNA was found in Cre expressing parathyroid glands. In comparison, mRNA levels for the Δ exon7-CaSR were increased about 2-fold was found, indicating an increased rate of CaSR transcription possibly in response to lost CaSR function. Protein levels of the full length CaSR were reduced by > 95 % while truncated CaSR protein expression levels were about 10 % compared to WT control. The latter result indicates that the Δ exon7-CaSR protein is more unstable and subject to rapid degradation despite the increased mRNA levels (Chang et al. 2008).

The promoter driving Cre was SM22 α , a mainly smooth muscle cell associated protein which locates to the cytoskeleton of these cells (Zhang et al. 2001a). The function of SM22 α has yet to be fully understood but seems to be connected to cell contraction, migration and tumour suppression (Assinder et al. 2009). Expression patterns of SM22 α proteins are different from the promoter construct and are highly variable depending on gene length (Xu et al. 2003). Specificity of the SM22 α -Cre promoter construct for murine VSMC is debated, but probably not complete. While earlier studies indicated sole VSMC specificity in adult mice (Li et al. 1996b; Moessler et al. 1996; Holtwick et al. 2002) and transient expression of SM22 α in the embryonic heart (Li et al. 1996a), more recent studies indicated expression of SM22 α -Cre in adult visceral and cardiac smooth muscle cells (Lepore et al. 2005) as well as myeloid and lymphoid cells (Shen et al. 2012).

Table 1: Studies performed on transgenic mouse models of CaSR deletion. Studies are ordered chronologically. Equal models are highlighted with the same colour. Studies using models of target specific gene deletion are highlighted in grey.

Model	Investigated system / deletion from	Observed effects	Reference
CaSR ^{-/-} (Δexon5)	Phenotypic characterisation, model generation	CaSR ^{+/-} mice show phenotype similar to FHH (elevated serum Ca ²⁺ and PTH levels), CaSR ^{-/-} mice show phenotype similar to NSHPT and have a lifespan < 1 month	(Ho et al. 1995)
CaSR ^{-/-} (Δexon5)	Keratinocytes	Δexon5-less splice variant described unable to sense Ca ²⁺ in keratinocytes	(Oda et al. 2000)
CaSR ^{-/-} -PTH ^{-/-} (Δexon5)	Phenotypic characterisation, model generation	PTH deficient background rescues phenotype of CaSR ^{-/-} mice by reducing PTH levels	(Kos et al. 2003)
CaSR ^{-/-} -Gcm2 ^{-/-} (Δexon5)	Phenotypic characterisation, model generation	Gcm2-deficient background rescues phenotype of CaSR ^{-/-} mice by reducing PTH levels	(Tu et al. 2003)
CaSR ^{-/-} (Δexon5)	Growth plate chondrocytes	Δexon5-less splice variant compensated for loss of full length CaSR in growth plate chondrocytes	(Rodriguez et al. 2005)
PTH-Cre x LoxP-CaSR (Δexon7)	Skeletal phenotype / <i>Parathyroid</i>	Growth retardation, inhibited bone formation, elevated PTH, serum and urine Ca ²⁺	(Chang et al. 2008)
2.3Col(I)-Cre x LoxP-CaSR (Δexon7)	Skeletal phenotype / <i>Osteoblasts</i>	Growth retardation, inhibited bone formation, early death	
Osx-Cre x LoxP-CaSR (Δexon7)	Skeletal phenotype / <i>Osteoblasts</i>	Growth retardation, inhibited bone formation, early death	
Col11-Cre x LoxP-CaSR (Δexon7)	Skeletal phenotype / <i>Chondrocytes</i>	Embryonically lethal, delayed growth plate development	
CaSR ^{-/-} -PTH ^{-/-} (Δexon5)	PTH independent role of the CaSR in Ca ²⁺ homeostasis	1,25-D3 mediated elevated Ca ²⁺ levels, reduced renal Ca ²⁺ excretion, increased intestinal Ca ²⁺	(Egbuna et al. 2009)
CaSR ^{-/-} -PTH ^{-/-} (Δexon5)	PTH independent role of the CaSR in Ca ²⁺ homeostasis	PTH independent hypercalcaemia on Ca ²⁺ rich or Pi deplete diet through reduced renal excretion and calcitonin levels	(Kantham et al. 2009)
CaSR ^{-/-} -PTH ^{-/-} (Δexon5)	Stomach	No gastrin and acid secretion in CaSR ^{-/-} -PTH ^{-/-} mice. CaSR acts as nutrient sensor in the stomach	(Feng et al. 2010)
CaSR ^{-/-} -1α-Hydroxylase ^{-/-} (Δexon5)	Skeletal phenotype	Rescue diet (high Ca ²⁺) normalises phenotype of 1α-Hydroxylase ^{-/-} but leads to hypercalcaemia in double KO. Reduced osteoclastic activity	(Richard et al. 2010)

CaSR ^{-/-} -PTH ^{-/-} , CaSR ^{-/-} -1 α - Hydroxylase ^{-/-} (Δ exon5)	Teeth	PTH deficient background rescues phenotype of CaSR ^{-/-} mice; 1,25-D3 deficient background reduces phenotype	(Sun et al. 2010)
Co3.6-Cre x LoxP-CaSR (Δ exon7)	Skeletal phenotype / <i>Osteoblasts</i>	Growth retardation, reduced osteoblast differentiation, increased RANKL expression	(Dvorak-Ewell et al. 2011)
CaSR ^{-/-} (Δ exon5)	Foetal lung development	Δ exon5-less splice variant compensated for loss of full length receptor in foetal lungs	(Finney et al. 2011)
CaSR ^{-/-} -PTH ^{-/-} , CaSR ^{-/-} -1 α - Hydroxylase ^{-/-} (Δ exon5)	Interaction of CaSR with PTH and 1,25-D3 in skeletal phenotype	PTH deficient background rescues phenotype of CaSR ^{-/-} mice; 1,25-D3 deficient background reduces phenotype, hypercalcaemia and PTHrP identified as major factor for CaSR ^{-/-} lethality	(Liu et al. 2011)
CaSR ^{-/-} -PTH ^{-/-} (Δ exon5)	Bone turnover in neonates	Dietary high Ca ²⁺ promotes bone formation in PTH ^{-/-} but not CaSR ^{-/-} -PTH ^{-/-} mice. CaSR mediates dietary Ca ²⁺ induced bone turnover	(Shu et al. 2011)
Six2-Cre x LoxP-CaSR (Δ exon3)	<i>Kidney</i>	No effect unchallenged, increased activation of NKCC2, reduced Ca ²⁺ excretion on high Ca ²⁺ diet	(Toka et al. 2012)
Vil-Cre x LoxP-CaSR (Δ exon7)	<i>Intestinal epithelial cells</i>	Increased epithelial proliferation, changes in crypt structure and β -catenin signalling	(Rey et al. 2012)
CaSR ^{-/-} -PTH ^{-/-} (Δ exon5)	Influence of PTH on bone in absence of CaSR	Attenuated PTH induced increase in bone turnover compared to PTH ^{-/-} single KO	(Xue et al. 2012)
PTH-Cre x LoxP-CaSR ^{+/-} (Δ exon7)	Influence of age and sex on development of hyperparathyroidism	Elevated PTH protects trabecular bone in male mice > 3 months, reduces trabecular bone in 3 month females which is revers in 12 month females	(Cheng et al. 2013)
CaSR ^{-/-} -PTH ^{-/-} (Δ exon5)	Colon	Increased inflammation and Wnt signalling, increased susceptibility for colonic aberrations	(MacLeod 2013)
CaSR ^{-/-} -PTH ^{-/-} (Δ exon5)	Erythrocytes	CaSR deletion rescues impaired erythrocyte phenotype caused by PTH deletion	(Romero et al. 2013)
CaSR ^{-/-} -PTH ^{-/-} (Δ exon5)	Interactions between Ca ²⁺ and Mg ²⁺ homeostasis	Reduced Mg ²⁺ levels in PTH ^{-/-} and CaSR ^{-/-} -PTH ^{-/-} mice which are normalised by dietary Ca ²⁺ , exacerbated hypercalcaemia with dietary Mg ²⁺	(Quinn et al. 2013a)
CaSR ^{-/-} -PTH ^{-/-} (Δ exon5)	Ca ²⁺ and Pi mediated regulation of FGF23	FGF23 production is activated by Ca ²⁺ and Pi independently of CaSR and PTH	(Quinn et al. 2013b)

1.6 Scope and objectives of the thesis

As I have introduced in the previous sections, multiple studies on the involvement of the vascular CaSR in control of vascular tone and vascular calcification have already been performed, but definitive answers explaining the actual physiological and pathophysiological role of the vascular CaSR are still missing. A thorough and systematic investigation of the specific functions of the VSMC CaSR, with emphasis on possible different roles in vascular tone regulation and protection from calcification, is therefore essential. To address these issues I characterised a mouse model of targeted deletion of the CaSR from VSMC (SM22 α -Cre x LoxP-CaSR) to elucidate the physiological and pathophysiological roles of the CaSR in VSMC. To achieve these goals, a variety of objectives were set for the thesis which I address in chapters 3-9:

- 1) Optimisation of experimental protocols for *in vitro* and *in vivo* investigation of the role of the CaSR in VSMC.
- 2) Gross description of the phenotype of the SM22 α -Cre x LoxP-CaSR mouse, including body weights, reproductive capabilities and overt phenotypic difference between WT and KO animals.
- 3) Investigation of the *in vitro* phenotype of cultured VSMC to study principal differences in CaSR expression and intracellular distribution as well as proliferation / apoptosis of VSMC isolated from control as well as WT and KO mice.
- 4) Characterisation of the effect of absence of the VSMC CaSR in the propensity for vascular calcification *in vivo*, *ex vivo* and *in vitro* and therefore the contribution of the VSMC CaSR on protection against vascular calcification.
- 5) *In vivo* characterisation of the cardiovascular system of the SM22 α -Cre x CaSR-LoxP mouse to determine the contribution of the VSMC CaSR to blood pressure regulation *in vivo*. This is of great importance as the specific role of the VSMC CaSR in blood pressure regulation is still unclear. Targeted deletion of the CaSR from VSMC allows for dissection of the effect of the VSMC CaSR independently of the effects of the perivascular and endothelial CaSR.

The best characterised role of the CaSR lies in maintenance of Ca²⁺ homeostasis. Therefore, the mineral ion metabolism of the SM22 α -Cre x LoxP mouse was studied *in vivo*, specifically by investigating the metabolism, bone and clinical chemistry of blood and urine of the animals.

2 Materials and Methods

2.1 Chemicals and substances

All chemicals were acquired from Sigma-Aldrich (Dorset, UK) unless otherwise stated. The calcimimetic R-568 was kindly provided by Amgen (Thousand Oaks, CA, USA).

2.2 Experimental animals

All experiments and animal procedures were performed adhering to UK Home Office guidelines. Founder animals for the smooth muscle cell specific CaSR knock-out were produced by W. Chang, Endocrine Research Unit, Department of Medicine, University of California, USA by breeding SM22 α -Cre⁺ mice (Li et al. 1996b; Holtwick et al. 2002) with mice containing LoxP sites flanking exon 7 of the murine CaSR gene (Chang et al. 2008) of mixed 129S1/SvImJ and C57/BL6 background. C57/BL6 mice were used as control animals where applicable. For the excision performance of the Cre-enzyme, homo- and hemizygous Cre presentation is considered equivalent. Mice of the following genotypes were considered “wild type” (WT): Cre⁺/flox^{-/-}, Cre⁻/flox^{+/+}, Cre⁻/flox^{+/-}, Cre⁻/flox^{-/-}. Mice of the following genotypes were considered “heterozygous” (HET): Cre⁺/flox^{+/-}, Cre⁺/flox^{-/+}. Mice of the following genotype were considered “knock-out” (KO): Cre⁺/flox^{+/+} (Table 2).

Mice were housed in standard cages housing a maximum of five animals in one cage and fed Rat and Mouse No. 3 Breeding diet, henceforth called “standard diet” (Special Diet Service, Essex, UK) and tap water *ad libitum*.

Table 2: Control, WT, HET and KO genotype depending on Sm22 α -Cre and CaSR-LoxP expression. ++ = two positive alleles, +-, -+ = one positive allele, -- = no positive alleles. Green = WT, dark green = control, yellow = HET, red = KO

		CaSR-LoxP			
		++	+-	-+	--
SM22 α -Cre	++	++ ++ KO	+- ++ HET	-+ ++ HET	-- ++ WT
	+-	++ +- KO	+- +- HET	-+ +- HET	-- +- WT
	-+	++ -+ KO	+- -+ HET	-+ -+ HET	-- -+ WT
	--	++ -- WT	+- -- WT	-+ -- WT	-- -- CTRL

Since HET mice were not extensively used in this study, the breeding strategy employed focused on producing a maximum number of WT and KO animals only. KO x KO breedings and WT x KO breedings, both resulting in WT and KO offspring as well as WT x WT breedings, resulting in WT offspring only, were employed.

2.3 Genotyping of SM22 α -Cre x loxP-CaSR mice

Deoxyribo nucleic acid (DNA) was extracted from ear biopsies using DirectPCR® Ear DNA Extraction system (Viagen, Los Angeles, CA, USA) with proteinase K (Bioline, London, UK) by adding 100 μ l “Direct PCR ® Ear + 4 μ l proteinase K 10 mg / ml per reaction to each biopsy and incubating overnight at 55 °C. Enzymatic digestion was then stopped by incubation at 85 °C for 45 min and samples were stored at -20 °C.

Genotype was determined using the SM22 α promoter and Cre coding region primers from (Holtwick et al. 2002) and the LoxP primers described in (Chang et al. 2008). See Table 3 for sequences and product sizes.

Table 3: Primer sequences and expected product sizes (Holtwick et al. 2002; Chang et al. 2008) for genotyping of SM22 α -Cre x LoxP-CaSR mice.

Primer	Sequence	Product size
SM22-Pro	5' -CAG ACA CCG AAG CTA CTC TCC TTC C-3'	500 bp for Cre containing allele(s) no product for WT
SM22-Cre	5' -CGC ATA ACC AGT GAA ACA GCA TTG C-3'	
CaSR fl Up	5' -GTG ACG GAA AAC ATA CTG C-3'	167 bp for floxed CaSR allele 133 bp for WT allele
CaSR fl Low	5' -CGA GTA CAG GCT TTG ATG C-3'	

Polymerase chain reactions (PCRs) were performed in 200 μ l individual nuclease free reaction tubes using deoxy-nucleotide triphosphates (dNTPs) and Biotaq® DNA Polymerase Kit (both Bioline). See Table 4 and Table 5 for the mastermix and thermocycler program for Sm22 α -Cre and Table 7 for the mastermix and temperature protocol for CaSR-LoxP.

Table 4: Mastermix for SM22 α -Cre PCR.

Reagent	1x Reaction	Concentration
10X Buffer (Bioline)	2.500 μ l	
BIOTaq DNA Polymerase	0.250 μ l	2 U
Sm22 Pro Primer	0.125 μ l	100 nM
Sm22 Cre Primer	0.125 μ l	100 nM
100 mM dNTPs (Bioline)	0.250 μ l	1 mM
50 mM MgCl ₂	2.000 μ l	4 mM
H ₂ O	18.250 μ l	
DNA sample	1.500 μ l	
Reaction volume	25.000 μ l	

Table 5: Thermocycler program for SM22 α -Cre PCR.

Step	Cycles	Time	Temperature
Initial denaturation	1	5 Min	95 °C
Denaturation		30 Sec	95 °C
Annealing	40	1 Min	50 °C
Extension		2 Min	72 °C
Final Extension	1	10 Min	72 °C
Hold			4 °C

Table 6: Mastermix for CaSR-LoxP PCR.

Reagent	1x Reaction	Concentration
10X Buffer (Bioline)	2.500 μ l	
BIOTaq DNA Polymerase	0.250 μ l	2 U
CaSR fl Up Primer	0.125 μ l	100 nM
CaSR fl Low Primer	0.125 μ l	100 nM
100 mM dNTPs (Bioline)	0.250 μ l	1 mM
50 mM MgCl ₂	2.000 μ l	4 mM
H ₂ O	18.250 μ l	
DNA sample	1.500 μ l	
Reaction volume	25.000 μ l	

Table 7: Thermocycler program for CaSR-LoxP PCR.

Step	Cycles	Time	Temperature
Initial denaturation	1	5 Min	95 °C
Denaturation		30 Sec	95 °C
Annealing	40	1 Min	47 °C
Extension		2 Min	72 °C
Final Extension	1	10 Min	72 °C
Hold			4 °C

2.4 In vitro assays

2.4.1 Culture media

2.4.1.1 Growth medium

Dulbecco's modified Eagle medium (DMEM) without CaCl_2 (Life Technologies, Grand Island, NY, USA), supplemented with 1.2 mM CaCl_2 , 50 U / ml penicillin-streptomycin, 2 mM L-glutamine, 10 % (v/v) foetal bovine serum (FBS), 1 mM Na-pyruvate and 1 % (v/v) amphotericin B solution (all Life Technologies). This medium is henceforth referred to as "growth medium".

2.4.1.2 VSMC culture medium

Growth medium without amphotericin B.

2.4.1.3 Supplemented media

Ca^{2+} and inorganic phosphate (Pi) concentrations of media were adapted to experimental requirements by the addition of sterile 1M CaCl_2 solution and inorganic 1M phosphate buffer (NaH_2PO_4 / Na_2HPO_4) pH 7.4.

2.4.2 HEK-CaSR cells

Frozen stocks of stably transfected CaSR overexpressing HEK 293 cells (HEK-CaSR cells) were available in house from a previous study (Maldonado-Perez et al. 2003) and were maintained by Dr. Sarah Brennan. HEK-CaSR cells were cultured in DMEM containing 1.8 mM Ca^{2+} 50 U / ml penicillin-streptomycin, 2 mM L-glutamine, 10 % (v/v) FBS and 1 mM Na-pyruvate.

2.4.3 pH assays

Growth medium containing 0.8, 1.2, 1.8 or 2.5 mM CaCl₂ or 1, 2 or 3 mM Pi was titrated for Pi (phosphate buffer) or CaCl₂ influence on medium pH. The medium was gassed with 5% CO₂ in air to simulate conditions in a tissue culture incubator. After equilibration of the pH, Pi or CaCl₂ were added to the media in 0.2 mM increments and the pH noted after equilibration.

2.4.4 Primary VSMC culture from explants

VSMC were prepared according to published procedure (Sage et al. 2011) with modifications. In brief, mice were killed by cervical dislocation and the thoracic aorta was dissected. Aortae of 2-5 mice of the same genotype were pooled for one cell batch and placed in growth medium and cleaned from the tunica adventitia and connective tissue. Segments of aorta ca. 1 mm in length were transferred to a culture flask and, after 10 minutes of drying in a tissue culture incubator, covered with growth medium and incubated at 37 °C / 95 % relative humidity / 5 % CO₂ until cells had grown out of the explants (ca. 2-4 weeks). The explants were removed by aspiration and the cells were passaged using 0.05 % (v/v) trypsin-ethylenediaminetetraacetic (EDTA) solution in sterile phosphate-buffered saline, pH 7.4 (PBS) without calcium chloride and magnesium chloride (all Life Technologies). Beginning with this passage VSMC culture medium was used instead of growth medium. Medium was changed every 3-4 days; see Figure 9 for a photo series of the process. Cells were used at passages 2-6 for experiments.

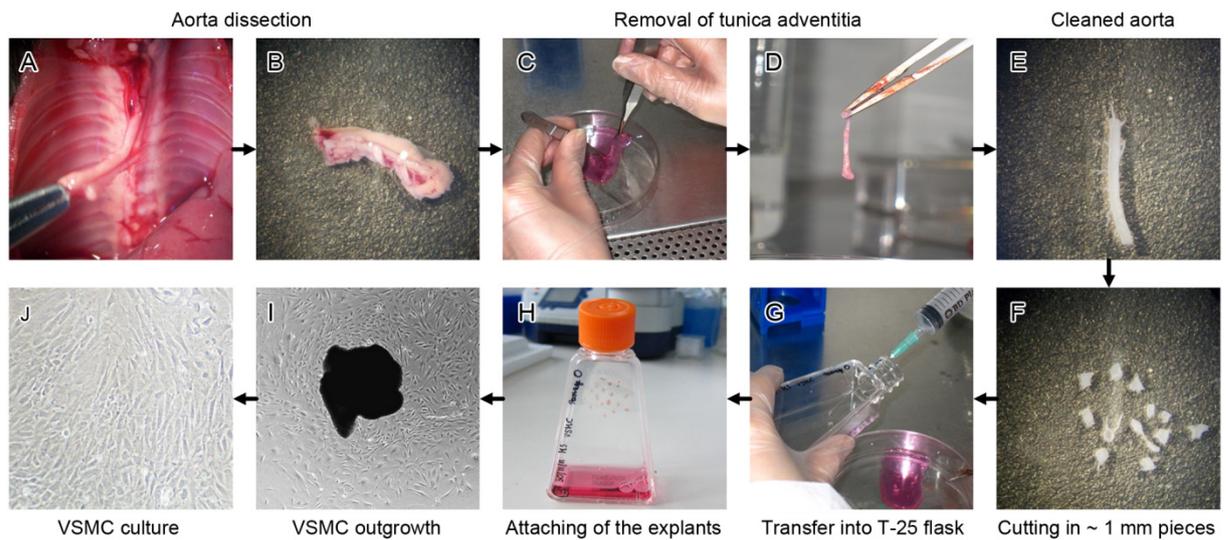


Figure 9: Generation of explant-derived aortic VSMC. The thoracic aorta is dissected from the spine (A) and removed to a Petri dish filled with sterile isolation medium (B) where the vessel is cleared from all tunica adventitia by gently pulling / scraping the connective tissue (C and D) until only the semi-translucent tunica media remains (E). The vessel is then cut into small (ca. 1 mm) pieces (F) which are then transferred into a T-25 cell culture flask by the use of a hypodermic needle (G). The flask is kept in an upright position at 37 °C for 10–15 minutes so that the explants are not in contact with medium and can attach firmly to the surface of the flask (H). 5 ml isolation medium is added and the explants are kept at 37 °C / 95 % relative humidity (rh) / 5 % CO₂ for ca. 7 days after which the medium is changed. VSMC will start to grow out of the explants (I). After ca. 2-3 weeks, the explants are removed and the VSMC passaged to generate a monolayer of cells (J). Cells at this point are considered to be at passage 1. From this step onwards, the cells are kept in growth medium (see definition in 2.4.2). Pictures A, B, E and F kindly provided by Dr. Thomas Davies.

2.4.5 Acute isolation of VSMC

VSMC from aortae were acutely isolated for immunostaining and calcium imaging following published protocol in (Moskalenko et al. 2010) by Dr. Polina Yarova. In brief, aortae were harvested and processed into 2 mm segments as described for the explant cultures, and the lumen was flushed with cold isolation medium. The segments were incubated in a 4-(2-hydroxyethyl)-1-piperazineethanesulfonic acid (HEPES) pH 7.4 buffered solution containing 1 mg / ml bovine serum albumin (BSA), 1 mg / ml papain, 1 mg / ml dithiothreitol, 2 mg / ml collagenase and 0.5 mg / ml soybean trypsin inhibitor at 37 °C for 30 minutes with stirring every 5-10 minutes. Following a quick wash in ice-cold HEPES pH 7.4 buffer, the segments were finally disaggregated into single cells in HEPES buffer pH 7.4 containing 1 mg / ml BSA by pipetting up and down. The supernatant then was centrifuged at 400 x g for 5 minutes and the cell pellet suspended in isolation medium for subsequent fixation and IF.

2.4.6 Double immunostaining of VSMC and HEK-CaSR cells

Cells were grown on sterilized glass coverslips of 13 mm diameter in 24 well plates as described in 2.4.2, 2.4.4 or 2.4.5. The culture medium was removed and the cells were fixed in 4 % (w/v) PFA in PBS for 15 minutes after which the cells were washed in 50 mM NH₄Cl in PBS to quench free aldehyde groups remaining from the fixation step. Permeabilisation and blocking of unspecific antibody binding was performed in a single step by incubating the fixed cells using 0.05 % (v/v) Triton X 100 + 1 % (w/v) BSA in PBS for 60 minutes (blocking buffer). For staining of the CaSR, a rabbit-derived polyclonal antibody, raised against the N-terminal domain of the human CaSR with 100% sequence homology with mouse was used (AnaSpec, 53286, Fremont, CA, USA). Staining of SM22 α was performed using a goat derived polyclonal antibody (Abcam, AB10135, Cambridge, UK). Cells were incubated overnight at 4 °C with both primary antibodies. Negative controls were performed by omission of the primary antibodies or replacement with an isotype control of rabbit IgG (Abcam). After washing in PBS, primary antibody binding was visualized using appropriate Alexa Fluor 488 and Alexa Fluor 594 fluorescence-dye coupled secondary anti IgG antibodies in a dilution of 1:500 in blocking buffer. Nuclei were counterstained with Hoechst 34580. Coverslips with adhering cells were then mounted on standard glass slides using ProLong Gold® (all Life Technologies).

Slides were visualized using a Leica DMRB microscope (Leica Microsystems). Epifluorescence images of immunostained tissues and cells were analysed and photographed with an Olympus BX61 automated microscope equipped with a 100 W high pressure mercury lamp, using AnalySIS software (Olympus Microscopy, Essex, UK). Confocal images were acquired using a Leica TCS SP2 AOBS spectral confocal laser-scanning microscope using Leica Confocal Software (Leica Microsystems). For subsequent quantitative analysis, slides were imaged using an automated immunofluorescence slide scanner (see 2.4.8).

Additional commercial anti-CaSR primary antibodies were tested on HEK-CaSR cells and kidney sections: rabbit derived polyclonal antibody against the C-terminal domain of the human CaSR with 100 % sequence homology with mouse (LifeSpan Biosciences, LS-C117834, Seattle, WA, USA), mouse-derived polyclonal antibody against the synthetic full length protein of the CaSR (Novus Biologicals, H00000846-B01P, Cambridge, UK), mouse derived monoclonal antibody against the N-terminal domain (ADD epitope) of the human CaSR, clone 5C10 (Abcam, AB19347). Furthermore, two in house available custom antibodies were tested: a previously produced rabbit antiserum raised against the N-terminal domain (ADD epitope) of the CaSR, titled 733 as well as a rabbit polyclonal affinity purified antibody raised against the N-terminal domain (ADD epitope), titled Shob, kindly donated by D. Shoback, University of California San Francisco, San Francisco, CA, USA).

2.4.7 Staining of apoptotic cells (TUNEL assay)

Batches of VSMC grown from WT and KO aortae were stained for apoptosis using the terminal deoxynucleotidyl transferase dUTP nick end labelling (TUNEL) method. The staining was performed by Dr Thomas Davies as described in (Davies 2013). In brief, near confluent VSMC were cultured in the presence of 1.2, 1.8 or 2.5 mM Ca²⁺ and either 1 mM or 3 mM Pi for 48 h after which they were fixed in 4 % (w/v) PFA in PBS. Apoptotic cells were labelled using terminal transferase with Biotin-16-dUTP (Roche Diagnostics, Burgess Hill, UK) as substrate which was stained using FITC-Avidin (Abcam). Nuclei were counterstained with Höchst 33258. VSMC were then stained for CaSR and SM22 α expression as described (see above) with the SM22 α primary antibody stained using a AlexaFluor 647 conjugated anti-goat IgG secondary antibody (Life Technologies) replacing the AlexaFluor 488 conjugated antibody used in VSMC immunofluorescence staining experiments without

apoptosis staining. Quantitative immunofluorescence was used to quantify the percentage of apoptotic cells (see 2.4.8).

2.4.8 Quantitative immunofluorescence

Quantitative immunofluorescence microscopy (e.g. (Bogusz et al. 2012)) to evaluate CaSR expression as well as apoptosis and cell density was performed by scanning slides with VSMC stained for apoptosis or SM22 α and CaSR using TissueFAXS® automated immunofluorescence microscopy hardware and software (TissueGnostics GmbH, Vienna, Austria) at the Institute for Pathophysiology and Allergy Research, General Hospital Vienna, Austria. Acquisition of the different slides were performed keeping the settings of exposure, contrast and camera gain exactly the same between the different slides, containing different batches of VSMC cells from either WT or KO mice. The acquired multispectral images (fields of view) were then fused into large images encompassing the total scanned region using an automated image stitching algorithm available in the TissueFAXS software. The obtained images of a whole region varied in size depending on the cell distribution on the individual coverslip, but generally consisted of 9x9 – 12x12 fields of view using a 40x objective. These regions were then analysed using TissueQuest® (TQ) software (TissueGnostics), yielding quantification of the expression levels of the different staining as well as percentages of cells positive or negative for the expression of a certain staining (e.g. positive for expression of SM22 α) enabling the sorting of the analysed cells into different categories (e.g. VSMC and non-VSMC). The detailed analysis procedure was as follows: All images of one batch of slides were loaded into the same TissueQuest project file. Every single image was then scrutinized manually and regions of interest (ROI) were defined for each image. The ROIs define the area of the images the software will analyse in the subsequent steps. Generally, the ROIs were selected to equal the entirety of the acquired image area included in the analyses. However, areas of extremely high cell density or areas of the images containing artefacts like dust or air bubbles (enclosed in the mounting medium of the coverslip) were manually removed from the ROIs to prevent generation of false results. In addition to these large ROIs for subsequent analysis, a number of smaller ROIs were manually drawn to allow for optimization of detection and analysis parameter settings before the actual analysis of the series of images. The TissueQuest software uses nuclei to detect single cells. The nuclei are detected by use of automatic and manual background thresholding

where positive objects (= nuclei) are discriminated from the background of the image using the image channel (colour) for the nuclear staining (Höchst). Settings for optimal detection of these nuclei (expected nuclear area, background threshold etc.) were optimized using the aforementioned small ROIs. Optimization of these parameters is highly important as wrong settings can lead to completely wrong image segmentation and therefore cell detection. Examples of false and correct nuclear detection parameters are shown in Figure 10.

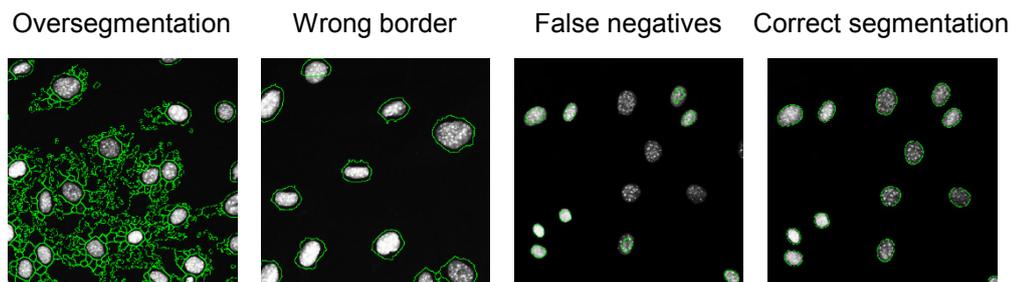


Figure 10: Examples for incorrect and correct segmentation of nuclei for cell detection in quantitative immunofluorescence measurements. The images show the nuclear channel of multispectral images from VSMC stained with Höchst nuclear dye for nuclei visualization. Green boundaries indicate detected nuclei by the TissueQuest software. In the first image from the left (Oversegmentation), a too low setting for background threshold resulted in the complete oversegmentation of the image, i.e. the false detection of too many nuclei in the image. In the second image from the left (Wrong border), the falsely detected small nuclei from the first image were removed by excluding nuclei below a certain area threshold. However, the too-low background threshold still resulted in wrongly shaped detection borders for the nuclei. In the third image (False negatives), the background threshold was set too high, resulting in undersegmentation and therefore false negatives. In the fourth image (Correct segmentation), the chosen parameters resulted in correct nuclear detection. Image contrast enhanced for better visualization.

After settings were optimised to allow the best possible nuclear detection results, these settings were used to analyse all ROIs containing VSMC from WT and KO cells. Evaluation of expression levels (= staining intensities) in the channels other than the nuclear channel (i.e. green fluorescence and red fluorescence) was performed in a ring-shaped area around the detected nuclei (= ring mask, Figure 11) with a diameter of 8 μm for stained targets located in the cytosol and membrane of the VSMC (SM22 α and CaSR) or in the area of the nuclei themselves for TUNEL stained cells (nuclear mask, Figure 12).

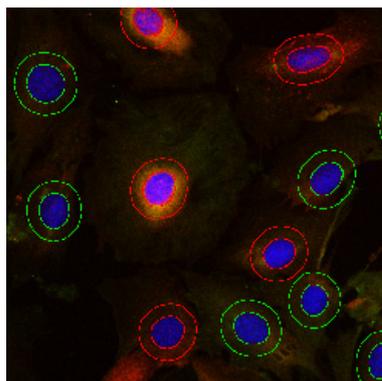


Figure 11: Example of ring masks for quantification of SM22 α and CaSR staining intensities. Mean and maximum pixel intensities are measured in the 8 μm measuring ring bordering the blue nuclei. Green borders indicate CaSR- cells, red borders indicate CaSR+ cells. Image contrast enhanced for better visualisation.

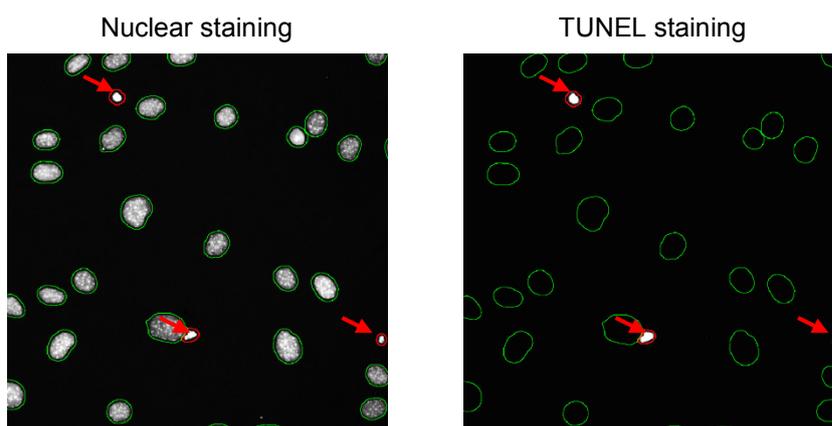


Figure 12: Example of a nuclear mask for detection of apoptotic cells visualized using TUNEL staining. Nuclear staining (Höchst) is used to detect all nuclei (cells) in the image (left image). Nuclei which also stain positively in the TUNEL assay are being detected by the software (right image, red borders). Red arrows indicate apoptotic cells.

During the analysis, mean and maximum pixel intensity values, (intensity resolution 8 bits, ranging from 0 to 255) for all detected cells are calculated. These values are then plotted by the software into scattergrams, allowing for gating of different populations of cells, similar to the analysis of flow cytometry data. Gates were then manually set to select only true positive detected cells (e.g. by removal of false positively detected nuclei, based on nuclear size). The mean intensity values for CaSR and SM22 α were then gated to divide the detected cells into

four populations: CaSR+/SM22 α +, CaSR+/SM22 α -, CaSR-/SM22 α + and CaSR-/SM22 α - (Figure 13).

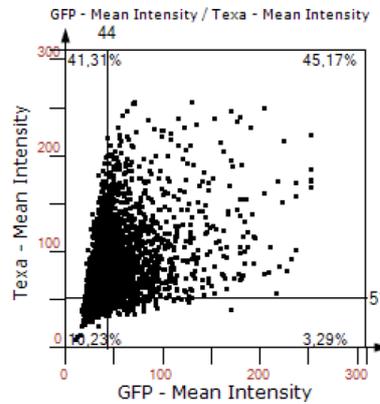


Figure 13: Example scattergram from TissueQuest® showing mean green fluorescence intensity (SM22 α) on the x axis (GFP – Mean Intensity) and mean red fluorescence intensity (CaSR) on the y axis (Texa – Mean Intensity). Gates were being set by visual observation and being kept constant for all batches of cells resulting in four populations of cells: CaSR+/SM22 α + (upper right quadrant), CaSR+/SM22 α - (upper left quadrant), CaSR-/SM22 α + (lower right quadrant) and CaSR-/SM22 α - (lower left quadrant).

To evaluate the different CaSR expression levels in VSMC isolated from WT and KO mice, the mean CaSR staining intensity values of only the VSMC in the total cell population (SM22 α + cells, thereby excluding all non-VSMC in the image) were normalised to their respective staining intensities for SM22 α . This step was performed to allow comparison of the various analysed VSMC batches as absolute staining intensities varied between VSMC batches. CaSR expression is therefore reported as CaSR intensity / SM22 α intensity for SM22 α + cells. To account for the different number of cells analysed in each image, the results were weighed with respect to the evaluated number of SM22 α + cells per batch (e.g. CaSR intensity from a ROI containing 100 cells would contribute 10 % to the total mean when pooled with a ROI containing 900 cells which contributes 90 %). Finally, the obtained values for relative CaSR expression of VSMC from KO mice was normalised to their respective WT controls from the same experiment (to allow comparability between the separately performed experiments which were stained, scanned and analysed at different dates). It has to be noted that the determination of the green fluorescence gate (SM22 α) and therefore the decision from

which staining intensity onwards a cell qualifies as positive for SM22 α had to be performed manually. However, since the same value for the green fluorescence gate was used for all investigated regions, comparisons between different batches of WT and KO cells are possible. Apoptotic cells (TUNEL+) are reported as % of VSMC (SM22 α +) cells.

2.4.9 VSMC numbers / proliferation

Cells were seeded at 7,500 cells per cm² in a 12-well plate and allowed to adhere to the bottom of the plate for 24 h. The medium was then changed to growth medium containing 1 % FBS for 24 h to synchronize cell cycles. Cells were then left in growth medium containing 10 % FBS supplemented with various CaCl₂ concentrations and then counted manually using a haemocytometer at the end of 5 and / or 10 days incubation. The medium was changed every 2-3 days.

2.5 Histomorphometry and immunofluorescence studies

2.5.1 Organ fixation and sectioning

Dissected organs were fixed by immersion fixation in 4 % (w/v) PFA in PBS for 4 hours and then washed in PBS and stored in 30 % (w/v) sucrose in PBS at 4 °C for cryoprotection. Tissues were embedded in optimal cutting temperature compound (TissueTek OCT, Sakura-Finetek, Alphen aan den Rijn, NL) on dry ice and 8-10 µm sections were prepared using a cryo-microtome (Leica 2300L, Leica microsystems, Milton Keynes, UK).

2.5.2 Immunofluorescence staining of tissues

For immunofluorescence, sections were rehydrated in PBS followed by incubation for 10 minutes in 50 mM NH₄Cl in PBS and then were antigen retrieved in steaming hot 10 mM citrate buffer pH 6 for 15 minutes followed by 5 minutes in 1 % sodium dodecyl sulphate (SDS) in PBS. Non-specific antibody binding was prevented using 1 % (w/v) BSA + 0.1 % (v/v) Tween 20 in PBS (blocking buffer) for 1 hour. Immunostainings and microscopic imaging were then performed as already described for cells (2.4.6).

For kidney sections, high autofluorescent background was quenched by incubation of the sections in 0.2 mM Sudan Black B in 70 % ethanol for 10 minutes in between the second secondary antibody and the nuclear counterstain (Sun et al. 2011).

2.6 Calcification assays

2.6.1 *In vitro* VSMC calcification

Cells were seeded in 24-well plates and were grown to 100 % confluency. The medium was then changed to growth medium supplemented with various CaCl_2 concentrations as specified in the results section. For induction of calcification, beta-glycero-phosphate (BGP) \pm alkaline phosphatase or inorganic Pi were added to the culture medium. Cells were left in culture for 10 days at the end of which they were fixed for 15 minutes in 4 % (w/v) PFA at room temperature and the amount of calcification was visualized by staining with 2 % alizarin red S (w/v) in water, pH 4.2 (Puchtler et al. 1969).

2.6.2 Staining for calcification on blood vessel sections

Cryosections of 4% (w/v) PFA fixed WT and KO aortae were stained for calcifications using Alizarin Red S as described in 2.6.1.

2.6.3 *Ex vivo* calcification of aortic explants

The assay was performed as described previously (Leroux-Berger et al. 2011). In brief, aortae were dissected as described for the primary VSMC isolation (see 2.4.2). After cleaning of the aortae from the tunica adventitia, the endothelial layer was destroyed by stretching the tissue over the whole length. The vessel was then cut into 3-4 pieces of approximately equal length (5–8 mm). The pieces were then incubated for 5 days in growth medium (see 2.4.2) supplemented with varying of CaCl_2 concentrations (1.2–2.5 mM) and 3 mM Pi, similarly to the VSMC calcification assays (see 2.6.1). After the incubation period, the explants were washed twice in PBS for 2 hours and deposited calcium was extracted by decalcifying the explants overnight in 0.6 N HCl at 37 °C. Eluted Ca^{2+} concentration in the supernatant was measured using the o-cresolphthalein complexone method (Moorehead and Biggs 1974; Jono et al. 1997). Ca^{2+} concentrations were normalised against the weight of the explants. Typical explant weights varied between 1.0 and 5.0 mg (measured on an analytical balance).

2.7 Cardiovascular analysis

2.7.1 Blood pressure measurement by tail cuff

Blood pressure of age- and sex-matched WT and KO mice were measured by tail cuff (Feng et al. 2008) using a 2-channel CODA system (Kent Scientific, Torrington, CT, USA) instruments and software, following the manufacturer's instructions. Mice were accustomed with the procedure by being restrained in either the supplied CODA restrainers or self-made restraining devices made from 50 ml syringes (Figure 14).

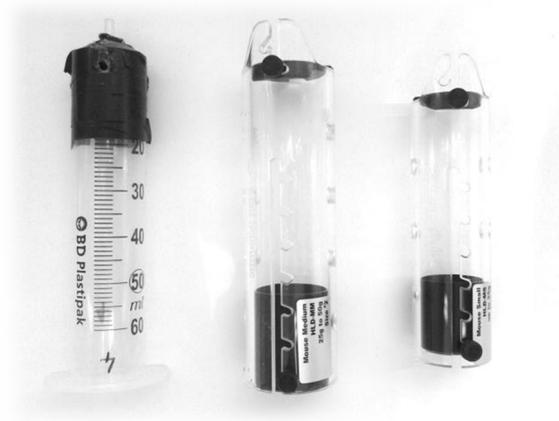


Figure 14: Mouse restrainers. Left: Restrainer made out of a 50 ml syringe. Middle: Large restrainer for mice up to 50 g. Right: Small restrainer for mice up to 25 g.

During the restraint and the actual procedure, the mice were warmed using an infrared lamp and temperature was monitored using an infrared thermometer, which was also used to measure the paw temperature of scruffed mice. For the final measurements, 15 acclimatization cycles of inflating and deflating of the cuff were granted to the animal to become accustomed to the sensation and to reduce struggling inside the restrainer. Blood pressure was then averaged from 10 successive measurement cycles and only measurements which were flagged as “OK” by the software were used for the averages. Measurements were performed in batches of age groups, alternating KO and WT mice. Measurements were performed over the course of two days at approximately the same time of day, either in the morning or during the night, to account for circadian variations in blood pressure (Li et al. 1999).

2.7.2 Blood pressure measurement by radiotelemetry

Blood pressure, heart rate and derived parameters (see Table 8) were measured by radiotelemetry (Boedtkjer et al. 2011) in collaboration with Professor Robert Fenton and Dr. Vladimir Matchkov (both Aarhus University, Denmark). HD-X11 radiotelemetry transmitters (Data Sciences International, USA) were implanted under general anaesthesia using a combination of fluanisone (10 mg / kg body weight), fentanyl (0.3 mg / kg body weight) and midazolam (1 mg / kg body weight). The transmitters were implanted in the aortic arch via the left carotid of 3 month old male animals (Figure 15) while the transmitter and power source were placed sub dermally in the abdominal region of the animal. Operations were performed by Dr. Vladimir Matchkov.

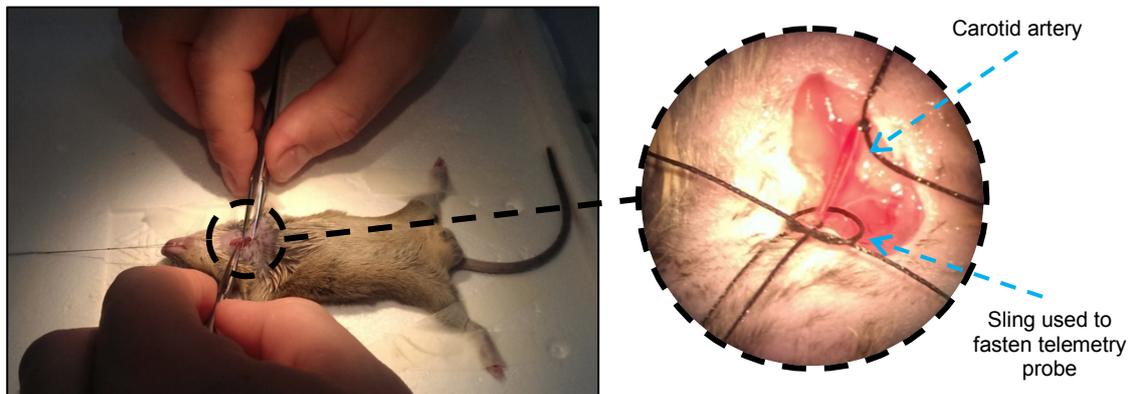


Figure 15: Implantation of radiotelemetry probes. The probes were implanted in the left carotid artery of the anaesthetized mouse and pushed forward into the aortic arch.

Mice were allowed to recover for 2 days before housing them in metabolic cages where they were kept on standard diet (see 2.2) for 4 days. Diet was then changed to a high salt diet (4% NaCl) for a period of 4 days. See chapter 2.8.1 for details on metabolic cage studies. For reasons of animal welfare, mice were then transferred back in normal housing cages and put back on standard diet. After a 3 days, drinking water of the mice was supplemented with 0.5 mg / l L-nitro-arginine-methyl-ester (L-NAME) for 2 days. See Figure 16 for an overview of the timeline of the telemetry experiment.

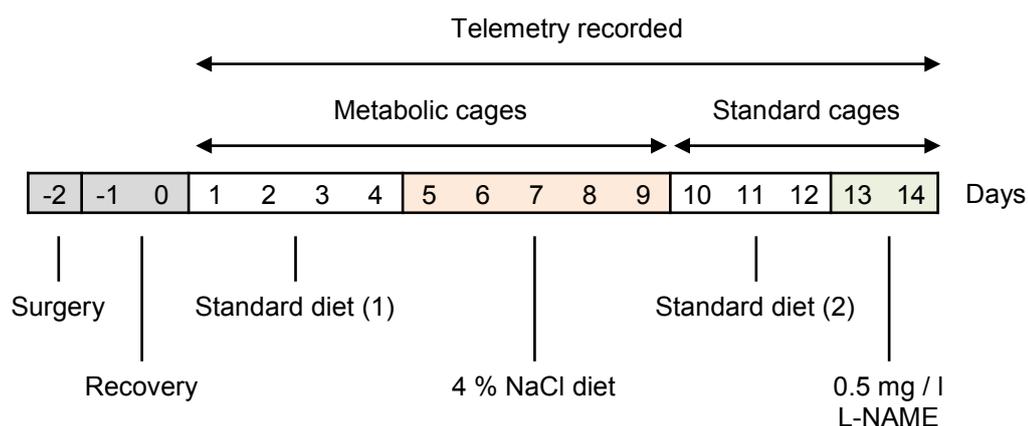


Figure 16: Timeline of telemetry experiments.

Telemetry signals from the probes were recorded for the whole duration of the experiment in intervals of 5 minutes in quintuplicates resulting in 60 measurements per hour. Parameters measured are given in Table 8. Raw data traces were generated with Ponemah analysis software 5.00 (Data Sciences International). Raw values were concentrated by combining all measurements for one hour. For smoothing of the traces, a rolling average (a new value is calculated for every hour based on the average of its adjacent hours) over 4 hours (data points) was applied (Figure 17) (Odenwald et al. 2006). Because of the different housing conditions, the standard diet vs. high salt diet and standard diet vs. 0.5 mg / l L-NAME diet phases were treated as two separate and incomparable experiments during analysis.

Table 8: Parameters obtained from radiotelemetry. Abbr. = Abbreviation

Parameter	Abbr.	Unit
Systolic blood pressure	Sys	mm Hg
Diastolic blood pressure	Dia	mm Hg
Mean arterial blood pressure	MAP	mm Hg
Heart Rate	HR	bpm
Pulse height (pulse pressure)	PH	mm Hg
positive 1 st derivative of the pressure curve	dp/dt	mm Hg / ms

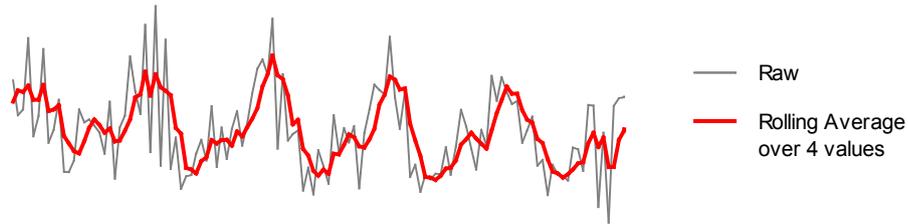


Figure 17: Example for use of a rolling average over 4 adjacent values for curve smoothing. The averaged curve follows the general trend while eliminating the large scatter of the raw data.

For statistical comparison of the different parameters between WT and KO mice, fixed three hour periods, one during the mice's active period and one during their resting period, on the last day of a diet regimen (e.g. standard diet, high salt diet, L-NAME) were selected on the basis of the average MAP curve for all mice (Figure 18). For the calculations, the raw values (not smoothed by rolling average) were used. An additional, new method of analysis is described in appendix B, 12.2.

The averaged values of the periods (specific three hour intervals which were the same for all mice) were averaged and compared using by two-way ANOVA for comparisons between WT and KO mice on different diets and individually during their active and resting period.

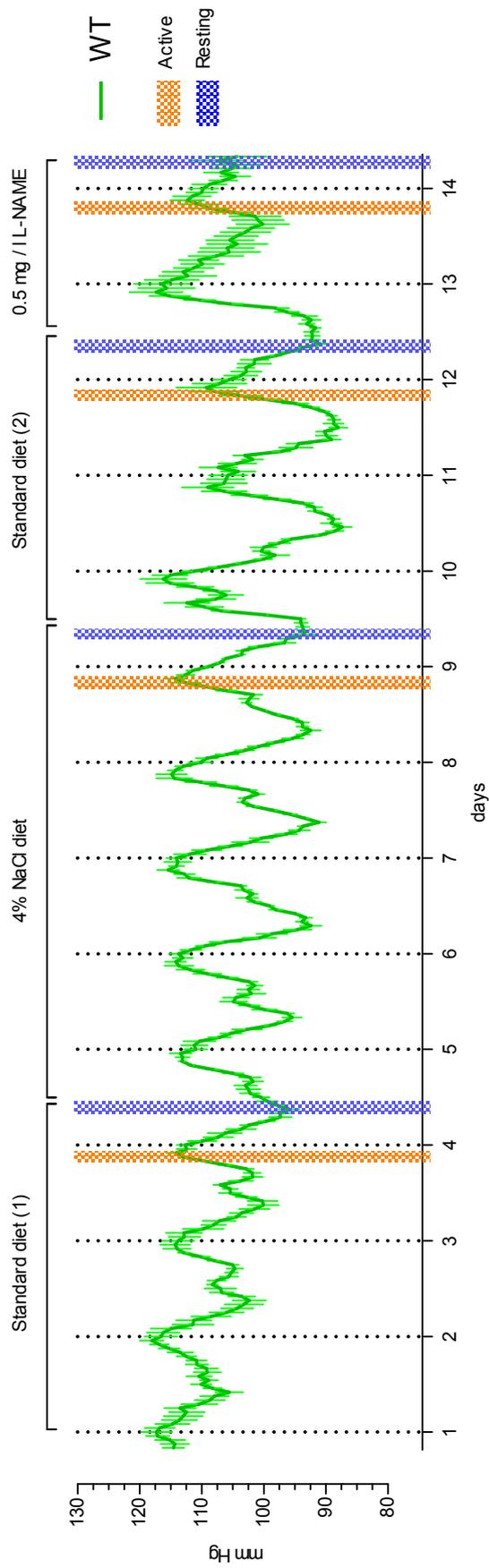


Figure 18: Fixed 3 hour intervals selected for comparison of telemetry derived parameters in active vs. resting state of the mice. The average MAP curves of the whole duration of the telemetry experiment for WT and KO mice are shown. Standard diet (1) and 4 % NaCl diet were administered in metabolic cages after which mice were transferred into normal housing cages. Time intervals from 8:00-10:00 (resting, blue) and 20:00-22:00 (active, orange) were used. For standard diet (1), 4 % NaCl diet and standard diet (2), the respective intervals of the last day before diet change were. Dotted lines indicate midnight. Curves smoothed using rolling average over 4 values. Mean \pm SEM, N = 5

2.7.3 Cardiac magnetic resonance imaging (MRI)

Cardiac cine-MRI scans were acquired using a Bruker Biospec 94/20 9.4 Tesla magnetic resonance imaging (MRI) system at the Experimental MRI centre (EMRIC) at Cardiff University. Details on the imaging system and preparation of the animals have been described previously (Kalogerou et al. 2011). In brief, the mice were anaesthetized using 1-5% (v/v) isoflurane in oxygen to achieve a breathing rate between 30-80 times per minute, as determined by pressure plate. Temperature of the animal was monitored by rectal probe and controlled by heated / cooled water tubing. 3-way electrocardiography (ECG) was applied. All measurements were performed using the Small Animal Monitor software and monitoring equipment (SA Instruments, Stony Brook, NY, USA). Bruker Paravision 5.0 was used to control the instrument. Details on cardiac analysis in rodents can be found in (Johnson 2008) and on cardiac cine-MRI specifically in (Schneider et al. 2006). Cardiac analysis in brief: the heart can be divided into two two-dimensional planes: The long axis, with the image plane going from the apex to the base of the heart, and the short axis which is oriented orthogonal to the long axis and therefore shows the diameter of the ventricles See Figure 19 for a graphical representation and example MRI images of the axes.

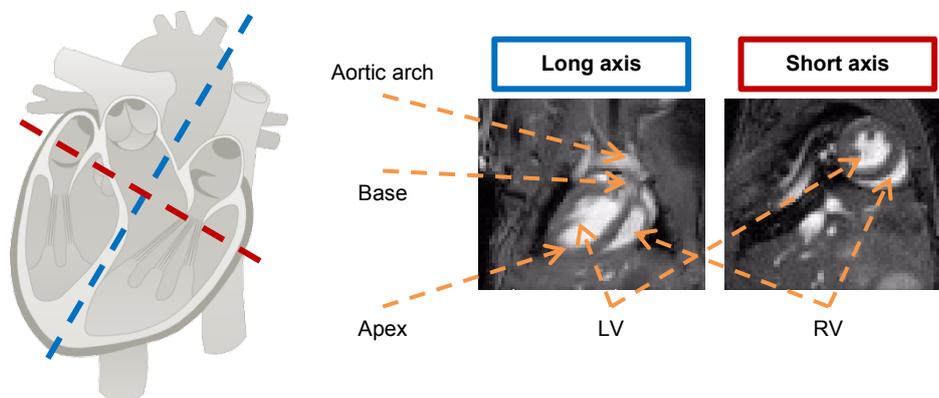


Figure 19: Short and long axes of the heart. Left panel: graphical representation of the heart with a blue broken line indicating the long axis and a red broken line indicating the short axis (image public domain). Right panel: Example long and short axis MRI images. Broken orange arrows indicate anatomical features. LV = left ventricle, RV = right ventricle.

To visualize the whole heart for analysis, it has to be analysed in all four dimensions. Multiple z-aligned 2D images of planes in the heart allow for a 3D reconstruction of the heart while

timed frames for all slices allow the tracking of the hearts movements during the heartbeat, which results in a “movie” of the beating heart (cine-MRI). To achieve this, the scanning sequence for all scans was coupled to ECG trace: every 5 ms following the R-wave, one frame for the final movie of a particular z-slice was recorded until the next R-wave was reached (Figure 20). During respiration, scanning was stopped to avoid the introduction of artefacts due to chest-motion.

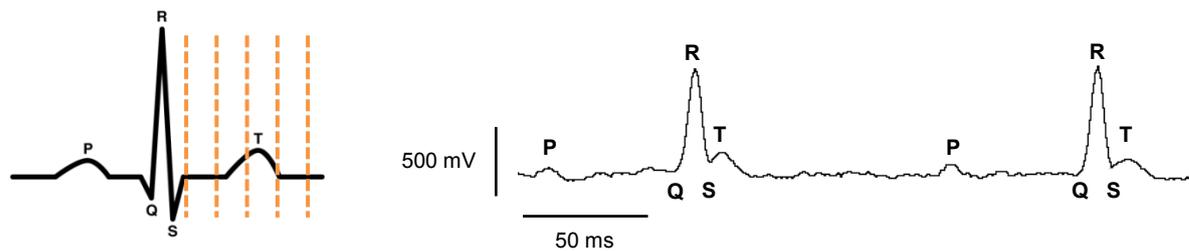


Figure 20: ECG-gated cardiac MRI. Left panel: idealised representation of an ECG trace showing MRI scans (orange broken lines) synchronized to the R-wave (image public domain). Right panel: Exemplary ECG trace of a mouse during MRI scan, showing clearly detectable R-waves which are detected by the monitoring software. Waves are indicated by their representative letters. The period (R to R) of this particular trace was 164 ms equating to a heart rate of approximately 365 bpm.: Modified cropped screenshot from Snapview 2.00 (SA Instruments).

Each mouse was scanned with a specific set of scans: One tri-axial pilot cine scan to determine the orientation of the heart followed by one long axis pilot cine scan with three slices depth to determine the geometry setup for the short axis scans. A high quality long axis scan with the image plane approximately going through the centre of the heart (for visualization and length measurement purposes) was then followed by eight high quality short axis scans ranging from above the base (ca. at the top of the aortic arch) to below the apex of the heart (so that the left ventricular cavity was no longer visible) for cardiac analysis. The mice were positioned and aligned and the scans performed by Mr Andrew Stewart, technician at the Cardiff EMRIC. The scanning sequence was programmed and optimized by Dr Pawel Tokarczuk, at Cardiff EMRIC. The completed scan cycle was then exported from the Bruker proprietary file format into files of the Digital Imaging and Communications in Medicine (DICOM) open standard and analysed using the academic version of Segment 1.9 (Medviso, Lund, Sweden). To exclude bias during the manual segmentation process, all DICOM files

were blinded by a third person prior to analysis (Dr. Isabella Ellinger, Medical University of Vienna, Austria).

The analysis was performed in a combined manual-automatic way. Left ventricular epicard and endocard of all slices and timeframes were manually marked up using the respective epi- and endo-cardium tools of Segment. This resulted in about 240 markups (average 20 frames x 6 slices with visible endocardium x 2 for epicardium and endocardium) per mouse. To preserve epicard continuity between the markups of the different slices and timeframes, the following procedure was observed (Figure 21): markups for endo- as well as epicard of the first timeframe of the most apical slice were drawn freehand. Both contours were then automatically refined using the respective software tool. These markups were then propagated one frame forward in time and adjusted manually or refined by the respective software tool. After finishing marking up the slice for all timeframes, the markups were propagated upward to the next slice in basal direction, where the manual and automatic refinement of the contours started anew at the first timeframe. Papillary muscles were excluded from the contour, i.e. they were included in the left ventricular volume. To avoid errors based on bias or experience, a re-iterative approach was chosen for the manual analysis. After all markups were complete and passed visual inspection, systole (= minimum LV volume) and diastole (= maximum LV volume) were auto-detected by the program using the respective tool. Right ventricle was marked up at the timeframes for systole and diastole as calculated by the LV markup and analysed in the same fashion. High quality long axis scans were used to measure heart length and diameter using the “ruler” tool in segment. All measured and calculated parameters are listed in Table 9.

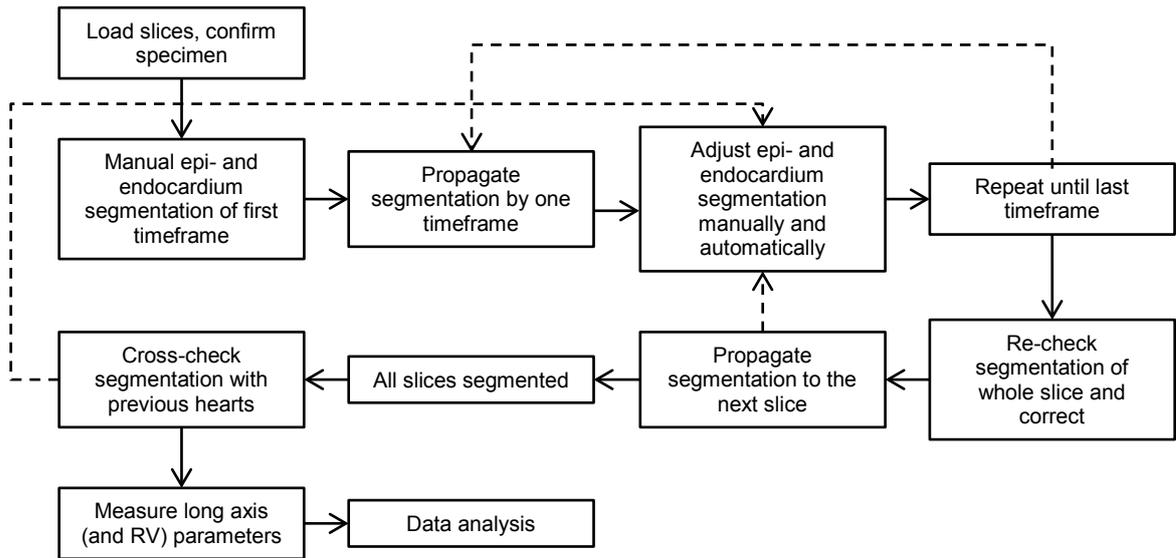


Figure 21: Workflow of the manual MRI analysis. Full arrows indicate normal workflow from first to last step. Broken arrows indicate iterations and re-evaluations. All samples were blinded to avoid bias during the segmentation process.

Table 9: Parameters obtained from cardiac cine MRI analysis. Abbr. = Abbreviation, LV = Left ventricle/ventricular, RV = Right ventricle/ventricular.

Parameter	Abbr.	Calculation	Notes
Total body weight	TBW		Volume of epicard as determined by markup. Density of heart tissue ~ 1.05 g / ml
LV-Mass	LVM		
LV-End diastolic volume	LV-EDV		Heart rate measurements not comparable because of general anaesthesia. Not used for analyses.
LV-End systolic volume	LV-ESV		
LV Stroke volume	LV-SV	LV-EDV - LV-ESV	
LV Ejection fraction	LV-EF	(SV/EDV) * 100	
Cardiac output	CO	LV-EF * heart rate	
LV Peak ejection rate	LV-PER		
LV-Peak fill rate	LF-PFR		
Diastolic remodelling index	DRI	LVM / LV-EDV	
Systolic remodelling index	SRI	LVM / LV-ESV	
End systolic length	ESL		Measured from long axis
End diastolic length	EDL		Measured from long axis
End systolic diameter	ESD		Measured from long axis
End diastolic diameter	EDD		Measured from long axis
LV average wall thickness	LV-WT		Average of second and third apical slices
RV end-diastolic volume	RV-EDV		
RV end-systolic volume	RV-ESV		
RV stroke volume	RV-SV	RV-EDV - RV-ESV	
RV ejection fraction	RV-EF	(RV-SV / RV-EDV) * 100	

2.8 Metabolism, clinical chemistry and bone

2.8.1 Metabolic cage studies

Mice were weighed and transferred to metabolic cages (Tecniplast, Buguggiate, IT) and then left for 48 hours to allow them to acclimatize to the new environment. Over the course of the following 24 hours, food and water intake, as well as faeces and urine production, were measured gravimetrically.

Additional metabolic cage studies were performed in collaboration with Professor Robert Fenton and Dr. Vladimir Matchkov (Aarhus University, Denmark). In these studies, mouse weight, food and water intake, as well as faeces and urine production were recorded over a period of 8 days where the mice were fed standard diet (see 2.2) for 4 days followed by a high salt diet (standard diet supplemented with 4 % w/w NaCl) for an additional 4 days.

Urine and faeces of all metabolic cage studies were stored at -80 °C for further analysis.

2.8.2 Clinical chemistry

Post-mortem blood collection from animals after neck dislocation was performed by quickly opening of the chest cavity and drawing blood directly from the heart using a 26 G needle. For serum collection, the blood was transferred into uncoated sterile tubes, for plasma collection, the blood was transferred into EDTA-coated collection tubes (BD Biosciences, Oxford, UK) and mixed by manual shaking. Blood was then left standing at room temperature for 30 minutes. The blood was centrifuged at 2,000 x g for 10 minutes and the supernatant transferred to a fresh tube and stored at -80 °C.

Blood collection from live animals was performed via tail nick, as described in (Sadler and Bailey 2013). In brief, animals were restrained as described in 2.7.1. The tail of the mouse was then cut at the position of one of the tail veins perpendicularly about 2 cm from the tip and about 0.5 mm deep using a razor blade. Blood was then collected in capillary haematocrit tubes coated with either Potassium-EDTA or sodium-heparin for plasma and uncoated haematocrit capillary tubes for serum. The collected blood was transferred to sterile un-treated tubes and left standing at RT for 30 minutes. The blood was then centrifuged at 2,000 x g for 10 minutes and the supernatant transferred to a fresh tube and stored at -80 °C.

Concentrations of electrolytes Na^+ , K^+ , Mg^{2+} , Ca^{2+} , Cl^- , and FGF 23 in serum as well as Na^+ , K^+ , Mg^{2+} , Ca^{2+} , Cl^- , Pi and Urea in urine were analysed by Mr Joao Graca and Dr Sally Price (Astra Zeneca, Macclesfield, UK) using a Roche modular P analyser (Roche diagnostics, and a commercially available ELISA kit for FGF 23 (Kainos Laboratories, Tokyo, Japan). Concentration of 1–84 PTH of plasma samples was analysed by Dr Donald Ward (University of Manchester, UK) using a commercially available ELISA kit (Immunotopics, San Clemente, USA). Concentration of 1,25-OH-Vitamin D3 (1,25-D3) of plasma samples were measured by Prof. Wenhan Chang (UCSF, CA, USA). Commercially available assays were used to measure concentrations of renin, aldosterone (both Abcam) and Fetuin A (R&D Systems, Abingdon, UK) according to the manufacturers' instructions. Clinical chemistry analyses of plasma and urine samples collected post-mortem in the course of the metabolic cage studies (see 2.8.1) were performed by a commercially available clinical pathology service (MRC Harwell, Oxford, UK).

2.8.3 Bone morphology

Femura of mice were analysed by micro X-Ray computed tomography (μ CT) analysis by Dr Wenhan Chang, UCSF, USA (Chang et al. 2008). Measured parameters are listed in Table 10.

Table 10: Bone structure parameters measured by μ CT (performed by Dr W. Chan, UCSF, USA).
Abbr. = Abbreviation

Parameter	Abbr.	Calculation
Distal Femur (trabecular bone)		
Total volume	Tb.TV	
Bone volume	Tb.BV	
Bone volume fraction	Tb.BV/TV	Tb.BV / Tb.TV
Connectivity density	Tb.CD	
Structure model index (Measure of trabecular shape)	Tb.SMI	
Number of trabeculae	Tb.N	
Trabecular thickness	Tb.Th	
Intratrabecular space	Tb.Sp	
Bone Mineral Density	Tb.BMD	
Tibio-fibular junction (cortical bone)		
Total volume	Ct.TV	
Bone volume	Ct.BV	
Bone volume fraction	Ct.BV/TV	Ct.BV / Ct.TV
Bone mineral density	Ct.BMD	
Cortical thickness	Ct.Th	

2.9 Statistical analysis

Data were organised using Microsoft Excel 2010 (Microsoft, Redmond, WA, USA). All statistics were performed using GraphPad Prism 5 (GraphPad Software, La Jolla, CA, USA). GraphPad Prism 5 does not report exact p-values for ANOVA post-tests. Where these tests were used, approximations (> 0.05 , < 0.05 , < 0.01 , and < 0.001) are listed in the respective results tables. Statistical sample size is reported as N (number of separate experiments / biological repeats) over n (technical repeats per sample, where applicable). The employed statistical tests and significance levels are specified in the respective results sections or in the figure legends.

3 Method development and optimisation

3.1 Introduction

Before the experiments to characterise the SM22 α -Cre x LoxP-CaSR mouse could commence, various protocols and assays had to be optimized. As loss of CaSR expression is accompanied by increased mineralization in bovine VSMC and human arteries (Alam et al. 2009), the ability of WT and KO derived VSMC to mineralize *in vitro* was to be investigated. Because of substantial discrepancy in the literature, e.g. (Son et al. 2006; Wang et al. 2007; Alam et al. 2009; Panizo et al. 2009; Prosdocimo et al. 2010; Sage et al. 2011; Villa-Bellosta and Sorribas 2011; Zhu et al. 2011; Ciceri et al. 2012a) in protocols for induction of calcification of VSMC, initial experiments to find the best conditions for calcification of murine VSMC had to be conducted using VSMC from control mice.

The potency of the CaSR is influenced by extracellular pH (Quinn et al. 2004) (Figure 23). Therefore, the influence of the used medium additives (namely different concentrations of Ca²⁺ and Pi) on medium pH had to be investigated in control experiments to ensure that potential observed Ca²⁺ mediated effects are ligand mediated and not the result of a change in pH, which ultimately would affect CaSR EC₅₀ values for Ca²⁺. To my knowledge, this is the first time that the effects of possible pH changes in culture medium effected by experimental conditions is investigated when studying CaSR-mediated responses.

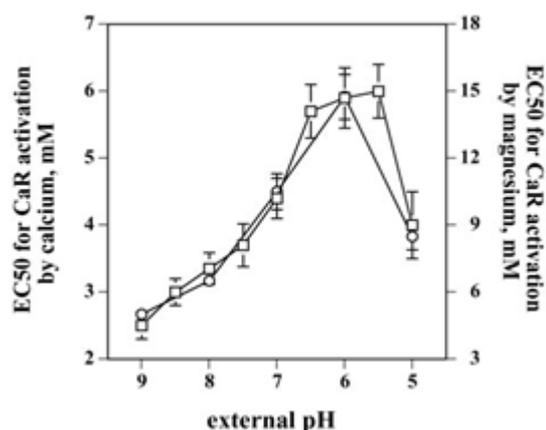


Figure 22: Influence of external pH on EC₅₀ for CaSR activation by Ca²⁺ and Mg²⁺ (Quinn et al. 2004). Image used with permission of The American Society for Biochemistry and Molecular Biology.

For investigation of CaSR expression in tissues and VSMC preparations, it is important to use a well characterised antibody. One of the best characterised antibodies for the CaSR is a mouse monoclonal antibody, clone 5C10, directed against an antigenic region in the amino-terminus of the CaSR (residue 215-235, termed “ADD”). This antibody recognizes the non-glycosylated (120 kDa), high-mannose (130-140 kDa) and fully glycosylated forms (150-160 kDa) of the CaSR as well as dimers and oligomers (250–300 kDa) of the receptor in western blot analysis (Weston et al. 2005; Alam et al. 2009; Magno et al. 2011) and is also widely used in immunohistochemical analyses (Weston et al. 2005; Alam et al. 2009). However, since the host species of this particular antibody is mouse, it is not ideally indicated for use on mouse tissue or cells as required in this study. Other in-house available antibodies as well as other available commercial antibodies were therefore compared to the “ADD” antibody using HEK cells stably transfected to express the (human) CaSR (Maldonado-Perez et al. 2003).

Frozen sectioned murine kidney tissue, which acts as a positive control for CaSR expression and which in the course of the holistic characterisation approach of the SM22 α -Cre x LoxP-CaSR mouse will be widely used for immunohistochemistry studies, is especially known for high autofluorescence (Viegas et al. 2007; Sun et al. 2011). Therefore, this tissue was widely used for optimisation protocols for antibody staining and specific autofluorescence quenching.

3.2 Results

3.2.1 Influence of addition of different concentrations of Ca²⁺ and Pi on the pH of the culture medium

pH is known to modulate CaSR affinity for Ca²⁺ with alkalisation enhancing it while acidification inhibiting it (Quinn et al. 2004). As an initial control for my experiments, the impact of the experimental additives Ca²⁺ and Pi on medium pH was tested to ensure observed functional changes in *in vitro* assays are the result of changes in ion concentration and not a shift in medium pH, which would ultimately influence CaSR affinity for its agonists. Addition of Pi did not change medium pH in the range of the used Pi concentrations (1–3 mM Pi). Addition of CaCl₂ decreased medium pH by approximately -0.1 over the range of the investigated conditions (0.8–2.5 mM CaCl₂) (Figure 23). Since the shift of CaSR EC₅₀ for Ca²⁺ caused by a pH shift of -0.1 would be expected to be in the micromolar range (Quinn et al. 2004) (*c.f.* Figure 22), the effect of addition of Ca²⁺ (in the form of a 1M solution of CaCl₂) and / or Pi (in the form of a 1 M phosphate buffer pH 7.4, composed of NaH₂PO₄ and Na₂HPO₄) on medium pH was considered small.

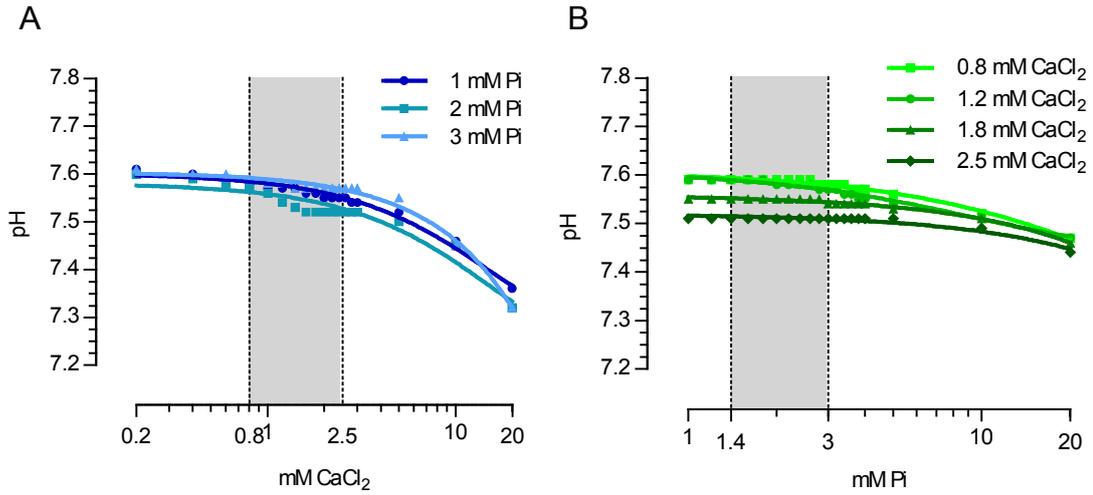


Figure 23: Influence of addition of different concentration of Pi (phosphate buffer pH 7.4, composed of NaH_2PO_4 and Na_2HPO_4) or CaCl_2 on medium pH. Growth medium was bubbled with a mixture of 5 % CO_2 in air. The figure shows that pH did not drop below pH 7.6 irrespective of equilibration time. Grey areas indicate concentrations used in this study (0.8–2.5 mM CaCl_2 , 1–3 mM Pi). Increasing CaCl_2 concentrations lead to a small drop in medium pH in the concentrations used in this study (A). Increasing Pi concentrations did not influence pH in the concentration range used in this study but a definite drop in medium pH was observed between the lower (0.8 and 1.2 mM) and higher (1.8 and 2.5 mM) CaCl_2 concentrations (B) as expected from the results in (A). N = 1

3.2.2 *In vitro* VSMC calcification protocol development

Initial mineralization assays were carried out using BGP as a phosphate source for the mineralization process, as described previously (Alam et al. 2009; Panizo et al. 2009; Zhu et al. 2011). However, in our study, calcification could not be observed either in the presence of 5 mM BGP after 6 weeks of incubation (data not shown) or with 10 mM BGP after an incubation period of 2 weeks (albeit moderate calcification was observed after 4 weeks) (Figure 24, left panels). It is possible that these negative results were caused by a lower endogenous alkaline phosphatase (ALP) activity (A. Sage, University of California Los Angeles, CA, USA, personal communication) in murine VSMC in contrast to bovine or human derived VSMC. Experiments carried out with medium supplemented with 6 U / ml ALP resulted in abundant calcification of all VSMC regardless of extracellular Ca^{2+} concentration (Figure 24, middle panels). Finally, a Pi buffer (pH 7.4, composed of NaH_2PO_4 and Na_2HPO_4), as described in (Sage et al. 2011), was used and resulted in time-, Ca^{2+} - and Pi-dependent calcification of murine VSMC (Figure 24, right panels).

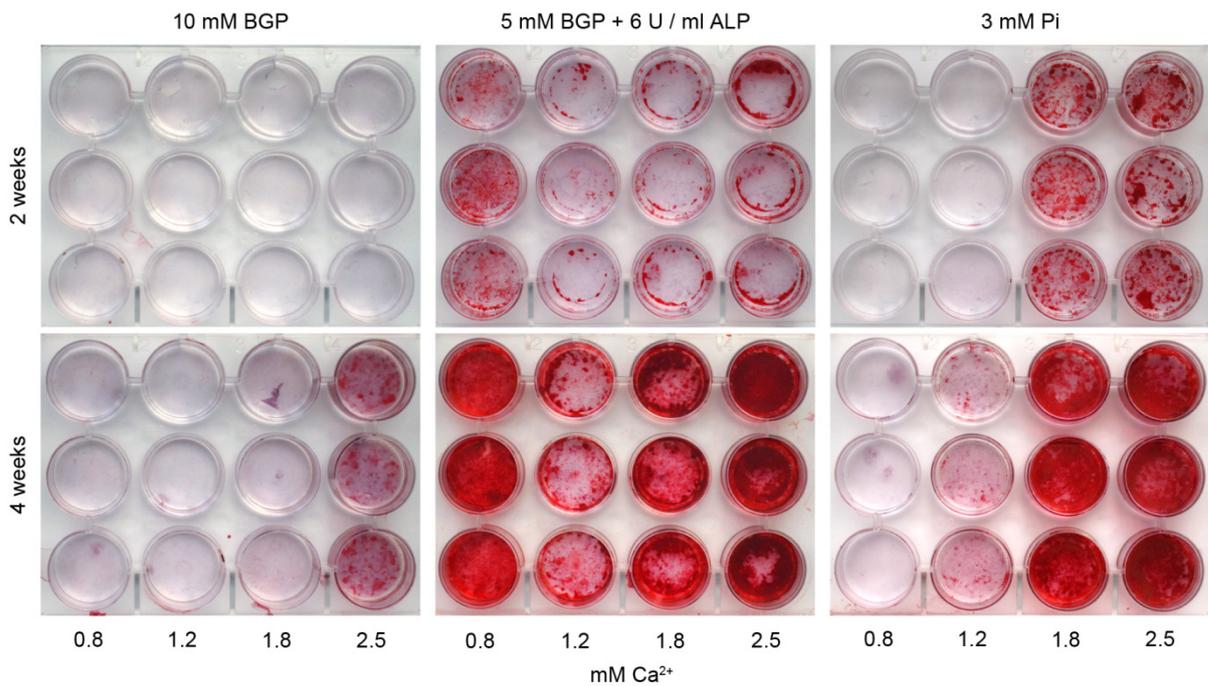


Figure 24: Optimization of *in vitro* mouse primary VSMC calcification assay. Alizarin red S staining of confluent VSMC derived from aortic explants from control mice. In the presence of medium containing 2.5 mM Ca^{2+} , treatment with 10 mM β -glycerol phosphate (BGP) did not induce calcification in cells cultured for two weeks and induced only moderate calcification after four weeks. 6 U alkaline

phosphatase (ALP) / ml medium + 5 mM BGP resulted in weak calcification after two weeks in culture and high levels of calcification after four weeks irrespective of Ca^{2+} concentrations in the culture medium. Addition of 3 mM phosphate to the culture medium, supplied as Pi buffer pH 7.4 (Pi), resulted in moderate calcification after two weeks in the presence of medium containing either 1.8 or 2.5 mM Ca^{2+} . Treatment for 4 continuous weeks resulted in mild calcification in the presence of 1.2 mM Ca^{2+} and high levels of calcification in the presence of 1.8 and 2.5 mM Ca^{2+} . Because of the concentration and time dependant calcification response to Pi, this phosphate source was chosen as additive for subsequent calcification experiments.

3.2.3 Immunofluorescence staining optimisation

3.2.3.1 Anti-CaSR antibody comparison in HEK293 cells stably transfected with the human CaSR (HEK-CaSR)

The ability of several commercially and non-commercially available antibodies to perform against a “gold-standard” commercially available 5C10 antibody (Abcam ADD, which detects amino acid 214-230 of the human CaSR) was tested in immunofluorescence double staining experiments on stably transfected HEK-CaSR cells (Maldonado-Perez et al. 2003). Two in-house available custom antibodies from previous studies, “733”, provided by Prof. Daniela Riccardi (Cardiff University) and “Shob”, kindly provided to us by Dr Dolores Shoback (UCSF, USA) and two commercially available rabbit polyclonal antibodies, as well as a mouse polyclonal antibody raised against the synthetic human full length protein were tested in comparison. Figure 25 shows that both the Shob and the AnaSpec antibodies gave results comparable to the Abcam ADD antibody. The 733 antibody produced no staining while the LifeSpan C-terminal directed antibody stained exclusively the nucleus (Figure 25). The antibodies were also tested for specificity and comparability in western blot analysis of CaSR-HEK cell lysates and the AnaSpec antibody produced comparable results as the 5C10 antibody (S. Brennan, personal communication). See Table 11 for a list of the tested antibodies.

Thus, given that the commercial AnaSpec antibody is readily available and detects CaSR immunoreactivity of the predicted size in HEK-CaSR cells, it was chosen as antibody for future CaSR detection and immunolocalization studies in cells and tissue.

Table 11: List of tested anti-CaSR antibodies. N-term = N-terminal, C-term = C-terminal, N/D = not disclosed

Antibody	Supplier	Type	Source	Antigenic region
ADD	Abcam	Monoclonal IgG	Mouse	N-term 214-235
Anaspec	Anaspec	Polyclonal IgG	Rabbit	N-term, N/D
Lifespan C-term	Lifespan	Polyclonal IgG	Rabbit	C-term aa 854-903
733	In house	Polyclonal IgG	Rabbit	N-term 214-235
Shob	In house	Polyclonal IgG	Rabbit	N-term 214-235
Full Length	Novus Biologicals	Polyclonal IgG	Mouse	1 – 1078 aa

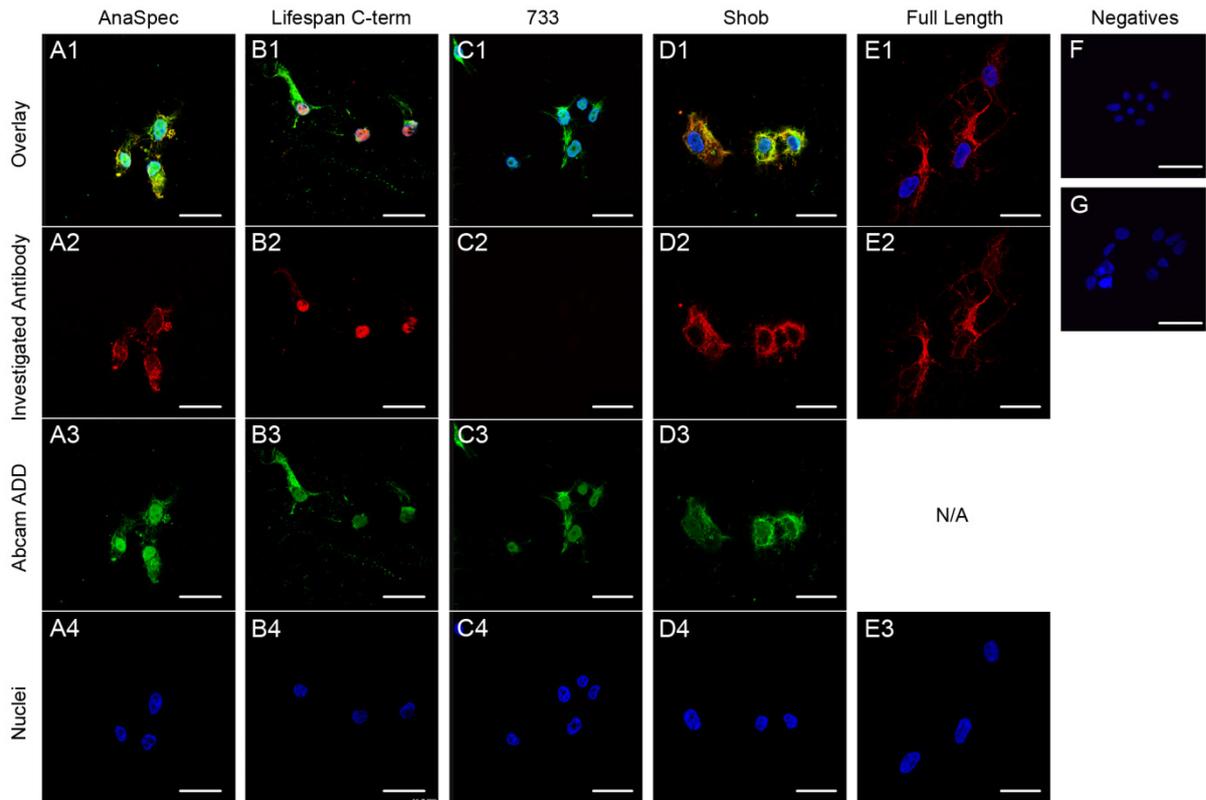


Figure 25: Test of anti CaSR antibodies on HEK293 cells stably transfected with human CaSR (HEK-CaSR). Confocal images of PFA fixed HEK-CaSR cells shown with (row 1) or without (rows 2 and 3) overlay of all channels and Hoechst 34580 nuclear counterstaining, shown on its own in (row 4). Cells were double stained with the reference mouse monoclonal anti-CaSR antibody, clone 5C10 (Abcam ADD) and one out of four rabbit polyclonal anti-CaSR antibodies. Of the two tested commercial antibodies, the AnaSpec antibody, which is directed against the N-terminal domain of the CaSR showed a very similar staining pattern (A2) as the Abcam ADD staining (A3), although the latter produced more pronounced nuclear staining. The LifeSpan antibody, directed against the C-terminal domain, directed produced exclusive nuclear staining (B2) which was in stark contrast to the ADD staining pattern (B3). The 733 antibody, which was produced in house for a previous study, failed to produce any staining (C2) while the Shob antibody, donated by D. Shoback (University of California San Francisco, San Francisco, CA, USA) produced similar staining results (D2) as the Abcam ADD (D3) antibody. A mouse polyclonal antibody, raised against the synthetic full-length peptide of the CaSR, produced staining of similar appearance (E) to the previously observed Abcam ADD stainings. Negative controls, shown as overlay of all channels and Hoechst 34580 nuclear staining, included goat anti mouse (F) or goat anti rabbit (G) secondary antibodies and no primary antibodies and showed no staining. N/A: not available (only single stainings were performed using this antibody). Scale bars represent 30 μm .

3.2.3.2 Optimization of immunofluorescence kidney stainings

The different antibodies were tested on kidney tissue by immunostaining. However, this approach proved difficult because of very high background autofluorescence of the tissue,. Common quenching methods, which included the use of NH_4Cl and glycine incubation, proved ineffective, as only signals from pecam-1 or sm22 α positive tissue, but no CaSR staining were detectable (Figure 26).

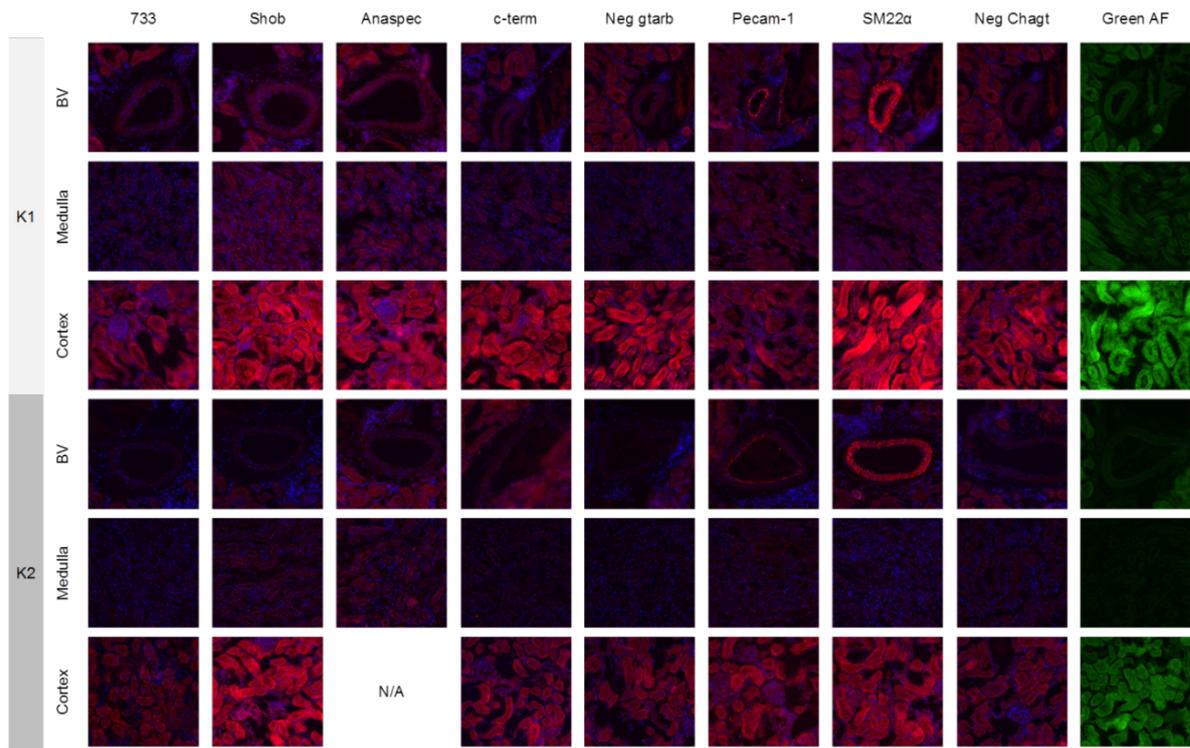


Figure 26: Antibody staining trial on control kidney sections. Four different rabbit polyclonal antibodies against the CaSR were tested for their ability to detect CaSR expression in PFA-fixed murine cryosections from kidneys of two C57/Bl6 animals (K1 and K2). Pictures show a renal blood vessel (BV), the medulla and the cortex of the kidneys as overlay of the antibody's respective channel (red) with Hoechst 34580 nuclear counterstain. The column "green AF" shows pictures of the autofluorescence present in the tissue at 488 nm emission wavelength. The commercially available (Anaspec and LifeSpan) C-terminal, the in house 733 and Shob antibodies were tested. As a control for the staining procedure, the endothelium- and VSMC-specific markers pecam-1 and sm22 α were used, respectively. The latter two stainings worked in both kidneys, while no staining for the CaSR was observed regardless of the antibody used. Autofluorescence of the tissue was very high in both 488 and 594 channels and especially prominent in the cortex of the kidneys. N/A: not available due to tissue loss. Scale bar = 100 μm in all pictures.

To overcome this problem, a protocol using Sudan Black B, as described in (Sun et al. 2011), was developed and optimized to quench autofluorescence effectively in all channels (Figure 27), although at the cost of lower contrast due to reduced black-levels in the embedding medium, but with a marked increase in staining visibility, as demonstrated by CaSR staining on cryosections of the same mouse kidney once non-quenched and Sudan Black B quenched respectively. In the non-quenched section specific staining was very hardly distinguishable from autofluorescence (negative control by omission of primary antibody) while specific, high contrast staining was observed when the section was quenched using Sudan Black B with background fluorescence almost reduced to zero (Figure 28).

Immunostainings and investigation of the kidneys of WT and KO mice will be performed in the future.

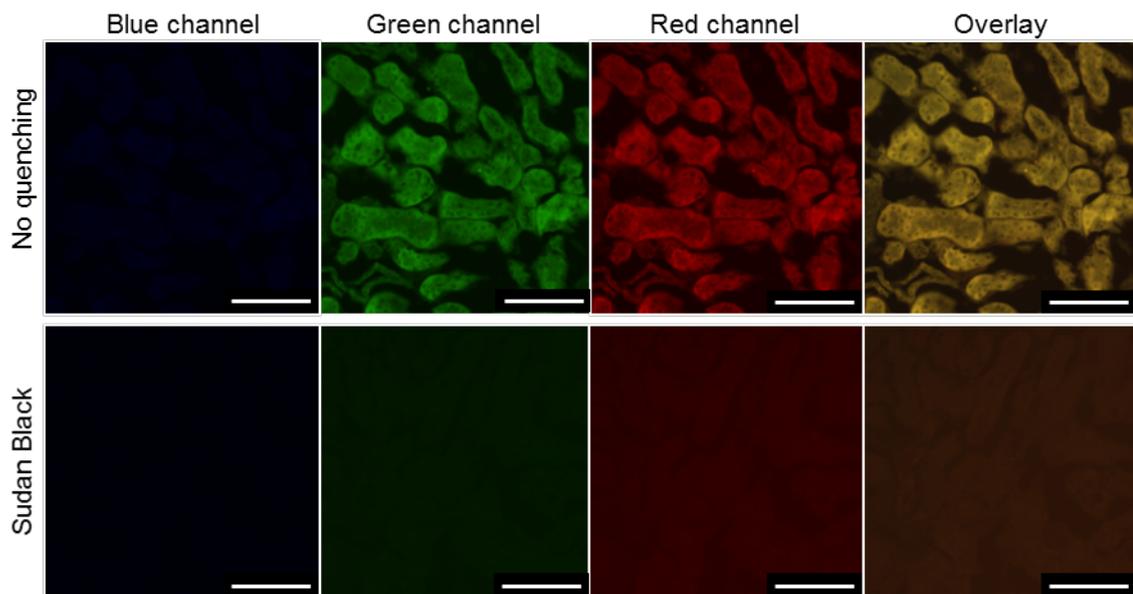


Figure 27: Quenching of high autofluorescence in the kidney using Sudan Black B. Epifluorescence images of PFA fixed 8 μm cryosections of mouse kidney tissue without staining. Without quenching (top row) no background was visible in the blue channel, but very high autofluorescence remained in both the green and red channels. Autofluorescence quenching with 0.2 % Sudan Black B in 70 % ethanol (bottom row) reduced background fluorescence significantly in all channels. Scale bars = 100 μm

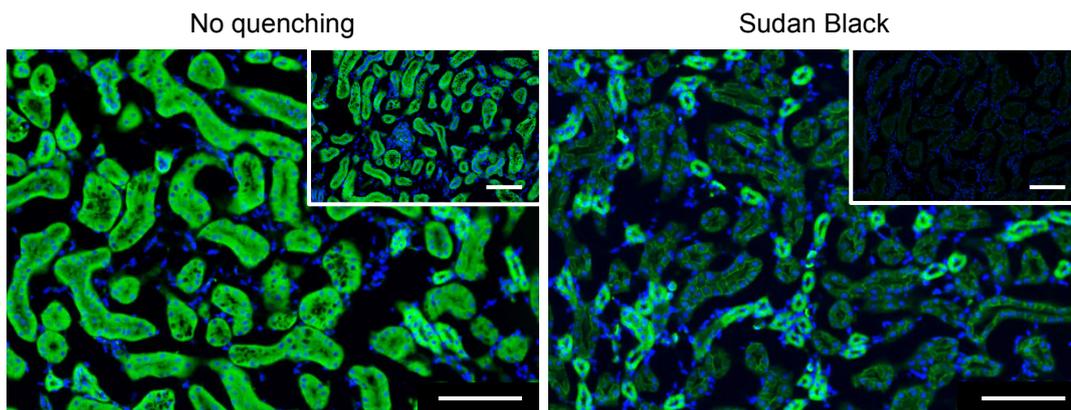


Figure 28: Effect of autofluorescence quenching using 0.2 % Sudan Black B in 70 % ethanol on PFA fixed 8 μm cryosections of mouse kidney stained for the CaSR. All images were acquired using the same exposure. Negatives (no primary antibody) in top right corners. Scale bars = 100 μm

3.3 Discussion

In this chapter I optimized and developed protocols which were I then used during my PhD (influence of pH on culture conditions, calcification conditions, determination of CaSR antibodies for VSMC stainings) and future use (immunofluorescence staining protocol for kidney sections).

In addition to Ca^{2+} , a variety of Pi sources were investigated as potential mineralisation inducers. Pi was selected as phosphate source for the experiments. I determined that in the presence of various Ca^{2+} concentrations, the best phosphate source for an *in vitro* calcification assay of murine cultured VSMC is free ionised Pi in the form of a Na_2HPO_3 / NaH_2PO_3 buffer. Even though higher Pi concentrations have been used in other studies (Prosdocimo et al. 2010; Leroux-Berger et al. 2011), I chose to use concentrations of 1.4, 2.0 and 3.0 mM Pi to mimic control normo-, and hyper-phosphataemic conditions in which calcification of VSMC has been demonstrated to occur (Villa-Bellosta and Sorribas 2011). I also determined that this Ca^{2+} and Pi supplementation of the culture medium does not influence medium pH sufficiently to induce changes in CaSR EC_{50} for Ca^{2+} . Furthermore, an anti-CaSR antibody was selected for immunostainings and an immunofluorescence protocol was developed which allows high-contrast staining and suppression of the endogenous autofluorescence in murine kidney tissue. This method will be used in the future (not in the course of this thesis) to investigate the renal phenotype of the SM22 α -Cre x LoxP-CaSR mouse.

3.4 Conclusions

- *Optimal experimental protocols were developed for in vitro murine VSCM calcification.*
- *Addition of Pi and Ca^{2+} to culture medium of murine VSMC in vitro does not significantly alter medium pH, ruling out an effect of pH on CaSR function.*
- *The best possible antibody was selected for immune-staining of the CaSR.*
- *Immunofluorescence staining protocols for murine kidney sections were optimized.*

4 General phenotype of the CaSR-LoxP x SM22 α -Cre mouse

4.1 Introduction

The very first step towards investigating the phenotype of the SM22 α -Cre x LoxP-CaSR mouse was to establish a method for accurate determination of the mice's genotype. Tissue specificity of the SM22 α -Cre promoter had been demonstrated previously (Moessler et al. 1996; Holtwick et al. 2002). Within this project, it was investigated if the mice showed any obvious differences in behaviour, reproductive capabilities, lifespan or body weights to explore any immediate effects of deleting the CaSR from the vasculature. Due to the large animal numbers used during this project overall, this part of the work was performed in collaboration with Dr Thomas Davies, see also (Davies 2013). Finally, expression of the CaSR in murine blood vessels was confirmed in this chapter.

4.2 Results

4.2.1 Genotyping and cursory phenotypic differences

Genotyping of the mice performed on ear biopsies showed expression of SM22 α driven Cre expression as well as floxed CaSR alleles in wild-type (WT), heterozygous (HET) and knock-out (KO) mice as expected (Figure 29).

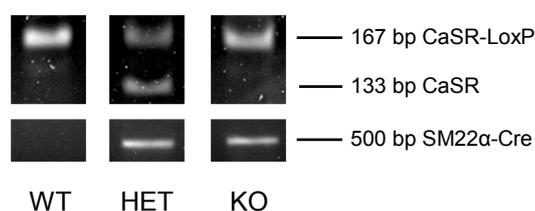


Figure 29: Exemplary genotyping results from mice of genotypes used in this study. Following PCR amplification, samples were electrophoretic separated using a 15 % (v/v) acrylamide gel for LoxP-CaSR and a 2 % (w/v) agarose gel for Cre, Upper panels: a 167 bp band is expected for a floxed CaSR allele and a 133 bp band for the WT allele. Lower panels: presence of the sm22 α -Cre construct is shown by a 500 bp band. Mice expressing two floxed CaSR alleles (LoxP-CaSR^{+/+}) but no Cre-recombinase (Cre⁻) are defined as WT (left panel, WT), mice expressing one floxed CaSR allele (LoxP-CaSR^{+/-}), one WT-CaSR allele and Cre-recombinase (Cre⁺) are defined as HET (middle panel, HET), mice expressing two floxed CaSR alleles and Cre-recombinase (Cre⁺) are defined as KO (right panel, KO). Bands are shown for illustrative purposes and do not correspond to particular mice used in this study. Image contrast has been enhanced for better visibility.

In terms of overall appearance, no phenotypic differences could be found between wild type (WT), heterozygous (HET) and KO genotypes (Figure 30) as mice of all three genotypes appeared healthy, well groomed, alert and inquisitive and lived out normal lifespans, at least beyond 18 months (see also Figure 31), but also beyond 24 months by observation.



Figure 30: Photographs of exemplary WT, HET and KO mice. Image modified after (Davies 2013).

4.2.2 Body weight

Body weights of the mice over time showed a significant difference only for female mice 1 month after birth, with a mean weight of $14.87 \text{ g} \pm 0.40$ ($N = 35$) for WT and $12.27 \text{ g} \pm 0.75$ ($N = 21$) for KO animals ($p < 0.01$, mean \pm SEM, two-way analysis of variance (ANOVA), Bonferroni post-test) but this difference was lost as the mice grew older (Figure 31). No difference was seen in WT and KO male mice up to 18 months of age. All values for the weights are reported in Appendix A, Table 14.

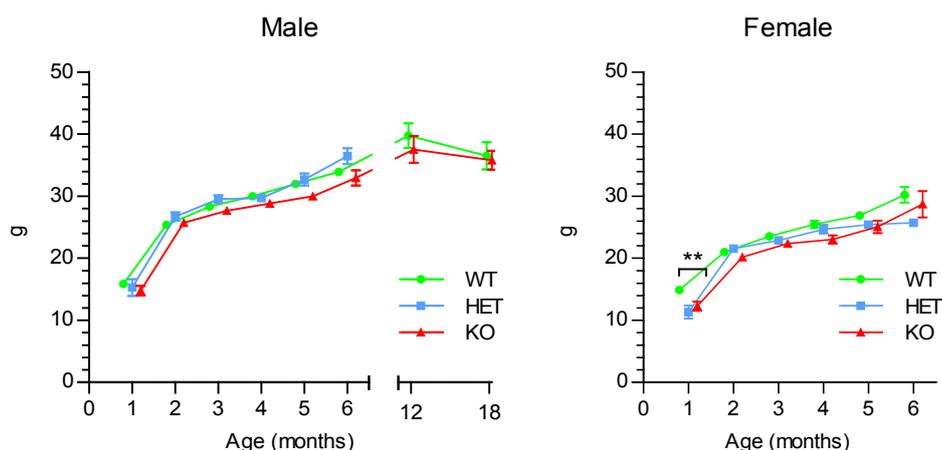


Figure 31: Body weight of male and female WT, HET and KO mice over the course of 18 (male) or 6 (female) months of age. A significant difference was observed between one month old female mice WT and KO. N = 3–65 (details in), mean \pm SEM. ** P < 0.01 vs. WT, Two-way ANOVA with Bonferroni post-test. 1–6 month by Dr. Thomas Davies (Davies 2013), 12 and 18 month data by MS.

4.2.3 Reproductive capabilities

Reproductive capability of WT, HET and KO mice was comparable and did not show any significant differences (Figure 32). See (Davies 2013) for detailed analysis of Mendelian ratios and breeding ratios.

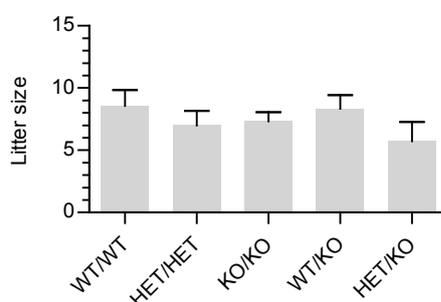


Figure 32: Reproductive capabilities of WT, KO and HET mice. Litter sizes were comparable irrespectively of the genetic background of the parents. N = 7-9 litters, mean + SEM, ANOVA. Data collected by Dr Thomas Davies (Davies 2013).

4.2.4 Expression of the CaSR in the vasculature

In a pilot study on a mesenteric artery of a control (C57/Bl6) mouse, CaSR expression was found in all three layers of the blood vessel by immunofluorescence staining, as shown by co-localisation of CaSR immunoreactivity with pecam-1 (endothelial marker, which showed the strongest signal), SM22 α (VSMC) and cells of the tunica adventitia (Figure 33). These results are consistent with previous publications in mouse/rat/human (Bukoski et al. 1997; Weston et al. 2005; Molostvov et al. 2007; Loot et al. 2013).

Trial immunostaining for CaSR on sections of WT and KO aortae showed only a very weak signal in the tunica media, consisting of SM22 α ⁺ VSMC, while high levels of staining for the CaSR was observed in the tunica intima, *i.e.* the pecam-1 positive endothelium of the blood vessels. The observed background in the negative controls was, however, very high, which could have accounted for the weak CaSR staining in the VSMC (Figure 34). Several optimisation protocols were tested to improve upon CaSR detection in mouse aortae and mesenteric arteries from WT and KO animals, but did not yield better results (not shown).

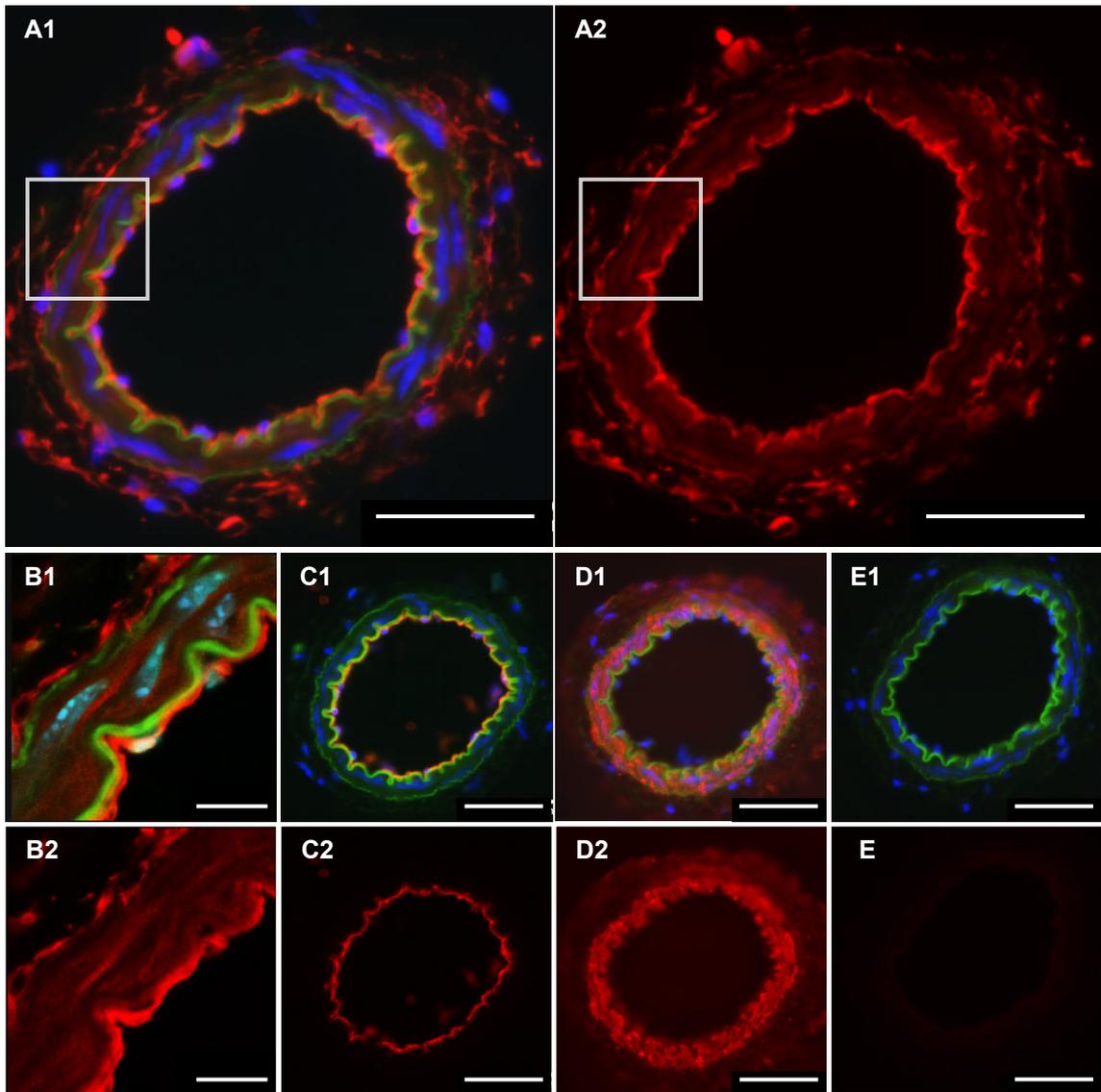


Figure 33: Immunolocalization of the CaSR, pecam-1 and SM22 α in transverse sections of mesenteric arteries from control mice. Epifluorescence images (A and C-E) and confocal images (B) from the area marked by the squares in (A) of PFS fixed 7 μ m cryosections. Staining for CaSR (red) with (A1 and B1) and without (A2 and B2) overlay of Hoechst 34580 counterstaining for nuclei (blue) and elastin autofluorescence (green). Expression of the CaSR was observed in the endothelial layer as well as in some smooth muscle cells. Staining for endothelial marker pecam-1 (red) in a consecutive section of the same mesenteric artery shown with (C1) and without (C2) Hoechst 34580 and elastin overlay demonstrates that the endothelium is intact throughout the vessel ring and localized in the same region of the tissue as the observed CaSR staining. Staining for SM22 α (red) with (D1) and without (D2) overlay of Hoechst 34580 and elastin overlay shows high expression of SM22 α in the smooth muscle cell layer of the artery. A negative control, performed by omitting the primary antibody, shown with (E1) and without (E2) Hoechst 34580 and elastin overlay, displayed no staining. Scale bar represents 50 μ m for (A and C-E) and 10 μ m for (B).

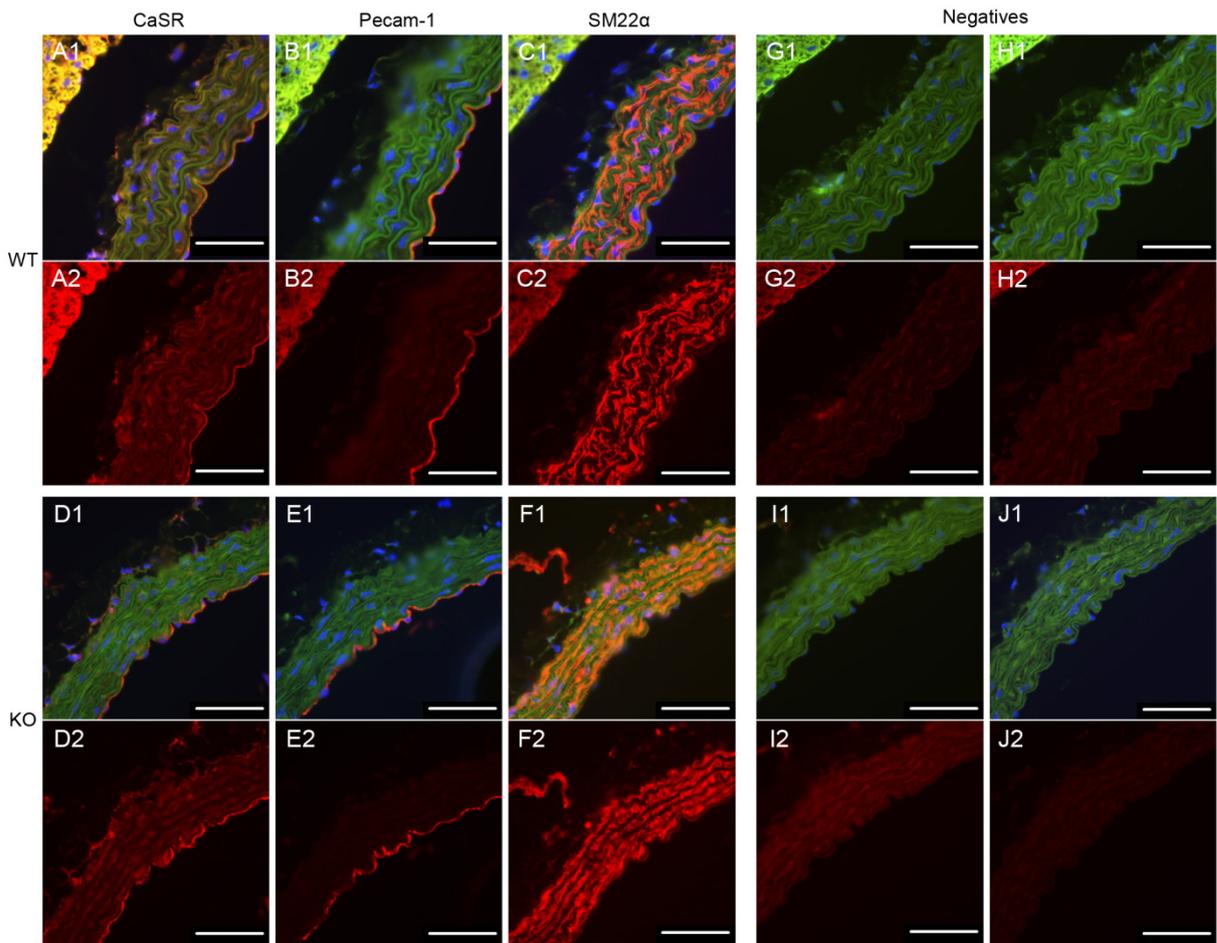


Figure 34: Immunolocalization of the CaSR, Pecam-1 and SM22 α in transverse section of aortae from WT and KO mice. Epifluorescence images of PFA-fixed 7 μ m cryosections. CaSR staining (red) in aortae from WT (A) and KO (D) mice shown with (A1 and D1) and without (A2 and D2) overlay of Hoechst 34580 nuclear counterstain (blue) and elastin autofluorescence (green) showing expression of the CaSR in the endothelium and, to a lesser extent, in the VSMC. Pecam-1 staining (red) shown with (B1) and without (B2) Hoechst 34580 and elastin overlay illustrates the localization of the endothelium. Staining for SM22 α (red) shown with (C1) and without (C2) Hoechst 34580 and elastin overlay illustrates the localization of VSMC. In (A-C), the tunica adventitia exhibits high autofluorescence. Negative controls, realised through omission of the respective primary antibodies, using anti-rabbit secondary antibody only shown with (G1, I1) and without (G2, I2) Höchst 34580 and elastin overlay as well as anti-goat secondary antibody only shown with (H1, H1) and without (H2, J2) Höchst 34580 and elastin overlay show high background fluorescence in the tissue but no specific staining. The lumen is located at the bottom right corners of the images. Scale bars = 50 μ m.

4.3 Discussion

Δ exon 7 CaSR KO mice appeared grossly undistinguishable from the WT controls in that no differences in appearance, body weight, reproductive capabilities or survival rates were found. It was therefore decided to concentrate the in-depth phenotypic characterisation of WT and KO animals, setting aside that of HET mice at this stage. The fact that KO mice live out a full lifespan compared to WT control furthermore indicates that targeted deletion was at least insofar successful as a more generalized knock-out of the CaSR would have led to a much more severe and lethal (Ho et al. 1995), or at the very least obvious, phenotype (Chang et al. 2008). CaSR expression was observed in all three layers of mesenteric arteries vessels from control C57/Bl6 mice, thus combining the previously separately observed localisations of the CaSR in the vasculature (Bukoski et al. 1997; Wonneberger et al. 2000; Weston et al. 2005; Molostvov et al. 2007; Loot et al. 2013). Using an antibody directed against the amino-terminus of the CaSR, the immunostaining patterns in aortae from WT as well as KO mice were comparable, and no obvious difference in staining intensities was observed between blood vessels from the two genotypes. This result could be explained by the remaining presence of the Δ exon7 fragment of the CaSR which, albeit not functional, is still produced by KO cells (Chang et al. 2008) and should remain antigenic to antibodies directed against the N-terminus of the CaSR, like the ones used in this study (*c.f.* the discussion of the next chapter and Figure 44). Unfortunately a reliable antibody directed against the C-terminal end of the receptor, which should not bind to the truncated remaining fragment present in KO cells, is to date, not available (*c.f.* Figure 25). Additional studies on immunofluorescence stained VSMC isolated from WT and KO mice were performed and are described in 5.2.1. The effects of CaSR deletion from VSMC on specific cytological and physiological systems were investigated and described in the following chapters.

4.4 Conclusions

- *SM22 α -Cre x LoxP-CaSR mice do not present an immediately apparent phenotype.*
- *CaSR expression was confirmed in all three layers of arteries.*
- *Reliable tissue immunostaining for determination of CaSR expression in Δ exon7 CaSR KO mice requires a not yet available C-terminal anti-CaSR antibody.*

5 Effect of CaSR deletion on cultured VSMC

5.1 Introduction

Blood pressure regulation *in vivo* is extremely complex and encompasses a variety of regulatory and compensatory mechanisms of e.g. endothelium-VSMC crosstalk, circulatory factors, etc., all of which are very difficult to control. Because the CaSR is expressed in all three layers of the vasculature, the complexity of this system makes it challenging to dissect the function of the VSMC CaSR independently of that of the endothelium. To discern these cell-type specific roles of the CaSR, in the first instance, I investigated the role of the VSMC CaSR in an isolated and controlled *in vitro* system.

In this chapter, the effects of targeted CaSR deletion from VSMC were investigated. The first step was to validate the culture system and the effectiveness of the genetic manipulation at producing tissue-specific CaSR ablation by investigating the expression of a VSMC-specific marker, namely SM22 α , as well as CaSR protein and their expression patterns using immunolocalization experiments. Quantitative immunofluorescence was used to measure the amount of expression of CaSR in VSMC isolated from WT and KO mice. Furthermore, the CaSR has been implicated in control of VSMC proliferation. Rat aortic VSMC were shown to react with increased proliferation to rising concentrations of Ca²⁺ in the culture medium, although it was unclear whether this response was purely CaSR mediated (Smajilovic et al. 2006). In human aortic smooth muscle cells, neomycin led to increased proliferation while knock-down of the receptor (using siRNA) resulted in reduced proliferation (Molostvov et al. 2008). Studies on VSMC lacking the CaSR cultured from KO mice will allow us to confirm whether these effects are CaSR mediated.

Importantly, VSMC were cultured in the presence of physiologically relevant 1.2 mM Ca²⁺ in the culture medium, in contrast to the 1.8 mM Ca²⁺ present in most media, as previous studies have shown that 1.8 mM Ca²⁺ leads to loss of CaSR expression by downregulation (Alam et al. 2009).

5.2 Results

5.2.1 CaSR expression in VSMC

Cultured VSMC were immunostained for CaSR expression to determine the abundance of the wild-type CaSR by co-localizing the CaSR with a smooth muscle marker, SM22 α . Four populations were identified in the colonies: CaSR+/SM22 α +, CaSR+/SM22 α -, CaSR-/SM22 α + and CaSR-/SM22 α - (see Figure 35 for a representative picture from VSMC isolated from C57/BL6 mice). Quantitative immunofluorescence microscopy showed that approximately half of the cells present in all investigated batches of cells from both WT and KO mice could be classified as VSMC (staining positively for SM22 α), with some degree of variation between batches (54.0 ± 8.7 % for WT and 58.3 ± 10.4 % for KO, N = 9) (Figure 36).

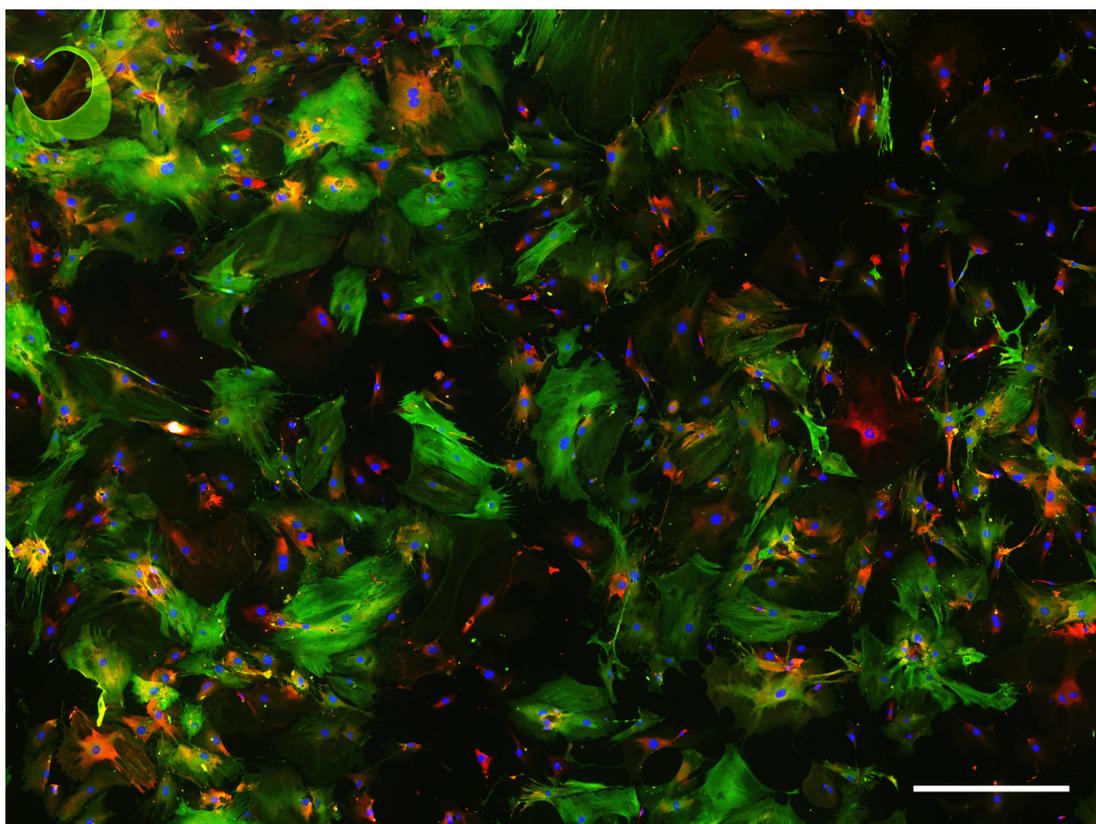


Figure 35: Representative picture of VSMC cultured from aortic explants of C57/BL6 mice. Double stainings of explant derived VSMC for CaSR (red) and SM22 α (green) shown as overlay. Nuclei appear in blue and were counterstained with Hoechst 34580). Scale bar = 500 μ m.

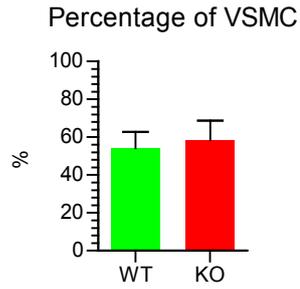


Figure 36: Average percentage of VSMC in all analysed batches of VSMC grown from WT and KO aortae. N = 9 (WT), N= 6 (KO), mean + SEM, two-tailed T-test.

Cellular distribution of the CaSR was mainly cytosolic and seemed to be denser in a diffuse pattern around the nucleus while SM22 α immunostaining exhibited the filamentous structure of the cytoskeleton. Staining of acutely isolated control VSMC showed a very diffuse cytosolic pattern for the CaSR with an even density across the cells while SM22 α exhibited a more granular appearance (Figure 37).

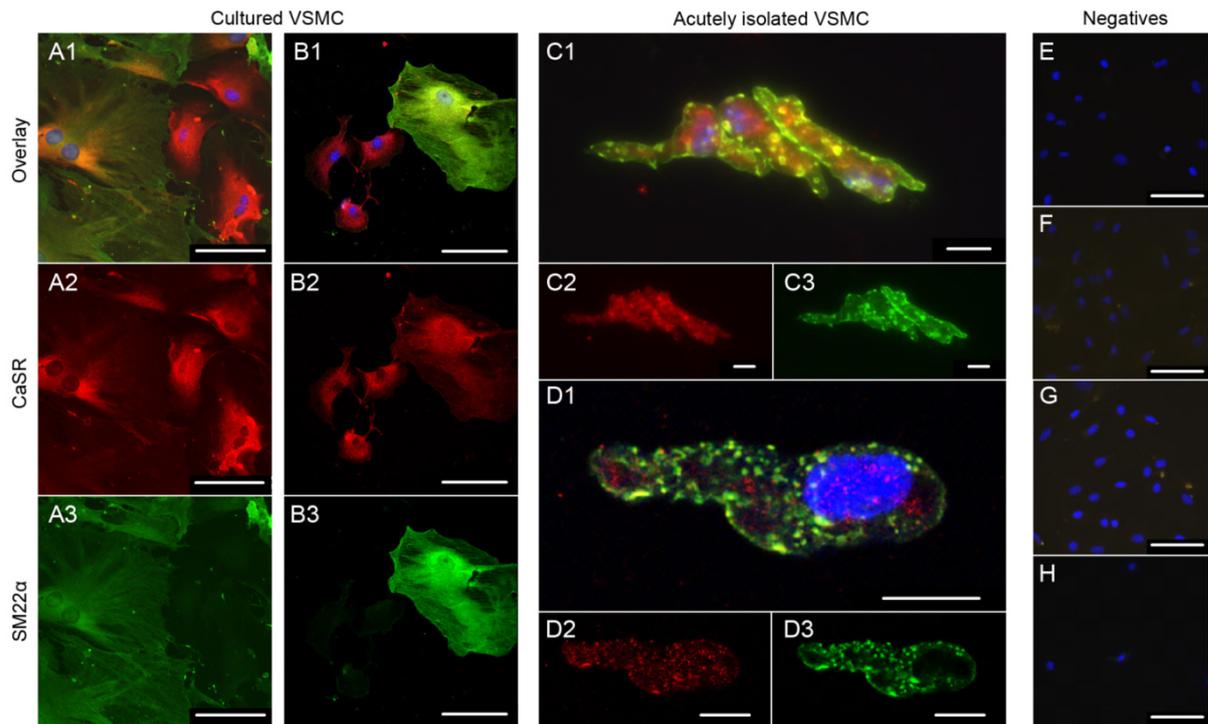


Figure 37: Immunolocalization of the CaSR in VSMC. Epifluorescence (A, C) and confocal images (B, D) of PFA fixed cultured (A and B) and acutely isolated (C and D) VSMC from control mice. Cells were stained using the Anaspec CaSR (red) and SM22 α (green) antibodies, shown as overlay (A1, B1, C1, D1) including nuclear counterstaining with Hoechst 34580 (blue) and separately (A2, B2, C2 for CaSR and A3, B3, C3 for SM22 α). In cultured VSMC from aortic explants, the CaSR is mainly distributed around the nucleus (A2, B2) and was present in SM22 α positive and negative cells (A3, B3). In acutely isolated aortic VSMC, CaSR staining appeared much more granular and evenly distributed across the cytosol and nucleus of the cells (C2 and D2), which was similar to that seen for SM22 α with the exception of the latter's absence from the nucleus (C3 and D3). Negative controls, shown as overlay of all channels, showed no staining in cultured (E) and acutely isolated (H) VSMC. Cross-negative controls including rabbit anti CaSR primary antibody, with chicken anti goat secondary antibody (F) and goat anti SM22 α antibody with goat anti rabbit secondary antibody (G) showed no significant immunoreactivity ascribed to primary antibodies. Scale bars = 100 μ m in (A, B E–G), 10 μ m in (C and D) and 50 μ m in (H).

When comparing VSMC derived from KO explants with those from WT mice, CaSR immunostaining in WT VSMC was the same as in VSMC derived from control mice, but staining intensity in KO VSMC was markedly reduced compared to WT control (Figure 38).

Expression levels of CaSR in cultured WT vs. KO VSMC of passages 2-6 were measured using quantitative immunofluorescence analysis. Nine WT and 6 KO individual VSMC preparations, each containing VSMC grown from aortae of 2–3 mice, were analysed at

different passages and in multiple technical repeats with a total of 37,125 cells in 50 ROIs for WT and 54,414 cells in 27 ROIs for KO. For negative controls, 3,066 cells in 19 ROIs from 6 preparations were analysed for WT and 5,898 cells in 6 ROIs from 3 preparations for knockouts. Preparation, culture maintenance and stainings of VSMC preparations were performed in collaboration with Dr. Thomas Davies (Davies 2013), image acquisition, quantitative immunofluorescence and data analysis were performed by myself.

Normalised to expression of SM22 α and relative to the expression of CaSR in VSMC from WT control, CaSR expression levels in KO VSMC were reduced significantly by about 32 % when looking at all cells in the cell preparation. Background fluorescence, as determined by negative controls performed by omission of the primary antibodies, exhibited about 9–17 % of the fluorescence of the positively stained samples (Figure 39). When focusing only on VSMC (cell population staining positive for SM22 α , *c.f.* Figure 36), CaSR staining intensity was significantly reduced by about 44 % (Figure 40). All numerical results are reported in Appendix A, Table 15.

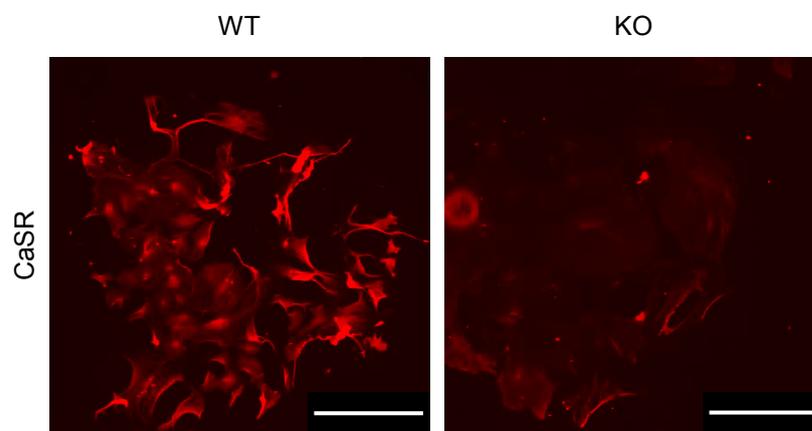


Figure 38: CaSR expression in cultured WT and KO VSMC. Epifluorescence overview images of PFA fixed cells showing large areas of cells. Immunostaining of VSMC derived from explants from WT and KO mice was performed using an Anaspec CaSR rabbit polyclonal antibody. KO cells show a large reduction in staining intensity compared to the WT control. Image contrast was enhanced for better visibility by the same amount in both images. Scale bars = 500 μ m.

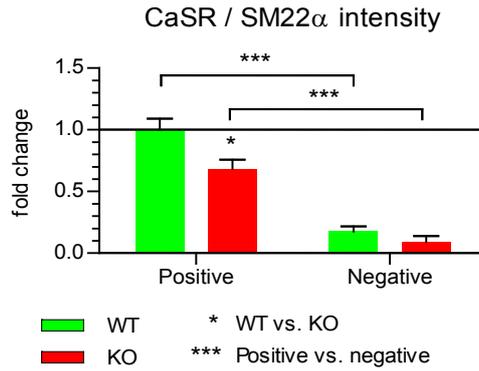


Figure 39: Quantitative immunofluorescence analysis of CaSR expression levels in all cells present in VSMC preparations of passages 2-6 cultured from WT and KO aortae. CaSR staining intensities were normalised to the SM22 α intensity of the respective cell batch and weighed in respect to the cell number in the respective batch. Staining intensity of KO positive and all negative cells is expressed as fold change compared to WT positive. N = 9 (WT positive), 6 (KO positive), 6 (WT negative), 3 (KO negative), Mean + SEM, * p < 0.05, *** p < 0.001, two-way ANOVA with Bonferroni post-test.

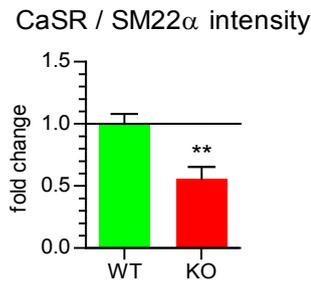


Figure 40: Quantitative immunofluorescence analysis of CaSR expression levels in the population of VSMC (staining positive for SM22 α) in VSMC preparations of passages 2-6 cultured from WT and KO aortae. CaSR staining intensities were normalised to the SM22 α intensity of the respective cell batch and weighed in respect to the VSMC number in the respective batch (. Staining intensity of KO cells is expressed as fold change compared to WT. N = 9 (WT), 6 (KO), Mean + SEM, ** p < 0.01, two-tailed T-test.

5.2.2 VSMC proliferation

The conditions to test the effects of Ca^{2+} on VSMC in WT and KO cells were initially optimised by incubating VSMC explanted from C57/Bl6 mouse aortae in medium containing different extracellular Ca^{2+} concentrations. VSMC proliferation was measured at two different time points (day 5 and day 10) by cell counting using a haemocytometer. Normalization against the cell numbers obtained in the presence of medium containing 1.2 mM Ca^{2+} at day 5 showed a highly significant difference in the increase in cell number after 10 days of incubation in the presence of medium containing 2.5 mM Ca^{2+} ($p < 0.001$) (Figure 41). When this protocol was employed to compare VSMC numbers from WT and KO mice kept in culture for 10 days (normalized against cell numbers of WT measured in the presence of medium containing 1.2 mM Ca^{2+}), proliferation in the KO cells was not increased in the presence of medium containing 2.5 mM Ca^{2+} (Figure 42). All numerical results of the proliferation studies are reported in Appendix A, Table 16.

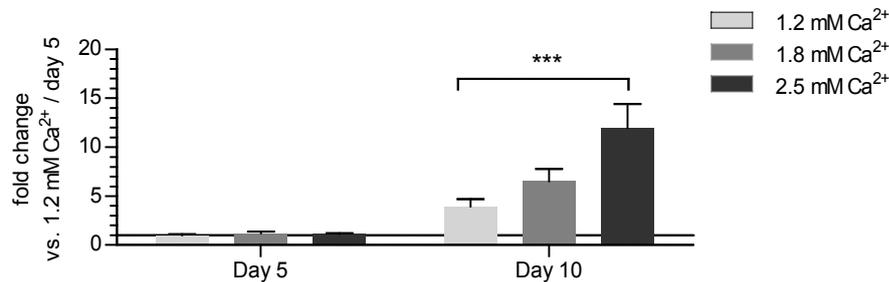


Figure 41: Number of VSMC from C57/BL6 control mice after 5 and 10 days of incubation in three different Ca^{2+} concentrations. 2.5 mM Ca^{2+} lead to a significant increase in control VSMC number compared to that measured in cells grown in the presence of medium containing 1.2 mM Ca^{2+} . Data are normalized to cell number measured after 5 days incubation in medium containing 1.2 mM Ca^{2+} (line). *** $p < 0.001$ vs. 1.2 mM Ca^{2+} of the respective day. $N = 5$, $n = 3$, mean + SEM, two way ANOVA and Bonferroni post-test.

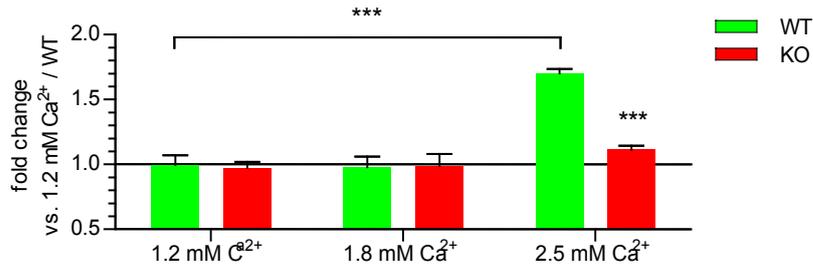


Figure 42: Number of VSMC from WT and KO mice after 10 days of incubation in the presence of medium containing different Ca²⁺ concentrations. The Ca²⁺ induced increase in proliferation observed in VSMC from WT mice is lost in VSMC from KO mice. Data are normalized to WT cell number at 1.2 mM Ca²⁺. *** p < 0.001. N = 1, n = 3, mean + SEM, two way ANOVA and Bonferroni post-test.

After my initial observations, these experiments were repeated by Thomas Davies in the course of his PhD thesis (Davies 2013). The observed results were very much comparable to the ones presented here. WT VSMC showed a Ca²⁺ dependent increase in cell proliferation while this response was not found in KO cells (Figure 43).

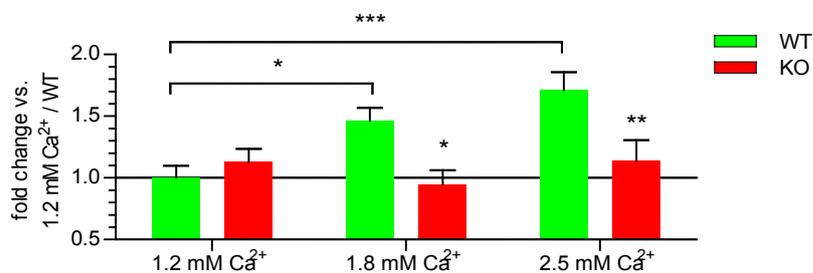


Figure 43: Replicate of the WT/KO VSMC proliferation experiment shown in Figure 42 by Dr. Thomas Davies. Number of VSMC from WT and KO mice after 10 days of incubation in the presence of medium containing different Ca²⁺ concentrations. Data are normalized to WT cell number at 1.2 mM Ca²⁺ (line). * p < 0.05, ** p < 0.01, *** p < 0.001. N = 5 (WT), N = 4 (KO), n = 2, mean + SEM, two way ANOVA and Bonferroni post-test.

Because “cell proliferation” here is expressed as total cell counts, which includes live and dead cells, apoptosis of these cells has to be taken into consideration as well. Experiments on VSMC apoptosis were performed on VSMC prepared in collaboration with Dr. Thomas Davies. Generally, VSMC (SM22α+) exhibited a similar percentage of apoptosis, irrespective

of genotype or extracellular Ca^{2+} and Pi concentrations. However, while the TUNEL assay itself as well as the quantification by quantitative immunofluorescence produced consistent results, the available VSMC preparations showed exceedingly high phenotypic variability in staining intensity for SM22 α as well as CaSR thereby making a reliable interpretation of these data difficult. If accepted to be correct, the equal levels of apoptosis would suggest that the observed Ca^{2+} dependent increase in cell number in WT VSMC is in fact driven by an increase in cell proliferation rather than decreased apoptosis. Results of these experiments are reported in Appendix B, 12.1.

5.3 Discussion

5.3.1 CaSR expression in VSMC

After optimization of an immunostaining protocol and selection of the most specific antibody (AnaSpec), it was confirmed that the CaSR is expressed in VSMC and that this expression is reduced in VSMC from KO mice.

In this chapter, I have shown that the cell populations in the commonly used culture model for VSMC are rather heterogeneous with approximately 50 % of the cells present in the culture being VSMC, which is comparable to what others have found in passaged cultures of VSMC (Shanahan et al. 1993). The reason for this seemingly low purity of the culture can be found in the ready ability of cultured VSMC to undergo phenotypic transformation *in vitro* which goes along with the loss of VSMC markers (Shanahan et al. 1993). This heterogeneity of *in vitro* VSMC cultures has long been known and the expression patterns of VSMC markers depends on a variety of factors like animal age or species (Shanahan and Weissberg 1998). I hypothesise that the non SM22 α -positive cells are either of fibroblastic origin – as CaSR expression has been demonstrated in fibroblasts of various, although not vascular origin (Ogata et al. 2006; Pacheco and Macleod 2008; Hattori et al. 2011) – or result from VSMC dedifferentiation which has been shown to occur in mineralizing VSMC (Shanahan et al. 1994; Steitz et al. 2001). However, the heterogeneity and the percentage of VSMC were present and comparable in VSMC cultures from both genotypes while the culture and isolation was performed in exactly the same way for both genotypes. Since the classification into populations is based on the setting of an arbitrary (manually) set threshold for SM22 α staining intensity, the population analyses are reflecting a subjective opinion of positive staining for SM22 α . However, the introduced bias would have the same effect on both VSMC isolated from both WT and KO mice. Therefore, I suggest that it is possible to compare results from population and expression analyses as well as functional assays between WT and KO isolated cells. Ideally, a “pure” VSMC culture should be used for analysis of VSMC, which seemed not achievable with the explant derived VSMC cultures. For future experiments, we will consider digestion-based cell isolation methods, which might provide a purer and more stable VSMC culture (Prof. Cecilia Giachelli, University of Washington, USA, personal communication).

Immunoreactivity to CaSR in VSMC is present mainly in the cytosol and around the nucleus, which is in agreement with the fact that most of the CaSR present in the cell is stored in the endoplasmic reticulum and that trafficking from this pool to the membrane is a very important part of the regulation of CaSR signalling (White et al. 2009; Cavanaugh et al. 2010; Grant et al. 2011) A similar distribution pattern for the CaSR was observed in other cell types, e.g. human umbilical vein endothelial cells (HUVECs) (Bonomini et al. 2012), human oocytes (Dell'Aquila et al. 2006) or rat medullary thyroid carcinoma cells (Tharmalingam et al. 2011). Interestingly, while cultured VSMC showed the typical filamentous staining pattern (Ross et al. 2006) for SM22 α , staining in acutely isolated VSMC had a very granular appearance. Since SM22 α is localized to smooth muscle actin (Zhang et al. 2001a), these results suggest depolymerisation of filamentous F-actin to granular G-actin in response to the isolation procedure, which might also explain the granular appearance of CaSR staining in these cells, as the CaSR has been shown to bind to the actin-binding filamin A (Pi et al. 2002).

CaSR expression was found in WT as well as KO VSMC (positive for SM22 α) but expression levels were significantly lower in KO compared to WT VSMC. It was shown previously that the loss of the C-terminal exon 7 of the CaSR does not result in total loss of receptor expression: indeed, a truncated Δ exon7 variant of the receptor is still expressed, but this truncated receptor is non-functional (Chang et al. 2008). Since the antigenic region of the used AnaSpec antibody is N-terminal and since the Δ exon7 protein, which consists of the N-terminal domain of the CaSR, can still be expressed by the KO cells, the reduction in staining in KO VSMC for CaSR indicates that total receptor expression is downregulated as a result of the genetic manipulation. In parathyroid gland specific CaSR knock-out mice mRNA abundance of the CaSR was increased but Δ exon7 CaSR protein levels were decreased to 10 % of full length protein in wild type controls. Furthermore, total knock out of the wild type receptor in the same mice has been shown to be ca. 95 %, suggesting that the tissue specific ablation is high but not complete (Chang et al. 2008). This, together with the presence of the truncated remains of the CaSR, can explain the remaining signal in KO VSMC (Figure 44). To determine the exact amount of knock-out of the receptor in the SM22 α -Cre x CaSR-LoxP mouse, western blot and RT-qPCR analyses are currently being performed by other members of the laboratory. Nevertheless, even in the absence of these results, the observed reduction in CaSR staining, together with the observed tissue specific phenotypes described in the following chapters point towards successful partial deletion of the CaSR from VSMC.

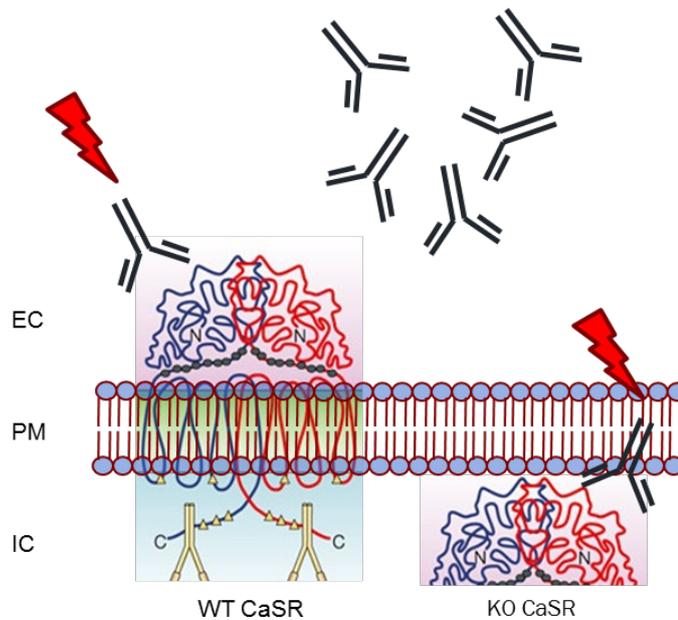


Figure 44: Presumed cause for remaining CaSR immunostaining in VSMC from KO mice. The rabbit polyclonal antibody currently used for my studies binds the N-terminal (extracellular) domain of the CaSR. In the exon 7 KO model, transmembrane and carboxy-terminal domains of the CaSR are deleted while the extracellular domain, encoded by exon 1-6, can still be produced. When expressed in heterologous systems, this truncated form is unstable, non-functional and lacks plasma membrane retention motifs (Chang et al. 2008). The antigenic region of the Anaspec antibody, which resulted to be the most specific of those commercially and non-commercially available, is located in the putative amino terminus of the CaSR and therefore residual antigen-antibody binding in KO cells can still be visualised (red arrows). EC = extracellular space, PM = plasma membrane, IC = intracellular space. CaSR structure illustration modified after (Hofer and Brown 2003).

5.3.2 Regulation of VSMC proliferation by the CaSR

Previous studies have shown that in several cell types the activation of the CaSR influences cell proliferation. For instance, in colonic epithelial cells (Rey et al. 2010) CaSR activation reduces proliferation while in other cells, such as breast cancer-derived (El Hiani et al. 2009), osteoblast (Dvorak et al. 2004) or mesangial cells (Kwak et al. 2005), receptor activation promotes proliferation. For the vasculature, CaSR inhibition in human pulmonary artery smooth muscle cells reduced cell proliferation (Yamamura et al. 2012) and human aortic smooth muscle cells responded with increased proliferation in response to incubation with the orthosteric CaSR ligand, neomycin (Molostvov et al. 2008). In rat aortic VSMC, which are probably most comparable to the murine VSMC used in this study, elevated extracellular Ca^{2+} concentrations also induced an increase in cell proliferation, DNA synthesis and increased

ERK activation without significantly affecting Ca^{2+}_i signalling (Smajilovic et al. 2006). The authors suggested that the observed lack Ca^{2+}_i response to CaSR agonists in rat aortic VSMC could mean that these Ca^{2+} elicited effects on proliferation are not necessarily mediated exclusively by the CaSR but possible also by other calcium sensing receptors which might be present in VSMC (Farzaneh-Far et al. 2000; Smajilovic et al. 2006) namely GPRC6A (Harno et al. 2008). The definite role of GPRC6A in VSMC remains to be determined.

I have shown in this study that incubation of wild-type VSMC in medium containing 2.5 mM Ca^{2+} led to an increase in VSMC cell numbers, when compared with medium mimicking normocalcaemic conditions (1.2 mM Ca^{2+}), which is in agreement with previous observations. Most importantly, this effect was lost in VSMC from KO mice. For human aortic VSMC, silencing of the CaSR with siRNA yielded similar, but not quite as large results (Molostvov et al. 2008). Together, these observations suggest that the CaSR mediates Ca^{2+} -dependent VSMC proliferation in murine VSMC.

The significance of these results and their translatability from the *in vitro* to the *in vivo* situation remain has to be investigated further but the increased cell density in KO VSMC cells, together with the known effect of the CaSR on proliferation in cardiomyocytes (Sun et al. 2006) indicates that loss of CaSR in SM22 α positive cells could play a role in the cardiac remodelling observed in KO hearts (see chapter 7.3.9). Furthermore, it substantiates the hypothesis that CaSR activation by extracellular Ca^{2+} could be involved in aortic remodelling as observed in atherosclerosis (Smajilovic et al. 2006). Future experiments aimed at determining the intracellular signalling mechanism by which Ca^{2+} exerts its influence on VSMC proliferation should be performed should clarify this issue further.

5.4 Conclusions

- Cultured VSMC express the CaSR, although cell populations in VSMC preparations were quite heterogeneous.
- CaSR expression appears largely cytosolic in cultured VSMC.
- CaSR was ablated from VSMC of the SM22 α -Cre x LoxP-CaSR mouse.
- Extracellular Ca^{2+} promotes VSMC proliferation via the CaSR *in vitro*.

6 Effect of CaSR deletion on vascular calcification

6.1 Introduction

Several *in vivo* and *in vitro* studies suggest that the CaSR plays a role in protection against vascular calcification, e.g. (Alam et al. 2009; Koleganova et al. 2009; Mendoza et al. 2011; Ciceri et al. 2012b; Ciceri et al. 2013; Henaut et al. 2014). As already outlined in the general introduction, vascular calcification is a major complication in CKD and is associated with highly increased cardiovascular morbidity and mortality (London et al. 2005). It has been shown that both extracellular Pi and Ca²⁺ levels are directly associated with the development of vascular calcification and the transdifferentiation of VSMC into osteoblast-like cells (Villa-Bellosta et al. 2011). The CaSR directly controls Ca²⁺ levels via regulation of parathyroid hormone secretion, which account for the observed positive effects of calcimimetic on cardiovascular events, at least in animal models of CKD (Ogata et al. 2003; Koleganova et al. 2009) and human studies even though the latter are contradictory or methodologically problematic (Block et al. 2010; Raggi et al. 2011; Carney 2013; Chow et al. 2014). However, as already discussed, the CaSR is also present in VSMC and therefore may have a direct protective effect against vascular calcification. This possibility was explored previously in our group where it was found that calcified human arteries had lost all expression of the CaSR compared to non-calcified control tissue. In the same study *in vitro* cultured bovine VSMC were transfected with a dominant negative form of the CaSR exhibited a large increase in calcification compared to empty vector control. Because stimulation of the CaSR with the calcimimetic R-568 prevented calcification in bovine VSMC (Alam et al. 2009), these results suggested that loss of CaSR expression exacerbates vascular calcification. However, these results *in vitro* do not conclusively prove that the VSMC CaSR protects against vascular calcification *in vivo*.

For this reason, to elucidate the contribution of the vascular CaSR towards protection against vascular calcification, the impact of CaSR ablation from VSMC on calcification was investigated *in vivo* in whole animals, *ex vivo* using aortic explants and *in vitro* calcification using cultured aortic VSMC.

6.2 Results

6.2.1 *In vivo* blood vessel calcification

μ CT analysis performed by Dr. Wenhan Chang (UCSF, USA) showed no aortic calcification in 12 month old WT or KO animals (W. Chang, personal communication).

Staining of aorta sections from 12 month old male WT and KO mice with alizarin red S was performed under direction by an undergraduate student, Miss Amber Wheatley, and showed no mineral deposits in aortae from WT or KO mice (Figure 45).

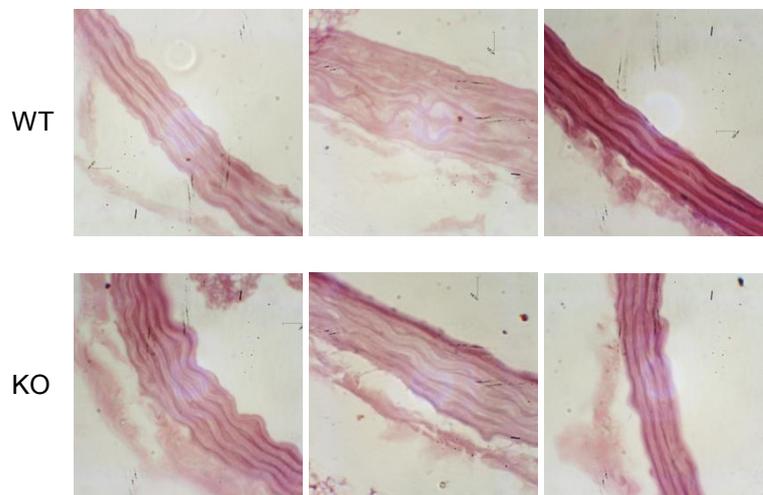


Figure 45: Alizarin Red S stainings of three thoracic aortae from 12 month old WT and KO animals. No calcification or calcified lesions could be detected. Contrast of all images was enhanced. Staining and pictures by Miss Amber Wheatley.

6.2.2 *In vitro* VSMC calcification

The ability of aortic VSMC from WT and KO mice to mineralize *in vitro* was investigated by alizarin red S staining. No calcification was observed in WT VSMC cultured in presence of 2 mM Pi over a range of 0.8 to 2.5 mM extracellular Ca^{2+} . In the presence of 3 mM Pi calcification is visible in cells incubated in medium containing 1.6 mM Ca^{2+} . In VSMC derived from KO cells however, visible calcification was found already in the presence of medium containing 2 mM Pi and 1.6 mM extracellular Ca^{2+} and already in the presence of medium containing physiological 1.2 mM extracellular Ca^{2+} and 3 mM Pi (Figure 46 and Figure 47). Densitometric quantification of Alizarin Red S stainings, performed by Dr. Thomas Davies after my initial observations (Davies 2013) showed comparable results (Figure 48).

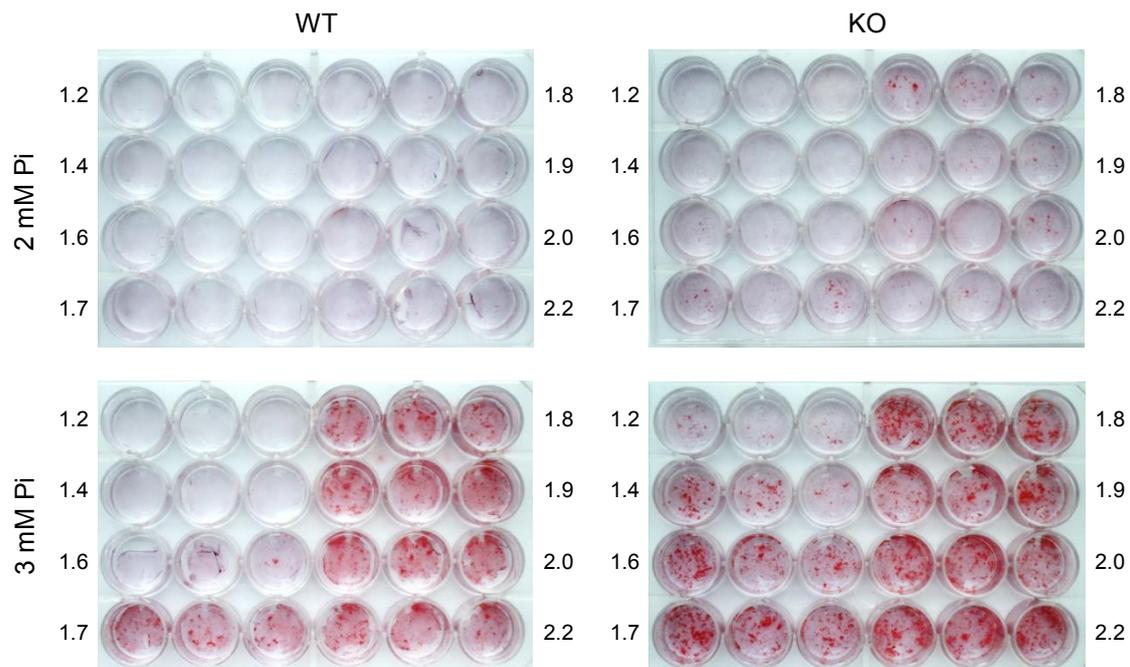


Figure 46: Photographs of WT and KO mouse derived VSMC cultured in 24-well plates stained with alizarin red S after 10 day incubation in medium containing different Ca^{2+} and Pi concentrations. Numbers indicate Ca^{2+} concentration in three horizontally adjacent wells. No calcification of WT cells was observed in the presence of medium containing 2 mM Pi regardless of Ca^{2+} concentration (upper left panel) while cell incubation in medium containing 3 mM Pi resulted in calcification starting at 1.6 mM Ca^{2+} (lower left panel). In KO cells, Ca^{2+} -deposition was found starting in cells incubated in medium containing 1.6 mM Ca^{2+} in the presence of 2 mM Pi (upper right panel) and at 1.2 mM Ca^{2+} in the presence of 3 mM Pi (lower right panel).

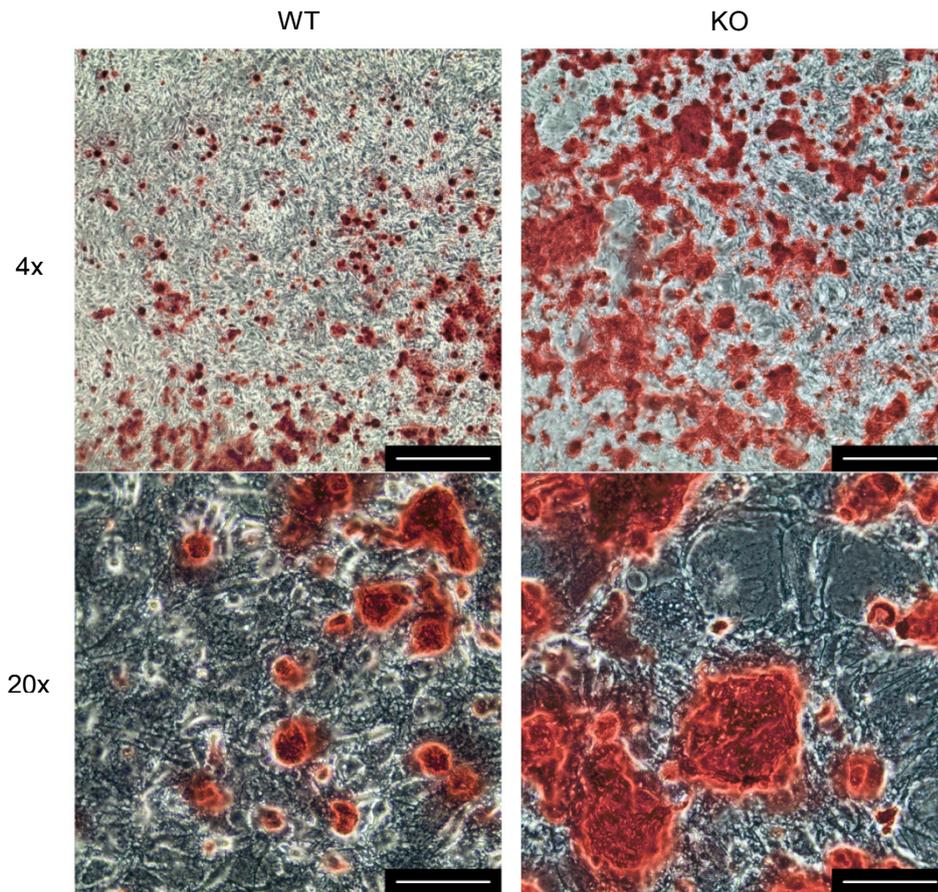


Figure 47: Representative phase-contrast microscopic images of WT and KO alizarin red S staining for VSMC incubated for 10 days with medium containing 2 mM Pi and 2 mM Ca^{2+} . KO cells exhibit a marked increase in calcification compared to WT control. Scale bars = 500 μm (4x), 100 μm (20x).

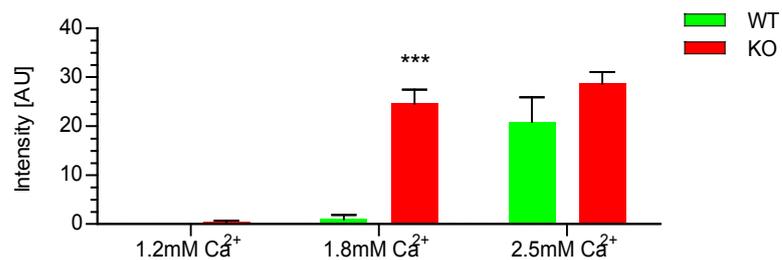


Figure 48: Densitometric quantification of alizarin red S staining of VSMC incubated in the presence of medium containing different Ca^{2+} concentrations and 3 mM Pi (performed by Dr. Thomas Davies (Davies 2013)). Staining for calcium deposits is significantly greater in KO cells compared to WT control. *** $p < 0.001$, $N = 2$, $n = 4$, mean + SEM, two way ANOVA and Bonferroni post-test (Davies 2013).

Quantification of Ca^{2+} incorporation via o-cresolphthalein complexone assay, performed by Dr. Thomas Davies (Davies 2013), showed a Ca^{2+} and Pi concentration dependent increase in calcification in WT as well as KO mice derived VSMC.

In the presence of medium containing 1.4 mM Pi, calcium incorporation (normalized to amount of calcification measured in the presence of medium containing 1.2 mM Ca^{2+}) was significantly increased in the presence of 2.5 mM Ca^{2+} vs. 1.2 mM Ca^{2+} in KO cells (1.52 ± 0.15 , vs. 1.00 ± 0.028 , $p < 0.001$, $N = 2$, $n = 8$, Two-way ANOVA and Bonferroni post-test) but not in WT cells. In the presence of medium containing supraphysiological (3 mM) Pi, the increase in calcium incorporation in the presence of 1.8 as well as 2.5 mM Ca^{2+} was not different from that measured in the presence of 1.2 mM Ca^{2+} in WT and KO cells (Figure 49). Taken together, these results, as well as the alizarin red S staining experiments, suggest that CaSR ablation increases VSMC calcification *in vitro* in conditions mimicking hyperphosphataemia and hypercalcaemia.

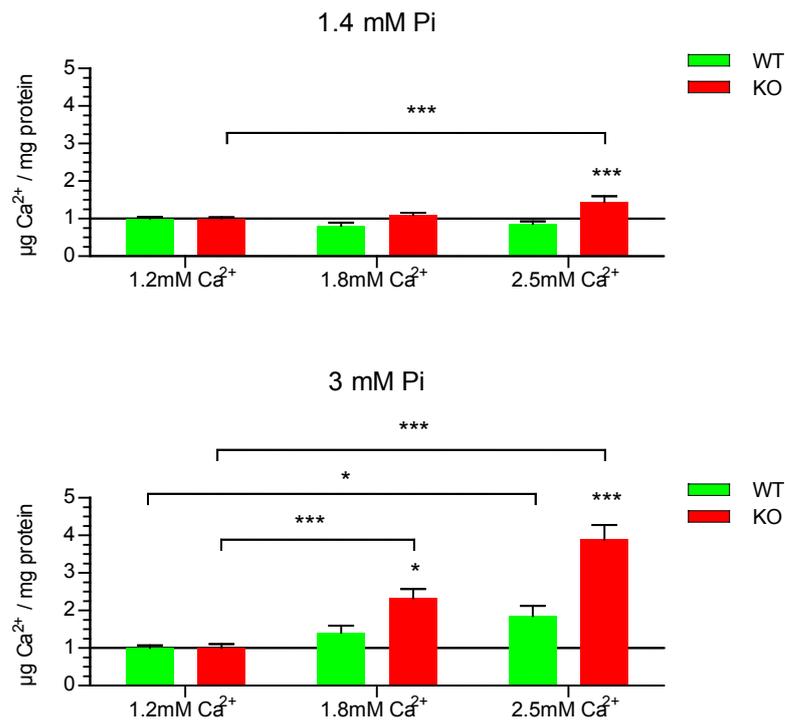


Figure 49: Quantification of Ca²⁺ deposition using cresolphthalein complexone assay (performed by Dr. Thomas Davies (Davies 2013)). WT / KO data normalised to the WT / KO values at 1.2 mM Ca²⁺ (line). Compared to WT cells, mineral deposition in KO cells increased significantly in the presence of medium containing a Ca²⁺ concentration of 1.4 mM or above (upper panel) and 3 mM Pi (lower panel). * p < 0.05, ** p < 0.01, *** p < 0.001 vs. respective WT values, unless otherwise indicated by parenthesis, N = 2, (1.4 mM Pi), N = 5 (3 mM Pi), n = 4, two way ANOVA followed by Bonferroni post-test.

6.3 Ex vivo calcification of aortic explants

Aortic explants from 6 month old WT and KO male mice (N = 6) were subjected to the same conditions as in the in vitro experiment with cultured VSMC. To determine possible influences of the endothelium on the occurrence and magnitude of calcification, explants with intact endothelium were compared with explants which's endothelial layer had been destroyed by air-bubbling. Either vehicle DMSO 1:1,000 or 10 nM of the calcimimetic R-568 were added to the incubation medium. After 10 days incubation in the presence of medium containing 3 mM Pi and 1.8 mM Ca²⁺, explants from KO mice showed no difference in incorporation of Ca²⁺, as determined by o-cresolphthalein complexone assay, compared to WT control, whether the endothelium was intact or destroyed and independently of the addition of 10 nM R-568 (Figure 50). All numerical results are listed in Appendix A, Table 17.

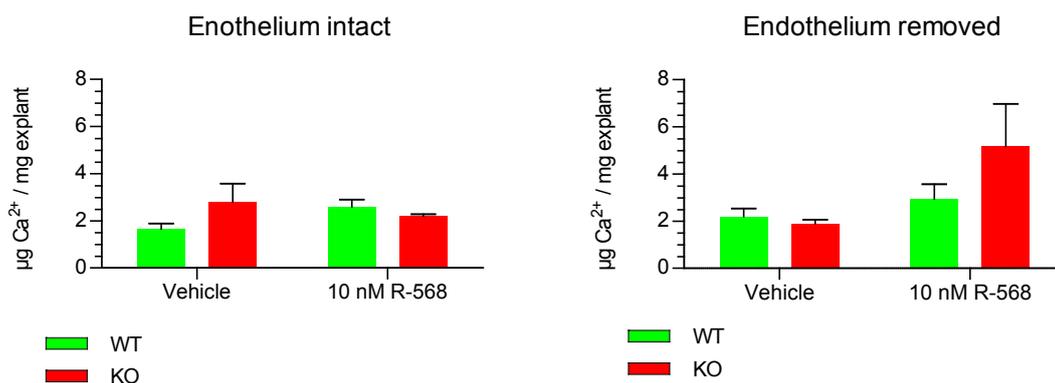


Figure 50: *Ex vivo* calcification of aortic explants from 6 month old male WT and KO mice incubated for 10 days in the presence of 3 mM Pi and 1.8 mM Ca²⁺ and either presence or absence of 10 nM R-568 with intact (left graph) or destroyed endothelium (right graph). N = 6, mean + SEM, two way ANOVA and Bonferroni post-test

6.4 Discussion

6.4.1 *In vitro* calcification

A main complication of CKD is vascular calcification (London et al. 2005) and previous observations in human and animal models suggested a protective role of the CaSR. Transfection with a dominant negative construct of the CaSR increased calcification of bovine aortic VSMC *in vitro* and CaSR expression is lost in calcified human arteries *in vivo* and in the presence of extracellular Ca^{2+} concentrations greater than 1.2 mM (Alam et al. 2009). To further explore the possible link between the CaSR and vascular calcification, we investigated the influence of different Ca^{2+} concentrations in the medium on mineralization of WT and KO VSMC *in vitro*. Experimental conditions for these studies had to be extensively optimized before any experiments could be carried out (see 3.2.2).

Overall our results have consistently shown that CaSR ablation from VSMC leads to a significantly increased calcification *in vitro*, compared to that observed in VSMC isolated from WT mice. However, in these experiments, substantial variability in the absolute amounts of Ca^{2+} incorporation was observed between the different cell batches. A possible reason for this finding could be the heterogeneity of VSMC cultures (*c.f.* chapter 5.2) as the phenotype of these cells is very variable and depends on factors like animal age (Li et al. 1997), or cell passage (Shanahan and Weissberg 1998; Halayko and Solway 2001). In order to be able to quantify the results between the batches and experiments, the data had to be double normalized to protein content and to the amount of calcification achieved in the presence of 1.2 mM Ca^{2+} . This procedure led to loss of information as only the relative differences between Ca^{2+} concentration groups can be compared between WT and KO mice but not the absolute Ca^{2+} incorporation. However, the differences in Ca^{2+} deposition between physiological (1.2 mM) vs. supraphysiological (1.8 and 2.5 mM) extracellular Ca^{2+} concentrations was significantly higher in KO mice derived VSMC than in WT derived cells.

Furthermore, Dr. Thomas Davies has demonstrated in the course of his PhD studies that the calcimimetic R-568 inhibits calcification of WT, but not KO VSMC. These findings are in agreement with previous studies (Alam et al. 2009) (Henaut et al. 2014) suggesting that the CaSR and its activation with calcimimetics can play a protective role against vascular calcification directly at the level of the cell, without a systemic influence.

Currently it is unclear how loss of CaSR expression from VSMC promotes this vascular calcification, and whether it directly drives osteogenic transdifferentiation of VSMC or leads to the loss of protective mineralization inhibitors, or a combination of both. Again, this is in agreement with the described putative effect of calcimimetics preventing transdifferentiation of VSMC into an osteoblastic phenotype (Koleganova et al. 2009; Ciceri et al. 2013) which is associated with the onset of vascular calcification (Jakoby and Semenkovich 2000; Tyson et al. 2003; Sage et al. 2010; Pai et al. 2011; Zhu et al. 2011). Such an experiment should be performed in the future, together with analyses for expression of other osteogenic and VSMC markers as well as the CaSR.

Calcified plaques in blood vessels consist mainly of hydroxyapatite (Tomazic et al. 1987), which is the principal mineral component of bone (Johnsson and Nancollas 1992), and indeed, *in vitro* mineralization achieved in experiments with a similar experimental protocol consists of hydroxyapatite and its precursors (Sage et al. 2011; Villa-Bellosta et al. 2011). To confirm that the calcification we observed in our studies is cell-dependent mineralization and not precipitation of $\text{Ca}_3(\text{PO}_4)_2$, X-ray diffraction analysis of the calcified deposits should be performed in the future.

6.4.2 *In vivo* calcification

In contrast to the *in vitro* findings, mice lacking the CaSR in VSMC did not show any vascular calcification *in vivo* even though blood Ca^{2+} levels have been shown to be increased in KO animals compared to WT control (see 8.2.2) and indeed no calcification in *ex vivo* experiments with isolated aortic rings. The absence of *in vivo* calcification can be explained by a number of possibilities, including *in vivo* – *in vitro* differences (1), changes in production of calcification inhibitors (2) and systemic effects (3).

(1) Our immunostaining experiments, as well as work by others (Weston et al. 2005), showed a high abundance of the receptor in the vascular endothelium and its involvement in nitric oxide synthesis (Ziegelstein et al. 2006; Loot et al. 2013). This is especially important in the light of the findings NO synthesis might be controlled by the CaSR in the endothelium, as NO was shown to be a potent inhibitor of vascular calcification by preventing osteogenic differentiation of VSMC (Kanno et al. 2008). This hypothesis should be tested by generating an endothelium specific or endothelium-VSMC double CaSR knock-out mouse in the future.

Finally, the *ex vivo* studies on isolated aortic rings of WT and KO mice proved rather inconclusive, with very low overall calcium deposition in either WT or KO explants, independent of the absence or presence of the endothelial layer. Therefore, the protective mechanism of the CaSR against vascular calcification might also simply be a function of the native 3D cell structure with completely differentiated VSMC still present in the explants, which is lost when VSMC are cultured (Shanahan et al. 1993). On the other hand, studies have shown that calcification of isolated human blood vessels is highly dependent on the state of uraemia of the patient those blood vessels were derived from. Blood vessels from uraemic patients showed marked calcification when incubated in a high Pi and Ca²⁺ containing medium, while blood vessels from healthy patients did not (Shroff et al. 2008). The KO mice show a marked alteration in blood biochemistry with elevated blood Ca²⁺ levels. However, blood Pi levels were unchanged and the animals exhibited marked hyperphosphaturia, which is in contrast to the situation in CKD. Therefore, it is possible that KO blood vessels are simply not “preconditioned” towards calcification.

(2) Fetuin A has been demonstrated to inhibit vascular calcification. Circulating fetuin A levels were shown to be unaltered between WT and KO mice (see 8.2.2), and while MGP remains to be assessed in the future, this suggest that at least the calcification inhibitor fetuin A is not responsible for the lack of observed *in vivo* calcification in the SM22 α -Cre x LoxP-CaSR mouse. However, fetuin A is enriched in sites of calcification (Reynolds et al. 2005) and circulating levels might not be directly correlated with risk for vascular calcification (Liabeuf et al. 2013). It therefore cannot be excluded, that fetuin A may play a local role in protection against vascular calcification in KO animals.

(3) It is possible that the protective effect of the CaSR against vascular calcification only asserts itself in the artificial environment of the *in vitro* experiment because no systemic phenomena (mineral homeostasis), either in a CaSR dependant way or not, can exert a protective influence against calcification. This suggests that the CaSR in VSMC is not solely responsible for protection from vascular calcification, at least not in healthy animals. It is possible that KO mice, which are lacking the CaSR from conception, have adapted to the elevated Ca²⁺ concentrations and require more severe pathophysiological conditions for the development of vascular calcification. *In vivo*, the CaSR might be protective of vascular calcification in pathological states only, e.g. advanced CKD / end stage renal disease, where the Ca x Pi product is markedly elevated (London et al. 2005); indeed, Pi excretion is highly elevated in KO mice compared to WT control (see chapter 8.2.2). I speculate therefore that in

the SM22 α -Cre x LoxP-CaSR mouse, vascular calcification does not occur despite the loss of the putative protective effect of the vascular CaSR and prevalence of hypercalcaemia because blood Pi levels are reduced below the threshold necessary for induction vascular calcification, as both Ca²⁺_o and Pi are important determinants for VSMC transdifferentiation and calcification, as reviewed in (Shroff et al. 2013). In future experiments in collaboration with Dr. Ann Canfield (University of Manchester, UK) this hypothesis will be investigated by inducing CKD in our animals to increase the risk for vascular calcification by performing 5/6 nephrectomy in combination with a high phosphate diet (Shobeiri et al. 2010; Lau et al. 2013).

It has to be noted that clinical trials showed no protective effect of activating the CaSR on vascular disease could be found (Raggi et al. 2011; Chertow et al. 2012). The technical shortcomings of these studies notwithstanding, these results raise the question if the observed protective effects of CaSR activation can be translated to the *in vivo* situation in patients and if the CaSR really is a valid target for therapy or prevention of vascular calcification or if the putative anti-calcifying effect of the vascular CaSR is only of academic interest.

6.5 Conclusions

- *CaSR ablation from VSMC does not lead to in vivo calcification, despite elevated blood Ca²⁺ levels, possibly because of decreased increased urinary Pi removal from the blood.*
- *The CaSR has a protective effect against in vitro VSMC calcification in a high Ca²⁺ and high Pi containing medium which can be enhanced by calcimimetics.*
- *The protective effect of the CaSR might therefore only assert itself in a pathophysiological context, which should be investigated using a challenged mouse model of renal failure.*

7 Effect of VSMC targeted CaSR deletion on cardiovascular function

7.1 Introduction

Previous studies have implicated the vascular CaSR in the regulation of vascular tone and of blood pressure in a variety of *in vitro* and *in vivo* studies, (see general introduction and (Smajilovic et al. 2011) for review). Special attention was therefore given to the investigation of the cardiovascular phenotype of the SM22 α -Cre – LoxP-CaSR mice. In this chapter, the impact of CaSR deletion on blood pressure, vascular tone regulation and cardiac function and morphology was studied. Data on vascular tone regulation were primarily obtained by wire myography studies performed by Dr. Thomas Davies, Dr. Polina Yarova and Mrs Irene Lopez. Principal findings of these wire myography studies are shown and put in context with other results in the discussion of this chapter to allow for a more thorough interpretation of the mice's cardiovascular phenotype.

First, blood pressure measurements were performed by tail cuff measurements, which have been established as simple non-invasive method with acceptable reliability (Johns et al. 1996; Feng et al. 2008). Following the tail cuff experiments, radiotelemetry experiments (Boedtkjer et al. 2011), were performed to accurately assess and confirm blood pressure changes in our mice. To maximize output from these experiments, the influence of two different diets, namely a supplementation of the mice chow with 4 % NaCl, termed high salt diet, as well as supplementation of the mice' drinking water with 0.5 mg / ml L-NAME (a pharmacological inhibitor of NO synthesis), on blood pressure and other cardiovascular parameters were investigated. Any differences observed between WT and KO mice in response to dietary changes would allow for a more thorough understanding of the mechanisms behind the CaSR influence on vascular tone regulation.

High salt containing diets have been shown to induce salt-sensitive hypertension in mice (Yu et al. 2004), although the induction of measurable hypertension in healthy mice, especially with a mixed C57/BL6 background, is being reported to develop only over several weeks (Gros et al. 2002). However, short-term treatment with a high salt diet can be used to determine whether the blood pressure of a specific animal model is particularly sensitive to NaCl, by mechanisms which might involve the systemic RAAS as well as local factors like α 2 adrenoreceptors regulating NO production (Makaritsis et al. 1999; Duling et al. 2006). Short-

time treatment with a high salt diet has been shown to rescue loss-of-ACE induced hypotension in mice (Carlson et al. 2002), thus allowing estimation if observed changes in blood pressure are salt sensitive or, by extent, related to changes in the RAAS.

Administration of L-NAME is a common method for increasing blood pressure through an increase in peripheral resistance by downregulation of endothelial NO production and therefore loss of an important part of endothelium-derived dilatory capability (Mattson 2001; Newaz et al. 2005) thus allowing to determine the influence of NO, and by extent the endothelium, on blood pressure regulation in the SM22 α -Cre x LoxP-CaSR mouse.

In my telemetry / metabolic cage experiments, there were only about 3 weeks available for the protocols because of quarantine issues with the mice at our collaborator's site at the University of Denmark. Thus, the time available for the different protocols (recovery from surgery, standard diet and altered diet phases) was limited to a few days each.

Finally, cardiac cine MRI, the gold-standard for assessing heart function (Schneider et al. 2006), was performed to assess the cardiac state of WT and KO mice.

7.2 Results

7.2.1 Blood pressure measurements by tail cuff

The blood pressure of 5 age groups, or batches, of male WT and KO mice was measured by use of the CODA tail cuff system. To begin with, it should be noted that the blood pressure of first two investigated groups, namely the groups of the 3–6 and 10–14 month old mice, were measured using a demonstration CODA unit. After the measurements were completed and the unit had been sent back to the company, I was informed by the company that the unit had a slight fault, which manifested itself in shifted values for both systolic and diastolic blood pressure. While the exact values for these age groups are therefore incorrect, all mice in these groups were measured using the same unit and channel and therefore it seems reasonable to assume that the relative differences observed between the genotypes are retained. However, in the final WT vs. KO comparison using normalised values (see below), two calculations were prepared, one containing the values from the “shifted” measurements and one where the values of the concerned age groups were omitted. The other three batches of mice (4 months, 9 months and 17 months) were measured with newly bought and calibrated equipment. Since these measurements were not planned from the beginning and had to be performed because of the aforementioned fault affecting the measurements of the 3-6 and 10-14 month old mice, the number of available animals for blood pressure measurement was not as high as desirable for statistical purposes. Nevertheless, the observed reduction in blood pressure was confirmed in experiments using radiotelemetry.

In the measurements with the loan unit, 3-6 month old male KO mice showed a significant ($p < 0.01$) reduction in systolic, diastolic and mean arterial pressure (MAP) compared to WT control (Figure 51), while there was no significant difference found in male mice of 10–14 months of age (Figure 52).

When measured with the new unit, 4 month old male KO mice showed a non-significant trend towards a slight reduction in diastolic, systolic and MAP compared to age matched WT control (Figure 53). A significant reduction ($p < 0.05$) in diastolic blood pressure was found in 9 month old male KO mice compared to WT. Although systolic blood pressure and MAP were also reduced in these mice, the difference did not quite reach statistical significance (Figure 54). Finally, for the group of 17 month old animals, no significant differences were found between WT and KO mice, although the trend towards reduced blood pressure in the

KO mice compared to WT which was observed in the other age groups was visible in these mice as well (Figure 55).

Blood pressure values obtained for WT and KO mice of all investigated age groups were normalised relative to the mean values for the WT mice of every age group. The so obtained average fold-changes in blood pressure between WT and KO mice showed a highly significant reduction in systolic blood pressure, diastolic blood pressure and MAP in KO mice compared to WT control of ~ 8–15 % (Figure 56). When excluding the measurements batches obtained with the faulty unit, diastolic blood pressure and MAP of KO mice remained significantly reduced by ~ 8–10 % compared to WT control, while systolic blood pressure showed a non-significant reduction by ~ 5 % (Figure 57).

Measurements of heart rates obtained with the CODA tail cuff system exhibited a substantial amount of variability and very often measurement would not succeed. Therefore, results are not reported.

Paw temperatures of the animals from the 3–6 and 10–14 month age groups were measured by Dr. Sarah Brennan by employing an infrared thermometer, since it is known that reduced blood pressure goes along with reduced temperature of the skin and limbs (Vazquez et al. 2010; National Heart 2013). In good agreement with the blood pressure results, 3-6 month old KO animals showed a significant reduction in paw temperature by about 0.52 °C ($p < 0.05$) compared to WT control. In 10-14 month old animals, this reduction in paw temperature was measured was not significant (Figure 58).

All numerical values of the blood pressure measurements and paw temperatures are listed in Appendix A, Table 18 and Table 19.

Blood pressure and heart rate measurements were repeated using radiotelemetry to confirm the observed reductions in blood pressure in the KO mice compared to WT control using radiotelemetry (see next chapter).

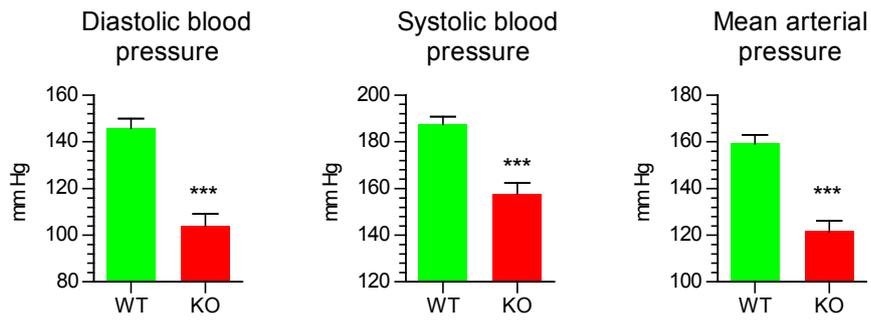


Figure 51: Diastolic, systolic and mean arterial pressure of 3–6 month old male WT and KO mice, measured by tail cuff. Note that the parameters are above those reported for C57/B6 mice (Mattson 2001). Following consultation with the company, a calibration error was detected, indicating an overestimation of these values (see text). *** $p < 0.001$, $N = 8$ (WT), 13 (KO), mean + SEM, two-tailed T-test.

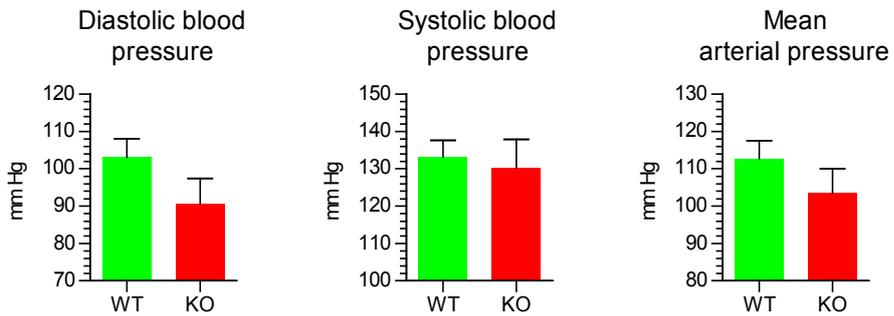


Figure 52: Diastolic, systolic and mean arterial pressure of 10–14 month old male WT and KO mice as measured by tail cuff. Note that the parameters are above those reported for C57/B6 mice (Mattson 2001). Following consultation with the company, a calibration error was detected, indicating an overestimation of these values (see text). $N = 3$ (WT), 7 (KO), mean + SEM, two-tailed T-test.

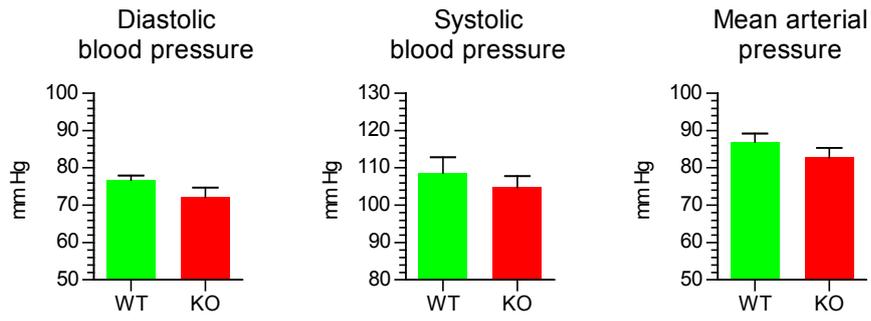


Figure 53: Diastolic, systolic and mean arterial pressure of 4 month old male WT and KO mice as measured by tail cuff. N = 3 (WT), 9 (KO), mean + SEM, two-tailed T-test.

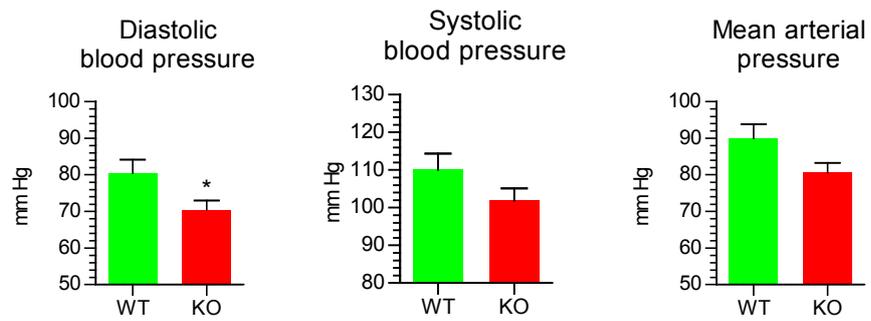


Figure 54: Diastolic, systolic and mean arterial pressure of 9 month old male WT and KO mice as measured by tail cuff. N = 5 (WT), 11 (KO), mean + SEM, two-tailed T-test.

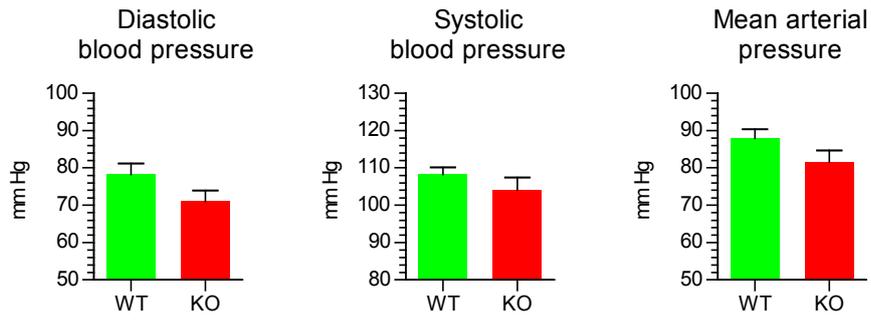


Figure 55: Diastolic, systolic and mean arterial pressure of 17 month old male WT and KO mice as measured by tail cuff. N = 3 (WT), 13 (KO), mean + SEM, two-tailed T-test.

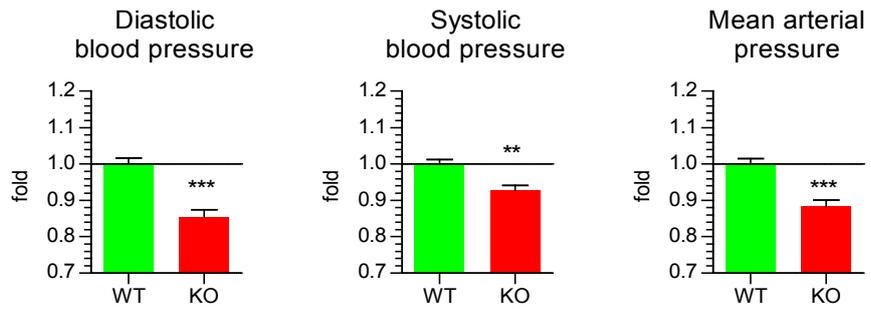


Figure 56: Combined normalised diastolic, systolic and mean arterial pressure of all age groups including the overestimated values of the 3-6 and 10-14 month age group measurements (see text). Normalised values are averages of all WT and KO values normalised to their respective age group's mean WT values (mean WT = 1, line). ** $p < 0.01$, *** $p < 0.001$ N = 22 (WT), 52 (KO), mean + SEM, two-tailed T-test.

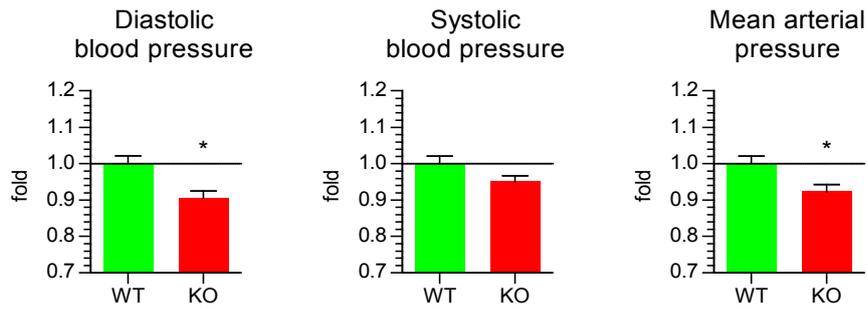


Figure 57: Combined normalised diastolic, systolic and mean arterial pressure of all age groups excluding the overestimated values of the 3-6 and 10-14 month age group measurements (see text). Normalised values are averages of all WT and KO values normalised to their respective age group's mean WT values (mean WT = 1, line). * $p < 0.05$, $N = 11$ (WT), 33 (KO), mean + SEM, two-tailed T-test.

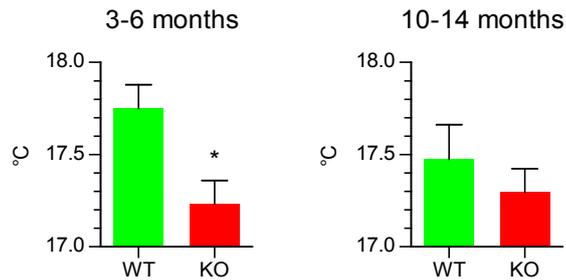


Figure 58: Average paw temperatures of 3–6 and 10–14 month old WT and KO mice used in the blood pressure study. $N = 10$ (WT, 3–6 months), 11 (KO, 3–6 months), 3 (WT, 10–14 months), 7 (KO, 10–14 months), * $p < 0.05$, two-tailed T-test. These observations were made by Dr. Sarah Brennan.

7.2.2 Blood pressure measurements by radiotelemetry

Tail cuff measurements strongly suggested that KO mice were mildly hypotensive. However, because tail cuff in mice is not widely accepted and the observed differences were small, to get greater information about the cardiovascular parameters of our genetically modified animals and because of the problems encountered with the loan unit, radiotelemetry experiments were planned and carried out on 3 month old WT and KO mice in collaboration with Prof. Robert Fenton and Dr. Vladimir Matchkov at the University of Aarhus, Denmark. Crucially, because the bacteriology tests of our animal facility did not allow our mice to be transferred into the Aarhus animal unit, all experiments were carried out while animals were kept in quarantine for the duration of the experiment. Initial experiments were performed in animals fed the same diet as in our animal facility in Cardiff to verify the reduced blood pressure of KO mice compared to WT control. In addition to the baseline recordings, mice were challenged by being fed a high salt diet (containing 4 % NaCl) and, after a “washout” period, they were treated with the NO synthase inhibitor L-NAME (0.5 mg / l in the drinking water). This treatment allowed us to determine if the previously observed reduction in blood pressure in KO mice is caused either by blood volume / kidney function (high salt diet) or TPR (L-NAME). Mice were housed in metabolic cages for the first part of the experiment (standard diet (1) vs. high salt diet), the results of which are described in chapter 8.2. For reasons of animal welfare, the mice were moved from metabolic cages into standard cages for the second part of the experiment (standard diet (2) vs. L-NAME). Because of this change in housing, the raw values from the two arms of the experiment cannot be directly compared. Read outs of the radiotelemetry probes which were analysed include diastolic blood pressure, systolic blood pressure, mean arterial pressure, pulse height (pulse pressure = difference between diastolic and systolic blood pressure), heart rate and the first derivative of the increase in the blood pressure curve (dp/dt) as a rough measure of left ventricular contractility (inotropy). The experimental plan and analysis methods are described in detail in the relevant methods section (2.7.2).

When looking at the traces alone, immediate differences between WT and KO mice became apparent. KO mice showed a marked and consistent reduction of diastolic, systolic and mean arterial blood pressure compared to WT control. This difference was more pronounced in the diastolic pressure than in systolic blood pressure and appeared greater during the active period of the mice (night-time) than during their resting period (daytime). The reduction observable in blood pressure as well as the normalisation of their circadian rhythms over the course of the

first few days indicates that, despite the mice having had two days of recovery following the implantation of the radiotelemetry probes, their stress level and therefore blood pressure was still declining during that phase of the experiment. Possibly as a result of this situation, no difference was apparent in the blood pressure of WT and KO mice when they were switched onto the high salt diet, where blood pressure remained stable for WT as well as KO mice, with KO mice consistently showing a lower blood pressure than WT mice. The small peaks in blood pressure observable around 12:00 noon every day for mice of both genotypes were caused by the handling of the mice and metabolic cages necessary for sample collection and cage maintenance (Figure 59). Pulse height of KO animals appeared markedly elevated while heart rates were reduced compared to WT control, independent of the diet the animals were fed with. dp/dt remained stable and comparable between WT and KO mice while on standard diet but decreased in WT mice when they were switched on a high salt diet while it remained stable in KO animals fed the high salt diet (Figure 60).

After 4 days on the high salt diet, mice were switched back on standard diet (standard diet (2)) and moved back in standard housing cages. In this phase, diastolic, systolic and mean arterial blood pressure of KO mice remained markedly lowered compared to WT, as already observed when the mice were fed standard diet (1). When drinking water was supplemented with 0.5 mg / l L-NAME, blood pressure of mice of both genotypes rose immediately and the difference between WT and KO mice disappeared on the second day of L-NAME treatment (Figure 61). The already observed elevation of pulse height in KO animals compared to WT increased further under the influence of the NO synthase inhibitor L-NAME (Figure 62), indicating a larger increase in systolic than diastolic blood pressure in KO mice (a larger difference between diastolic and systolic blood pressure, which could indeed be observed in the respective traces, *c.f.* Figure 61). Heart rate in KO animals remained reduced in KO animals compared to WT and dropped slightly in both genotypes with a reduction in the circadian profile when the animals on 0.5 mg / l L-NAME (Figure 62). dp/dt of KO animals showed the same small increase compared to WT, which had developed during the previous experimental stage (Figure 60), and independently of L-NAME supplementation. This could be accounted for by the fact that the mice had not fully recovered during the first stage of the experiment and that the post-operative stress masked the natural (i.e. lower) dp/dt of the WT animals which continued to lower over time while KO animals returned to a higher baseline contractility. For reasons of time constraint at the quarantine facility in Aarhus, Denmark, the experiment had to be terminated at this point.

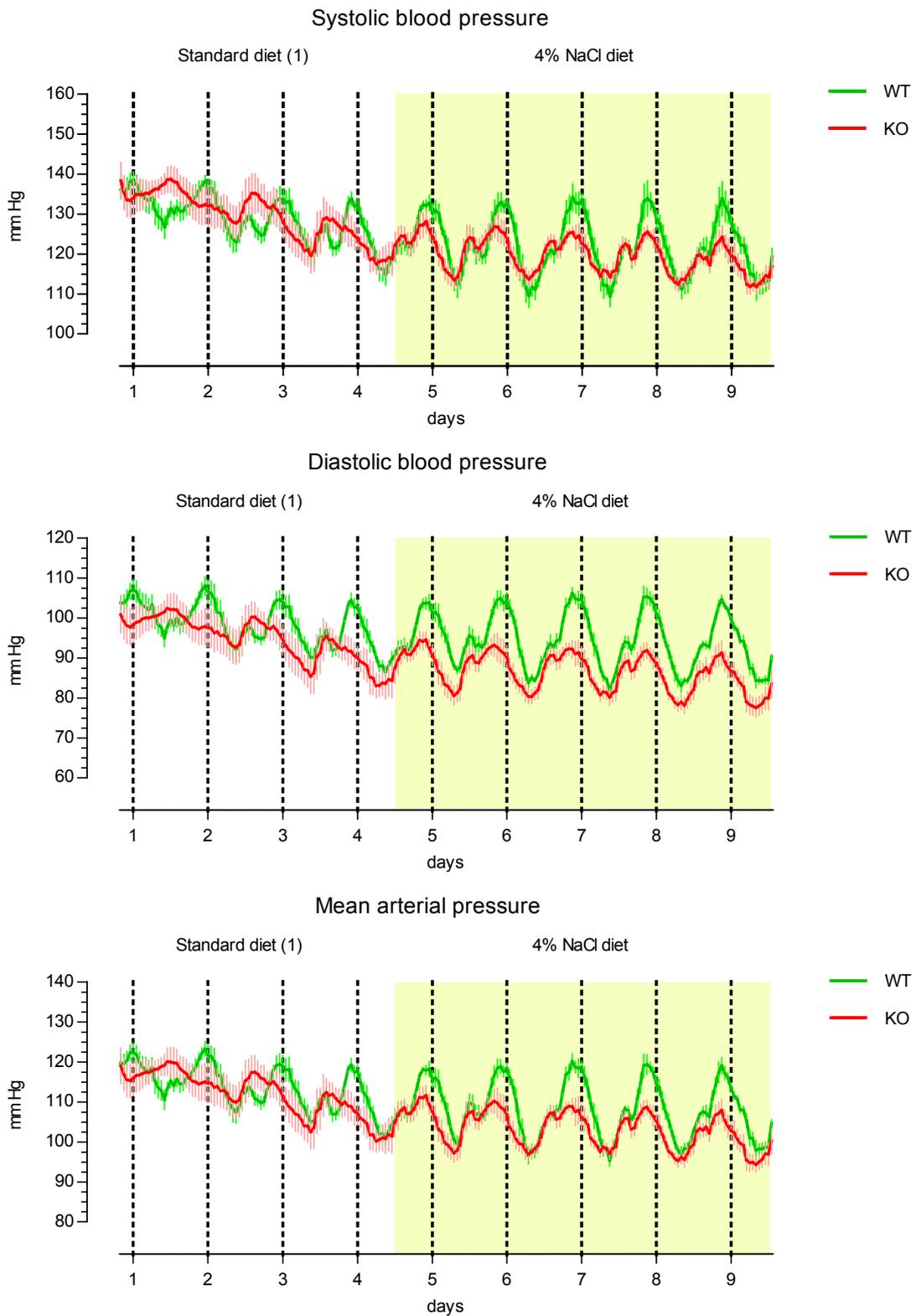


Figure 59: Systolic, diastolic and mean arterial pressure traces of WT and KO mice fed a standard diet or high salt diet as measured by radiotelemetry. X-axis indicates days of experiment; dotted lines indicate midnight; refer to Figure 16 for timeline. Mean \pm SEM, N=5.

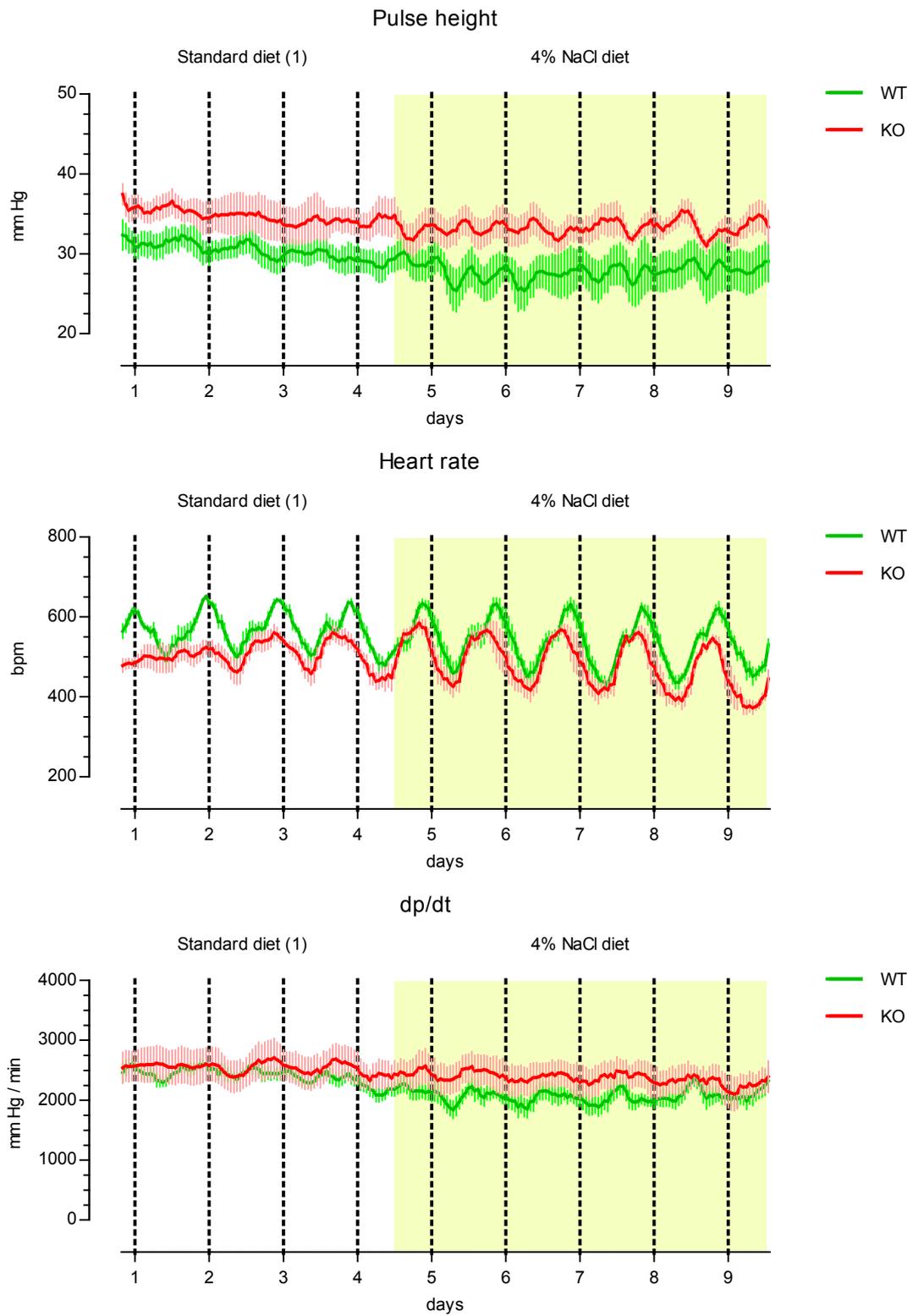


Figure 60: Pulse height, heart rate and dp/dt traces of WT and KO mice fed a standard diet or high salt diet as measured by radiotelemetry. X-axis indicates days of experiment; dotted lines indicate midnight; refer to Figure 16 for timeline. Mean \pm SEM, N=5.

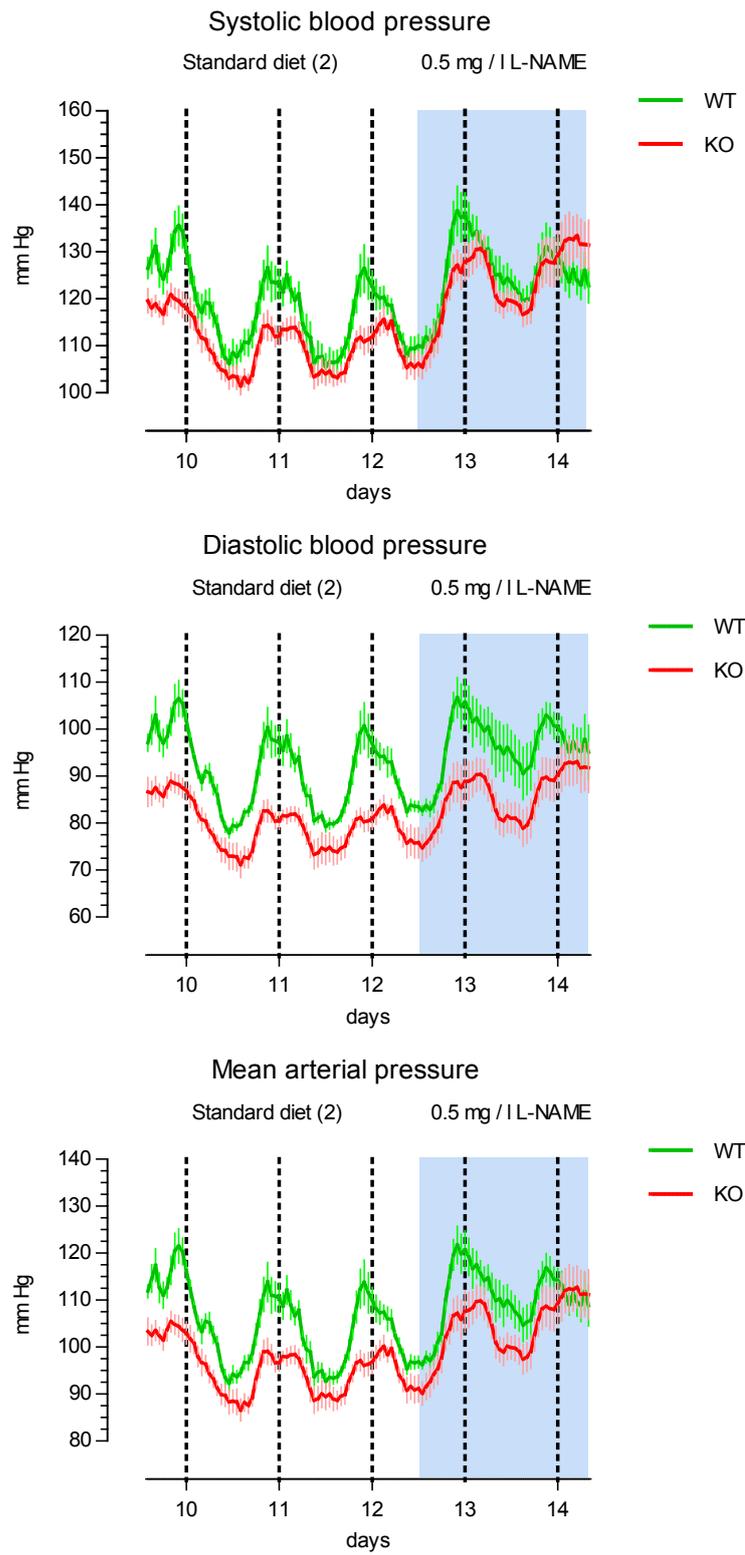


Figure 61: Systolic, diastolic and mean arterial pressure traces of WT and KO mice fed a standard diet or 0.5 mg / l L-NAME in the drinking water as measured by radiotelemetry. X-axis indicates days of experiment; dotted lines indicate midnight; refer to Figure 16 for timeline. Mean \pm SEM, N=5.

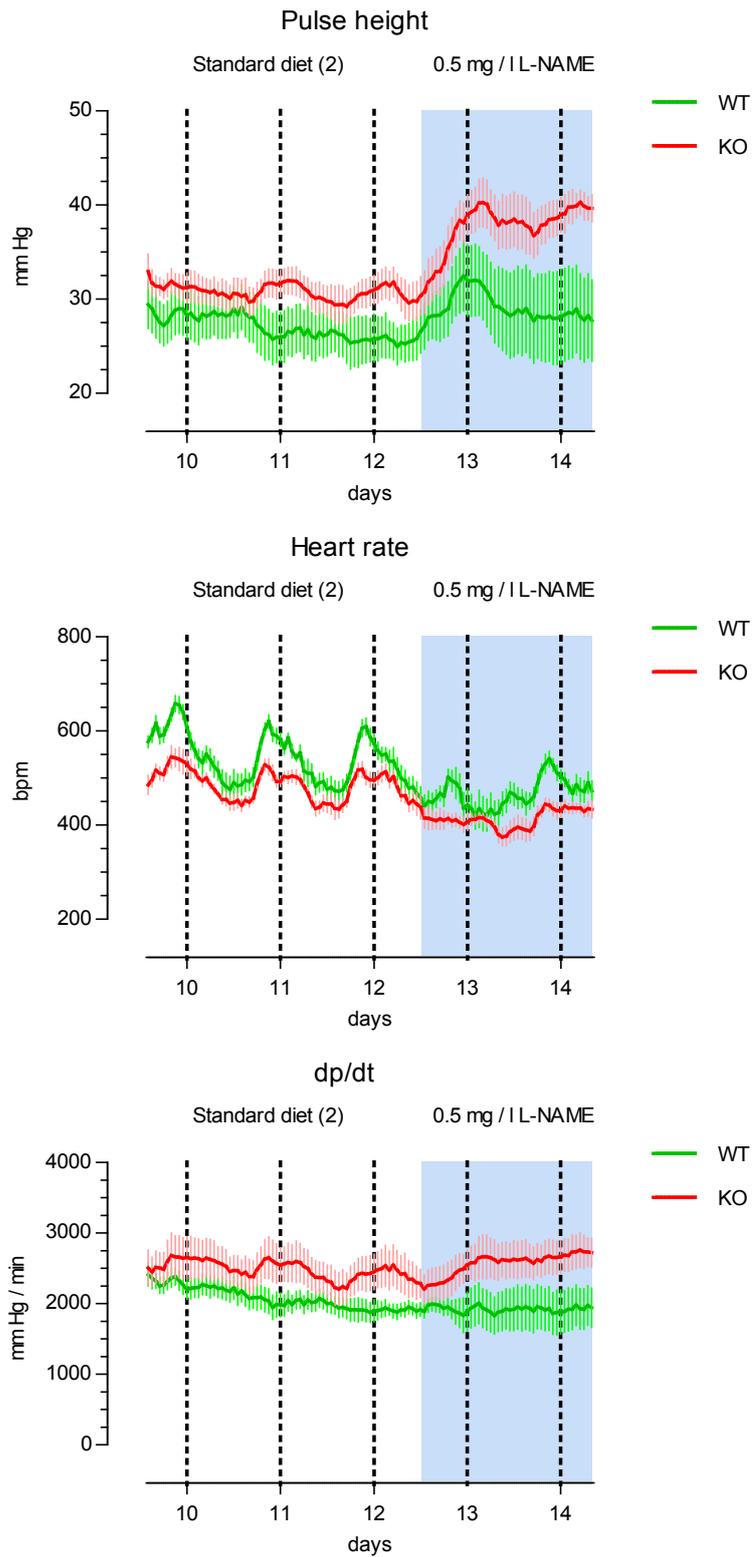


Figure 62: Pulse height, heart rate and dp/dt traces of WT and KO mice fed a standard diet or 0.5 mg / l L-NAME in the drinking water as measured by radiotelemetry. X-axis indicates days of experiment; dotted lines indicate midnight; refer to Figure 16 for timeline. Mean \pm SEM, N=5.

For statistical comparison of WT and KO mice and the effects of the different diets, averages of the read outs from fixed 3 hour intervals, 20:00-23:00 for active and 8:00-11:00 for resting phases, were selected across all mice on the last respective day of the four treatments.

When comparing read outs at fixed time points for active and resting phases of the mice, two-way ANOVA showed significant reductions in systolic ($p < 0.05$), diastolic ($p < 0.001$) and mean arterial pressure ($p < 0.01$) between WT and KO mice during their active phase when fed either standard or 4% NaCl containing diet. This reduction in blood pressure was especially pronounced in diastolic blood pressure where Bonferroni post-test showed significant reductions for KO mice compared to WT in standard ($p < 0.05$) as well as high salt diet ($p < 0.01$). No significant differences were found during the resting phase of the mice (Figure 63).

Pulse height showed a significant increase in KO mice compared to WT during the resting period of the animals ($p < 0.05$) but not for the individual diets. Heart rates of KO mice were highly significantly reduced during the active ($p < 0.001$) and resting phase ($p < 0.01$) of the mice. When the mice were active, the high salt diet did not influence heart rate in neither WT nor KO mice, while heart rate dropped significantly ($p < 0.05$) in KO, but not WT, mice compared to standard diet when the mice were resting. No differences were found in dp/dt between WT and KO mice and standard and high-salt diets (Figure 64).

All results of the fixed time period analysis for standard diet vs. 4 % NaCl containing diet are listed in Appendix A, Table 20.

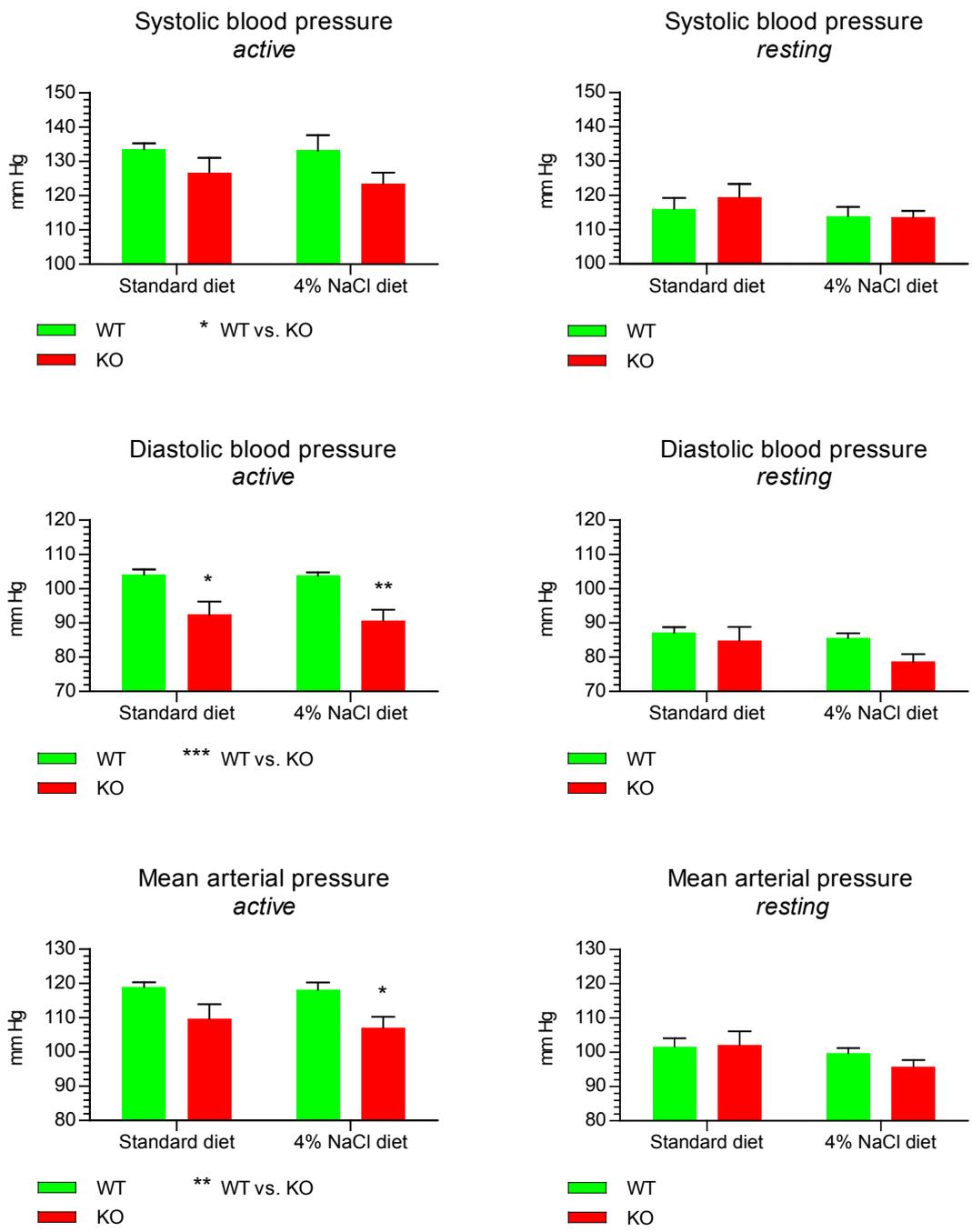


Figure 63: Systolic, diastolic and mean arterial pressure of WT and KO mice during their active and resting times of the day, fed on standard diet or high salt diet as measured by radiotelemetry. Active and resting time points calculated from average values at 20:00-22:00 (active) and 8:00-10:00 (resting) of the last day of the diet. * $p < 0.05$, ** $p < 0.01$, *** $p < 0.001$. $N = 5$, mean + SEM, two way ANOVA (reported below graphs) and Bonferroni post-test (bars).

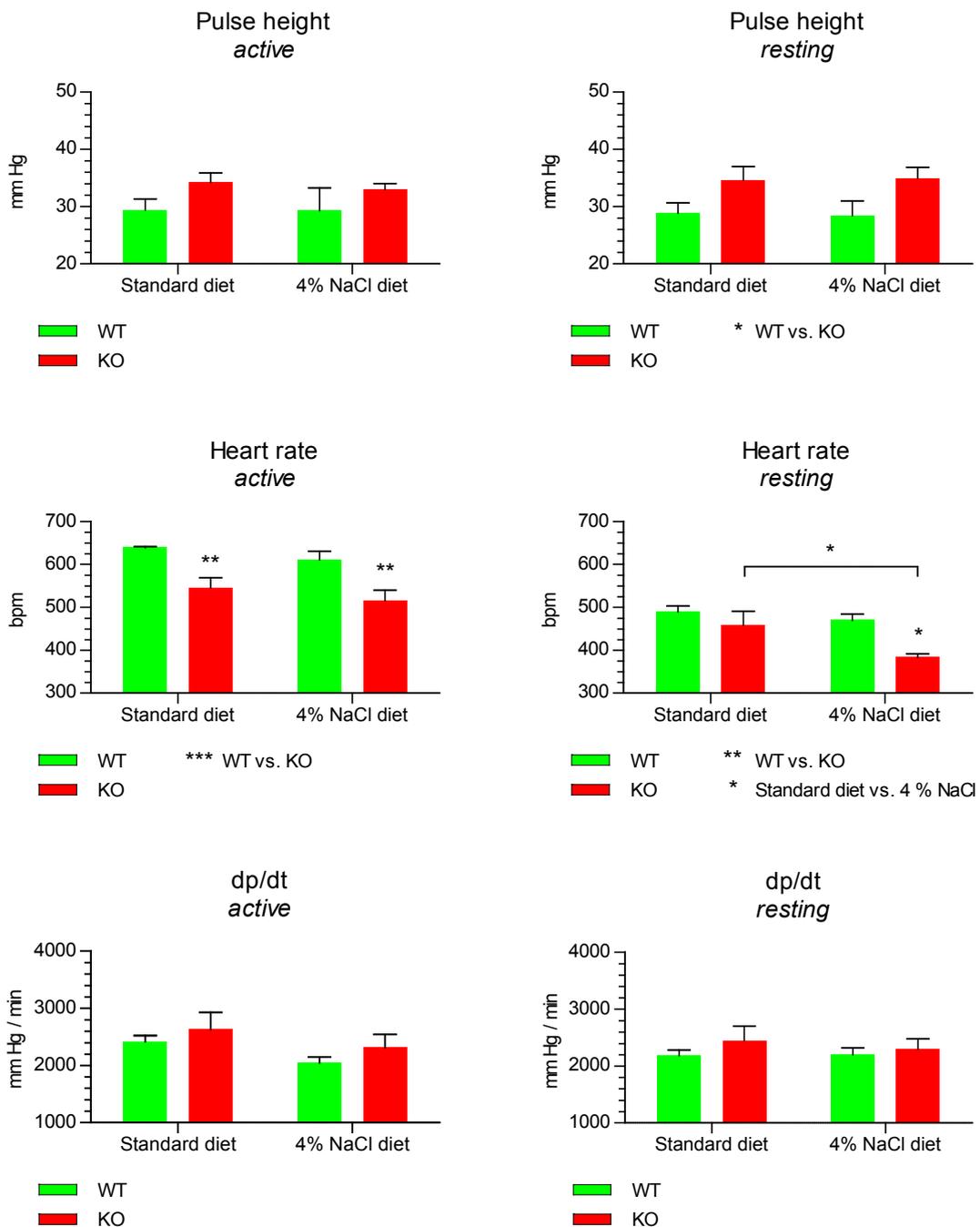


Figure 64: Pulse height, heart rate and dp/dt of WT and KO mice during their active and resting times of the day, fed on standard diet or high salt diet as measured by radiotelemetry. Active and resting time points calculated from average values at 20:00-22:00 (active) and 8:00-10:00 (resting) of the last day of the diet. * $p < 0.05$, ** $p < 0.01$, *** $p < 0.001$. $N = 5$, mean + SEM, two way ANOVA and Bonferroni post-test.

Supplementation of the drinking water of the mice with 0.5 mg / l L-NAME led to a profound effect on blood pressure of the mice. During their active phase, systolic blood pressure of KO mice showed a significant ($p < 0.05$) increase in blood pressure. For diastolic and mean arterial pressures Bonferroni post-test showed that the difference between WT and KO mice was only significant on standard diet but non-significant when the mice were treated with the NO synthase inhibitor. In the light of the blood pressure traces, it seems plausible that the remaining (non-significant) difference would have grown even smaller if it would have been possible to treat the mice with L-NAME for a longer period of time. During the resting phase of the mice, systolic ($p < 0.001$), diastolic ($p < 0.01$) and mean arterial blood pressure ($p < 0.001$) of WT as well as KO mice increased significantly when the mice were treated with L-NAME and did not show any differences between WT and KO mice (Figure 65).

As in the experiments with the high salt diet, pulse height of KO mice was significantly increased compared to WT in active ($p < 0.05$) as well as resting phases of the mice ($p < 0.01$). During the resting phase, L-NAME treatment increased pulse height significantly ($p < 0.05$) in KO mice but not WT mice. Heart rates of KO mice were significantly reduced in KO mice compared to WT control ($p < 0.001$) during the active phase of the mice. Supplementation of the drinking water of the mice with 0.5 mg / l L-NAME resulted in a further significant drop of the mice's heart rate in both WT ($p < 0.01$) and KO ($p < 0.05$) animals. In contrast, no differences in heart rate were observed during the mice' resting phase, neither between genotypes nor standard diet or L-NAME treatment. Dp/dt was increased significantly in KO mice compared to WT ($p < 0.05$) in active and resting phases alike (Figure 66).

All numerical results of the fixed time period analysis for standard diet vs. 0.5 mg / l L-NAME are listed in Appendix A, Table 21.

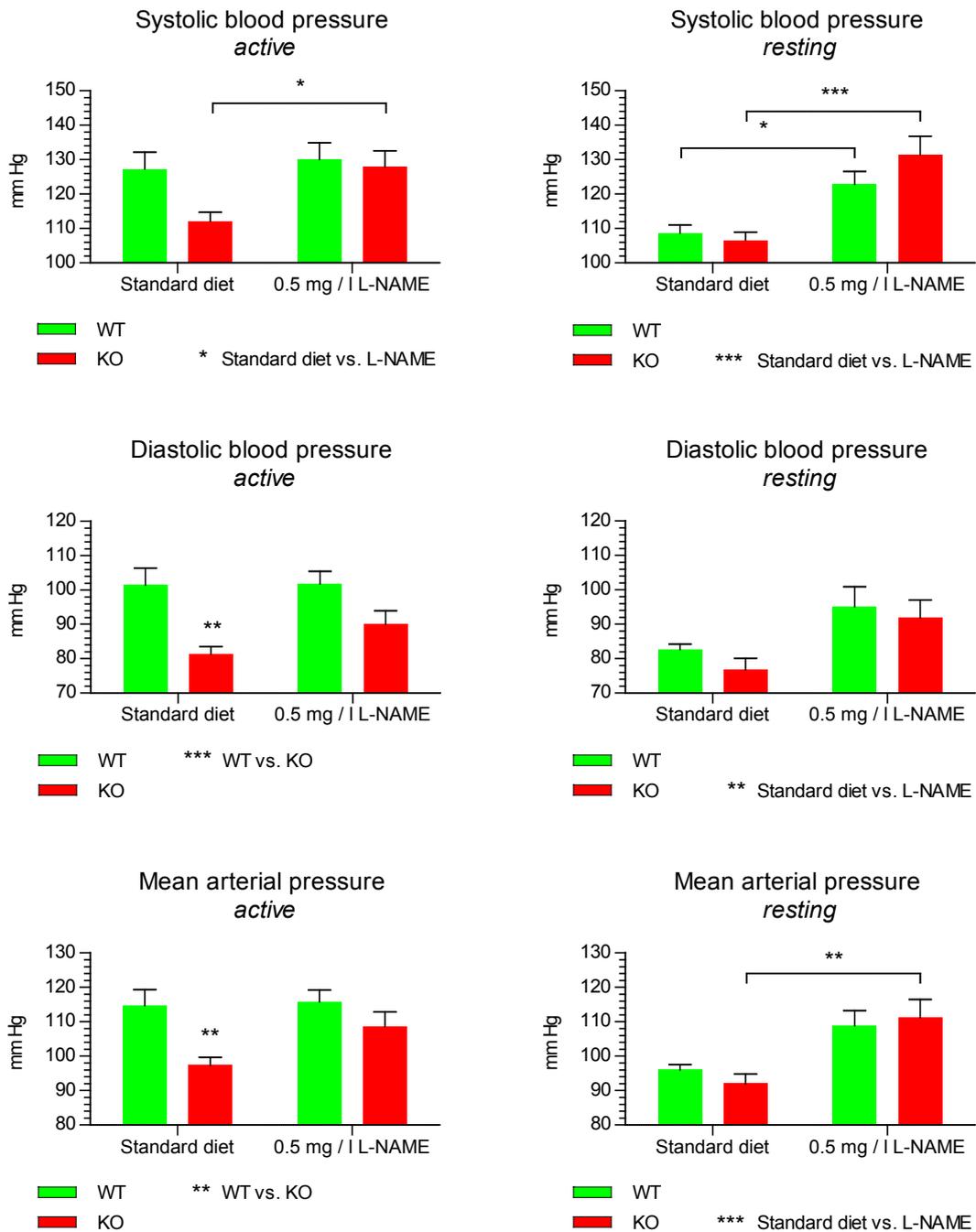


Figure 65: Systolic, diastolic and mean arterial pressure of WT and KO mice during their active and resting times of the day, fed on standard diet or 0.5 mg / ml L-NAME as measured by radiotelemetry. Active and resting time points calculated from average values at 20:00-22:00 (active) and 8:00-10:00 (resting) of the last day of the diet. * $p < 0.05$, ** $p < 0.01$, *** $p < 0.001$. $N = 5$, mean + SEM, two way ANOVA and Bonferroni post-test

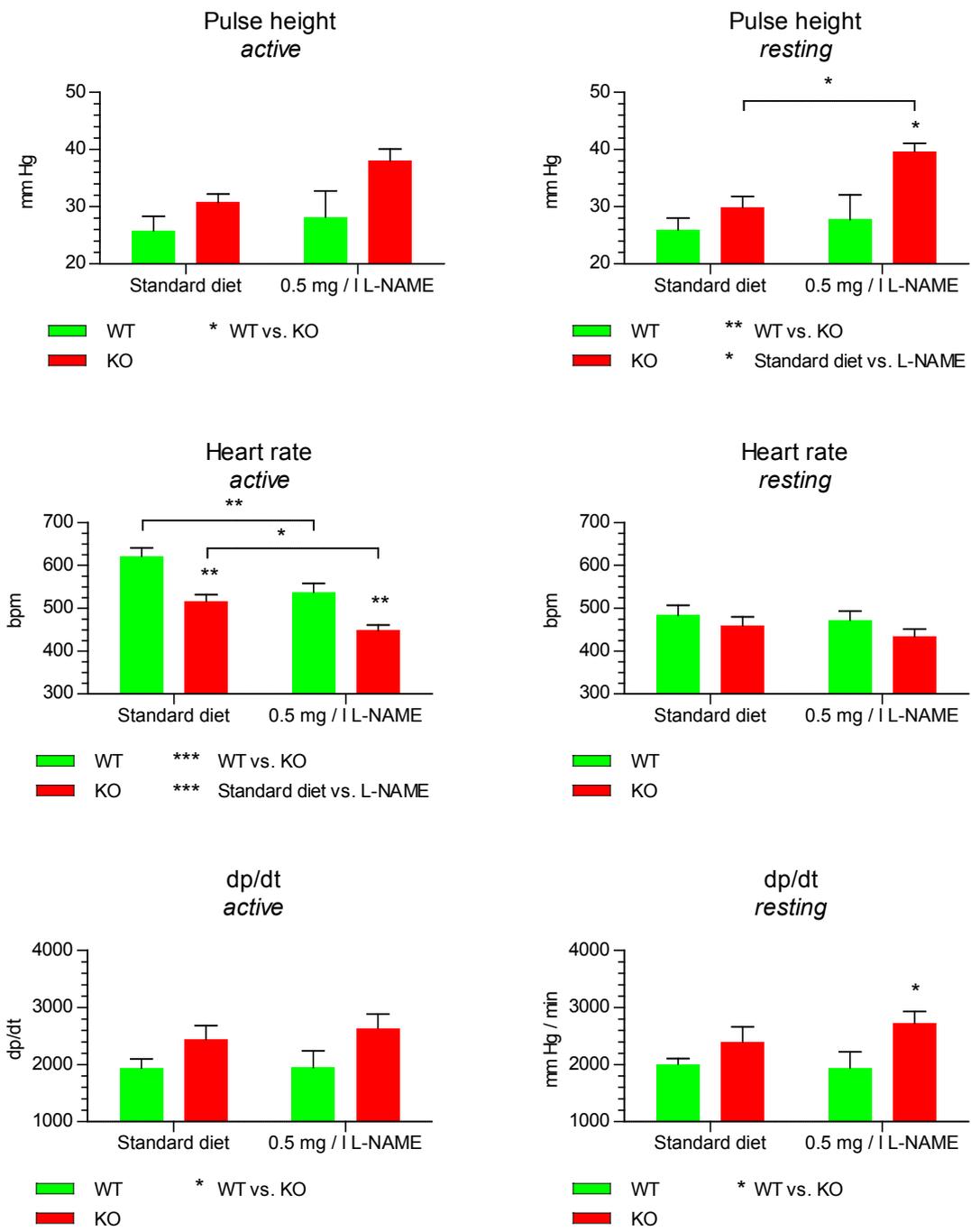


Figure 66: Pulse height, heart rate and dp/dt of WT and KO mice during their active and resting times of the day, fed on standard diet or 0.5 mg / ml L-NAME as measured by radiotelemetry. Active and resting time points calculated from average values at 20:00-22:00 (active) and 8:00-10:00 (resting) of the last day of the diet. * $p < 0.05$, ** $p < 0.01$, *** $p < 0.001$. $N = 5$, mean + SEM, two way ANOVA and Bonferroni post-test

7.2.3 Cardiac cine-MRI

Investigation of the impact of CaSR from VSMC on the heart function and morphology was carried out using cardiac cine-MRI. This method is the most accurate way of determining cardiac status in live mice and allows for measurements of all relevant cardiac parameters, such as left- and right-ventricular volumes, ejection fraction, and left ventricular flow rates (Schneider et al. 2006).

Scans were performed on age-matched 12, 14 and 18 month old WT and KO mice. Values for CO are not presented since the animals were imaged under general anaesthesia, which leads to changes in heart rates of the animals (Berry et al. 2009). Peak fill rate (PFR) and peak ejection rate (PER) are similarly difficult to interpret since these values relate flow rates per second, which is dependent on the speed of the cardiac cycle (i.e. heart rates). For the analysis of these parameters, all cardiac cycles were normalized to a period of one second.

7.2.3.1 12 month-old animals

Visual observation of the long axis (Figure 67) or short axis scans (Figure 68) did not show any obvious differences between the hearts of 12 month-old WT and KO mice. In agreement with this observation, no differences were found in the measured heart parameters of the 12 month cohort (Figure 69). Calculation of remodelling indices showed no difference for systole but a small but significant reduction in the diastolic remodelling index, (DRI, indicates reduced diastolic volume compared to total weight of the left ventricle) of KO hearts compared to WT (Figure 70). These results are somewhat surprising in light of the findings in the 14 month cohort (largely increased DRI in KO hearts, see below). However, the observed difference is much smaller than the one found in the 14 month old KO animals showing visible cardiac remodelling and might be attributed to chance. Long-axis cardiac dimension measurements showed a significant increase in left ventricular end-systolic length (LV-ESL) in KO compared to WT animals but no changes in end-systolic diameter or end-diastolic dimensions (Figure 71). When the measured cardiac parameters were normalised to total body weight (TBW), this difference in ESL disappeared. All other normalised values did not show a difference between heart of 12 month old WT and KO mice as well (Figure 72).

All numerical results from cardiac cine MRI of 12 month old animals are listed in Appendix A, Table 22.

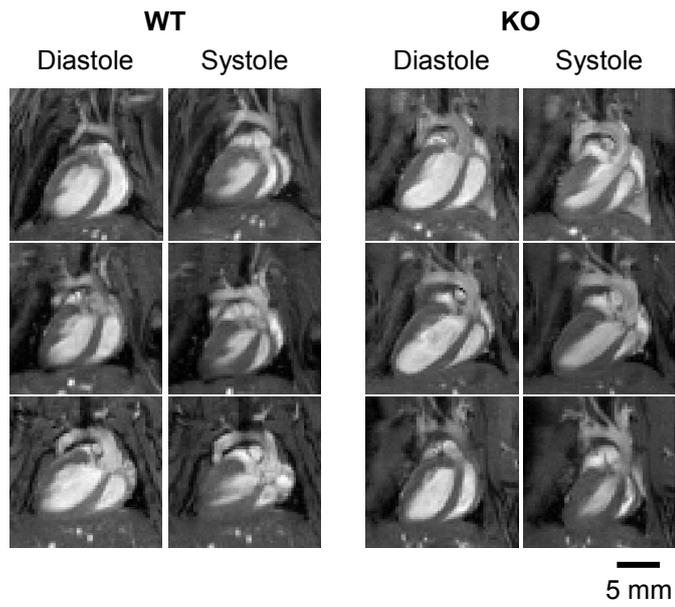


Figure 67: Long axis cardiac MRI scans of hearts from 12 month old WT and KO mice during diastole and systole.

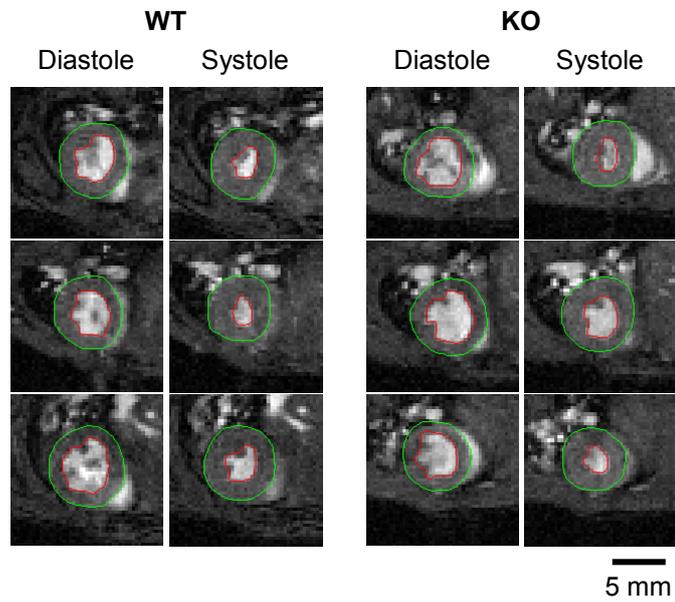


Figure 68: Short axis cardiac MRI scans of the third basal slice of hearts from 12 month old WT and KO mice showing diastole and systole. Green = epicardium, red = endocardium.

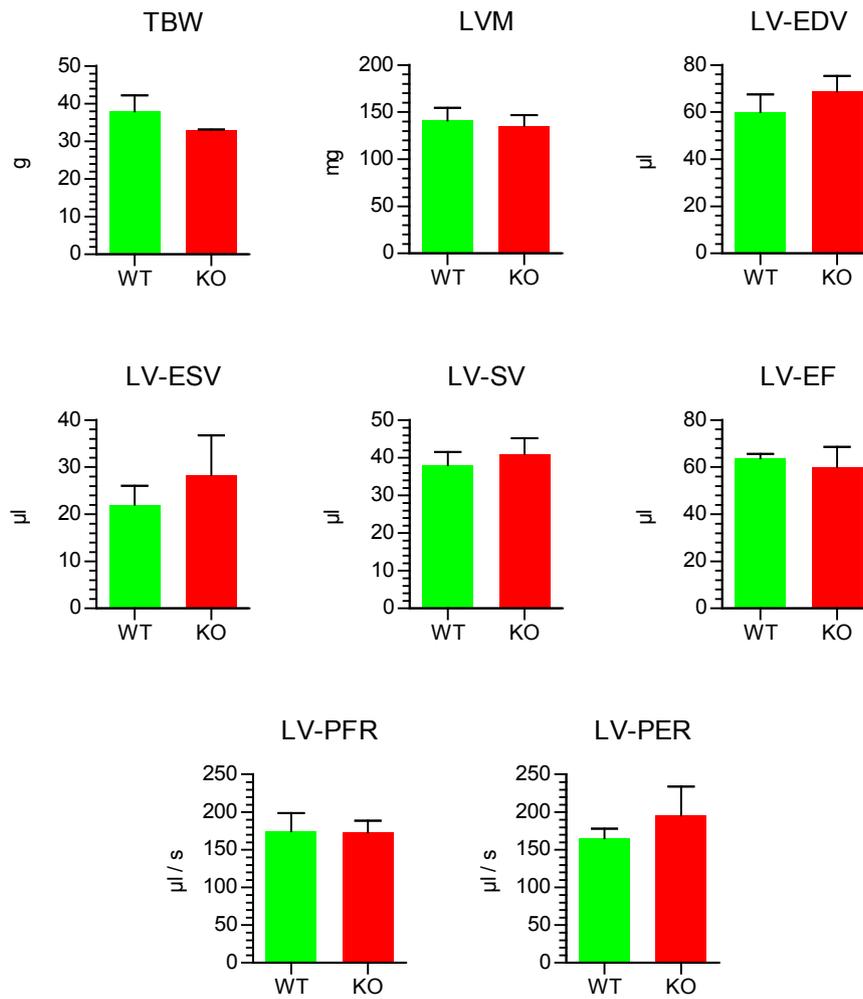


Figure 69: Measured and calculated left-ventricular cardiac parameters from short-axis cardiac cine-MRI scans of 12 month old WT and KO mice. LV = left ventricular, LVM = left ventricular mass, EDV = end diastolic volume, ESV = end systolic volume, SV = stroke volume, EF = ejection fraction, PFR = peak fill rate, PER = peak ejection rate. N = 3, mean + SEM.

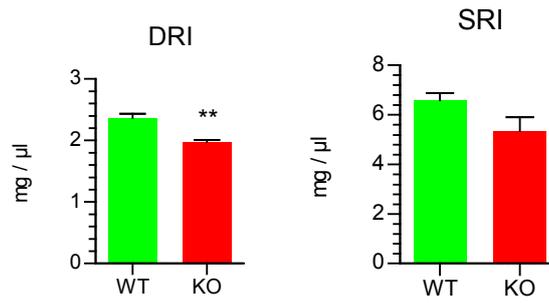


Figure 70: Calculated cardiac remodelling indices of from short-axis cardiac cine-MRI scans of 12 month old WT and KO mice. DRI = end-diastolic remodelling index, SRI = end-systolic remodelling index. ** $p < 0.01$, $N = 3$, mean + SEM, two-tailed T-test.

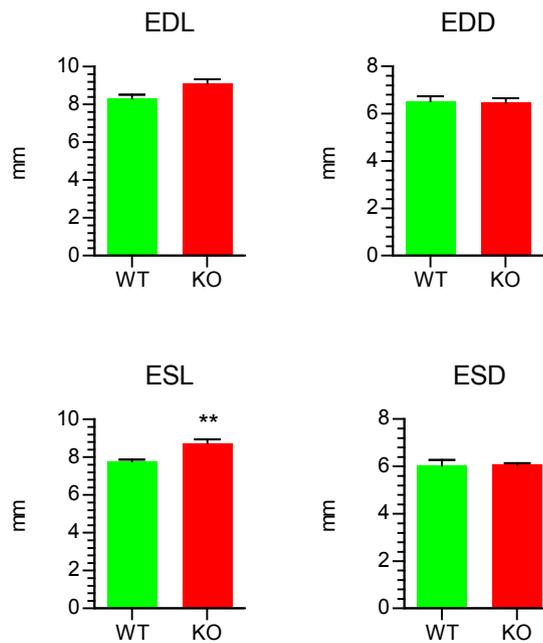


Figure 71: Measured heart dimensions from long-axis cardiac cine-MRI scans of 12 month old WT and KO mice. LV = left ventricular, ESL = end systolic length, ESD = end systolic diameter, EDL = end diastolic length, EDD = end diastolic diameter. ** $p < 0.01$, $N = 3$, mean + SEM, two-tailed T-test.

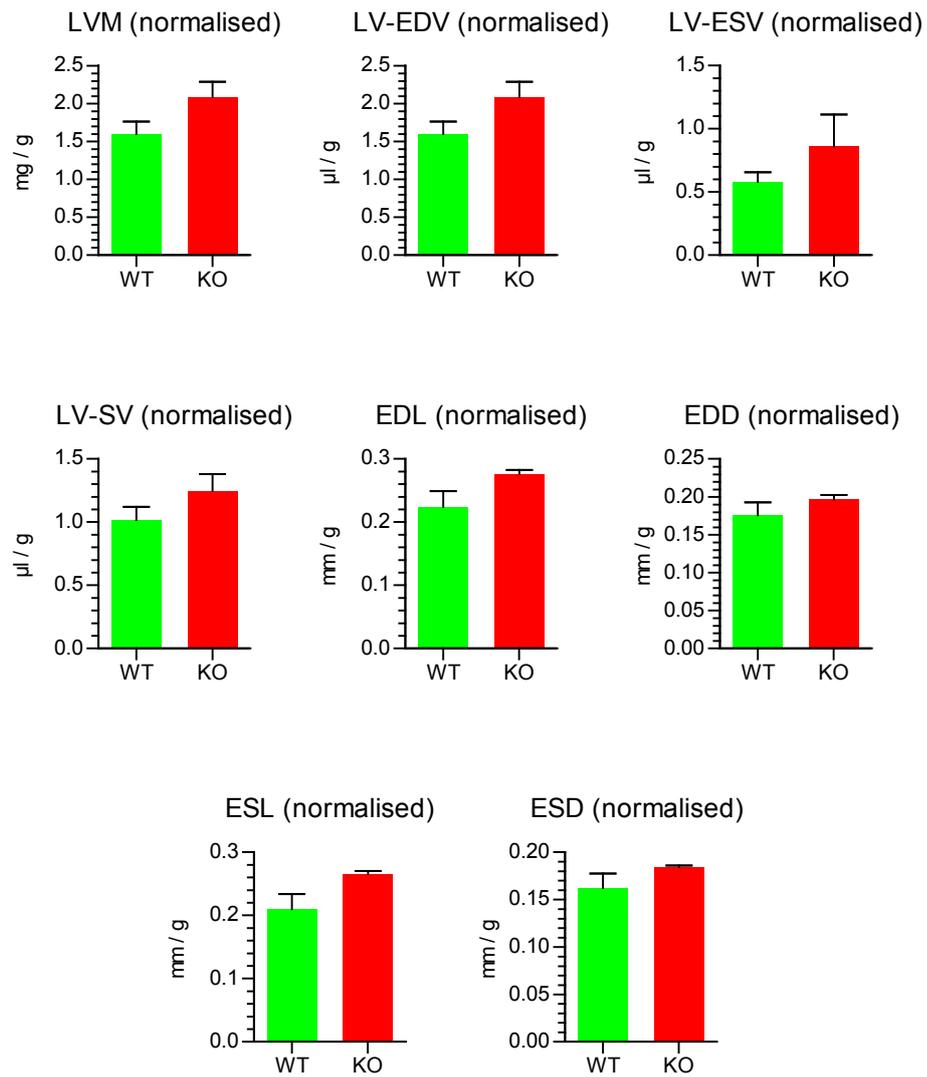


Figure 72: Parameters obtained from cardiac cine-MRI scans of 12 month old mice normalised to TBW. See Table 9 for abbreviations. N = 3 (WT), 3 (KO), mean + SEM, two-tailed T-test.

7.2.3.2 14 month old animals

In contrast to the findings on the 12 month old mice, visual observation of the long axis of 5 WT and 11 KO hearts of 14 month old animals showed no difference in end-diastole but a striking difference in end-systole in 5 out of the 11 hearts from KO animals. In these 5 hearts from KO mice, the left ventricle closed up the apical left ventricular cavity completely while the apical left ventricular cavity was still visible at the end-systole of the WT mice and the other 6 KO mice (Figure 73). Thus, the hearts of the KO mice were separated in two groups, those without obvious visual remodelling (termed “no rem” in figures and graphs) and those where remodelling was observed (termed “rem” in figures and graphs). This narrowing of the left ventricular cavity could be observed in the third basal short axis slices (representative images in Figure 74) of the remodelled KO hearts but was especially obvious in more apical sections (representative images in Figure 75), indicating a funnel-like shape of the end-systolic left-ventricle in KO mice which could be seen in 3D reconstructions of the left ventricle after analysis was complete (representative images in Figure 76). These observations were reflected in numerous changes in cardiac parameters of 14 month old KO mice compared to WT. Left ventricular end-diastolic (EDV) as well as end-systolic volumes (ESV) were non-significantly decreased in KO mice compared to WT and non-remodelled KO hearts while ejection fraction (EF) was significantly increased in the remodelled hearts. No significant change was observed in stroke volume (SV), left ventricular mass (LVM), total body weight (TBW), peak ejection rate (PER) or peak flow rate (PFR) between all groups (Figure 77).

End-diastolic (DRI) and end-systolic (SRI) remodelling indices, measures of the size of the ventricle vs. the end-diastolic and -systolic volumes, were significantly increased in remodelled hearts from KO mice compared to WT confirming the visually observed cardiac remodelling in this group of five 14 month old KO mice compared to WT and non-remodelled KO (Figure 78).

Because of the observed changes in the left ventricle, the right ventricle was also analysed. No changes in right ventricular EDV, ESV, SV and EF were found between hearts from WT and remodelled hearts from KO mice. However, right ventricular EDV was significantly increased in non-remodelled hearts from KO mice (Figure 79). This result can be attributed to the presence of one “outlier heart” in the non-remodelled KO group, which exhibited an enormously sized

right ventricle (blue arrow in Figure 73). Since a similar enlarged right ventricle was not observed in any of the other hearts.

Measurements of length and width of the hearts based on long central long axis scans showed no significant differences when comparing end-diastolic length (EDL), end-diastolic diameter (EDD), end-systolic length (ESL) and end-systolic diameter (ESD) between all the groups (Figure 80).

The same results as described above were found when the measured volumes and size parameters (excluding already normalized parameters like EF, PFR, PER, DRI, SRI) were normalised to TBW, except that there was a significant difference in normalised SV in non-remodelled KO hearts compared to WT (Figure 81). As mentioned above, this result can be attributed to the large right ventricle present in one of the KO hearts which can very probably be classified as an outlier.

All numerical results from cardiac cine MRI of 14 month old animals are listed in Appendix A, Table 23 and Table 24.

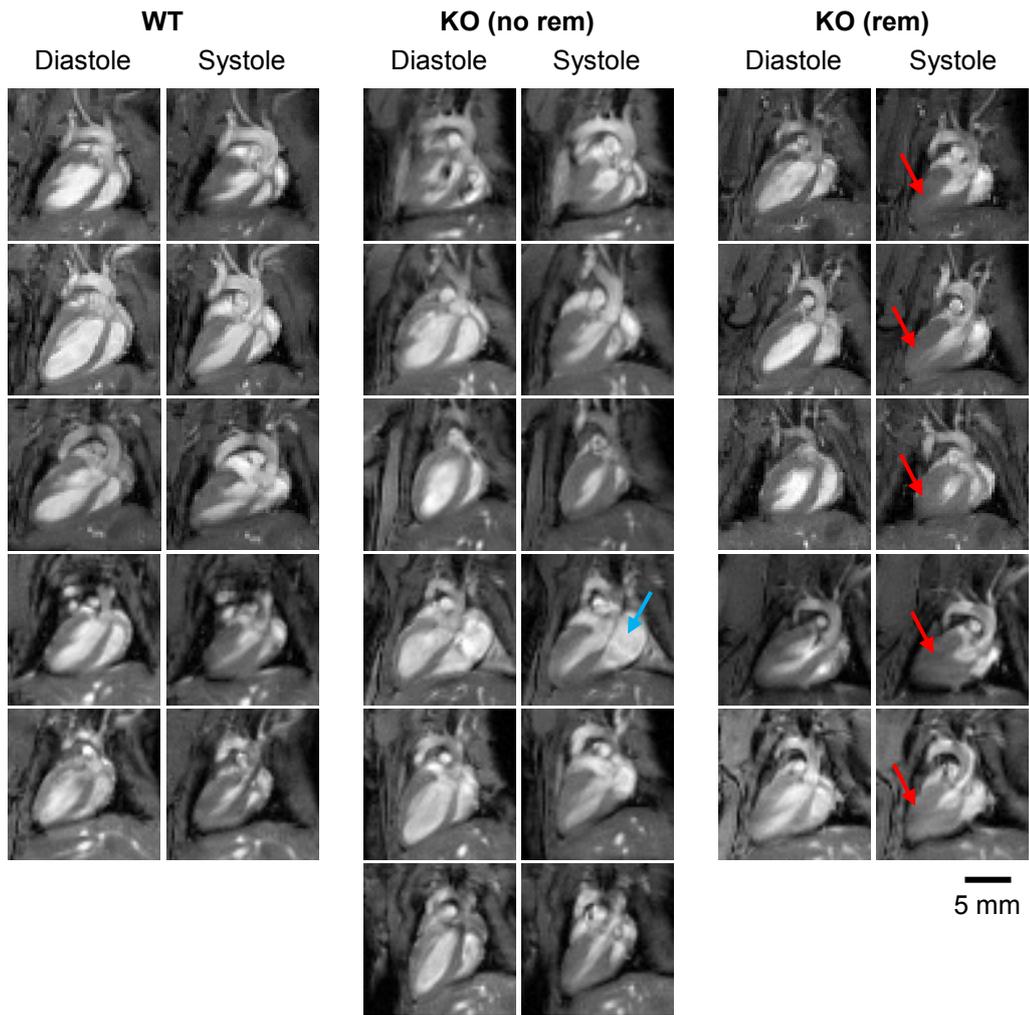


Figure 73: Long axis cardiac MRI scans of hearts from 14 month old WT and KO mice showing diastole and systole. While 6 KO hearts appeared comparable to WT (KO no rem) 5 out of 11 investigated KO hearts (KO rem) exhibited marked narrowing of the apical left ventricular cavity in systole with almost no lumen visible (red arrows) while the others. One of the KO hearts showed an excessively large right ventricle (blue arrow). Rem = remodelling.

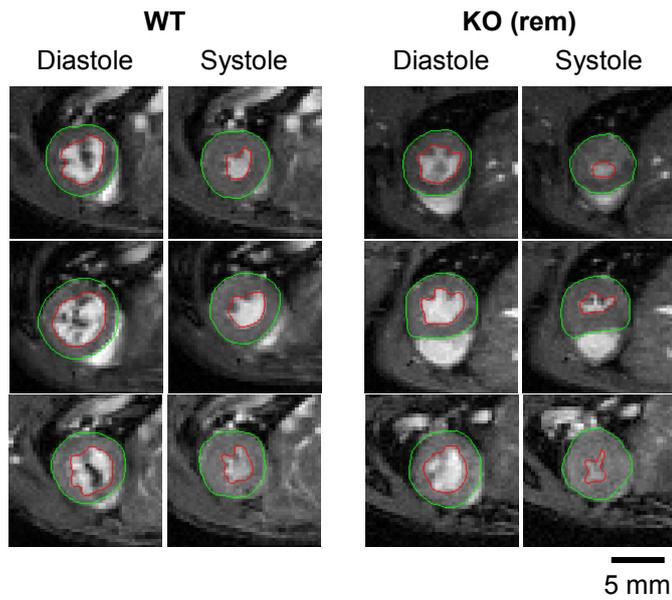


Figure 74: Short axis cardiac MRI scans of the third basal slice of hearts from 3 representative hearts from 14 month old WT and KO mice with visible remodelling (KO rem) showing diastole and systole. Green = epicardium, red = endocardium. The left ventricular lumen is in systole is visibly narrower in hearts from KO mice compared to WT.

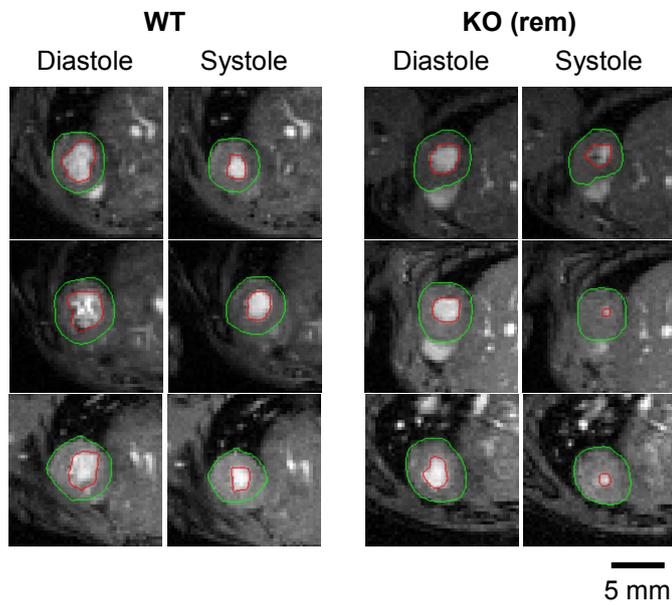


Figure 75: Short axis cardiac MRI scans of the second apical slice of 3 representative hearts from 14 month old WT and KO mice with visible remodelling (KO rem) showing diastole and systole. Green = epicardium, red = endocardium. The left ventricular lumen is in systole is considerably narrower in hearts from KO mice compared to WT.

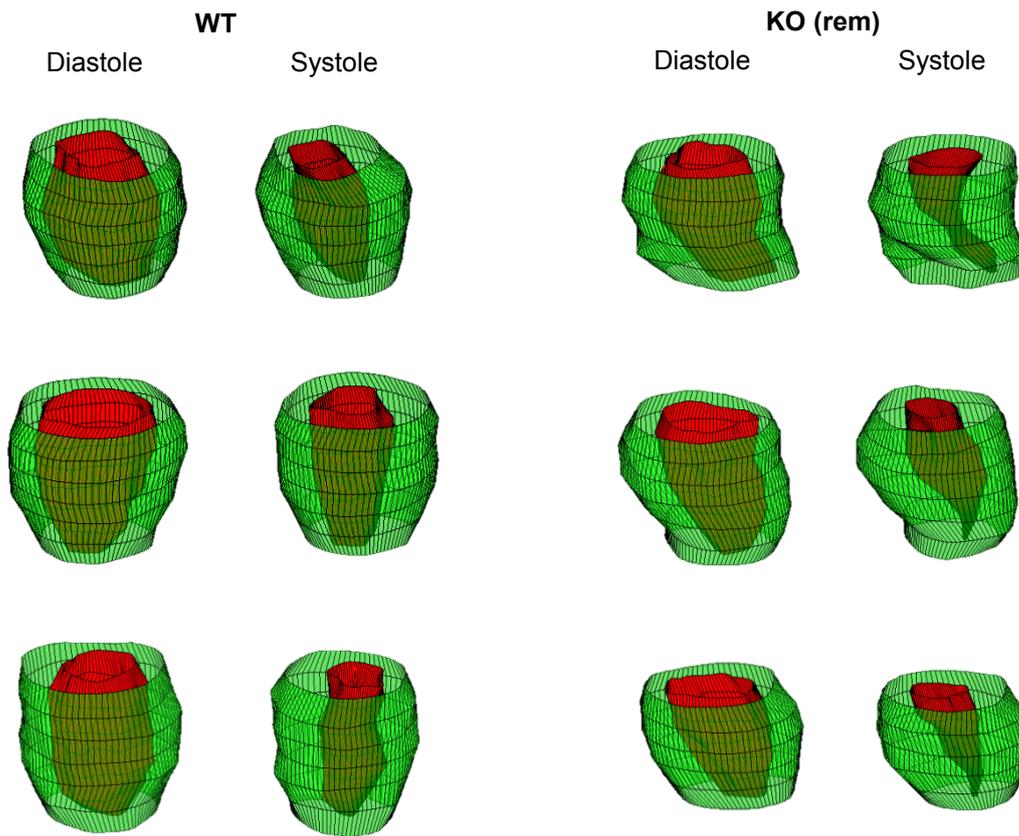


Figure 76: 3D reconstruction of the manually segmented left ventricles of 3 representative hearts from 14 month old WT and KO mice with visible remodelling (KO rem). Green = epicardium, red = endocardium. Apex and base were not segmented. In contrast to WT (and non-remodelled KO hearts, not shown), left ventricular cavities of hearts KO of mice with visible remodelling showed a funnel-like shape in systole indicating apical wall-thickening.

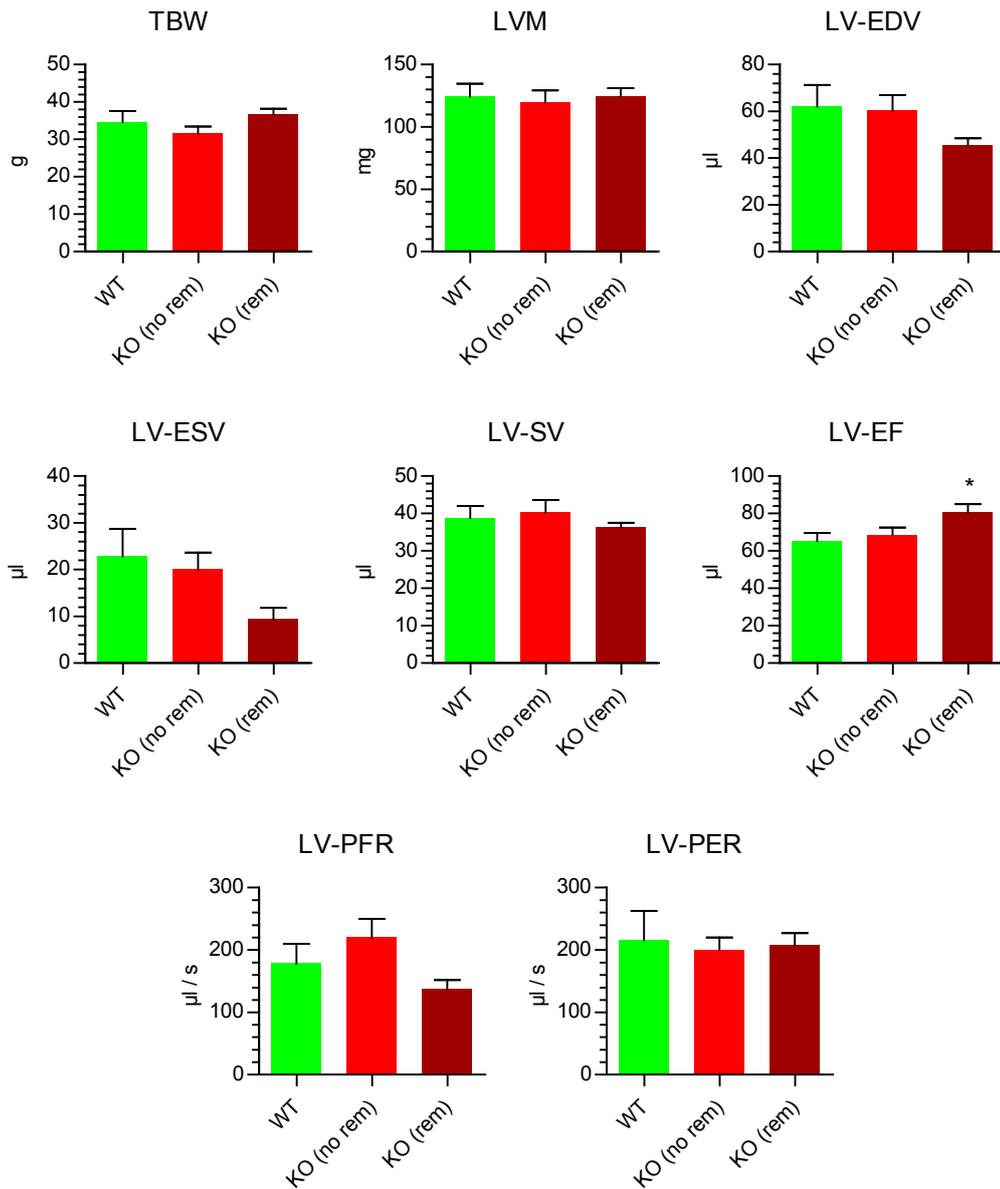


Figure 77: Measured and calculated left-ventricular cardiac parameters from short-axis cardiac cine-MRI scans of 14 month old WT, KO mice without visible cardiac remodelling (KO (no rem)) and KO mice with visible remodelling (KO (rem)). See Table 9 for abbreviations. * $p < 0.05$, $N = 5$ (WT), 6 (KO (no rem)), 5 (KO (rem)), mean + SEM, ANOVA with Dunnet post-test vs WT.

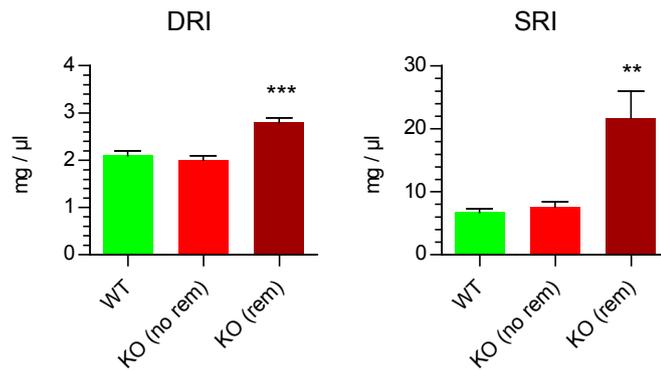


Figure 78: Calculated cardiac remodelling indices of from short-axis cardiac cine-MRI scans of 14 month old WT, KO mice without visible cardiac remodelling (KO (no rem)) and KO mice with visible remodelling (KO (rem)). See Table 9 for abbreviations. ** $p < 0.01$, *** $p < 0.001$ N = 5 (WT), 6 (KO (no rem)), 5 (KO (rem)), mean + SEM, ANOVA with Dunnet post-test.

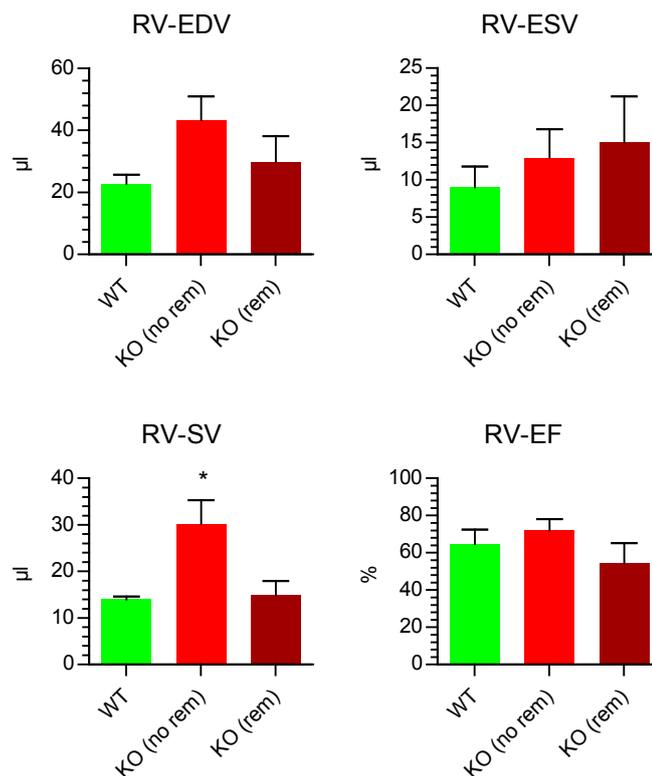


Figure 79: Measured right ventricular cardiac parameters from short-axis cardiac cine-MRI scans of 14 month old WT, KO mice without visible cardiac remodelling (KO (no rem)) and KO mice with visible remodelling (KO (rem)). See Table 9 for abbreviations. * $p < 0.05$, N = 5 (WT), 6 (KO (no rem)), 5 (KO (rem)), mean + SEM, ANOVA with Dunnet post-test vs WT.

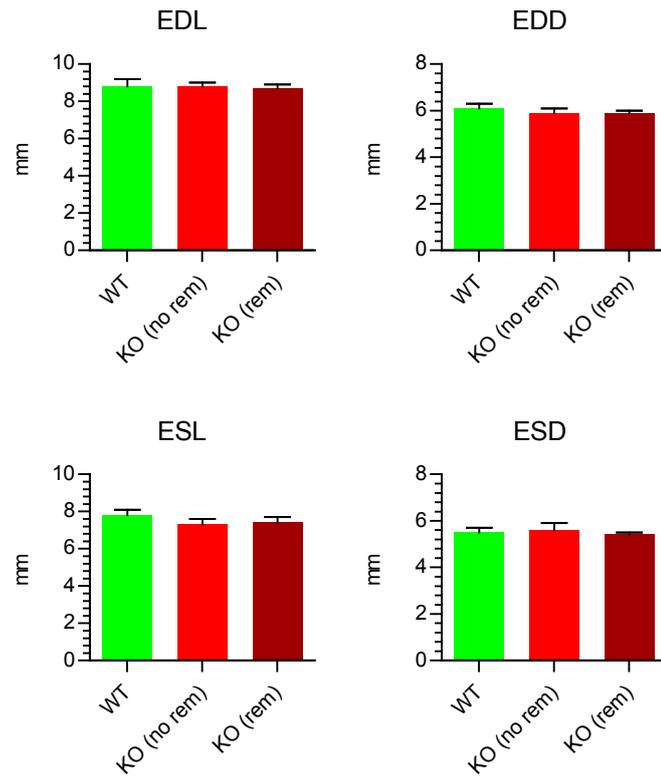


Figure 80: Measured heart dimensions from long-axis cardiac cine-MRI scans of 14 month old WT, KO mice without visible cardiac remodelling (KO (no rem)) and KO mice with visible remodelling (KO (rem)). See Table 9 for abbreviations. N = 5 (WT), 6 (KO (no rem)), 5 (KO (rem)), mean + SEM, ANOVA with Dunnet post-test vs WT.

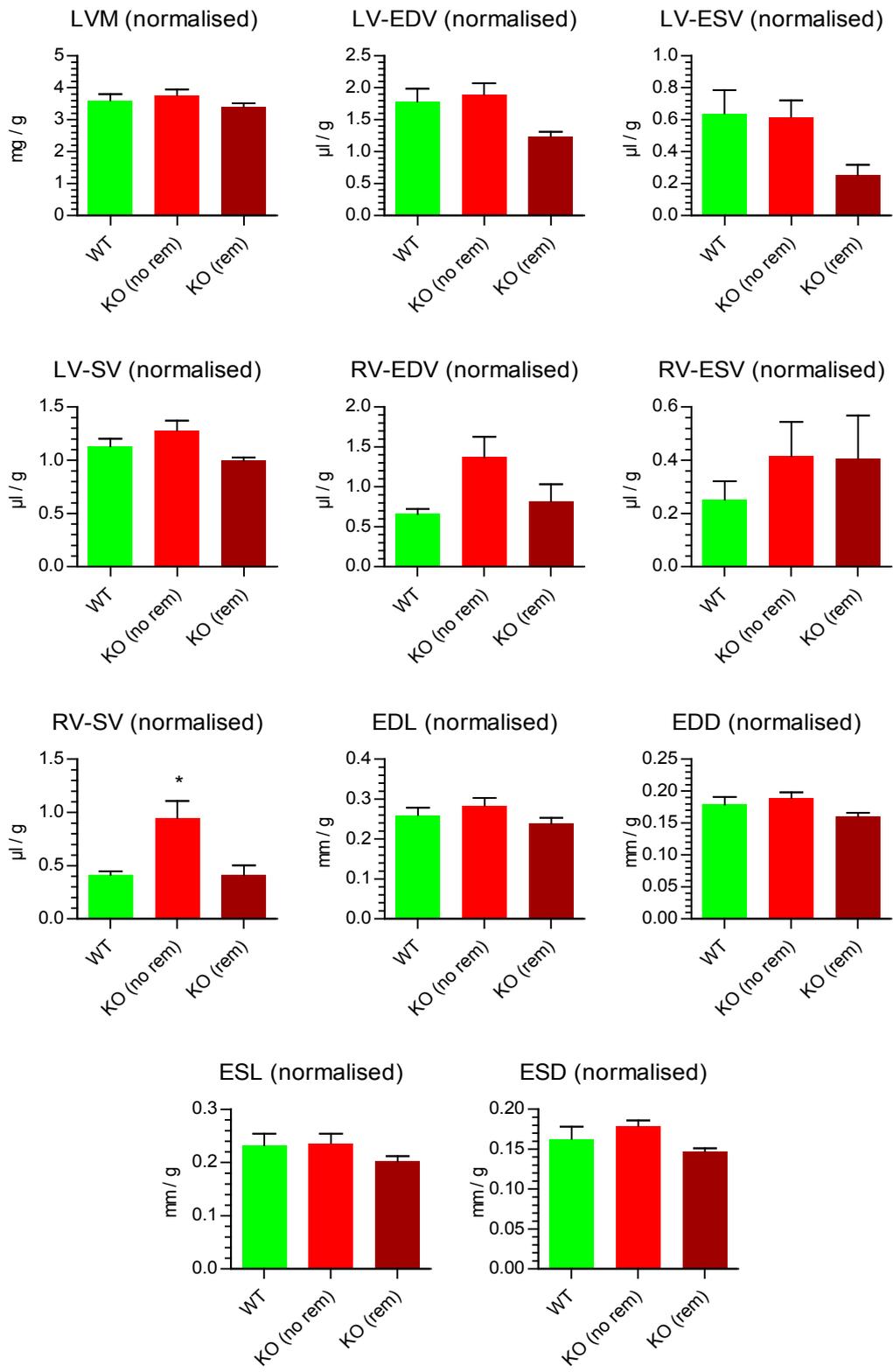


Figure 81: Parameters obtained from cardiac cine-MRI scans of 14 month old mice normalised to TBW. See Table 9 for abbreviations. N = 5 (WT), 6 (KO (no rem)), 5 (KO (rem)), mean + SEM, ANOVA with Dunnet post-test vs WT.

7.2.3.3 18 month old animals

Measurements at 18 months of age proved difficult as 2 of the mice in the KO cohort and 1 of the mice in the WT cohort died under anaesthesia prior to completion of the short axis scans. The KO group at this age was therefore reduced to $N = 2$, which does not allow statistical analysis. For this reason, results of the cardiac cine-MRI analysis of 18 month old animals are reported in Appendix B, 12.3.

7.3 Discussion

In the following sections, I will discuss the cardiovascular phenotype of the SM22 α -Cre x LoxP-CaSR mouse, which was assessed by tail cuff and radiotelemetry analysis as well as cardiac cine-MRI. I will describe observed changes in baseline blood pressure and the possible mechanisms behind them, as well as the specific effects observed when the mice were challenged with high salt and L-NAME diets. Furthermore, I will compare and explain *ex vivo* wire myography data from experiments performed in our group by Dr. Thomas Davies (*c.f.* (Davies 2013)), Dr. Polina Yarova and Mrs. Irene Lopez to allow for better understanding of these mechanisms. Finally, I will discuss the cardiac phenotype of the mice.

7.3.1 Blood pressure measured by tail cuff

A systematic problem in the tail cuff experiments was the post-hoc detection of a defect in the first used tail cuff equipment, leading to reading being overestimated. For repeated measurements with new equipment, only a limited number of mice were available, thus resulting in low N numbers, especially for WT mice. However, because of the later performed radiotelemetry studies, tail cuff experiments were not followed up further.

Tail cuff experiments demonstrated that mice lacking the CaSR in VSMC had decreased blood pressure, which was more pronounced in diastolic than systolic blood pressure. The combined result for all tail cuff measured mice, showed a significant reduction by about 8 % or 12 % (MAP) respectively, depending on the ex- or inclusion of the overestimated values (see below). Interestingly, the KO paw temperatures of 3–6 month old KO animals were significantly lower than the ones of WT control animals, in line with the observed hypotensive phenotype in KO mice.

(Systolic) blood pressure of mice has been shown to increase with age in a linear fashion by about 20 mm Hg from 2 to 12 months of age (Gros et al. 2002). However, no such increase was found in WT mice of 4, 9 and 17 month of age, which all showed comparable blood pressure.

Stress due to handling and unknown environments is generally known to cause elevated blood pressure in mice (Mattson 2001; Hoorn et al. 2011) and high variability between tail cuff vs. telemetry as well as inter-study inconsistency have been described (Mattson 2001). Moreover,

differences of 10 mm Hg and more are common in murine blood pressure on an hour to hour basis (Mattson 2001) which can seriously affect measurement accuracy and precision, especially if the “real” difference between two measured groups, as is the case in this study on WT and KO mice, is equal or lower than this natural scatter in murine blood pressure.

To address these issues, radiotelemetry studies with continuous 24 h blood pressure recording were performed.

7.3.2 Baseline blood pressure measured by radiotelemetry

Telemetry analysis showed a very significant and immediately obvious reduction in blood pressure of KO mice compared to WT control that was greater in diastolic than systolic blood pressure. The general trend of the blood pressure curves followed a downward direction over the course of the first few days of the experiment (while the mice were on standard diet). Differences in blood pressure as well as other parameters such as dp/dt only asserted themselves shortly before the mice were changed to a high salt containing diet. This effect can be easily explained by the time constraints we had to adhere to when performing the experiments. Telemetry data was recorded beginning from day 2 post operation. It is therefore very probable that mice had not fully recovered from the post-operation stress in addition to being transferred to a new and uncomfortable environment (metabolic cages) on day 1 of the experiment (Mattson 2001; Hoorn et al. 2011). This hypothesis is confirmed by the evidence that, as the mice acclimatized and recovered, downwards trend in the blood pressure curves were observed. Interestingly, while the mice were assumedly under high levels of stress, i.e. on the first days of the experiment, circadian rhythms were shifted in KO mice compared to WT control. This suggests a different stress or light / dark cycle responses in the SM22 α -Cre x LoxP-CaSR mouse, which could be the direct consequence of VSMC CaSR (blood vessels are everywhere, hence also in the CNS), or could be a secondary response to the reduced blood pressure or due to other metabolic changes observed in these mice (see chapter 8). Further investigation of the circadian rhythms of these animals might prove interesting for future studies.

Once the mice had acclimatized and recovered, and circadian rhythms had synchronised between WT and KO mice, the magnitude of the difference between WT and KO mice showed a large dependence on the circadian rhythm: while the difference in BP between WT

and KO mice was small to non-existent during the resting phase of the mice at daytime, especially for systolic blood pressure, it peaked at their active period during the night. This indicates that the difference between WT and KO mice was highest when sympathetic drive (active phase) was highest, therefore suggesting either directly reduced sympathetic drive or a reduction in response to sympathetic drive in KO mice (see next section).

Keeping with the basic physiology formula of blood pressure being the product of CO and TPR, the reduced blood pressure observed in the SM22 α -Cre x LoxP-CaSR mouse could be caused by a reduction in CO, a reduction in TPR or a combination of both. Additionally, secondary mechanisms attributing to one or the other include changes in the RAAS or sympathetic drive. These possibilities are discussed in the course of the following sections.

7.3.3 Role of the heart and arterial compliance

7.3.3.1 Influence of the heart rate on blood pressure of KO mice

Heart rate of animals lacking the VSMC CaSR was reduced, suggesting a reduction in CO as possible cause for the reduction in blood pressure. Heart rate dropped in response to L-NAME treatment, probably as a compensatory response to the increased TPR elicited by the compound. Salt loading further depressed heart rate in resting, but not active, KO animals. This result is somewhat difficult to interpret, as a reduction in heart rate would normally be accompanied with an increase in blood pressure when indeed, if anything the opposite was the case. When analysing the traces, a marked drop in heart rate compared to standard diet (and in fact WT animals) can only be identified on the last day of the high salt diet which was selected pre-analysis for statistical comparison of the different diets' effects. One might speculate that unknown external circumstances could have contributed to this singular event, but it is possible of course that the effects of the high salt diet requires time to develop and only manifested on the last day, although this seems unlikely.

Nevertheless, the lower blood pressure of KO animals does not seem to be caused solely by the reduced heart rate. A reduction in heart rate goes along with a reduction in CO ($CO = \text{heart rate} \times SV$) if the stroke volume is constant which seems to be the case between WT and KO animals, even in the group of KO animals with remodelled hearts. On the assumption that SV is constant between WT and KO mice, reduced CO would primarily lead to lower systolic and not diastolic blood pressure. The opposite was found in KO mice where diastolic blood

pressure showed a much greater reduction than systolic blood pressure, which argues against a direct (exclusive) effect of CO on blood pressure of these mice. Of course the weakness of this assumption is that heart rates and SV were measured on mice of very different ages (3 months for heart rate, 14 months for SV). The situation might very well be different in hearts of 3 months old animals where differences in SV could be present, with the heart in ageing mice having adapted over time. Since CO was not directly measured and SV and general cardiac analysis was performed only on older animals where the blood pressure profile or heart rates might have changed through adaptation, this question cannot be answered at this time. Further studies measuring CO directly and cardiac MRI studies of (younger) animals will be required to define the role of the heart in blood pressure regulation of these animals. As a matter for speculation dp/dt was elevated in KO mice independently of salt loading or L-NAME treatment. This could be interpreted in such a way that increased inotropy of the heart was compensating for the reduction in chronotropy, again possibly arguing against CO as major component of the reduced blood pressure observed in the KO mice.

7.3.3.2 Possible causes for reduced heart rates in KO mice

The question remains why KO mice show such a pronounced reduction in heart rate. Systemic administration of cinacalcet was shown to have no influence on heart rate of normal and uremic rats (Fryer et al. 2007). While this may only be circumstantial, it indicates that globally, CaSR does not affect heart rate to a great extent. Reduction in blood pressure is normally compensated by an increase in heart rate or vice versa via the baroreflex response (Wang et al. 2004). The fact that hypotension is accompanied with bradycardia in the SM22 α -Cre x LoxP-CaSR mouse could be attributed to a reduction in baroreflex response, which occurs through increased arterial stiffness (Phillips et al. 2014). However, increased arterial stiffness generally goes along with elevated systolic pressure, which was not the case in KO mice. Further no vascular calcification was detected in aortae of KO mice (see chapter 6) and lastly, the administration of L-NAME in the drinking water led to a significant reduction in heart rate of KO (and WT) animals, which suggests intact baroreflex action in response to the increase in TPR through L-NAME. This probably baroreflex mediated reduction of heart rate through L-NAME administration has already been suggested previously (Sheriff et al. 2000; Fellet et al. 2003; Jones et al. 2004). Taken together, these findings make reduced arterial

compliance and therefore impaired baroreflex response as cause for the reduced heart rate in SM22 α -Cre x LoxP-CaSR mice unlikely if sympathetic drive is not impaired.

Indeed, a possible explanation could be seen in a reduction in sympathetic drive in these animals, suggesting that baroreflex, or more accurately baroreceptors, is in actual fact working but cannot exert its function due to reduced action of the sympathetic nervous system or reduced susceptibility of the heart towards adrenergic stimulation. This could be suggested by the fact that differences in heart rate between WT and KO animals were most developed during the active period of the mice (where sympathetic drive is highest). However, it is unclear by which way the vascular CaSR would elicit such a response. Systemically, it is feasible that undetermined changes in the microvasculature caused by the lack of the VSMC CaSR influence adrenalin production in the adrenal glands. Indeed such a phenomenon has been described for vascular changes in a model of diabetic rats, but in this case widening of adrenal capillaries was associated with increased adrenal function (Sricharoenvej et al. 2009) which is in contrast to what we would expect in the SM22 α -Cre x LoxP-CaSR mice. The CaSR has also been found to be expressed in sympathetic neurons (Vizard et al. 2008) indicating a role in regulation of the sympathetic nervous system. Stimulation of the CaSR with poly-L-arginine in cirrhotic and normal rats, while decreasing portal vein but not systemic pressure, did not result in changes in plasma noradrenaline levels (Sansoe et al. 2013), pointing again away from a possible direct effect of the CaSR on adrenergic stimulation. Finally, although only circumstantial, the already mentioned baroreflex elicited reduction in heart rate when the mice were treated with L-NAME also points away from an impaired autonomous drive. Possible systemic influences are discussed in chapter 7.3.5.

Finally, a direct effect of CaSR knock-out on the heart is plausible, especially in relation to the sporadic cardiac remodelling observed in KO mice, and the documented transient embryonic expression of SM22 α in mice (Lepore et al. 2005). The CaSR might directly potentiate adrenergic signalling in the heart as a mechanism for the potentiation of Ca²⁺ dependent contractions has been described, albeit for blood vessels (Loot et al. 2013). The possibilities and implications of direct CaSR mediated effects on the heart are discussed in chapter 7.3.9.

7.3.4 Role of TPR

On standard diet, baseline diastolic blood pressure exhibited a greater reduction than systolic pressure in KO mice compared to WT control. As already mentioned above, diastolic blood pressure is generally recognised to be mainly influenced by TPR, while CO is more related to systolic pressure. This strongly points to reduced TPR as the main cause for reduced blood pressure in these mice. Pulse height was elevated in KO mice compared to WT control. Elevated pulse height can be a sign of reduced arterial compliance, though as already discussed, this is apparently not the case in the SM22 α -Cre x LoxP-CaSR mouse; the increased pulse pressure, again as its major component is a reduction in diastolic and not an increase in systolic pressure (as would be expected in case of reduced arterial compliance) can therefore be attributed to the loss of TPR.

7.3.5 Systemic influences

The observed hypercalcaemia in KO mice (see next chapter) is probably not associated with the observed hypotension. Even though elevated dietary intake of Ca²⁺ is generally recognised to lower blood pressure, pathological hypercalcaemia is associated with elevated blood pressure. Acute hypercalcaemia in animal models consistently leads to blood pressure increase (Iseki et al. 1986; Thorin et al. 1990) and total serum calcium levels were found to be associated with hypertension in a large cross sectional clinical study (Sabanayagam and Shankar 2011). Vitamin D supplementation was shown to have very mild blood pressure lowering effects (Forman et al. 2013; Kunutsor et al. 2013). Yet, high levels of 1,25-D3, as present in the KO mice, are more associated with the onset of vascular calcification, increased blood vessel stiffness (Bas et al. 2006) and subsequent hypertension.

Furthermore, an effect of the systemic hypercalcaemia (as described in the next chapter) is thinkable, although evidence in the literature on this is conflicting. While classical physiology indicates that acute hypercalcaemia is associated with bradycardia, patients suffering from primary hyperparathyroidism, who are chronically hypercalcaemic, do not present changes in heart rate (Rosenqvist et al. 1992; Barletta et al. 2000; Farahnak et al. 2010; Birgander et al. 2012).

At this point it is not possible to determine whether increased 1,25-D3 levels or hypercalcaemia would have an influence or contribution to blood pressure and heart rate in

the SM22 α -Cre x LoxP-CaSR mouse, especially because of the multitude of other possible influences. A potential way to determine the magnitude of a putative influence of the 1,25-D3 levels as well as the elevated blood Ca²⁺ levels would be the generation of a SM22 α -Cre x LoxP-CaSR x 1- α -Hydroxylase^{-/-} mouse, thereby feasibly normalising the changes in blood Ca²⁺ and Pi levels making an estimation of the independent, direct actions of the CaSR in blood vessels on blood pressure possible.

7.3.6 Effect of salt loading on blood pressure

Salt loading with a 4 % NaCl containing diet did not have an increasing effect on blood pressure of WT as well as KO mice. If anything, blood pressure further decreased in WT as well as KO animals (not statistically significant), which can probably be attributed to the continuing acclimatisation process of the mice to their environment in the metabolic cages rather as a direct effect of salt loading. This conclusion is also supported by the marked drop in blood pressure once the mice were transferred into more comfortable standard cages and back onto standard diet after the high salt phase was concluded. Had the blood pressure decrease been caused by salt loading, blood pressure would have increased following unloading. On the other hand, such an effect cannot be entirely disregarded. Metabolic cage studies described in the next chapter showed that while urine production and water consumption was increased in animals on both genotypes, urine production in KO animals was further increased compared to WT control without a concomitant increase in water consumption on the high salt diet. This could suggest that blood pressure in KO mice could have dropped on the high salt diet as a result of reduced blood volume.

The missing effect of salt loading on WT mice was expected as high salt diet induced hypertension takes weeks to assert itself in healthy mice, especially on a part-C57/B16 background (Gros et al. 2002). Nevertheless, the missing effect of salt loading on KO mice suggests that the hypotonic phenotype of these animals is not salt sensitive, thus excluding Na⁺ imbalance as cause for the observed hypotension. Indeed, biochemical studies described in the next chapter demonstrated that Na⁺ and Cl⁻ serum as well as urinary excretion levels are unchanged between WT and KO mice.

Finally, the absence of increased blood pressure in KO animals in response to salt loading points away from an involvement of the RAAS in the hypotension observed in these animals.

Transgenic animals lacking ACE ($ACE^{-/-}$) have a phenotype of extensive hypotension, in all likelihood caused by impaired angiotensin II production and bradykinin breakdown. Salt loading leads to an immediate increase and normalisation of the blood pressure of these mice which is thought to be caused by a failure of the RAAS to detect high plasma Na^+ levels (Carlson et al. 2002). The hypertension prevalent in chronic renal failure, which is associated with low renin levels and increased arterial stiffening, was also shown to be salt sensitive in rats after only 5 days of a 4 % NaCl containing diet (Nguy et al. 2013). The fact that SM22 α -Cre x LoxP-CaSR mice did not react with blood pressure normalisation to the high salt diet therefore provides some evidence that the RAAS, or at least ACE activity, in these mice is not impaired which is substantiated by the unchanged renin and aldosterone plasma levels observed in KO mice compared to WT as described in the next chapter. At first, this may seem surprising as the natural response to a drop in blood pressure would be the activation of the RAAS to combat the hypotension. However, it has to be kept in mind that the SM22 α -Cre x LoxP-CaSR mouse is not an acute, but rather a chronic model. Consequently, the set-point for blood pressure maintenance and therefore action of the RAAS might be altered compared to mice being born with a functional vascular CaSR. Taken together these results indicate that kidney function and the RAAS are probably not causative in the hypotensive phenotype of these mice.

7.3.7 Effect of NO synthesis inhibition on blood pressure

As expected, blood pressure of both WT and KO mice increased when being given 0.5 mg / l of the NO synthase inhibitor L-NAME in their drinking water (Mattson 2001). Importantly, this increase was much larger in KO animals, particularly in systolic blood pressure, but also in diastolic pressure to the point that the difference between WT and KO animals was lost. This rectifying outcome of NO synthesis inhibition, together with the larger reduction in diastolic blood pressure again strongly points towards compromised TPR in mice lacking the VSMC CaSR and that this reduction in TPR might be caused by excessive NO synthesis / production in KO mice.

Heart rate dropped significantly in both genotypes when the mice were awake, probably as a baroreflex mediated result compensating for increased TPR induced by L-NAME. The increase in pulse height, resulting from a greater increase in systolic than diastolic blood pressure, could indicate elevated CO in response to L-NAME. This is somewhat surprising as

heart rate was decreased. Dp/dt however showed a slight but significant increase in KO animals, suggesting a (further) elevated inotropy in KO hearts which could account for the greater increase in systolic than diastolic blood pressure. In light of the large(er) increase in contraction of KO blood vessels than WT control when treated with L-NAME (see below), it is also possible that systolic blood pressure increased because of increased stiffening of conductance arteries such as the aorta (Ruiz et al. 2008).

7.3.8 Direct influence of the vascular CaSR on vascular tone

The telemetry studies strongly pointed towards a reduction in TPR as cause for the hypotensive phenotype of the SM22 α -Cre x LoxP-CaSR mouse.

Direct interaction of the VSMC CaSR with contraction and / or dilation of VSMC and therefore changes in TPR seems to be the most probable explanation for the reduced blood pressure. One, or a combination of the following ways of interaction at the level of the blood vessels to achieve a lower TPR by CaSR deletion seems possible: direct contracting action of the CaSR on VSMC, direct inhibition relaxation of VSMC, indirect inhibition of relaxation of VSMC by decreasing NO sensitivity in VSMC and indirect promotion of contraction by increasing adrenergic stimuli (Figure 82).

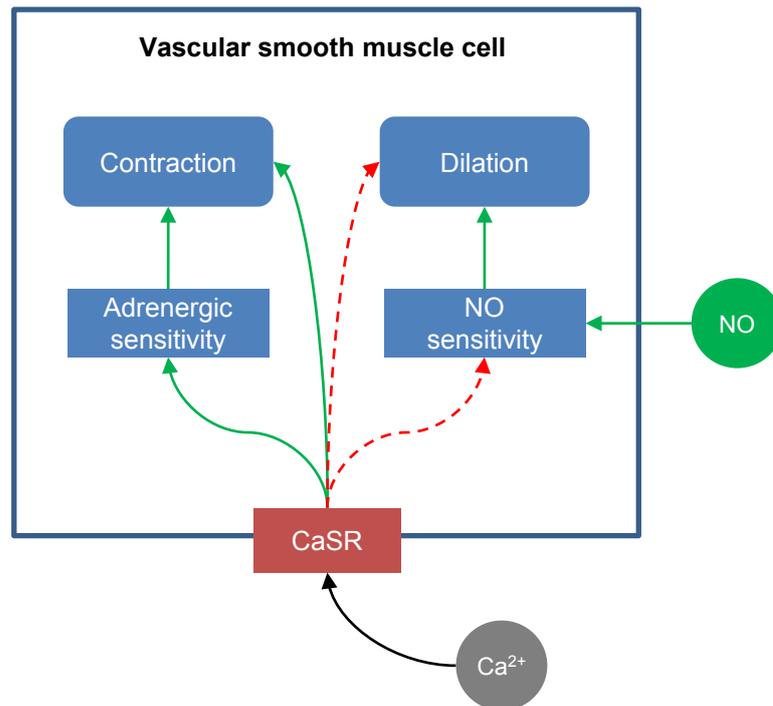


Figure 82: Possible mechanisms of direct interaction of the VSMC CaSR with contraction and dilation of VSMC. Actions of the CaSR on VSMC to promote an increase in TPR, explaining the reduced blood pressure in KO mice. The CaSR could interact with adrenergic sensitivity, have a direct effect on contraction, inhibit NO sensitivity or inhibit VSMC dilation. Green arrows: stimulation, Red broken arrows: inhibition.

To investigate these assumptions and a possible NO related mechanism (implied by the reduced difference in blood pressure elicited with L-NAME treatment), in collaboration with Dr David Edwards (Heart Centre, Cardiff University), Dr. Thomas Davies, Dr. Polina Iarova and Mrs. Irene Lopez of our group performed *ex vivo* wire myography studies on isolated blood vessels. In their experiments, rings of aortae of KO 3-6 month old KO animals showed a marked reduction of maximum contractility in response to phenylephrine compared to WT control (Figure 83A). Of note, potency of phenylephrine to evoke contraction was the same in WT and KO aortae (not shown), thereby excluding an effect of the VSMC CaSR on adrenergic sensitivity of VSMC. This observation is especially revealing in the light of the observation that the hypotension of KO mice compared to WT was most pronounced during the animals' active phase, i.e. when sympathetic drive was greatest. This occurrence can therefore be explained by the reduced contractile activity elicited by phenylephrine and – by extension – adrenergic activity *in vivo*, on the microvasculature and therefore TPR and blood pressure. In addition to this loss of contractility in response to adrenergic stimuli, aortic

explants contracted less in response to high extracellular K^+ , which causes depolarisation and subsequent Ca^{2+}_i rise and contraction, which indicates that not only adrenergic contraction (Figure 83B), but the contractile ability of the blood vessels in general is impaired by loss of VSMC CaSR.

In agreement with the observed effect of L-NAME on blood pressure *in vivo*, inhibition of NO synthesis with L-NAME increased general contractility and abolished the difference between WT and KO aortae (Figure 83C). Additional experiments with the NO donor S-Nitroso-N-acetylpenicillamine (SNAP) (Dahboul et al. 2014) on endothelium denuded mesenteric arteries performed by Dr. Vladimir Matchkov (Aarhus University, Denmark) showed that there was no difference in NO potency between blood vessels of WT and KO mice (not shown).

These results suggest that the VSMC CaSR contributes to blood vessel contraction by counterbalancing NO mediated dilation via a direct contractile effect. Such a contractile effect was already suggested by Ohanian and colleagues who observed a biphasic effect of Ca^{2+} on rat subcutaneous small arteries, causing contraction at lower and dilation in higher concentrations of Ca^{2+} , although the authors believed that the contractile effect was probably not CaSR-mediated (Ohanian et al. 2005). However, we have found the same biphasic effect in WT aortae, while the contracting component was lost in KO aortae which only exhibited dilation in response to increases in extracellular Ca^{2+} (Figure 83D). This result clearly suggests that the VSMC CaSR is responsible for the Ca^{2+} induced contractions in these blood vessels.

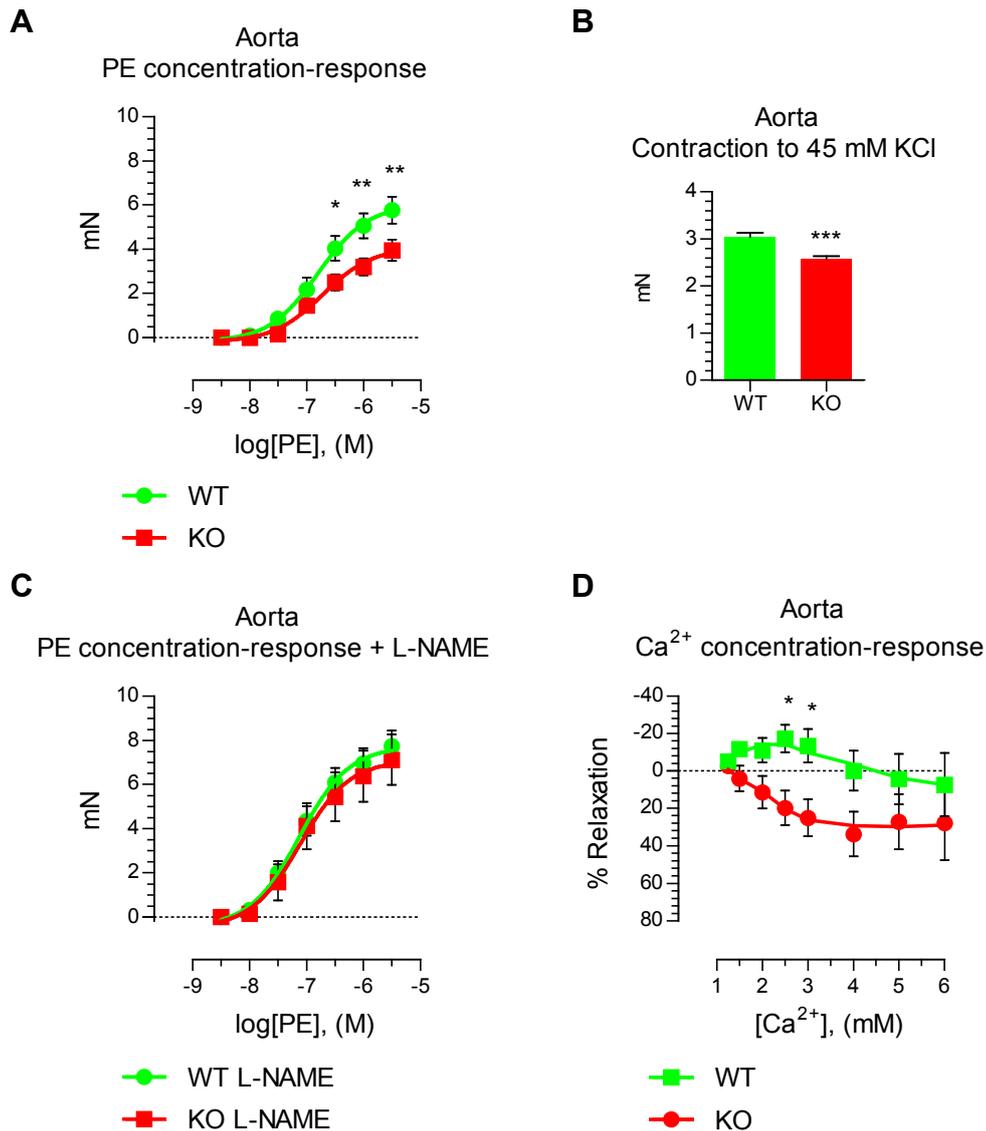


Figure 83: Wire myography experiments performed by Dr. Polina Yarova and Dr. Thomas Davies (Davies 2013). A: Phenylephrine (PE) concentration response curves of WT and KO aortae. Mean \pm SEM, N = 5, * $p < 0.01$, ** $p < 0.01$, two-way ANOVA with Bonferroni post-test. B: Contraction response of aortae to 45 mM KCl. Mean \pm SEM, *** $p < 0.001$, N = 11, two-tailed T-test. C: Phenylephrine (PE) concentration-response curves of WT and KO aortae in the presence of 100 μ M L-NAME. Mean \pm SEM, N = 6 (WT), 7 (KO), two-way ANOVA with Bonferroni post-test. D: Ca²⁺ concentration-response curves of WT and KO aortae following preconstruction with 0.3 μ M phenylephrine. Mean \pm SEM, * $p < 0.01$, N = 4-8 (WT), 7-9 (KO), two-way ANOVA with Bonferroni post-test.

The intracellular signalling mechanisms involved which could be responsible for contraction of VSMC have recently been uncovered for human aortic smooth muscle cells, where CaSR activation leads to an increase in cytosolic Ca^{2+}_i via PLC/PKC pathway, releasing Ca^{2+} from intracellular stores via IP_3 and activating TRPC receptor-operated Ca^{2+} -channels (Chow et al. 2011). My findings showing abundant CaSR expression in the vascular endothelium as well as studies by others (Ziegelstein et al. 2006; Loot et al. 2013) indicate that the CaSR also stimulates endothelial NO production (Awumey et al. 2013), thus suggesting a dual role for the vascular CaSR: contracting in VSMC and dilating in the endothelium (Figure 84).

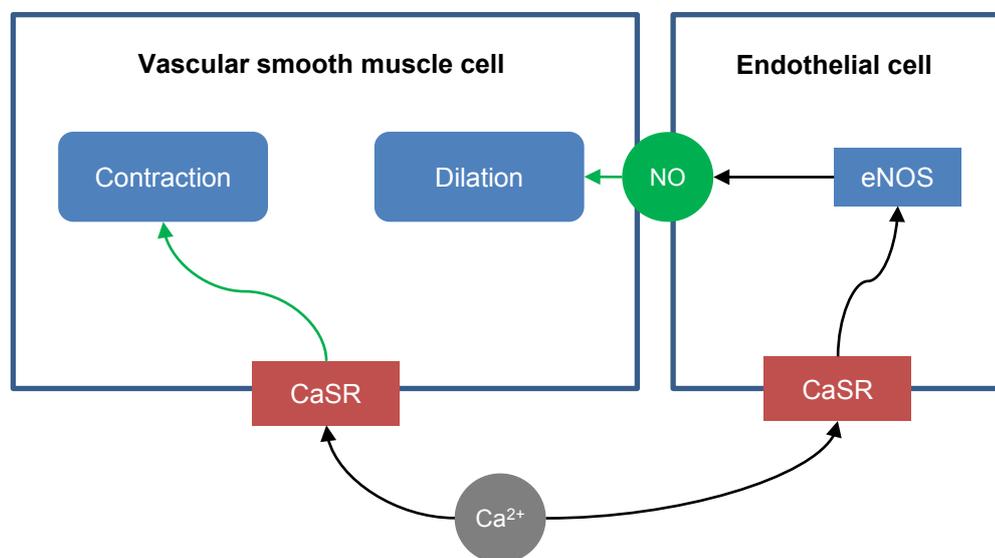


Figure 84: Simplified model of balanced CaSR action on VSMC and the endothelium. Green arrows indicate activation and black arrows indicate Ca^{2+} pathways. The VSMC CaSR directly elicits contraction in VSMC while the endothelial CaSR activates NO oxide production leading to dilation. Loss of VSMC CaSR in SM22 α -Cre x LoxP-CaSR mice leads to an increase in NO dependant dilation and thus reduced blood pressure.

However, this model is likely to be an oversimplification. While it can explain the effects I have described here to a certain extent, CaSR interaction with vascular contraction and dilation is very probably exceedingly more complex, as demonstrated by the numerous, partly contradictory effects of the CaSR on isolated blood vessels and blood pressure, as detailed in the introduction and reviewed by (Smajilovic et al. 2011). Loot and colleagues have recently found that murine blood vessels, in which the CaSR was inhibited via calcilytics, showed attenuated contraction in response phenylephrine as well as high K^+ induced blood vessel

contractions. This is in agreement with our findings. In addition, Loot and colleagues also reported that blood vessels from animals fed a high fat diet showed also attenuated responses to phenylephrine which they attributed to increased cleavage of the VSMC CaSR by calpain during metabolic stress (Loot et al. 2013).

Importantly, phenylephrine and K^+ evoked contractions are driven by influx of extracellular Ca^{2+} . This extracellular Ca^{2+} is then transported out of the VSMC and into the interstitium where it can again activate the CaSR (Hofer and Brown 2003; Loot et al. 2013). This autocrine self-amplifying pathway of VSMC contraction via the CaSR is then lost when mice blood vessels are treated with calcilytics (Loot et al. 2013). Indeed, loss of this mechanism in VSMC, together with increased or even unchanged NO production could explain the reduced, NO dependent, VSMC contractility in the SM22 α -Cre x LoxP-CaSR mouse. Furthermore, Ca^{2+}_i transported out of the cell could activate CaSR present on endothelial projections in the myo-endothelial space (Dora et al. 2008), thus acting as in a negative feedback loop against VSMC contraction, providing a possible explanation for assumed increased NO levels in KO mice as cause for reduced vascular tone, which could explain the restored contractility of KO aortas and blood pressure when subjected to L-NAME. In KO animals, adrenergic stimulation would still lead to increased levels of Ca^{2+}_i which would be removed from the VSMC. However, because of the lack of a VSMC CaSR, no potentiation of the contraction would occur while the still functional endothelial CaSR would react with increasing NO production to the elevated Ca^{2+}_i levels in the myo-endothelial space. Figure 85 shows this proposed signalling mechanism. Extensive molecular biological work combined with mice with targeted CaSR deletion from the endothelium will be needed to investigate this hypothesised signalling mechanism.

The contribution of NO mediated reductions in dilation warrants further investigation on the role of the endothelium in the SM22 α -Cre x LoxP-CaSR mice by measuring circulating NO levels, eNOS expression and activity, as well as a thorough investigation in the role of the endothelial CaSR, potentially via a mouse model of targeted gene deletion, e.g. using the angiotensin receptor Tie-2 promoter for driving Cre recombinase (Kisanuki et al. 2010), which would also allow the generation of a VSMC – endothelium double knock out mouse.

In conclusion, I propose that the CaSR in VSMC counteracts NO-mediated reductions in blood vessel tone, possibly via a direct contribution to VSMC contraction via auto- / paracrine potentiation of Ca^{2+} dependent contractions. The loss of this potentiating mechanism is

responsible, or at least contributes, to the observed hypotension in the SM22 α -Cre x LoxP-CaSR mouse.

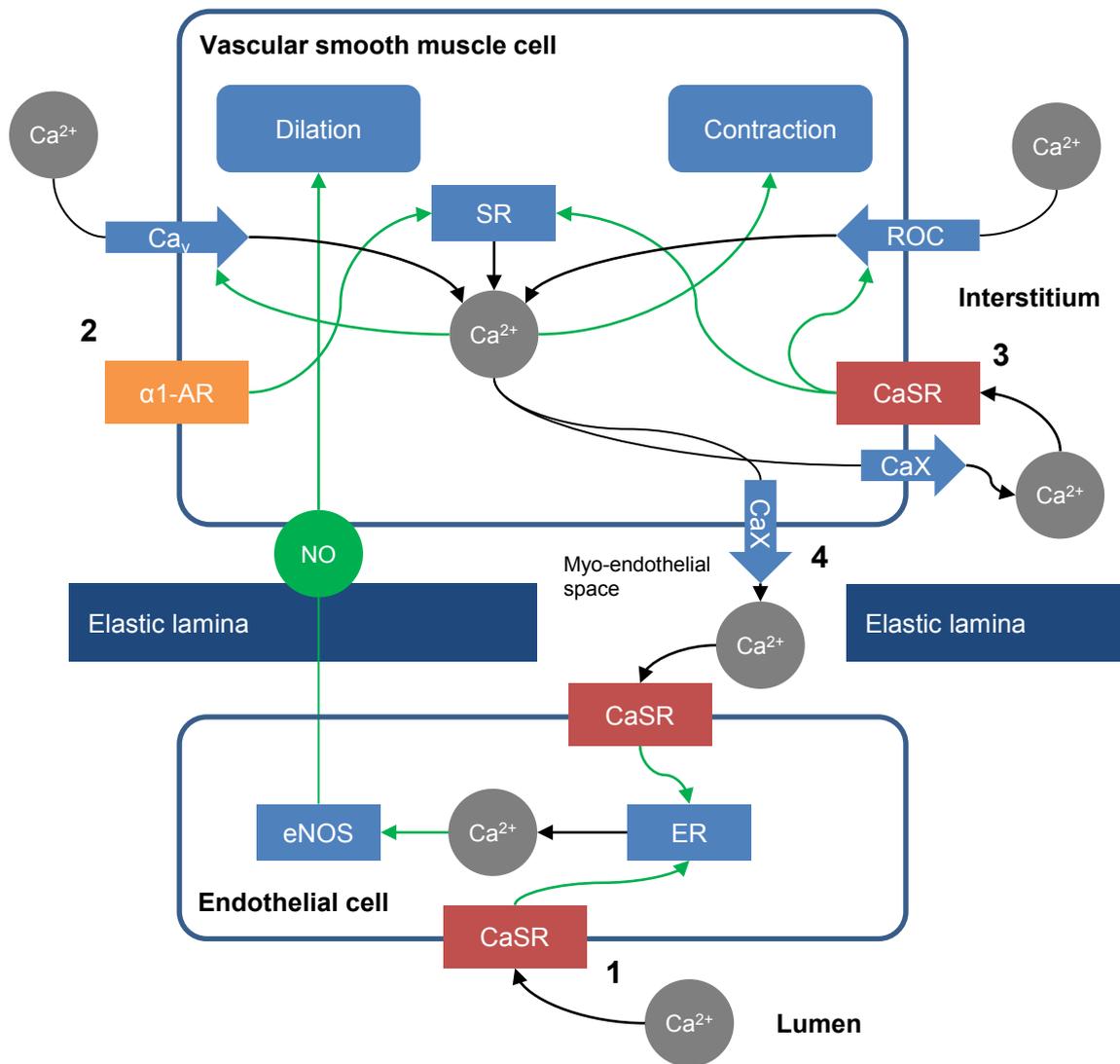


Figure 85: Proposed mechanism of the CaSR in VSMC and endothelial cells. Green arrows indicate activations; black arrows indicate Ca²⁺ pathways. (1) Ca²⁺ activates the endothelial CaSR, leading to increased Ca²⁺_i levels through release from the endoplasmic reticulum (ER) which in turn activates NO production via eNOS which diffuses into VSMC promoting dilation (Ziegelstein et al. 2006). (2) Adrenergic stimulation via α1-adrenoreceptors (α1-AR) leads to increased Ca²⁺_i levels via Ca²⁺ release from the sarcoplasmic reticulum (SR) leading to depolarisation and activation of voltage gated Ca²⁺ channels (Ca_v) and subsequent contraction. Ca²⁺_i is then removed from the cell via various mechanisms (CaX), including the Na-Ca-exchanger and Ca²⁺-ATPase, into the interstitium (3) where it can act on CaSR which in turn activates TRPC receptor activated Ca²⁺ channels (ROC) (Chow et al. 2011) and releases Ca²⁺ from the SR leading to potentiated contraction (Loot et al. 2013). Ca²⁺_i is also removed into the myoendothelial space where it can activate CaSR on endothelial projections (Dora et al. 2008) again promoting NO production. Note that this schematic does not include alternative proposed signalling mechanisms of EDH, i.e. K⁺ clouds or hyperpolarisation transfer via gap junctions (Weston et al. 2005) nor the influence of perivascular nerves. This signalling mechanism was devised with the help of Dr. Polina Yarova and is based on ideas proposed in (Loot et al. 2013).

7.3.9 Cardiac remodelling

No cardiac remodelling was visible in hearts from 12 month old animals irrespective of genotype. However, at 14 months of age, cardiac remodelling was observed in five out of eleven investigated hearts of KO mice, while no remodelling was found in hearts of WT mice. As an age difference of only 2 months is probably not likely to elicit such a marked increase in remodelling, and seeing that only less than half of the 14 month old animals presented with cardiac remodelling, it is possible that the effect was just missed in the 12 month old animals because only 3 mice of each genotype were investigated.

The remodelled hearts were immediately apparent in the long axis scans, where the apical left ventricular cavity was closing up completely during systole, while appearing normal during diastole. In 3D reconstructions, this was seen as a marked change in the shape of the left ventricular cavity exhibiting a funnel-like appearance. Based on this visual observation, the hearts were divided into three groups, hearts from WT mice, non-remodelled KO hearts and remodelled KO hearts. In the cardiac parameters, the remodelling presented itself with (borderline non-significantly) decreased LV-EDV and LV-ESV, in combination with significantly increased LV-EF, while LVM, SV, PFR and PER were unchanged between all three groups. The remodelling index is a relatively new parameter to assess changes in heart geometry in relation to function (De Castro et al. 2007). DRI and SRI were both significantly increased in remodelled KO animals compared to WT control, expressing the striking visual change into comparable numbers. Compared with published values in the literature on 12 month old C57/B110 mice, LV-EDV and LV-ESV of WT mice were lower (by about 10-13 μ l) while EF was elevated by about 5 % (Stuckey et al. 2012). However, these differences can probably be attributed to differences in mouse strain, age and detection method.

Importantly, when re-analysing for wall thickness in the WT and KO hearts from the 14 month age group, Mr Peter Edwards, an undergraduate student working in our laboratory, found that wall thickness appears to be generally increased in hearts from KO mice compared to WT control, even in the non-visibly remodelled KO group (Peter Edwards, personal communication). This indicates beginning remodelling in all KO mice with some presenting an exacerbated phenotype pointing to individual differences in the susceptibility for development of cardiac remodelling or of the mice which at the moment cannot be explained.

Probably the most unexpected feature of the visibly remodelled KO hearts was the increased EF, resulting from the respectively greater reduction in systolic than diastolic volume

compared to WT mice. Classical cardiac remodelling as a marker of heart failure is generally associated with reductions in EF caused by reduced inotropy (Klabunde 2005), while increased EF is associated with cardiac health. At the same time, SV was equal across all genotypes. In the telemetry studies on 3 month old animals, KO mice were shown to have markedly reduced heart rate. If this difference in heart rate persists in 14 month old animals, this could be indicative of lower CO in KO animals compared to WT. The fact that EF is increased in the KO could thus be interpreted as a compensating increase in inotropy, which is also suggested by the increased dp/dt values in the telemetry experiments (although again on different age groups) possibly in response to lower blood pressure. However, tail cuff measurements of 14 and 17 month old animals failed to detect a significantly reduced blood pressure in these mice.

7.3.9.1 Possible change in inotropic response

The underlying cause for the cardiac remodelling could be a compensatory response in form of increased inotropy (but not chronotropy) of the hearts in KO mice to the reduced blood pressure which develops over time and possibly in an individual specific manner. Supporting the notion of an acquired cardiac phenotype, Dr. Thomas Davies has shown that while heart weights of 6 month old animals did not differ, hearts of 18 month old animals were significantly heavier than hearts from age matched WT control (Davies 2013). A higher inotropy in hearts from KO mice is supported by the general increase in dp/dt observed in KO mice compared to WT control. This increase in inotropic contraction in the KO hearts could also be a function of the hypercalcaemia present in these mice, as elevated Ca^{2+}_o causes increased contractile force of the heart. This relationship has been shown for hypercalcaemic hyperparathyroidism patients before and it subsided after parathyroidectomy (Otto et al. 2003).

7.3.9.2 Possible deletion of the CaSR from the heart

Hypotension, presented together with cardiac remodelling, is uncommon but has been reported previously (Wang et al. 2010; Schreier et al. 2013). Interestingly, in one of the studies the observed cardiac hypertrophy was caused by knocking out the epidermal growth factor receptor EGFR (a receptor tyrosine kinase) from VSMC and cardiomyocytes using the

SM22 α -Cre mouse for target specific ablation. EGFR KO mice also showed a phenotype of reduced diastolic and mean arterial blood pressure through reduced TPR, although those SM22 α -Cre x LoxP-EGFR mice, in contrast to the SM22 α -Cre x LoxP-CaSR mouse, had a much higher mortality than WT control and more severe cardiac remodelling (Schreier et al. 2013). These results act as a reminder that the SM22 α -Cre promoter is not fully target specific for VSMC. SM22 α is also expressed transiently in the heart (and other cells of myogenic lineage) of mouse embryos (Li et al. 1996a), and possibly the adult heart (Lepore et al. 2005), which suggests deletion of the CaSR from cardiac tissue.

The CaSR is expressed in various cell types in the heart (Wang et al. 2003; Klein et al. 2008), though like in VSMC cells, its roles there are not yet fully understood. However, several studies strongly point towards a protective role for the cardiac CaSR against cardiac remodelling which would be in-line with the increased prevalence in cardiac remodelling observed in the hearts of SM22 α -Cre x LoxP-CaSR mice.

In vitro, expression of the receptor has been demonstrated in cultured neonatal rat cardiomyocytes (Tfelt-Hansen et al. 2006) where it has been suggested to promote apoptosis (Sun et al. 2006; Qi et al. 2013) and in a recent study, the cardiac CaSR has been found to be associated with the promotion of proliferation of cardiac fibroblasts (Zhang et al. 2014). Indeed, in this study, although performed on cells grown from aortic explants, cells derived from KO aortae showed increased cell density and reduced levels of apoptosis, the latter not being the case when adjusted for VSMC only (see chapter 12.1). *In vivo*, the cardiac CaSR has been implicated in protecting the cardiac tissue from ischemic preconditioning (Sun and Murphy 2010) and diabetic cardiomyopathy (Bai et al. 2012; Qi et al. 2013). Importantly, in a model of uremic rats, treatment with the calcimimetic R-568 attenuated cardiac fibrosis and the expression of hypertrophy and fibrosis marker proteins although left ventricular mass remained unchanged (Mizobuchi et al. 2011). These results show that complete ablation of the CaSR from the heart could have a profound influence on cardiac function and structure.

I also speculate that, if the VSMC CaSR directly contributes to VSMC contractility, possibly via autocrine potentiation of Ca²⁺ dependant contractions (see above and (Loot et al. 2013)), a similar mechanism might exist in the heart and the observed reduction in heart rate could be a direct result of CaSR deletion in the cardiomyocytes, which might be independent of the discovered role of the CaSR in vascular tone regulation. On the other hand, this would

probably associate with reduced inotropic responses as well, which argues against that hypothesis.

7.3.9.3 Systemic influences

Apart from a direct effect of CaSR deletion on heart tissue and cardiomyocytes, it is conceivable that cardiac remodelling could even be a direct effect of CaSR deletion from coronary blood vessels, e.g. by reduced tone and therefore blood supply. Alternatively cardiac remodelling could also be caused by the chronic exposure of the mice's hearts to elevated FGF23 levels that were observed in 3 and 18 month old mice. FGF23 was shown to induce left ventricular hypertrophy independently of its renal co-factor klotho in isolated rat cardiomyocytes, in mice intracardially injected with FGF23 as well as in klotho-deficient mice which have upregulated systemic levels of FGF23 (Faul et al. 2011).

Furthermore, the striking changes in the mineral ion metabolism of the mice could play a role in the development of the cardiac remodelling. As argued in the following chapter, the mice present a phenotype resembling primary hyperparathyroidism. Primary hyperparathyroidism can be, but does not have to be associated with cardiac hypertrophy (Stefenelli et al. 1993; Farahnak et al. 2010; Walker et al. 2010). However, hypertrophy is commonly attributed to the increased blood pressure and calcifications (Stefenelli et al. 1993) while the KO mice are, due to decreased vascular contractility, hypotensive and show no ectopic calcifications. Other studies have inferred that PTH itself could be the cause for left ventricular remodelling (Schiffl and Lang 2011) although in the light of the results by Faul and colleagues, it is possible that indeed FGF23 is the main factor in cardiac hypertrophy in primary hyperparathyroidism.

7.3.9.4 Future prospects

To determine if the observed changes in remodelled KO hearts are indeed caused by ventricular remodelling, we will have to perform histological examination of mouse hearts specifically aimed at detecting markers of fibrosis and hyperplasia.

Irrespective of all these possibilities, it should be emphasised that the results obtained from the cine-MRI studies produced somewhat ambiguous results (no remodelling of KO hearts at

12 months, remodelling in 5 out of 11 investigated hearts at 14 months). On the other hand, heart rate was consistently reduced in younger animals, suggesting that the reduction in heart rate takes precedence over a possibly long-term acquired cardiac remodelling.

Further studies with additional methods to assess cardiac function are therefore necessary in the future. Indeed, at the time of the submission of this thesis, talks on collaboration to achieve these ends are already in progress. In all likelihood, *ex vivo* Langendorff experiments on isolated hearts from WT and KO animals will be performed in collaboration with Prof. Kenneth Broadley (Cardiff University) for precise measurement of innate heart contractility and frequency of WT and KO mice, thus allowing us to answer the question if the hearts from the SM22 α -Cre x LoxP-CaSR mice are intrinsically different from their WT counterparts. In addition, we are discussing the possibility of performing high frequency echocardiography in collaboration with Dr. Rene Botnar, (Kings College, London, UK) which will allow determination of CO *in vivo* and thus the contribution of their cardiac phenotype to the hypotension observed in KO mice. Finally, electrophysiological experiments on isolated cardiomyocytes should be performed to allow the assessment of contractility and ion channel expression in these cells.

As already mentioned, to dissect the direct influences of the VSMC CaSR on the heart as well as the vasculature and blood pressure from putative systemic influences, generation of a SM22 α -Cre x LoxP-CaSR – 1- α -Hydroxylase^{-/-} mice, which could rescue the phenotype of extensive changes in mineral ion metabolism (see next chapter) could be revealing.

7.4 Conclusions

- *The VSMC CaSR is involved in blood pressure regulation; SM22a-Cre x LoxP-CaSR KO mice show reduced blood pressure which can be attributed to impaired arterial contractility (reduced TPR) and possibly reduced heart rate, but not the RAAS.*
- *Inhibition of NO synthesis restores blood pressure in KO mice and contractility in isolated aortic rings. The VSMC CaSR therefore has a direct contractile effect on blood vessels which counterbalances NO induced dilation.*
- *Sporadic cardiac remodelling and reduced heart rate in KO animals could be caused by a compensatory effect to the hypotension, direct CaSR deletion from cardiac tissue, influence of chronic exposure to high FGF23 levels or changes in the cardiac vasculature. Further studies are required to elucidate the cardiac function of the SM22a-Cre x LoxP-CaSR mouse.*

8 Effect of VSMC specific CaSR deletion on metabolism and mineral ion homeostasis

8.1 Introduction

In this chapter, I describe metabolism and mineral ion homeostasis in the SM22 α -Cre x LoxP-CaSR mouse.

Metabolism of the mice was assessed using metabolic cage studies when the mice either fed a standard or a high salt (containing 4 % (w/w) NaCl) diet. The mice of these experiments were subsequently used for telemetry analysis of their blood pressure, allowing measuring the influence of the high salt diet on metabolism together with blood pressure. As already described in the previous chapter, high salt diets are generally recognised to induce hypertension and, although this effect can take weeks to manifest itself in mice (Gros et al. 2002), it can be useful short-term to determine a NaCl-sensitive phenotype (Carlson et al. 2002). The high salt diet in the context of the analysis of food and water metabolism can also be seen as a test for renal function.

The CaSR has been shown to be expressed all along the gastrointestinal tract where it acts as nutrient sensor (Brennan et al. 2014), and is also expressed in the small and large intestines (Chattopadhyay et al. 1998) where it is involved in the inhibition of fluid and Cl⁻ secretion (Cheng et al. 2002) induced by natural secretagogues as well as bacterial enterotoxins (Geibel et al. 2006). This anti-secretory effect seems to be elicited through a combination of direct action on epithelial cells as well as through an influence on the intestinal nervous system (Cheng 2012). A knock-out study using the same LoxP-CaSR mouse as in this study, revealed a role for the colonic epithelial CaSR in controlling cell proliferation and maintenance of crypt structure possibly via wnt/ β -catenin signalling (Rey et al. 2012). Furthermore, CaSR localised in colonic myofibroblasts regulates epithelial differentiation (Pacheco and Macleod 2008). Since SM22 α is expressed in colonic myofibroblasts, investigation of possible gastrointestinal changes in the SM22 α -Cre x LoxP-CaSR mouse could provide further insight in CaSR mediated action of myofibroblasts. Since this study focuses mainly on the vascular roles of the CaSR, investigation of the gastrointestinal phenotype of the mice exceeding metabolic cage studies will be investigated in collaboration with Dr. Enikő Kallay and Mr. Abhishek Aggarwal (University of Vienna, Austria).

Similarly to the gastrointestinal tract, the renal / urogenital tract of the mice is of particular interest in connection with the CaSR. The CaSR has been shown to play a major role in the kidney where it is expressed in all nephron segments (Riccardi et al. 1998). The main function of the renal CaSR is by directly promoting urinary Ca^{2+} excretion by the thick ascending limb upon it sensing elevated blood Ca^{2+} levels, in concert with its role as suppressor of PTH production by the parathyroid glands, indirectly resulting in decrease urinary Ca^{2+} reabsorption. In addition, the CaSR suppresses renin release (Maillard et al. 2009), regulates PTH-inhibited phosphate reabsorption in the proximal tubule, inhibits Na^+ , Ca^{2+} and Mg^{2+} reabsorption in the thick ascending limb and Ca^{2+} reabsorption in the distal tubule and promotes urine acidification and polyuria in the collecting duct, as reviewed in (Riccardi and Brown 2010). Although these effects are elicited by CaSR expressed in renal cells, the kidney is an extremely highly vascularised organ, which makes an influence of the VSMC CaSR on renal function plausible. While an investigation of the renal phenotype of the SM22 α -Cre x LoxP-CaSR mouse is planned as part of the general characterisation of this mouse model, it was not a primary aim of this thesis. The changes in blood pressure of these mice (see chapter 7.2) implied an involvement of the kidney in this process, by controlling diuresis, TPR or both. To assess kidney function, urine production and ionic composition were assessed when the mice were fed either standard diet, or a high salt diet (containing 4 % (w/w) NaCl).

Blood and urine clinical chemistry was of particular interest in the characterisation of the SM22 α -Cre x LoxP-CaSR mouse. Blood chemical analysis included measurements of electrolytes, creatinine, blood urea nitrogen and total protein as an estimate for the animal's renal health. Furthermore, CaSR-regulated hormones involved in mineral ion homeostasis, namely PTH and 1,25-(OH) $_2$ -Vitamin D $_3$ (1,25-D $_3$) were measured. In addition, because of its role as phosphaturic hormone and in its ability to induce cardiac remodelling (Faul et al. 2011) of KO mice (see chapter 7.2.3), serum FGF23 levels were also measured.

Renin and aldosterone plasma levels were measured to investigate a potential involvement of the renin angiotensin aldosterone system (RAAS) in the observed changes in blood pressure in the SM22 α -Cre x LoxP-CaSR mice. Finally, plasma concentration of the calcification inhibitor fetuin A was measured.

Because of the involvement of the kidney and the renal CaSR in mineral ion metabolism, especially Ca^{2+} excretion, urine composition of WT and KO mice was investigated. Creatinine acts as a general marker of kidney function, as its excretion rate is exclusively tied

to glomerular filtration and can therefore be used to normalise electrolyte excretion to kidney function. Urea, total protein and uric acid levels in urine were measured as markers of kidney function and health.

Finally, the bone status of the SM22 α -Cre x LoxP-CaSR mice was assessed. As already outlined, the bone plays a major role in mineral ion metabolism as it acts as the major reservoir for Ca²⁺. The CaSR plays a major role in bone biology (Chang et al. 1999), especially in promotion of osteoblastic activation and incorporation of Ca²⁺ in the bone (Chang et al. 2008).

8.2 Results

8.2.1 Metabolic cage studies

The metabolism of 12-18 month old male WT and KO mice was investigated using metabolic cages. Monitoring over 24 hours showed an increased amount of faeces excreted by KO mice compared to WT control while there were no differences in food, water consumption and urine excretion over a 24 h period (Figure 86). By observation, faeces of KO mice had a damper appearance than faeces from WT mice. The metabolic cages used in this experiment are optimized for rat. The obtained results should therefore be interpreted with caution.

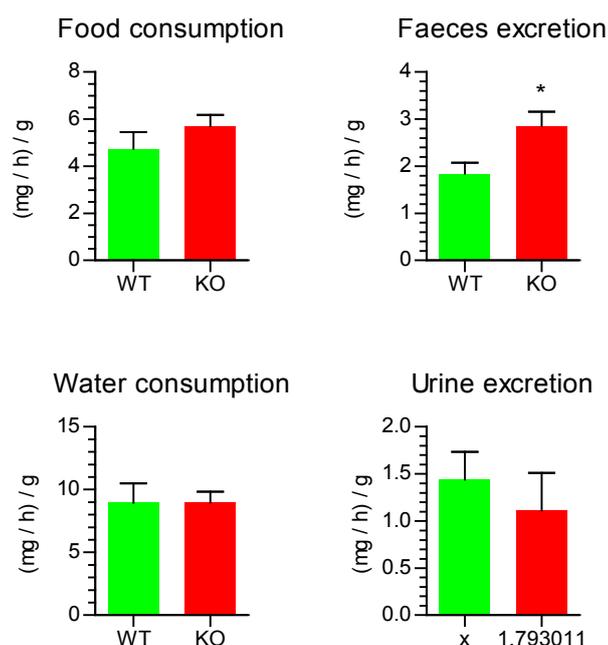


Figure 86: Metabolic cage studies of WT and KO mice. Data were normalised to daily collection periods and animal body weight. * $p < 0.05$, $N = 6$ (food consumption, faeces excretion and water consumption), 5 (urine excretion), mean + SEM, two-tailed T-test.

Additional metabolic cage studies were performed on 3 month old animals in collaboration with Prof. Robert Fenton and Dr. Vladimir Matchkov (Aarhus University, Denmark) in metabolic cages specifically designed for mice and over a period of 9 days. After 4 days, the diet of the investigated mice was changed from standard diet to a high salt (containing 4 % NaCl) diet to investigate the capabilities of the KO mice to handle high salt load in terms of blood pressure (see chapter 7.2.1) and metabolism.

Like the 12-18 month old animals, no difference in food and water consumption, nor faeces and urine excretion was observed between WT and KO animals while they were fed a standard diet. Levels of food consumption rose during the first two days but remained stable afterwards which can be attributed to the mice not adjusting to their new environment in the metabolic cages. When the diet was changed to a high-salt (containing 4% NaCl) diet, food consumption and faeces excretion remained unchanged compared to the standard diet in both WT and KO animals. As expected, the high-salt diet resulted in large increase in both water consumption and urine excretion in mice of both genotypes. On the high salt diet, KO mice showed a significantly higher urine excretion than WT mice. See Figure 87 for traces and Figure 88 for direct comparisons between diets and genotypes.

All numerical results of the metabolic cage studies are listed in Appendix A, Table 25.

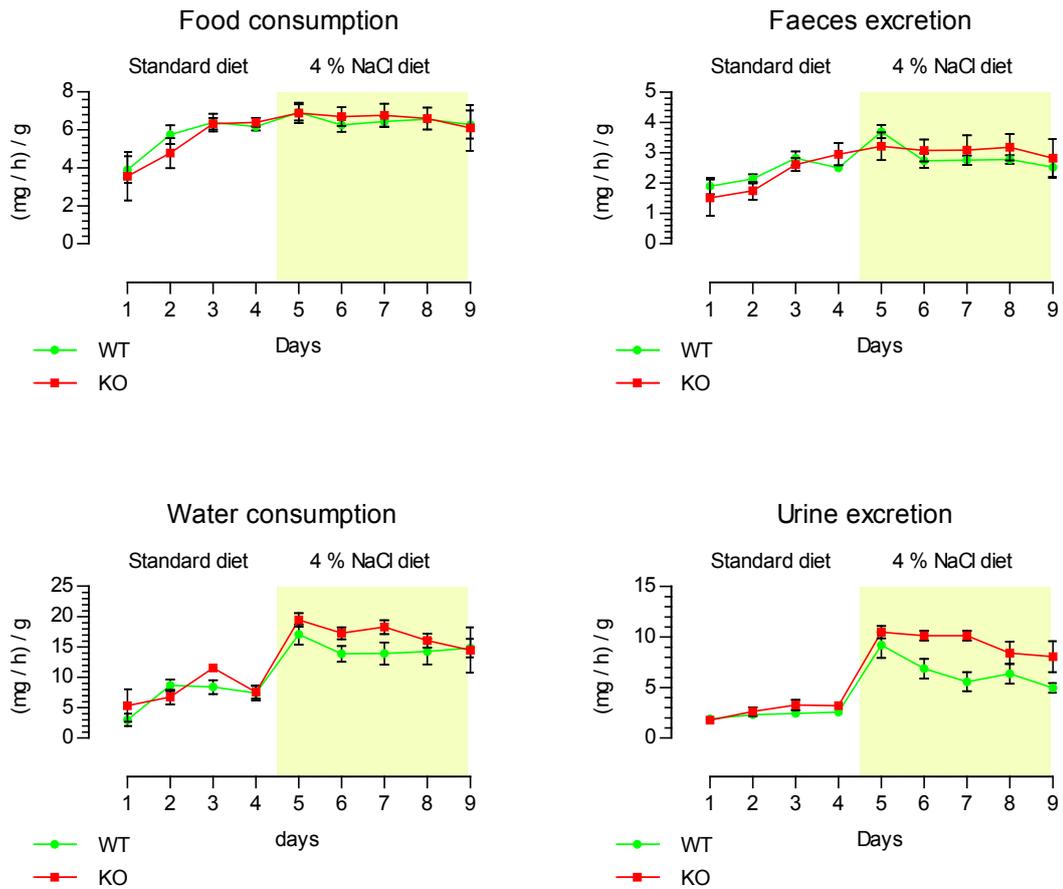


Figure 87: Metabolic cage studies of 3 month old male WT and KO mice. The traces show food consumption, faeces excretion, water consumption and urine excretion over a course of 9 days. Standard diet was changed to a high salt (containing 4% NaCl) diet (yellow area). Data were normalised to daily collection periods and animal body weight.

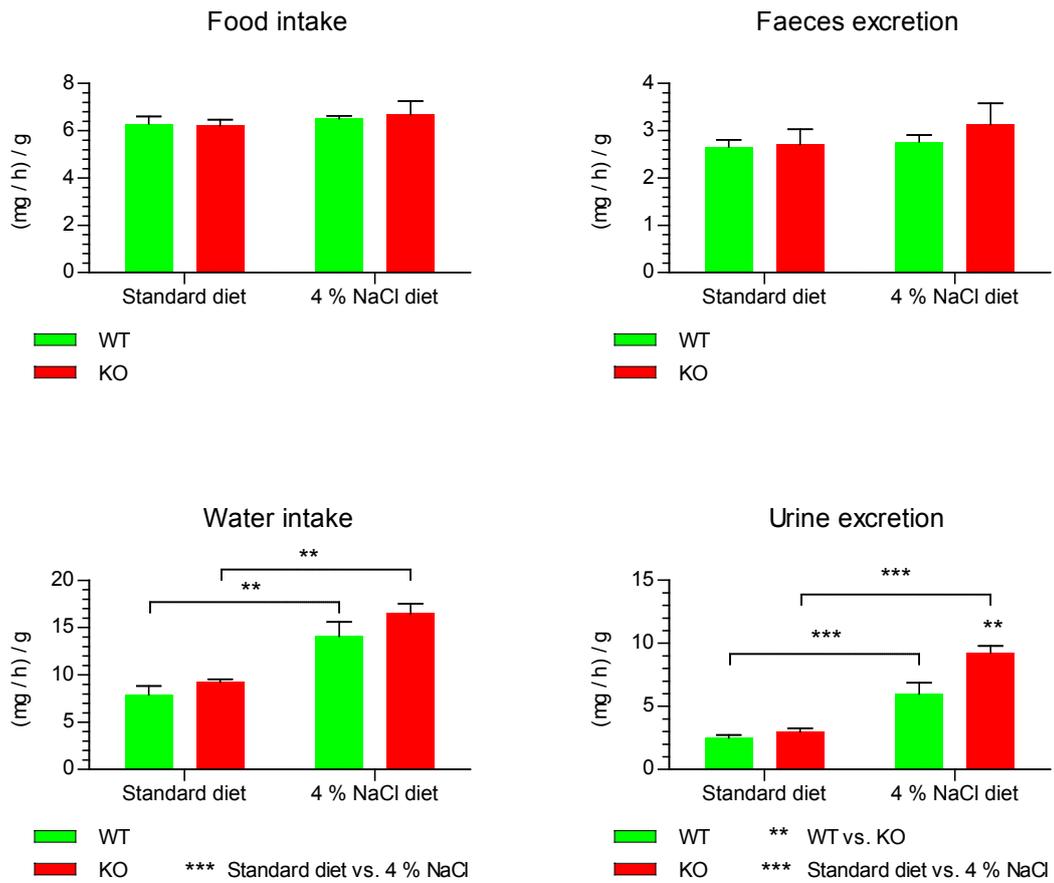


Figure 88: Metabolic cage studies of 3 month old male WT and KO mice. Comparisons between averages of data for standard diet vs. 4 % NaCl diet are shown (see Figure 87). Data were normalised to daily collection periods and animal body weight. ** $p < 0.01$, *** $p < 0.001$, $N = 6$ per genotype, mean + SEM, two-way ANOVA with Bonferroni post-test

8.2.2 Clinical chemistry

8.2.2.1 Blood

Serum of 3 (Figure 89) as well as 18 month (Figure 90) old KO mice showed a significant increase in Ca^{2+} levels control ($p < 0.01$ and $p < 0.05$ respectively). As the samples showed some haemolysis, K^+ levels are not reported. Mg^{2+} , Na^+ and Cl^- levels did not differ between the genotypes. FGF23 levels were significantly increased in 3 (Figure 91) as well as 18 month old KO animals (Figure 92) compared to WT control ($p < 0.01$ and $p < 0.05$ respectively).

Plasma from a further batch of 3 month old mice was analysed for the concentrations of biomarkers for calcium metabolism, kidney function and protection from calcification. PTH (intact PTH) levels showed a slight increase in KO mice compared to WT control, although this difference was not significant and the mice showed a high variability in PTH levels independent of genotype. 1,25-D3 levels were significantly elevated ($p < 0.01$) in KO mice compared to WT control, showing an about two-fold increase. No differences were found in renin and aldosterone level, as well as pyrophosphate and fetuin A levels between WT and KO mice (Figure 93).

Clinical chemistry results from plasma of the 3 month old male mice used for telemetry and metabolic cage analysis in collaboration with Prof. Robert Fenton and Dr. Vladimir Matchkov (University of Aarhus, Denmark) are reported separately, as it was obtained following 2 days of the mice being fed 0.5 mg / ml L-NAME in their drinking water. Na^+ and creatinine levels showed a significant ($p < 0.05$) reduction in KO mice compared to WT. In good agreement with the previously obtained results, Ca^{2+} levels were highly significantly ($p < 0.001$) elevated in these mice. Plasma Pi concentration showed a non-significant trend towards reduction in the KO mice compared to WT ($p = 0.0679$), which is in agreement with hypophosphataemia in the same mice reported to us from our collaborator Prof. Wenhan Chang (personal communication). K^+ , Cl^- , Mg^{2+} , blood urea nitrogen and total protein levels were unchanged between WT and KO mice (Figure 94).

Numerical values for all clinical chemistry blood analyses are listed in Appendix A, Table 26.

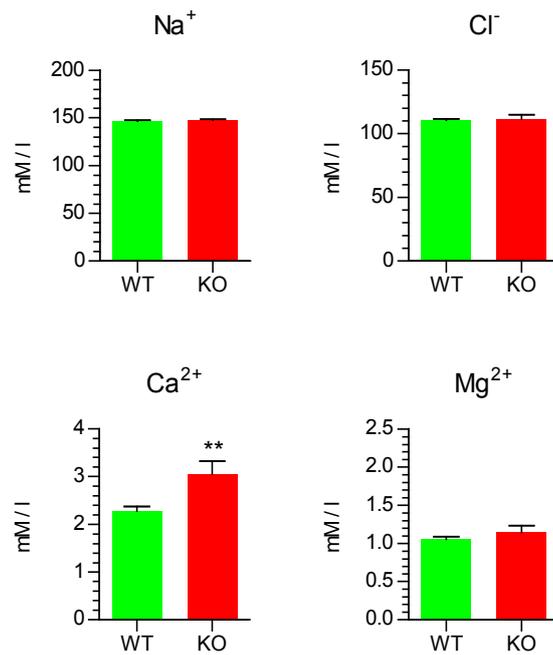


Figure 89: Electrolyte analysis of sera collected from 3 month old WT and KO mice. ** $p < 0.01$, $N = 11$ (WT), 4-6 (KO), mean + SEM, two-tailed T-test.

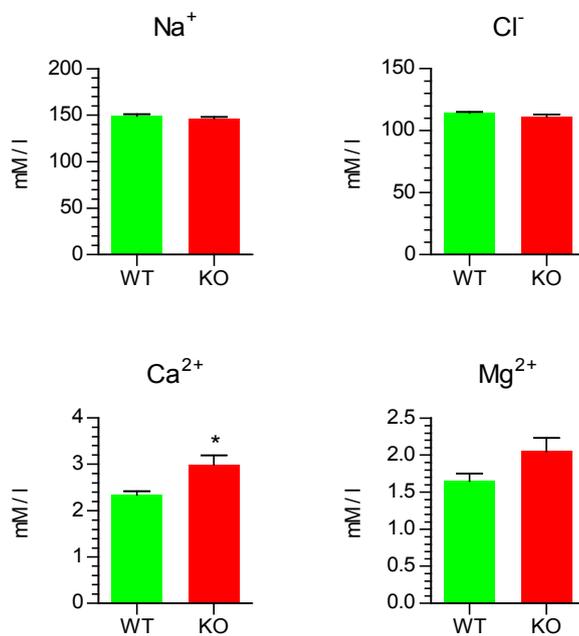


Figure 90: Electrolyte analysis of sera collected from 18 month old WT and KO mice. * $p < 0.05$, $N = 3$, mean + SEM, two-tailed T-test.

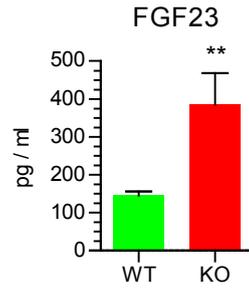


Figure 91: FGF23 levels of sera collected from 3 month old WT and KO mice. ** $p < 0.01$, $N = 11$ (WT), $N = 6$ (KO), mean + SEM, two-tailed T-test.

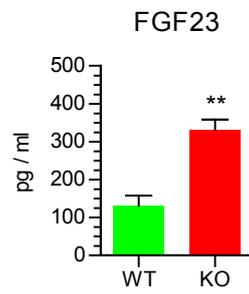


Figure 92: FGF23 levels of sera collected from 18 month old mice. ** $p < 0.01$, $N = 3$, mean + SEM, two-tailed T-test.

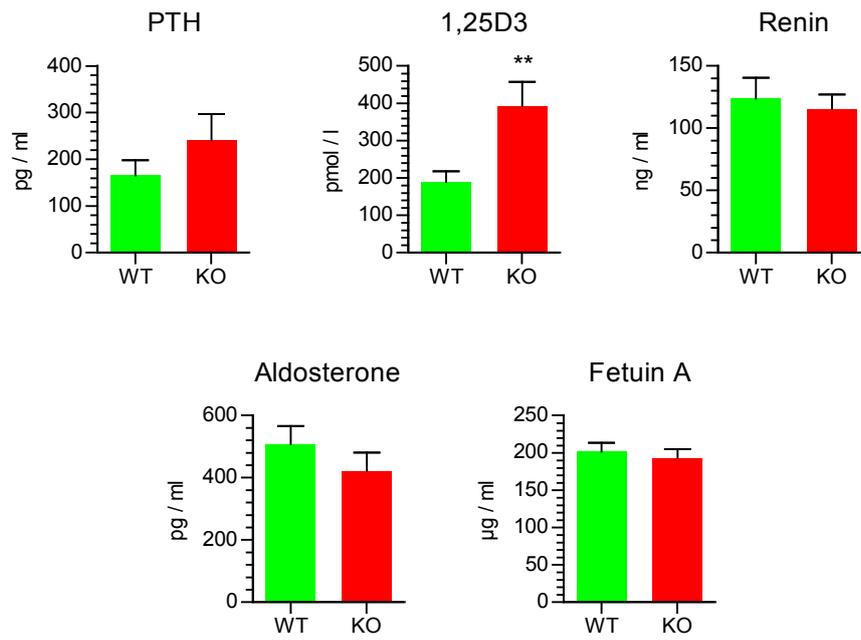


Figure 93: PTH, 1,25-D3, renin, aldosterone and fetuin A levels of plasma collected from 3 month old male WT and KO mice. ** $p < 0.01$, $N = 12$ (WT), $N = 12$ (KO), mean + SEM, two-tailed T-test.

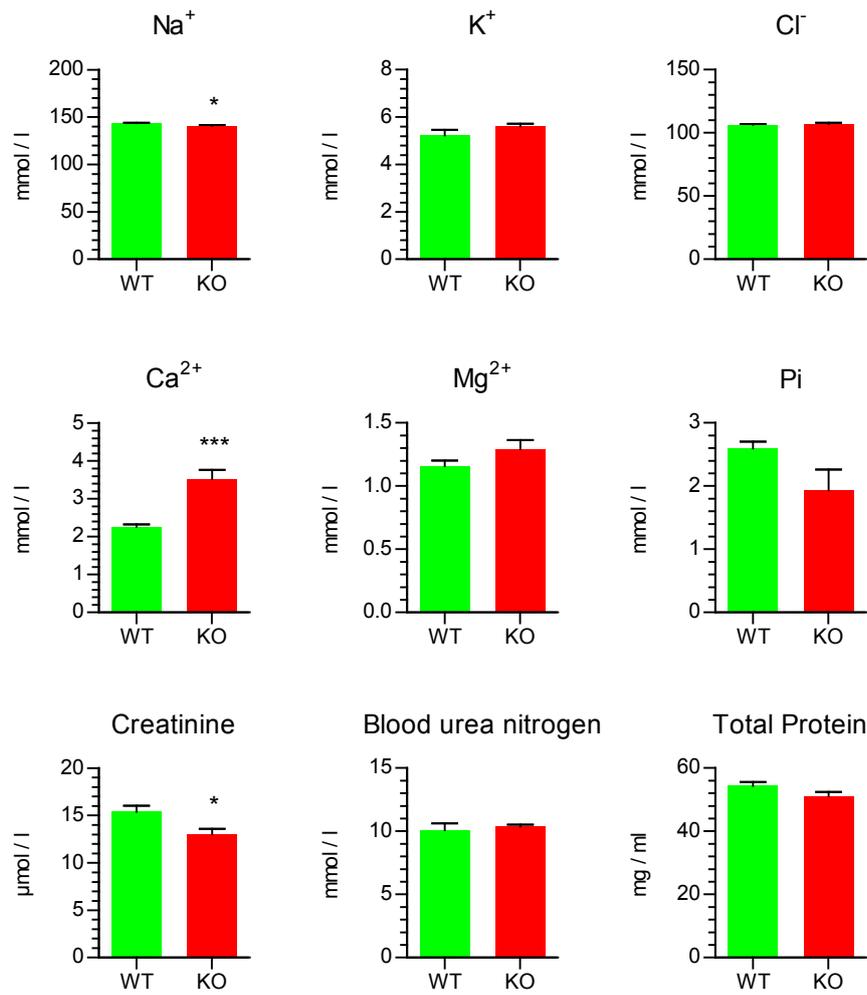


Figure 94: Electrolyte, creatinine, blood urea nitrogen and total protein levels of sera collected from male WT and KO mice following metabolic cage studies and 2 days of 0.5 mg / ml L-NAME (drinking water) administration. * p < 0.05, *** p < 0.001, N = 6, mean + SEM, two-tailed T-test.

8.2.2.2 Urine

Urine of the 3 month old male mice used for telemetry and metabolic cage studies (see 8.2.1) was analysed. 24 h urine collections were performed while the animals were fed standard diet or a high salt diet containing (4 % (w/w) NaCl. Electrolyte concentrations are reported as ion:creatinine ratio (abbreviated as ion:Cr), other clinical urine biomarkers (creatinine, total protein, urea and uric acid) are reported as excreted amount per day and total body weight (TBW).

When fed standard diet, urine of WT and KO animals showed no differences in $\text{Na}^+:\text{Cr}$, $\text{K}^+:\text{Cr}$, $\text{Cl}^+:\text{Cr}$ and $\text{Mg}^{2+}:\text{Cr}$. $\text{Ca}^{2+}:\text{Cr}$ and $\text{Pi}:\text{Cr}$ were both highly significantly ($p < 0.001$) elevated in KO animals compared to WT. On the high salt diet, electrolyte excretion generally increased in animals of both genotypes compared to the standard diet, with $\text{Na}^+:\text{Cr}$, $\text{Cl}^+:\text{Cr}$, $\text{K}^+:\text{Cr}$, and $\text{Pi}:\text{Cr}$ showing a highly significant ($p < 0.001$) and $\text{Ca}^{2+}:\text{Cr}$ and $\text{Mg}^{2+}:\text{Cr}$ a significant increase ($p < 0.05$). On the high salt diet, in addition to the persisting large elevation in KO mice of $\text{Ca}^{2+}:\text{Cr}$ and $\text{Pi}:\text{Cr}$ compared to WT control which was already seen on the standard diet ($p < 0.001$), $\text{K}^+:\text{Cr}$ as well as $\text{Mg}^{2+}:\text{Cr}$ of KO mice were highly significantly increased ($p < 0.01$) compared to WT animals (Figure 95).

No significant differences were found in creatinine, total protein and urea excretion irrespective of genotype or standard vs high salt diet. Uric acid excretion was significantly elevated on the high salt diet ($p < 0.01$) vs standard diet in both genotypes (Figure 96).

Numerical values for all clinical chemistry urine analyses are listed in Appendix A, Table 27.

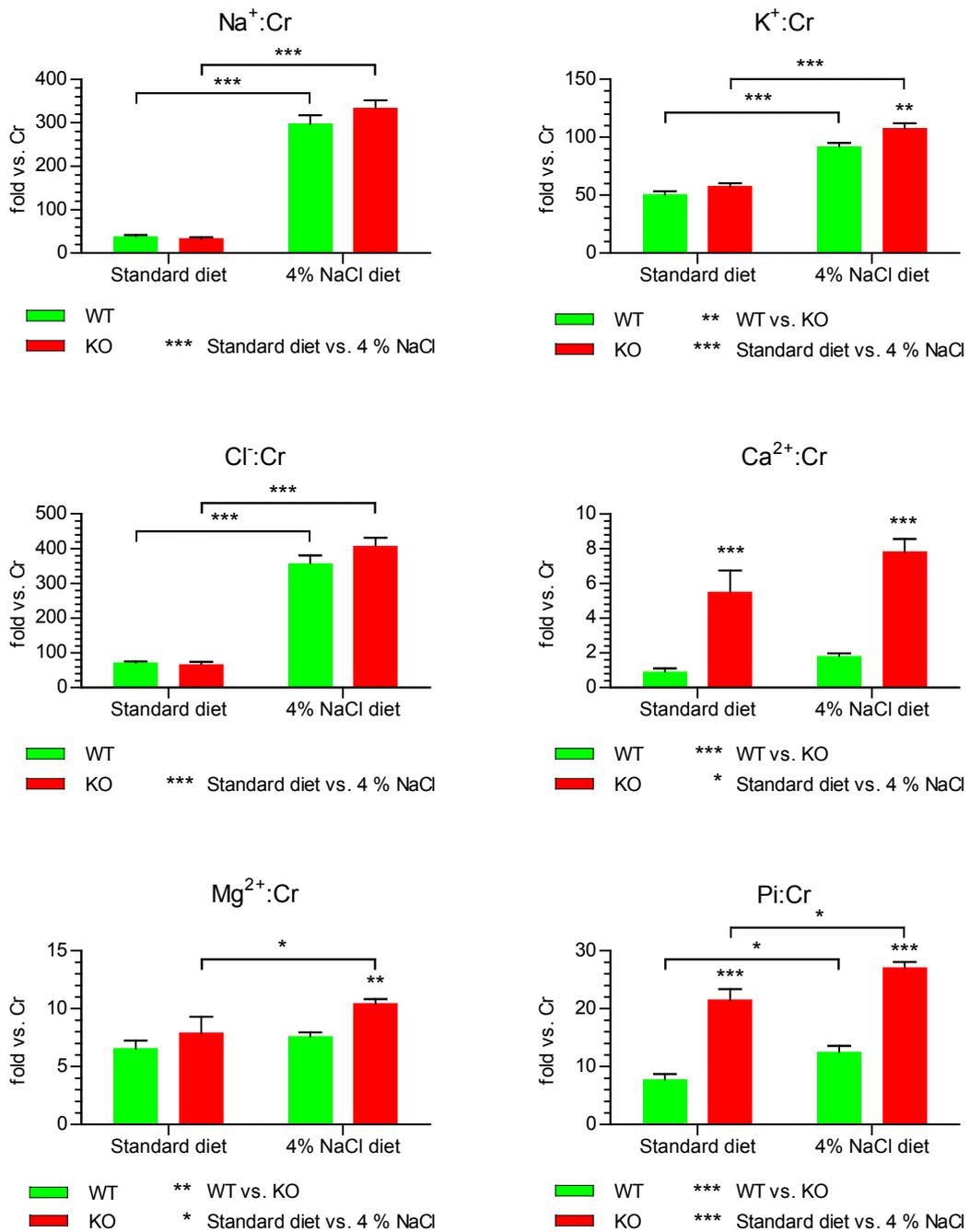


Figure 95: Electrolyte concentrations of urine from 24 h collections using metabolic cages from 3 month old WT and KO mice on standard or high salt (containing 4 % (w/w) NaCl) diet. Concentrations shown as ion:creatinine (Cr) ratio. * p < 0.05, ** p < 0.01, *** p < 0.001, N = 5-6, 4 (Mg²⁺ WT), 3 (Mg²⁺ KO), mean + SEM, two-way ANOVA with Bonferroni post-test.

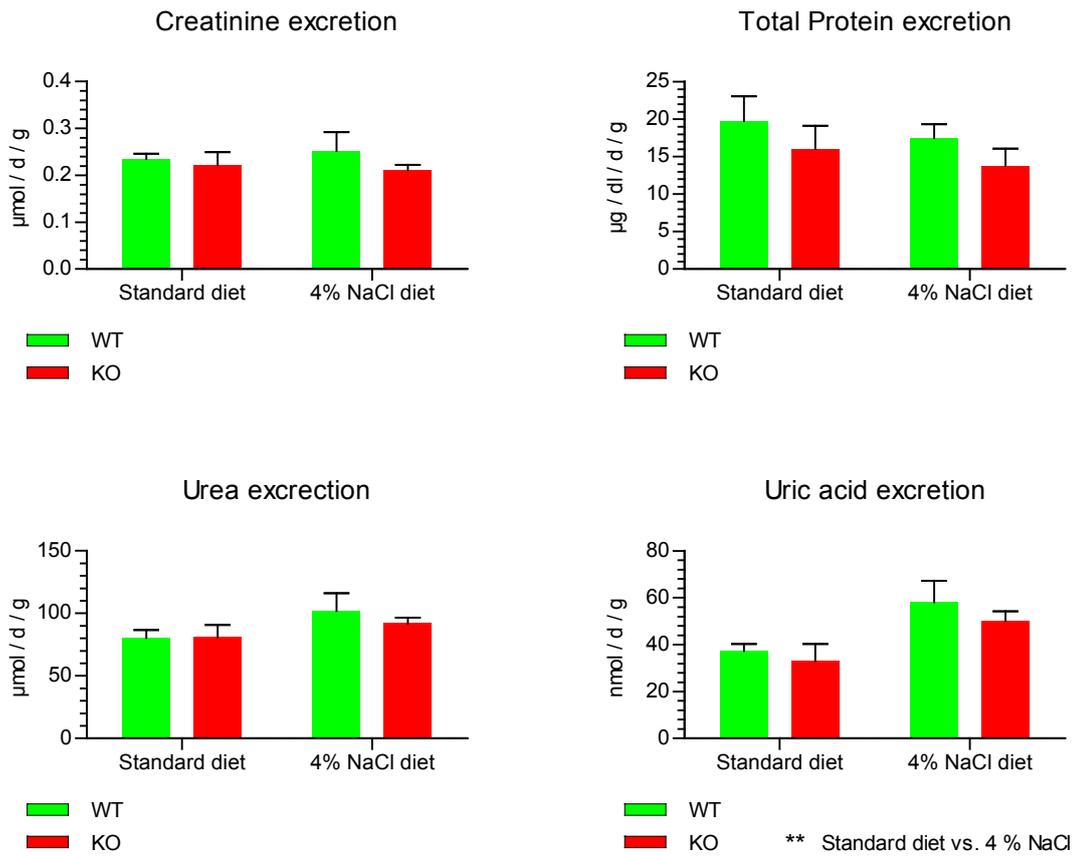


Figure 96: Clinical chemistry of urine from 24 h collections using metabolic cages from 3 month old WT and KO mice on standard or high salt (containing 4 % (w/w) NaCl) diet. Concentrations shown as excreted amount per day and TBW. * $p < 0.05$, ** $p < 0.01$, *** $p < 0.001$, $N = 5-6$, mean + SEM, two-way ANOVA with Bonferroni post-test.

8.2.3 Bone

Hind-leg bones (femur, tibia and fibia) of 3 month old WT and KO animals were analysed by μ CT by Dr. Wenhan Chang, UCSF, USA. Trabeculae of the distal femur as well as cortical bone of the tibio-femoral junction were analysed. Reductions in bone quality were indicated by significant changes in all measured femoral trabecular bone parameters (Figure 97), i.e. total volume (Tb.TV), bone volume (Tb.BV), bone volume fracture (Tb.BV/TV), connectivity density (Tb.CD), structure model index (Tb.SMI.), trabecular number (Tb.N), trabecular spacing (Tb.Sp) and trabecular bone mineral density (Tb.BMD). In cortical bone, only bone mineral density (Ct.BMD) was significantly reduced (Figure 98). Results and statistical analysis of all investigated bone parameters are reported in Appendix A, Table 28.

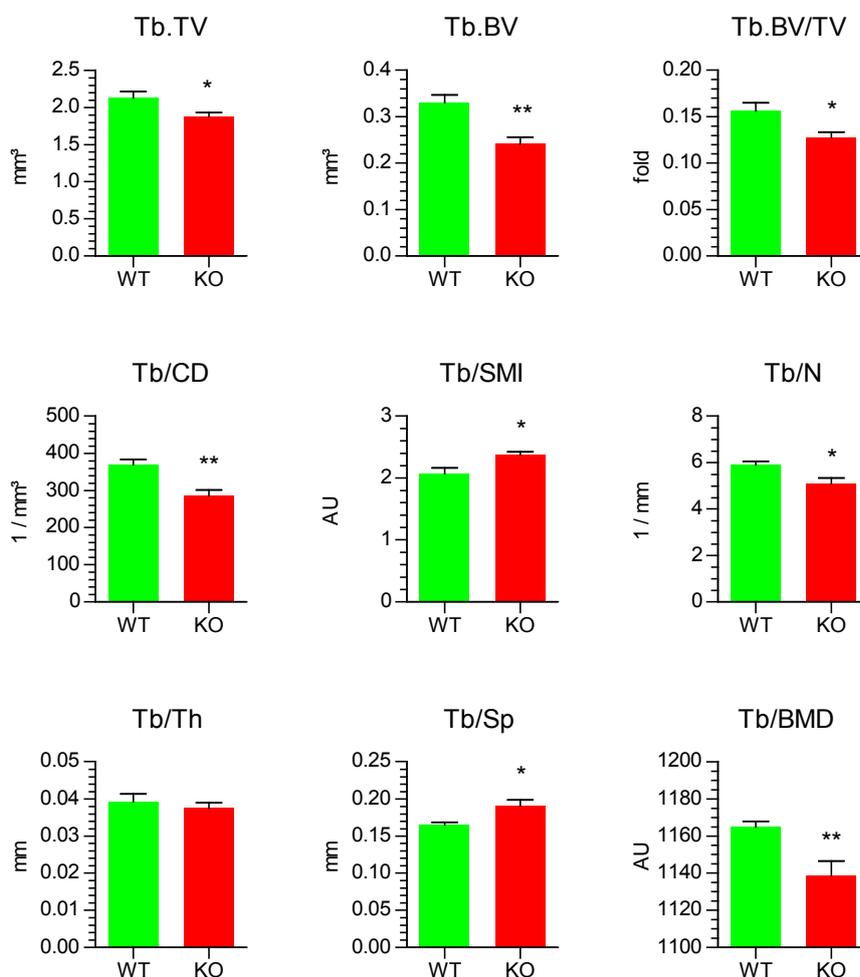


Figure 97: Bone parameters of the trabecular bone of the distal femur of 3 month old WT and KO mice as determined by μ CT. Tb = trabecular bone of distal femur, TV = total bone volume, BV = bone volume, BV/TV = bone volume ratio, CD = connectivity density, SMI = structure model index, N =

number of trabeculae, Th = trabecular thickness, Sp = trabecular spacing, BMD = bone mineral density (arbitrary units). * $p < 0.05$, ** $p < 0.01$, two-tailed T-test.

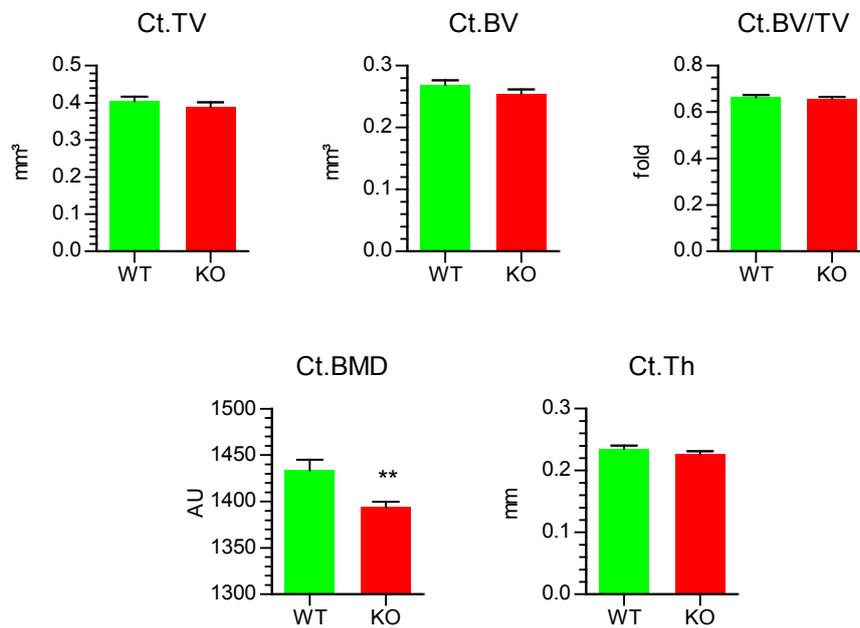


Figure 98: Bone parameters of the cortical bone of tibio-fibular junction of the distal femur of 3 month old WT and KO mice as determined by μ CT. Ct = Cortical bone of tibio-fibular junction, TV = total bone volume, BV = bone volume, BV/TV = bone volume ratio, BMD = bone mineral density (arbitrary units), Th = thickness. ** $p < 0.01$, two-tailed T-test.

8.3 Discussion

From the initial hypothesis for deletion of the CaSR in VSMC, namely the role of the VSMC CaSR in vascular calcification, we were surprised to see the large differences in mineral ion homeostasis in KO mice. The SM22 α -Cre x LoxP-CaSR presented striking differences in Ca²⁺ and Pi handling, namely a phenotype of hypercalcaemia, hypercalciuria and hyperphosphaturia, going along with changes in calciotropic and phosphaturic hormones. These changes are discussed in the following sections.

8.3.1 Food and water metabolism

Visual observation of the faecal output of SM22 α -Cre x LoxP-CaSR KO mice pointed to an increase in faecal water content, as faeces of KO mice appeared stickier by cursory observation. The metabolic cage studies on 3 month old animals showed no difference between food intake and faeces excretion between WT and KO mice, irrespective of a high salt diet suggesting that food metabolism is not influenced by VSMC specific CaSR deletion. Again, faeces of KO animals had a damper appearance than those of WT control. The CaSR is believed to modulate intestinal motility (Geibel et al. 2006). SM22 α -Cre expression in visceral smooth muscle cells of the intestine has been reported (Lepore et al. 2005). It is therefore possible that deletion of the CaSR from intestinal visceral smooth muscle cells could attribute to a potentially imbalanced water homeostasis in the gastrointestinal tract. The intestinal phenotype of these mice is currently being investigated by our collaborators Dr. Enikő Kallay and Mr Abhishek Aggarwal (Medical University of Vienna, Austria).

It has to be noted that the metabolic cages available in Cardiff University and used in the earlier study were designed for housing rats. The much smaller size of the mice resulted in the animals being able to defecate and urinate in the food container. The faeces were carefully separated from residual food but there is a very high probability that at least the gravimetric urine measurement was influenced by this systematic problem. Differences between the two age groups can therefore be attributed to the different metabolic cages these two groups of experiments were carried out in. The technical issues in the experiment with the 12-18 month old animals notwithstanding, no differences between WT and KO mice was detected in older mice which is in agreement with the results obtained in the study performed on the 3 month old animals in Denmark while on a low salt diet.

The high-salt diet (4 % NaCl) did not induce any changes in faecal output or food consumption. As expected, the high salt diet induced polyuria in WT as well as KO mice and increased water consumption in both genotypes. However, urine output was significantly more elevated in KO animals compared to WT. This can probably be attributed to the high urinary Ca^{2+} (and Pi) excretion levels of KO animals (see below). High salt induces polyuria because of the large increase in urine osmolarity, sensed by the macula dense and juxtaglomerular apparatus in the kidney, which suppresses the RAAS (Kobori et al. 2007). Because of the high concentration of ions already excreted in the KO animals, the high salt diet would increase the polyuria even more in the KO than WT animals. In light of a recent discovery by Renkema and colleagues, the observed polyuria could therefore be a protective mechanism against the formation of kidney stones, which, together with increased urinary acidification, was recently shown to be mediated by the CaSR in the collecting duct (Renkema et al. 2009).

8.3.2 Effect of L-NAME on plasma chemistry

Before discussing the results of the blood plasma analyses, it is necessary to make a point about the samples used for analysis in the second batch of plasma. This batch was collected on the last day of the telemetry experiments (see previous chapter), where animals had received the nitric oxide synthase inhibitor L-NAME for 2 days in their drinking water. L-NAME increases blood pressure through inhibition of nitric oxide production (Mattson 2001) and it is known that L-NAME induced hypertension goes along with changes in plasma and urine biochemistry due to pressure diuresis by the kidney. It was shown that blood pressure elevating concentrations of L-NAME induce increased Na^+ excretion (Lahera et al. 1991). In pregnant rats, chronic L-NAME treatment reduced blood plasma Ca^{2+} levels by about 0.1 mmol / l (Ebose et al. 2007). Urea and plasma creatinine were shown to be elevated as a consequence of L-NAME treatment (Hropot et al. 1994; Cardoso et al. 2013), although this happened after 6 weeks of treatment. Taken together, it seems likely that the short-term L-NAME treatment in my experiments did not have a profound effect on the observed plasma levels of Ca^{2+} and Mg^{2+} , while a small effect on Na^+ and plasma creatinine and blood urea nitrogen is to be expected. Because the obtained values from this analysis might therefore not be completely comparable with blood samples from untreated animals, they were not used to

calculate creatinine clearance. However, comparisons between genotypes should be unaffected.

8.3.3 KO mice are hypercalcaemic, hypercalciuric and hyperphosphaturic

Plasma Na^+ levels exhibited a small but significant reduction in L-NAME treated KO animals while there was no such difference in the other experimental groups. It is possible that L-NAME induced increased Na^+ excretion, as detailed above, leading to a decrease in Na^+ levels in the blood in this particular experiment. Mg^{2+} , Cl^- and K^+ were unchanged.

However, compared to WT control, KO mice showed robust and unexpected changes in their Ca^{2+} and Pi metabolism. KO mice were distinctively hypercalcaemic, had elevated serum FGF23 and 1,25-D3 levels. Again surprisingly, PTH levels were not significantly different between KO mice compared to WT control. At the same time, the KO animals showed dramatically increased urinary Ca^{2+} and Pi excretion when fed a standard diet.

The high salt diet protocol was mainly devised for to assess the influence of salt loading on blood pressure, but urines were collected on high NaCl diet as well. Compared to standard diet, electrolyte excretion was elevated for all ions in both WT and KO animals, as expected (Luft et al. 1979; Goulding and Campbell 1983; Yatabe et al. 2012). On the high salt diet, KO animals exhibited a greater increase of K^+ and Mg^{2+} excretion than the WT controls, while there was no difference in the excretion of those ions when animals were kept on a normal diet. The increased K^+ and Mg^{2+} excretions of the KO animals can probably be related to the increased urine volume observed in KO mice on a high salt diet compared to WT. As suggested in the previous section, this is probably a normal response to the increased filtrate osmolarity due to the excretion of already high levels of Ca^{2+} and Pi in these mice to prevent the formation of urolithiasis. The increase in Mg^{2+} and K^+ excretion of KO mice on high salt diet suggested an effect on the distal nephron and should be investigated further by collecting information concerning plasma values for high salt intake (which currently are not available).

In the following chapters I will attempt to discuss the possible mechanisms that could lead to the striking changes in mineral ion metabolism between WT and KO mice.

8.3.3.1 Influence of the kidney on Ca²⁺ homeostasis

The kidney is highly involved in Ca²⁺ homeostasis via a PTH independent regulation of Ca²⁺ and Mg²⁺ excretion mediated by the CaSR. In essence, CaSR activation by high plasma Ca²⁺ levels reduces Ca²⁺ reabsorption, as reviewed in (Riccardi and Brown 2010).

Therefore, the increased blood Ca²⁺ levels could be the result of reduced CaSR activity in the kidney. However, expression of a functional CaSR in the kidney appears not be affected in KO mice as this would at the same time lead to markedly reduced Ca²⁺ excretion, as shown for a kidney specific CaSR KO mouse (Toka et al. 2012). However, the opposite effect, increased urinary Ca²⁺ excretion, was found in the SM22 α -Cre x LoxP-CaSR mouse.

Furthermore, blood urea nitrogen, urea and uric acid excretion were comparable in WT and KO mice, suggesting normal kidney function. Importantly, serum creatinine levels were not elevated and urine creatinine excretion was not reduced in KO animals compared to WT. Indeed, while urinary creatinine excretion was equal between WT and KO mice, plasma creatinine levels were slightly reduced in KO animals. The reduction in plasma creatinine in KO mice compared to WT could possibly be explained by the hypotensive phenotype. Currently, the state of the renal microvasculature is unknown in these animals, but I would predict that, owing to the gene deletion from VSMC, both afferent and or efferent arterioles would be affected. Since these two arterioles are known to react differently to various contractile and dilatory stimuli (Ito et al. 1993; Liu et al. 2012), it is possible that the afferent arteriole would be dilated more than the efferent one, therefore potentially leading to an increase in GFR. Nevertheless, even though GFR could not be calculated because of the limitations of the experimental protocol (influence of L-NAME), these data still suggest that kidney function in KO animals was equal, if not better than in WT animals. However, dedicated studies to measure GFR in these animals should be performed in the future.

In addition to measurements of GFR, the high excretion of Ca²⁺ and Pi would point towards formation of nephrolithiasis, which was, at least by cursory observation and considering the long life span of these mice, not the case or not a major problem. Histological investigation of the kidneys of WT and KO mice is currently underway.

8.3.3.2 KO mice exhibit a phenotype similar to models of primary hyperparathyroidism

As reviewed in (Hu et al. 2013), Ca^{2+} , Pi, PTH, 1,25-D3 and FGF23 are controlled by a highly regulated mechanisms consisting of multiple positive and negative feedback loops (*c.f.* Figure 4). PTH controls 1,25-D3 production in the kidney and promotes bone resorption and FGF23 production. 1,25-D3 promotes Ca^{2+} and Pi reabsorption from kidney and Ca^{2+} absorption from the intestine and also stimulates FGF23 production in bone. Conversely, 1,25-D3 and Ca^{2+} inhibit PTH release via negative feedback. FGF23 promotes Pi excretion and also inhibits PTH secretion.

1,25-D3, Ca^{2+} and FGF23 are all markedly elevated in our KO mice. Because of the negative feedback mechanisms by 1,25-D3, Ca^{2+} and FGF23 on PTH production one would assume that PTH levels were markedly reduced in SM22 α -Cre x LoxP-CaSR mice. However, PTH levels of these mice are not only non-decreased compared to WT control animals – they even show a trend towards elevation, albeit non-significant. Therefore, PTH levels might be slightly elevated, but are at least surprisingly unchanged, in the face of the elevations of Ca^{2+} , FGF23 and 1,25-D3. This leads to the conclusion that might in fact be PTH which drives the elevations of the elevations of Ca^{2+} , FGF23 and 1,25-D3.

Indeed, the phenotype of the KO mice seems similar to what is seen in mice that are heterozygous for the CaSR in the parathyroid gland (Chang et al. 2008). These mice are hypercalcaemic, hypercalciuric and have reduced bone density. However, the PTH-Cre x LoxP-CaSR HET mice have about 2-fold elevated PTH levels compared to controls which was not observed in our animals. Furthermore, the total phenotype of the SM22 α -Cre x LoxP-CaSR mouse shows a resemblance to what was described for a mouse model of primary hyperparathyroidism induced by parathyroid-specific cyclin D1 overexpression (Imanishi et al. 2001). Cyclin D1 is a potent oncogene that is involved in the development of parathyroid adenomas (Motokura et al. 1991). Like the SM22 α -Cre x LoxP-CaSR mouse, the PT-cyclin D1 mice lived up to two years and older, and were comparable to WT controls in body weight, serum albumin, blood urea nitrogen and creatinine levels. Furthermore, like the SM22 α -Cre x LoxP-CaSR mouse, the PTH-cyclin D1 mice were hypercalcaemic, normohypophosphataemic and showed elevated FGF23 and 1,25-D3 levels and non to moderately increased PTH levels depending on age, together with impaired bone structure. The principal component of all these changes were the cyclin D1 induced hyperplasia of the parathyroid

gland, and a concomitant reduction of parathyroid CaSR expression (Imanishi et al. 2001; Kawata et al. 2007).

Indeed, these changes are indicative of primary hyperparathyroidism (Ward et al. 2012), with the noticeable exception of 1,25-D3. The 1,25-D3 levels in the PT-cyclin D1 mice were elevated compared to WT control, although this elevation appeared only in later stages of their life (Kawata et al. 2007). The two-fold elevated 1,25-D3 levels present in the SM22 α -Cre x LoxP-CaSR mice might therefore not be explainable by a PTH driven phenotype alone. Indeed, the absence of elevated PTH levels in KO mice could suggest that other factors are contributing to the phenotype of the mice as well and that 1,25-D3 suppresses abnormally elevated PTH production (Ritter et al. 2006). Still, the marked absence of a reduction in PTH levels points to PTH production being at least involved in the observed phenotype. Importantly, the PT-cyclin-D1 mice only develop their phenotype over a matter of months, with increased plasma Ca²⁺ levels appearing before an increase in plasma PTH (Kawata et al. 2007). I have shown increased Ca²⁺ and FGF23 levels at 3 as well as 18 months of age, suggesting the onset of the phenotypical changes is occurring more rapidly than in PT-cyclin D1 mice. For further studies, it might be interesting to investigate the SM22 α -Cre x LoxP-CaSR mice at a younger age as well.

8.3.3.3 Other possible influences

The proposed form of mild primary hyperparathyroidism seems like the best-fitting explanation for the observed changes in the mineral ion metabolism of the SM22 α -Cre x LoxP-CaSR, however other explanations can be put forward. This is especially relevant as, even though PTH levels in these mice showed a trend towards elevation, a significant change in plasma PTH was not detected in KO mice. Yet, the absence of a significant reduction in PTH levels suggests PTH is involved in the observed phenotype, because an elevation in Ca²⁺, 1,25-D3 and FGF23 would be expected to suppress PTH secretion (Brown 2013).

In addition to the primary hyperparathyroidism-like hypothesis, a possible explanation for the observed changes in our KO mice could be an increase in 1,25-D3 levels. Primary elevated 1,25-D3 levels would increase FGF23 levels (hence phosphaturia) and promote Ca²⁺ and Pi absorption from the intestine while the phosphaturia induced by FGF23 would induce bone loss. Increased 1,25-D3 plasma levels (Ritter et al. 2006) and the resulting hypercalcaemia

would however suppress PTH release in the presence of a functional CaSR in the parathyroid gland, while PTH levels were equal to slightly increased in KO animals compared to WT. These findings would suggest that, for 1,25-D3 to be a principal component of the phenotype, CaSR function would have to be impaired in the parathyroid gland in addition to a putative hypervitaminosis D.

1-alpha hydroxylase, the rate limiting enzyme for 1,25-D3 synthesis was shown to be expressed in VSMC (Somjen et al. 2005). Ca^{2+} was shown to suppress 1-alpha hydroxylase activity directly, possibly via the CaSR (Bland et al. 1999). Therefore, it seems at least possible that deletion of the CaSR from VSMC resulted in upregulation of 1,25-D3 through increased 1-alpha-hydroxylase activity. If such a hypothetical elevation could be responsible for a large increase in 1,25-D3 levels as observed in the SM22 α -Cre x LoxP-CaSR mouse is unknown. On the other hand, if such a mechanism would be present in addition to changes in the parathyroid gland, as detailed in the next section, this could explain the blunted PTH response (i.e. unexpectedly equal or slightly elevated PTH levels despite characteristics of primary hyperparathyroidism) as well as the elevated 1,25-D3 levels.

Similarly, it could be speculated that FGF23 is the principal component in the phenotype of the KO animals. However, FGF23 production is believed not to be regulated by the CaSR directly (Quinn et al. 2013b) and principally elevated FGF23 levels would inhibit 1,25-D3 as well as PTH production which was not observed in the KO mice. On the other hand, it was recently shown that FGF23 is not able to suppress PTH secretion in a uremic state (Canalejo et al. 2010), which could indicate that in KO mice, which are hypercalcaemic, PTH would not be suppressed by FGF23. However, FGF23 was recently shown not to be expressed in human blood vessels (Donate-Correa et al. 2013), and VSMC targeted deletion of Klotho, the co-factor for FGF23, did not result in changes in mineral ion metabolism or vascular calcification (Lindberg et al. 2013) therefore making a putative mechanism of increased FGF23 production by VSMC CaSR deletion difficult to explain.

Klotho, has not been studied here but could play a role in the phenotype of these mice. Klotho^{-/-} mice exhibit hypervitaminosis D (Kuro-o et al. 1997; Yoshida et al. 2002). Klotho reduces 1,25-D3 levels and inhibits PTH secretion (Hu et al. 2013). However, Klotho^{-/-} deficient mice are extremely hyperphosphataemic and show enhanced ageing process (Kuro-o et al. 1997) which was not the case in SM22 α -Cre x LoxP-CaSR mice.

Because of the similarity of the mouse models of PT-cyclin D1 and the phenotype present in the SM22 α -Cre x LoxP-CaSR mouse, I hypothesize that indeed a form of primary hyperparathyroidism, possibly in combination with other additional factors like changes in 1,25-D3 synthesis could be the driving force behind the observed change in mineral ion metabolism in these mice. Figure 99 shows a schematic of these hypothetical complex interrelations.

Primary hyperparathyroidism is often associated with hypertension which can be reversed by parathyroidectomy (Broulik et al. 2011). In a small human study, the hypertension observed in primary hyperparathyroidism was shown to go along with only very small increases in plasma renin activity and aldosterone levels, while smooth muscle contractility in response to noradrenalin was shown to be enhanced (Schiffl and Lang 2011). By extension these findings suggest that in the SM22 α -Cre x LoxP-CaSR mice, blood pressure was not elevated because of the lost contractility of their blood vessels. In addition, as already detailed in chapter 7.3.9, the cardiac remodelling observed in some of the KO hearts could be, amongst other factors, a direct consequence of the mineral ion metabolism phenotype, possibly because of the elevated FGF23 levels (Faul et al. 2011). Furthermore, as already explained in chapter 6, the absence of *in vivo* calcification in the SM22 α -Cre x LoxP-CaSR mice can be explained by the hyperphosphaturia and therefore normal blood Pi levels despite elevated 1,25-D3 levels, as Pi was shown to be highly associated with the onset of vascular calcification and the underlying phenotypic transdifferentiation of VSMC (Jono et al. 2000).

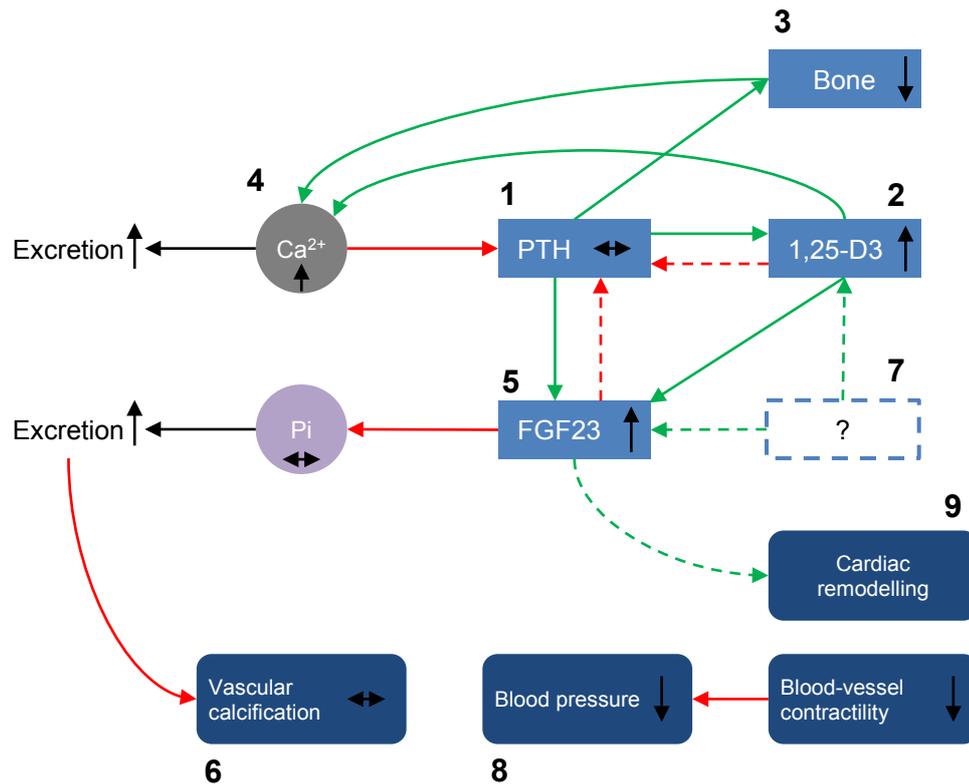


Figure 99: Possible mechanism of mineral ion homeostasis and related phenotypic phenomena in the SM22 α -Cre x LoxP-CaSR mouse. Green arrows indicate activation (or increased resorption), red arrows indicate inhibition. Solid arrows are established, dashed arrows are hypothetical. Upward pointing black arrows indicate increase, downward pointing black arrows indicate decrease, levelled black bi-headed arrows indicate no change (1) PTH promotes (2) 1,25-D3 production and (3) bone resorption which leads to (4) hypercalcaemia. Blood Ca²⁺ is excreted via the kidney, leading to hypercalciuria, and limits further PTH production via the parathyroid CaSR. (5) PTH and 1,25 D3 also increase FGF23 production in bone, leading to phosphaturia, (6) which in turn might be responsible for the prevention of vascular calcification. (7) Hypothetical undetermined influences could be responsible for increased 1,25-D3 and FGF23 levels as well, which in turn would counteract an increase in PTH, such as increased 1 α -Hydrolase activity, providing a possible explanation for the elevated 1,25-D3 and FGF23 levels with unchanged PTH. (8) The reduced blood vessel contractility prevents development of hypertension. (9) Elevated FGF23 levels could account for, or at least contribute to the observed sporadic cardiac remodelling.

8.3.4 Link between VSMC CaSR and changes in mineral ion metabolism

The possible interrelations between the different factors involved in the mineral ion metabolism in the SM22 α -Cre x LoxP-CaSR mice notwithstanding, the question remains how deletion of the VSMC CaSR can elicit these changes.

In Cre-LoxP systems of targeted gene deletion, the occurrence of off-target expression of the promoter and therefore deletion of the target gene in undesired tissues is known to happen. A small leak of the SM22 α -Cre allele was reported to have happened for renal epithelium (Malhowski et al. 2011). However, deletion of the CaSR from the kidney in KO mice can probably be excluded as Ca²⁺ excretion function appeared to be unaffected and a kidney deletion of the CaSR leads to hypocalciuria (Toka et al. 2012), which is the opposite of the phenotype present in KO mice. Similarly, a constitutive knock-down of the CaSR would lead to an FHH or NSHPT like phenotype, which would again characterised by hypocalciuria (Ho et al. 1995). If only some parathyroid cells were to have impaired CaSR expression, this could mean that those impaired cells would exhibit increased PTH production while the non-affected cells would have downregulated PTH production. We have tested for Ca²⁺ and FGF23 levels in advanced age of the mice (18 months) and the differences were comparable to what was seen in 3 month old animals. These observations point toward a non-progressing form of the phenotype observed in the KO mice. Furthermore, deletion of the CaSR specifically in parathyroid chief cells leads to only mild hypercalcaemia of about 14 % increase vs. control in case of heterozygous deletion (Chang et al. 2008), while our mice exhibited an increase of ~ 25-50 %, which would be more in line with homozygous deletion of the parathyroid CaSR (40 %) but these mice have a very severe phenotype of growth retardation (Chang et al. 2008). Finally, an expression of SM22 α or SM22 (the human isoform) or a leakage of SM22 α -Cre in the parathyroid or thyroid has not been reported previously. Nevertheless, a reduction of CaSR activity in the parathyroid chief cells seems a valid hypothesis to explain the biochemical changes in this mouse, making studies on parathyroid CaSR functionality (see below) imperative.

If specificity of the KO for smooth muscle and possibly heart cells (Li et al. 1996a; Lepore et al. 2005) is assumed, then the CaSR is still functionally expressed in the parathyroid gland. Again, this assumption is substantiated by the much more severe phenotype of parathyroid loss of the CaSR (Chang et al. 2008), which is clearly not the case in the SM22 α -Cre x LoxP-

CaSR mouse. The question arises how the vascular CaSR could influence mineral ion homeostasis in such a profound matter.

It seems possible that the CaSR in VSMC of blood vessels supporting the parathyroid gland contributes to the parathyroid gland's function as blood Ca^{2+} regulator so that deletion of the CaSR could lead to mild form of hyperparathyroidism via yet unknown paracrine actions.

It could be speculated that, since blood vessels permeate every organ in the body, not only the blood vessels themselves but all organs in the body would be affected by a vasculature specific KO of the CaSR. Similar effects of targeted gene deletion from the vasculature on other organ systems has been described e.g. for bone morphogenic protein receptor 1A, where VSMC specific deletion led to impaired brain development through impaired vascularization (El-Bizri et al. 2008).

One of the most striking features of the SM22 α -Cre x LoxP-CaSR mouse is the prevalent hypotension which seems to be caused by a reduction in TPR. This feature would indicate that blood flow in various organs should also be altered. The parathyroid gland certainly is highly vascularized (Murakami et al. 1995) and indeed, a relationship between blood flow and parathyroid hormone secretion has been described in humans where a higher vascular resistance was inversely correlated with blood PTH levels (Mohammadi et al. 2013). A similar influence of blood vessel diameter on gland function has also been described for the adrenal gland in diabetic rats (Sricharoenvej et al. 2009).

From this point of view, it is therefore possible that CaSR deletion from blood vessels could have multiple effects in different organs of the body. E.g. the CaSR has been found to be expressed in osteoclasts (Kameda et al. 1998), osteoblasts (Dvorak et al. 2004) and osteocytes (Chang et al. 1999) and has been shown to play a profound role in bone physiology as mice lacking the CaSR in osteoblasts show severe growth and skeletal impairment compared to control littermates (Chang et al. 2008). As with the parathyroid gland, the bone is a highly vascularized organ (Johnson et al. 2004) and vascular CaSR in bone blood vessels might contribute the aforementioned functions. By a similar mechanism, the vascular CaSR could play a role in suppressing 1- α -hydroxylase in the kidney (Bland et al. 1999), therefore loss of CaSR could increase 1,25-D3 production explaining the high levels of 1,25-D3 in our mice. Again, these hypotheses have to be investigated by investigations on parathyroid gland and the influence of 1,25-D3 and FGF23 by other methods (see below).

8.3.5 Bone

The results of the bone analysis by Dr. Wenhan Chang showed that KO animals had significant trabecular and cortical bone loss. Indeed, the impaired bone structure is probably linked to the profound changes in mineral ion metabolism, namely the increased Ca^{2+} and Pi urinary excretion. Indeed, in primary hyperparathyroidism, which the SM22 α -Cre x LoxP-CaSR mouse is similar to, bone turnover is generally increased and bone structure impaired (Christiansen et al. 1997; Chang et al. 2008).

8.3.6 Future directions

Taken together, it is clear that there are too many variables to draw any definitive conclusions from the biochemical changes alone. Substantial future investigations into the cause for the observed changes in mineral ion homeostasis are therefore clearly necessary to understand the primary driving force or possibly forces behind these changes.

For the described PT-cyclin-D1 mouse, which has a phenotype similar, albeit milder or slower progressing, phenotype to the SM22 α -Cre x LoxP-CaSR mouse, it was described that proliferation of parathyroid cells occurs before the onset of the symptomatic primary hyperparathyroidism (Mallya et al. 2005). To substantiate the hypothesis of a possible form of primary hyperparathyroidism, experiments to assess the status of the parathyroid glands in the SM22 α -Cre x LoxP-CaSR are clearly necessary and should encompass trials to investigate histology (i.e. presence of hyperplasia), expression levels of CaSR and functionality of the CaSR. Furthermore, the possible additional influences on 1,25-D3 and PTH could be investigated by breeding the SM22 α -Cre x LoxP-CaSR mouse with a 1- α -Hydroxylase or PTH deficient mouse.

8.4 Conclusions

- *KO mice show (Chertow et al. 2012) elevated blood Ca^{2+} , FGF23, 1,25-D3 levels and trends towards elevated PTH and reduced Pi levels.*
- *Urinary Ca^{2+} and Pi excretion was elevated in KO mice compared to WT control.*
- *These changes in mineral ion metabolism are associated with impaired bone structure and probably increased bone turnover.*
- *This phenotype is similar to a mild form of primary hyperparathyroidism.*
- *Kidney function appears to be unaffected in KO mice.*
- *The underlying cause for these differences in mineral ion metabolism remains to be determined but may be found in partial deletion of the CaSR from the parathyroid gland through "leaky" expression of the Cre enzyme, changes in parathyroid vascularisation or blood flow.*
- *Experiments assessing parathyroid gland histology, CaSR expression and CaSR functionality, as well as possible other influences (directly affected 1,25-D3 synthesis) are required in the future.*

9 Thesis conclusions and future directions

In the course of my thesis, I investigated these roles for the VSMC CaSR in a mouse model of VSMC targeted CaSR deletion. In the following section, I want to briefly recapitulate the three principal discoveries I have in the course of the phenotypic characterisation of this mouse model. All key results of the phenotypic characterisation are furthermore listed in Table 27. Key future experiments are listed in Table 13.

9.1 Protective effect of the VSMC CaSR against calcification

It has been shown before that loss of the VSMC CaSR increases *in vitro* VSMC susceptibility to mineralise by transfection with a dominant negative construct (Alam et al. 2009) or siRNA (Henaut et al. 2014). I was able to prove this protective effect of the VSMC CaSR against VSMC calcification in VSMC cultured from WT and KO mice. However, and very importantly, even though the KO mice exhibited increased blood Ca^{2+} levels, they did not show any ectopic calcification *in vivo*. It is therefore possible that this protective effect of the vascular CASR only asserts itself in the synthetic *in vitro* environment or only protects against vascular calcification in pathophysiological disease states of hyperphosphataemia as seen in CKD. Indeed, KO mice did not present any hyperphosphataemia but were in fact hyperphosphaturic. To investigate these possibilities, the KO animals should be challenged with hyperphosphataemia, for example by performing 5/6 nephrectomy followed by a high Pi-containing diet (Shobeiri et al. 2010; Lau et al. 2013). I anticipate that, if the CaSR protects against vascular calcification *in vivo* is correct, higher levels of vascular calcification should be observed in KO animals, compared to WT control.

9.2 The VSMC CaSR is involved in blood pressure regulation

I was able to demonstrate that loss of the vascular CaSR is associated with hypotension and that this reduction blood pressure is most likely due to reduced TPR. Other members of our group were able to demonstrate that CaSR deletion results in loss of arterial contractility in

response to high K^+ and phenylephrine which indicates a potentiating effect of the VSMC CaSR on blood vessel contraction. These results prove, for the first time, a role for the VSMC CaSR in blood vessel tone regulation and blood pressure regulation *in vivo*.

Since the CaSR is also highly expressed in the endothelium and inhibition of NO synthases abrogates the hypotension in KO animals, as well as the putative influence of the endothelial CaSR on NO production *in vitro* (Ziegelstein et al. 2006) the specific role of the endothelium CaSR should be investigated *in vivo*, for example by use of transgenic mice expressing Cre specifically in the endothelium (Kisanuki et al. 2010).

Furthermore, some hearts of KO animals showed signs of functional changes and remodelling as identified via cardiac cine-MRI and KO mice were bradycardic compared to WT animals. To elucidate a possible primary functional change in the hearts of these mice, potentially via deletion of the CaSR from cardiomyocytes, functional studies on isolated hearts of WT and KO mice should be performed in the future.

9.3 The VSMC CaSR is involved in mineral ion homeostasis

KO mice exhibited a rather unexpected phenotype of hypercalcaemia, hypercalciuria, hyperphosphaturia and elevated FGF23 and 1,25-D3 levels as well as impaired bone, while PTH levels were surprisingly unchanged compared to WT control. In addition, I have shown that kidney function is not impaired in KO animals. Since a primary elevation in 1,25-D3 or FGF23 should lead to depressed PTH levels, the best fitting explanation can be found in a form of mild primary hyperparathyroidism in these mice and their phenotype is indeed quite similar to such animals (Imanishi et al. 2001; Kawata et al. 2007). However, it seems plausible that other regulatory loops could be affected in these mice as well, e.g. the 1,25-D3 axis, providing possible angles for explaining the unchanged PTH levels. The underlying cause(s) for this phenotype will have to be identified in future studies, with one possibility being breeding the SM22 α -Cre x LoxP-CaSR mice with PTH $^{-/-}$ or 1- α -hydroxylase $^{-/-}$ mice which should allow identification of the primary cause of the mineral ion metabolism phenotype of KO mice. Nevertheless, this phenotype suggests that the vascular CaSR plays a role in regulation of mineral ion metabolism via a yet unknown mechanism.

Table 12: Summary of the observed phenotype of the SM22 α -Cre x LoxP-CaSR mouse in the course of this thesis.

CaSR involvement in	Phenotype	Interpretation
Cardiovascular system	Hypotension, Blood vessel contractility↓	Reduced TPR, CaSR acts on VSMC to potentiate contractions and on endothelium to promote NO production
	Bradycardia	Possible result of CaSR deletion from the heart, systemic influences
	Sporadic cardiac remodelling	Possible result of CaSR deletion from the heart, compensation to hypotension, systemic influences (FGF23)
Mineral ion metabolism	Blood Ca ²⁺ ↑, Ca ²⁺ :Cr↑, Pi:Cr↑, FGF23↑, 1,25-D3↑, Pi→, PTH→, bone structure↓	Phenotypic resemblance to primary hyperparathyroidism
	Plasma creatinine↓, urine creatinine→, BUN→, urine uric acid→, Na ⁺ :Cr→, K ⁺ :Cr→, Cl ⁻ :Cr→, renin→, aldosterone→	No renal involvement
Protection from calcification	Fetuin A→ no calcification <i>in vivo</i> , increased VSMC calcification <i>in vitro</i>	Protective mechanism possibly only in disease state of high Pi, or restricted to artificial conditions
Other	<i>In vitro</i> proliferation of VSMC is controlled by the CaSR	undetermined

Table 13: Future experiments to further the understanding of the VSMC CaSR and the phenotype of the SM22 α -Cre x LoxP-CaSR mouse. Note that only “large scale” experiments are listed.

Rationale	Experiment	Expected outcome
Functional involvement of the heart in phenotype unknown, possible deletion of CaSR from the heart	Langendorff preparation of isolated hearts, high frequency echocardiography	Measurement of heart contractility, pacemaker function, sensitivity against external stimuli independent of systemic phenotype
Phenotype similar to primary hyperparathyroidism	Histology, Ca ²⁺ imaging, immunostaining, western blot, RT-qPCR	Involvement of the parathyroid gland (hyperplasia, expression of functional CaSR)
No vascular calcification in KO mice	5/6 nephrectomy + high Pi diet	Determination if VSMC CaSR protects from vascular calcification in disease state of hyperphosphataemia
Moist appearance of faeces from KO mice, hypercalcaemia and hypercalciuria indicate elevated intestinal Ca ²⁺ absorption	Faeces composition, histology, etc.	Characterisation of gastrointestinal phenotype
Hypercalcaemia and hypervitaminosis D could contribute to cardiovascular phenotype	SM22 α -Cre x LoxP-CaSR x 1- α -hydroxylase ^{-/-} mice	Contribution of systemic changes in mineral ion metabolism to cardiovascular phenotype of bradycardia and hypotension
L-NAME reversible hypotension	Endothelium-VSMC double KO mouse	Involvement of the CaSR in NO production and contribution to hypotensive phenotype

10References

- Alam, M. U. et al. 2009. Calcification is associated with loss of functional calcium-sensing receptor in vascular smooth muscle cells. *Cardiovascular research* 81(2), pp. 260-268.
- Amann, K. and Ritz, E. 1998. Cardiovascular abnormalities in ageing and in uraemia--only analogy or shared pathomechanisms? *Nephrology, dialysis, transplantation : official publication of the European Dialysis and Transplant Association - European Renal Association* 13 Suppl 7, pp. 6-11.
- Amann, K. and Tyralla, K. 2002. Cardiovascular changes in chronic renal failure--pathogenesis and therapy. *Clinical nephrology* 58 Suppl 1, pp. S62-72.
- Armato, U. et al. 2013. Calcium-sensing receptor antagonist (calcilytic) NPS 2143 specifically blocks the increased secretion of endogenous Abeta42 prompted by exogenous fibrillary or soluble Abeta25-35 in human cortical astrocytes and neurons-therapeutic relevance to Alzheimer's disease. *Biochimica et biophysica acta* 1832(10), pp. 1634-1652.
- Assinder, S. J. et al. 2009. Transgelin: an actin-binding protein and tumour suppressor. *The international journal of biochemistry & cell biology* 41(3), pp. 482-486.
- Atchison, D. K. et al. 2010. Acute activation of the calcium-sensing receptor inhibits plasma renin activity in vivo. *American journal of physiology. Regulatory, integrative and comparative physiology* 299(4), pp. R1020-1026.
- Austin, C. P. et al. 2004. The knockout mouse project. *Nature genetics* 36(9), pp. 921-924.
- Awumey, E. M. et al. 2013. Nitric-oxide synthase knockout modulates Ca(2)(+)-sensing receptor expression and signaling in mouse mesenteric arteries. *The Journal of pharmacology and experimental therapeutics* 346(1), pp. 38-47.
- Ayachi, S. 1979. Increased dietary calcium lowers blood pressure in the spontaneously hypertensive rat. *Metabolism: clinical and experimental* 28(12), pp. 1234-1238.
- Ba, J. et al. 2003. Calcium-sensing receptor regulation of PTH-inhibitable proximal tubule phosphate transport. *American journal of physiology. Renal physiology* 285(6), pp. F1233-1243.
- Bai, M. et al. 1998. Dimerization of the extracellular calcium-sensing receptor (CaR) on the cell surface of CaR-transfected HEK293 cells. *The Journal of biological chemistry* 273(36), pp. 23605-23610.

Bai, S. Z. et al. 2012. Decrease in calcium-sensing receptor in the progress of diabetic cardiomyopathy. *Diabetes research and clinical practice* 95(3), pp. 378-385.

Barletta, G. et al. 2000. Cardiovascular effects of parathyroid hormone: a study in healthy subjects and normotensive patients with mild primary hyperparathyroidism. *The Journal of clinical endocrinology and metabolism* 85(5), pp. 1815-1821.

Bas, A. et al. 2006. Reversibility of calcitriol-induced medial artery calcification in rats with intact renal function. *Journal of bone and mineral research : the official journal of the American Society for Bone and Mineral Research* 21(3), pp. 484-490.

Belz, G. G. 1995. Elastic properties and Windkessel function of the human aorta. *Cardiovascular drugs and therapy / sponsored by the International Society of Cardiovascular Pharmacotherapy* 9(1), pp. 73-83.

Berry, C. J. et al. 2009. Effects of deep sedation or general anesthesia on cardiac function in mice undergoing cardiovascular magnetic resonance. *Journal of cardiovascular magnetic resonance : official journal of the Society for Cardiovascular Magnetic Resonance* 11, p. 16.

Birgander, M. et al. 2012. Adrenergic and cardiac dysfunction in primary hyperparathyroidism. *Clinical endocrinology* 76(2), pp. 189-195.

Blacher, J. et al. 2001. Arterial calcifications, arterial stiffness, and cardiovascular risk in end-stage renal disease. *Hypertension* 38(4), pp. 938-942.

Blacher, J. et al. 1999. Impact of aortic stiffness on survival in end-stage renal disease. *Circulation* 99(18), pp. 2434-2439.

Bland, R. et al. 1999. Constitutive expression of 25-hydroxyvitamin D3-1alpha-hydroxylase in a transformed human proximal tubule cell line: evidence for direct regulation of vitamin D metabolism by calcium. *Endocrinology* 140(5), pp. 2027-2034.

Block, G. A. et al. 1998. Association of serum phosphorus and calcium x phosphate product with mortality risk in chronic hemodialysis patients: a national study. *American journal of kidney diseases : the official journal of the National Kidney Foundation* 31(4), pp. 607-617.

Block, G. A. et al. 2010. Cinacalcet hydrochloride treatment significantly improves all-cause and cardiovascular survival in a large cohort of hemodialysis patients. *Kidney international* 78(6), pp. 578-589.

Boedtkjer, E. et al. 2011. Disruption of Na⁺,HCO₃⁽⁻⁾ cotransporter NBCn1 (slc4a7) inhibits NO-mediated vasorelaxation, smooth muscle Ca⁽²⁺⁾ sensitivity, and hypertension development in mice. *Circulation* 124(17), pp. 1819-1829.

Bogusz, A. M. et al. 2012. Quantitative immunofluorescence reveals the signature of active B-cell receptor signaling in diffuse large B-cell lymphoma. *Clinical cancer research : an official journal of the American Association for Cancer Research* 18(22), pp. 6122-6135.

Bonomini, M. et al. 2012. Calcimimetic R-568 and its enantiomer S-568 increase nitric oxide release in human endothelial cells. *PLoS one* 7(1), p. e30682.

Bradbury, R. A. et al. 1998. Expression of the parathyroid Ca⁽²⁺⁾-sensing receptor in cytotrophoblasts from human term placenta. *The Journal of endocrinology* 156(3), pp. 425-430.

Brennan, S. C. et al. 2014. Emerging roles of the extracellular calcium-sensing receptor in nutrient sensing: control of taste modulation and intestinal hormone secretion. *The British journal of nutrition*, pp. 1-7.

Broulik, P. D. et al. 2011. Improvement of hypertension after parathyroidectomy of patients suffering from primary hyperparathyroidism. *International journal of endocrinology* 2011, p. 309068.

Brown, E. M. 2010. Clinical utility of calcimimetics targeting the extracellular calcium-sensing receptor (CaSR). *Biochemical pharmacology* 80(3), pp. 297-307.

Brown, E. M. 2013. Role of the calcium-sensing receptor in extracellular calcium homeostasis. *Best practice & research. Clinical endocrinology & metabolism* 27(3), pp. 333-343.

Brown, E. M. et al. 1993. Cloning and characterization of an extracellular Ca⁽²⁺⁾-sensing receptor from bovine parathyroid. *Nature* 366(6455), pp. 575-580.

Brown, E. M. and MacLeod, R. J. 2001. Extracellular calcium sensing and extracellular calcium signaling. *Physiological reviews* 81(1), pp. 239-297.

Bruce, J. I. et al. 1999. Molecular and functional identification of a Ca⁽²⁺⁾ (polyvalent cation)-sensing receptor in rat pancreas. *The Journal of biological chemistry* 274(29), pp. 20561-20568.

Bukoski, R. D. 2001. Dietary Ca⁽²⁺⁾ and blood pressure: evidence that Ca⁽²⁺⁾-sensing receptor activated, sensory nerve dilator activity couples changes in interstitial Ca⁽²⁺⁾ with

vascular tone. *Nephrology, dialysis, transplantation : official publication of the European Dialysis and Transplant Association - European Renal Association* 16(2), pp. 218-221.

Bukoski, R. D. et al. 1997. Perivascular sensory nerve Ca^{2+} receptor and Ca^{2+} -induced relaxation of isolated arteries. *Hypertension* 30(6), pp. 1431-1439.

Caltabiano, S. et al. 2013. Characterization of the effect of chronic administration of a calcium-sensing receptor antagonist, ronacaleret, on renal calcium excretion and serum calcium in postmenopausal women. *Bone* 56(1), pp. 154-162.

Canaff, L. et al. 2001. Extracellular calcium-sensing receptor is expressed in rat hepatocytes. coupling to intracellular calcium mobilization and stimulation of bile flow. *The Journal of biological chemistry* 276(6), pp. 4070-4079.

Canalejo, R. et al. 2010. FGF23 fails to inhibit uremic parathyroid glands. *Journal of the American Society of Nephrology : JASN* 21(7), pp. 1125-1135.

Cardoso, A. M. et al. 2013. Physical training prevents oxidative stress in L-NAME-induced hypertension rats. *Cell biochemistry and function* 31(2), pp. 136-151.

Carlson, S. H. et al. 2002. Blood pressure and NaCl-sensitive hypertension are influenced by angiotensin-converting enzyme gene expression in transgenic mice. *Hypertension* 39(2), pp. 214-218.

Carney, E. F. 2013. Chronic kidney disease: No significant effect of cinacalcet on cardiovascular outcomes in patients undergoing dialysis--EVOLVE results. *Nature reviews. Nephrology* 9(1), p. 4.

Cavanaugh, A. et al. 2010. Calcium-sensing receptor biosynthesis includes a cotranslational conformational checkpoint and endoplasmic reticulum retention. *The Journal of biological chemistry* 285(26), pp. 19854-19864.

Chang, W. et al. 2008. The extracellular calcium-sensing receptor (CaSR) is a critical modulator of skeletal development. *Science signaling* 1(35), p. ra1.

Chang, W. et al. 1999. Expression and signal transduction of calcium-sensing receptors in cartilage and bone. *Endocrinology* 140(12), pp. 5883-5893.

Chattopadhyay, N. et al. 1998. Identification and localization of extracellular Ca^{2+} -sensing receptor in rat intestine. *The American journal of physiology* 274(1 Pt 1), pp. G122-130.

Cheng, S. X. 2012. Calcium-sensing receptor inhibits secretagogue-induced electrolyte secretion by intestine via the enteric nervous system. *American journal of physiology. Gastrointestinal and liver physiology* 303(1), pp. G60-70.

Cheng, S. X. et al. 2002. Expression of calcium-sensing receptor in rat colonic epithelium: evidence for modulation of fluid secretion. *American journal of physiology. Gastrointestinal and liver physiology* 283(1), pp. G240-250.

Cheng, Z. et al. 2013. Sex and age modify biochemical and skeletal manifestations of chronic hyperparathyroidism by altering target organ responses to Ca²⁺ and parathyroid hormone in mice. *Journal of bone and mineral research : the official journal of the American Society for Bone and Mineral Research* 28(5), pp. 1087-1100.

Chertow, G. M. et al. 2012. Effect of cinacalcet on cardiovascular disease in patients undergoing dialysis. *The New England journal of medicine* 367(26), pp. 2482-2494.

Chertow, G. M. et al. 2007. Evaluation of Cinacalcet Therapy to Lower Cardiovascular Events (EVOLVE): rationale and design overview. *Clinical journal of the American Society of Nephrology : CJASN* 2(5), pp. 898-905.

Chow, J. Y. et al. 2011. Calcium-sensing receptor modulates extracellular Ca²⁺ entry via TRPC-encoded receptor-operated channels in human aortic smooth muscle cells. *American journal of physiology. Cell physiology* 301(2), pp. C461-468.

Chow, K. M. et al. 2014. Effect of Cinacalcet Treatment on Vascular Arterial Stiffness among Peritoneal Dialysis Patients with Secondary Hyperparathyroidism. *Nephrology*.

Christensen, S. E. et al. 2011. Familial hypocalciuric hypercalcaemia: a review. *Current opinion in endocrinology, diabetes, and obesity* 18(6), pp. 359-370.

Christiansen, P. et al. 1997. Primary hyperparathyroidism: biochemical markers and bone mineral density at multiple skeletal sites in Danish patients. *Bone* 21(1), pp. 93-99.

Ciceri, P. et al. 2013. The Calcimimetic Calindol Prevents High Phosphate-Induced Vascular Calcification by Upregulating Matrix GLA Protein. *Nephron. Experimental nephrology* 122(3-4), pp. 75-82.

Ciceri, P. et al. 2012a. Combined effects of ascorbic acid and phosphate on rat VSMC osteoblastic differentiation. *Nephrology, dialysis, transplantation : official publication of the European Dialysis and Transplant Association - European Renal Association* 27(1), pp. 122-127.

Ciceri, P. et al. 2012b. The combination of lanthanum chloride and the calcimimetic calindol delays the progression of vascular smooth muscle cells calcification. *Biochemical and biophysical research communications* 418(4), pp. 770-773.

Clemmensen, C. et al. 2014. The GPCR, class C, group 6, subtype A (GPCRC6A) receptor: from cloning to physiological function. *British journal of pharmacology* 171(5), pp. 1129-1141.

Conigrave, A. D. et al. 2007. Aromatic L-amino acids activate the calcium-sensing receptor. *The Journal of nutrition* 137(6 Suppl 1), pp. 1524S-1527S; discussion 1548S.

Cunningham, J. et al. 2011. Secondary hyperparathyroidism: pathogenesis, disease progression, and therapeutic options. *Clinical journal of the American Society of Nephrology : CJASN* 6(4), pp. 913-921.

Dahboul, F. et al. 2014. S,S'-dinitrosobucillamine, a new nitric oxide donor, induces a better vasorelaxation than other S-nitrosothiols. *European journal of pharmacology*.

Dao, H. H. et al. 2005. Evolution and modulation of age-related medial elastocalcinosis: impact on large artery stiffness and isolated systolic hypertension. *Cardiovascular research* 66(2), pp. 307-317.

Davey, A. E. et al. 2012. Positive and negative allosteric modulators promote biased signaling at the calcium-sensing receptor. *Endocrinology* 153(3), pp. 1232-1241.

Davies, S. L. et al. 2006. Ca²⁺-sensing receptor induces Rho kinase-mediated actin stress fiber assembly and altered cell morphology, but not in response to aromatic amino acids. *American journal of physiology. Cell physiology* 290(6), pp. C1543-1551.

Davies, T. 2013. *Investigating the role of the extracellular calcium-sensing receptor (CaSR) in vascular pathophysiology using a novel mouse model of selective ablation of CaSR from mouse vascular smooth muscle cells*. PhD Thesis, Cardiff University.

De Castro, S. et al. 2007. Left ventricular remodelling index (LVRI) in various pathophysiological conditions: a real-time three-dimensional echocardiographic study. *Heart* 93(2), pp. 205-209.

de Francisco, A. L. et al. 2006. Impact of treatment with calcimimetics on hyperparathyroidism and vascular mineralization. *Journal of the American Society of Nephrology : JASN* 17(12 Suppl 3), pp. S281-285.

Dell'Aquila, M. E. et al. 2006. Localization and quantitative expression of the calcium-sensing receptor protein in human oocytes. *Fertility and sterility* 85 Suppl 1, pp. 1240-1247.

Donate-Correa, J. et al. 2013. Expression of FGF23/KLOTHO system in human vascular tissue. *International journal of cardiology* 165(1), pp. 179-183.

Dora, K. A. et al. 2008. Modulation of endothelial cell KCa3.1 channels during endothelium-derived hyperpolarizing factor signaling in mesenteric resistance arteries. *Circulation research* 102(10), pp. 1247-1255.

Duer, M. J. et al. 2008. Mineral surface in calcified plaque is like that of bone: further evidence for regulated mineralization. *Arteriosclerosis, thrombosis, and vascular biology* 28(11), pp. 2030-2034.

Duling, L. C. et al. 2006. Loss of alpha2B-adrenoceptors increases magnitude of hypertension following nitric oxide synthase inhibition. *American journal of physiology. Heart and circulatory physiology* 291(5), pp. H2403-2408.

Dvorak-Ewell, M. M. et al. 2011. Osteoblast extracellular Ca²⁺ -sensing receptor regulates bone development, mineralization, and turnover. *Journal of bone and mineral research : the official journal of the American Society for Bone and Mineral Research* 26(12), pp. 2935-2947.

Dvorak, M. M. et al. 2004. Physiological changes in extracellular calcium concentration directly control osteoblast function in the absence of calciotropic hormones. *Proceedings of the National Academy of Sciences of the United States of America* 101(14), pp. 5140-5145.

Ebose, E. J. et al. 2007. Electrolytes and pH changes in pre-eclamptic rats. *Clinica chimica acta; international journal of clinical chemistry* 384(1-2), pp. 135-140.

Edwards, G. et al. 2010. Endothelium-derived hyperpolarising factors and associated pathways: a synopsis. *Pflugers Archiv : European journal of physiology* 459(6), pp. 863-879.

Egbuna, O. et al. 2009. The full-length calcium-sensing receptor dampens the calcemic response to 1alpha,25(OH)₂ vitamin D₃ in vivo independently of parathyroid hormone. *American journal of physiology. Renal physiology* 297(3), pp. F720-728.

Egbuna, O. I. and Brown, E. M. 2008. Hypercalcaemic and hypocalcaemic conditions due to calcium-sensing receptor mutations. *Best practice & research. Clinical rheumatology* 22(1), pp. 129-148.

El-Bizri, N. et al. 2008. SM22alpha-targeted deletion of bone morphogenetic protein receptor 1A in mice impairs cardiac and vascular development, and influences organogenesis. *Development* 135(17), pp. 2981-2991.

El Hiani, Y. et al. 2009. Activation of the calcium-sensing receptor by high calcium induced breast cancer cell proliferation and TRPC1 cation channel over-expression potentially through EGFR pathways. *Archives of biochemistry and biophysics* 486(1), pp. 58-63.

Farahnak, P. et al. 2010. Cardiac function in mild primary hyperparathyroidism and the outcome after parathyroidectomy. *European journal of endocrinology / European Federation of Endocrine Societies* 163(3), pp. 461-467.

Farzaneh-Far, A. et al. 2000. Matrix gla protein is regulated by a mechanism functionally related to the calcium-sensing receptor. *Biochemical and biophysical research communications* 277(3), pp. 736-740.

Faul, C. et al. 2011. FGF23 induces left ventricular hypertrophy. *The Journal of clinical investigation* 121(11), pp. 4393-4408.

Felder, C. B. et al. 1999. The Venus flytrap of periplasmic binding proteins: an ancient protein module present in multiple drug receptors. *AAPS pharmSci* 1(2), p. E2.

Fellet, A. L. et al. 2003. Effect of acute nitric oxide synthase inhibition in the modulation of heart rate in rats. *Brazilian journal of medical and biological research = Revista brasileira de pesquisas medicas e biologicas / Sociedade Brasileira de Biofisica ... [et al.]* 36(5), pp. 669-676.

Feng, J. et al. 2010. Calcium-sensing receptor is a physiologic multimodal chemosensor regulating gastric G-cell growth and gastrin secretion. *Proceedings of the National Academy of Sciences of the United States of America* 107(41), pp. 17791-17796.

Feng, M. et al. 2008. Validation of volume-pressure recording tail-cuff blood pressure measurements. *American journal of hypertension* 21(12), pp. 1288-1291.

Finney, B. et al. 2011. An exon 5-less splice variant of the extracellular calcium-sensing receptor rescues absence of the full-length receptor in the developing mouse lung. *Experimental lung research* 37(5), pp. 269-278.

Forman, J. P. et al. 2013. Effect of vitamin D supplementation on blood pressure in blacks. *Hypertension* 61(4), pp. 779-785.

Fryer, R. M. et al. 2007. Systemic activation of the calcium sensing receptor produces acute effects on vascular tone and circulatory function in uremic and normal rats: focus on central versus peripheral control of vascular tone and blood pressure by cinacalcet. *The Journal of pharmacology and experimental therapeutics* 323(1), pp. 217-226.

Gattineni, J. et al. 2009. FGF23 decreases renal NaPi-2a and NaPi-2c expression and induces hypophosphatemia in vivo predominantly via FGF receptor 1. *American journal of physiology. Renal physiology* 297(2), pp. F282-291.

Gauthier-Bastien, A. et al. 2013. Vascular remodeling and media calcification increases arterial stiffness in chronic kidney disease. *Clinical and experimental hypertension*.

Geibel, J. et al. 2006. Calcium-sensing receptor abrogates secretagogue- induced increases in intestinal net fluid secretion by enhancing cyclic nucleotide destruction. *Proceedings of the National Academy of Sciences of the United States of America* 103(25), pp. 9390-9397.

Goulding, A. and Campbell, D. 1983. Dietary NaCl loads promote calciuria and bone loss in adult oophorectomized rats consuming a low calcium diet. *The Journal of nutrition* 113(7), pp. 1409-1414.

Grant, M. P. et al. 2011. Agonist-driven maturation and plasma membrane insertion of calcium-sensing receptors dynamically control signal amplitude. *Science signaling* 4(200), p. ra78.

Gros, R. et al. 2002. Effects of age, gender, and blood pressure on myogenic responses of mesenteric arteries from C57BL/6 mice. *American journal of physiology. Heart and circulatory physiology* 282(1), pp. H380-388.

Guyton, A. C. and Hall, J. E. 2006. *Textbook of medical physiology*. 11th ed. Philadelphia: Elsevier Saunders, pp. xxxv, 1116 p.

Habib, Z. and Camacho, P. 2010. Primary hyperparathyroidism: an update. *Current opinion in endocrinology, diabetes, and obesity* 17(6), pp. 554-560.

Halayko, A. J. and Solway, J. 2001. Molecular mechanisms of phenotypic plasticity in smooth muscle cells. *Journal of applied physiology* 90(1), pp. 358-368.

Harno, E. et al. 2008. Evidence for the presence of GPRC6A receptors in rat mesenteric arteries. *Cell calcium* 44(2), pp. 210-219.

Hattori, T. et al. 2011. Pharmacological evidences for the stimulation of calcium-sensing receptors by nifedipine in gingival fibroblasts. *Journal of pharmacology & pharmacotherapeutics* 2(1), pp. 30-35.

Hebert, S. C. 2003. Bartter syndrome. *Current opinion in nephrology and hypertension* 12(5), pp. 527-532.

Henaut, L. et al. 2014. Calcimimetics increase CaSR expression and reduce mineralization in vascular smooth muscle cells: mechanisms of action. *Cardiovascular research* 101(2), pp. 256-265.

Herberger, A. L. and Loretz, C. A. 2013. Vertebrate extracellular calcium-sensing receptor evolution: selection in relation to life history and habitat. *Comparative biochemistry and physiology. Part D, Genomics & proteomics* 8(1), pp. 86-94.

Ho, C. et al. 1995. A mouse model of human familial hypocalciuric hypercalcemia and neonatal severe hyperparathyroidism. *Nature genetics* 11(4), pp. 389-394.

Hofer, A. M. and Brown, E. M. 2003. Extracellular calcium sensing and signalling. *Nature reviews. Molecular cell biology* 4(7), pp. 530-538.

Holtwick, R. et al. 2002. Smooth muscle-selective deletion of guanylyl cyclase-A prevents the acute but not chronic effects of ANP on blood pressure. *Proceedings of the National Academy of Sciences of the United States of America* 99(10), pp. 7142-7147.

Hoorn, E. J. et al. 2011. High tail-cuff blood pressure in mice 1 week after shipping: the need for longer acclimation. *American journal of hypertension* 24(5), pp. 534-536.

Hropot, M. et al. 1994. Ramipril prevents the detrimental sequels of chronic NO synthase inhibition in rats: hypertension, cardiac hypertrophy and renal insufficiency. *Naunyn-Schmiedeberg's archives of pharmacology* 350(6), pp. 646-652.

Hu, M. C. et al. 2013. Fibroblast growth factor 23 and Klotho: physiology and pathophysiology of an endocrine network of mineral metabolism. *Annual review of physiology* 75, pp. 503-533.

Imanishi, Y. et al. 2001. Primary hyperparathyroidism caused by parathyroid-targeted overexpression of cyclin D1 in transgenic mice. *The Journal of clinical investigation* 107(9), pp. 1093-1102.

Iseki, K. et al. 1986. Effects of hypercalcemia and parathyroid hormone on blood pressure in normal and renal-failure rats. *The American journal of physiology* 250(5 Pt 2), pp. F924-929.

Ito, S. et al. 1993. Endothelium-derived relaxing factor/nitric oxide modulates angiotensin II action in the isolated microperfused rabbit afferent but not efferent arteriole. *The Journal of clinical investigation* 91(5), pp. 2012-2019.

Jakoby, M. G. t. and Semenkovich, C. F. 2000. The role of osteoprogenitors in vascular calcification. *Current opinion in nephrology and hypertension* 9(1), pp. 11-15.

John, M. R. et al. 2011. ATF936, a novel oral calcilytic, increases bone mineral density in rats and transiently releases parathyroid hormone in humans. *Bone* 49(2), pp. 233-241.

Johns, C. et al. 1996. Models of experimental hypertension in mice. *Hypertension* 28(6), pp. 1064-1069.

Johnson, E. O. et al. 2004. Vascular anatomy and microcirculation of skeletal zones vulnerable to osteonecrosis: vascularization of the femoral head. *The Orthopedic clinics of North America* 35(3), pp. 285-291, viii.

Johnson, K. 2008. Introduction to rodent cardiac imaging. *ILAR journal / National Research Council, Institute of Laboratory Animal Resources* 49(1), pp. 27-34.

Johnsson, M. S. and Nancollas, G. H. 1992. The role of brushite and octacalcium phosphate in apatite formation. *Critical reviews in oral biology and medicine : an official publication of the American Association of Oral Biologists* 3(1-2), pp. 61-82.

Jones, A. M. et al. 2004. Nitric oxide synthase inhibition with L-NAME reduces maximal oxygen uptake but not gas exchange threshold during incremental cycle exercise in man. *The Journal of physiology* 560(Pt 1), pp. 329-338.

Jono, S. et al. 2000. Phosphate regulation of vascular smooth muscle cell calcification. *Circulation research* 87(7), pp. E10-17.

Jono, S. et al. 1997. Parathyroid hormone-related peptide as a local regulator of vascular calcification. Its inhibitory action on in vitro calcification by bovine vascular smooth muscle cells. *Arteriosclerosis, thrombosis, and vascular biology* 17(6), pp. 1135-1142.

Kalogerou, M. et al. 2011. T2 weighted MRI for assessing renal lesions in transgenic mouse models of tuberous sclerosis. *European journal of radiology*.

Kameda, T. et al. 1998. Calcium-sensing receptor in mature osteoclasts, which are bone resorbing cells. *Biochemical and biophysical research communications* 245(2), pp. 419-422.

Kanno, Y. et al. 2008. Nitric oxide regulates vascular calcification by interfering with TGF-signalling. *Cardiovascular research* 77(1), pp. 221-230.

Kantham, L. et al. 2009. The calcium-sensing receptor (CaSR) defends against hypercalcemia independently of its regulation of parathyroid hormone secretion. *American journal of physiology. Endocrinology and metabolism* 297(4), pp. E915-923.

Karwowski, W. et al. 2012. The mechanism of vascular calcification - a systematic review. *Medical science monitor : international medical journal of experimental and clinical research* 18(1), pp. RA1-11.

Kawata, T. et al. 2007. Parathyroid hormone regulates fibroblast growth factor-23 in a mouse model of primary hyperparathyroidism. *Journal of the American Society of Nephrology : JASN* 18(10), pp. 2683-2688.

Kawata, T. et al. 2008. Cinacalcet suppresses calcification of the aorta and heart in uremic rats. *Kidney international* 74(10), pp. 1270-1277.

Kisanuki, Y. Y. et al. 2010. Low blood pressure in endothelial cell-specific endothelin 1 knockout mice. *Hypertension* 56(1), pp. 121-128.

Klabunde, R. E. 2005. *Cardiovascular physiology concepts*. Philadelphia ; London: Lippincott Williams & Wilkins, pp. ix, 235 p.

Klein, G. L. et al. 2008. Cardiovascular distribution of the calcium sensing receptor before and after burns. *Burns : journal of the International Society for Burn Injuries* 34(3), pp. 370-375.

Kobori, H. et al. 2007. The intrarenal renin-angiotensin system: from physiology to the pathobiology of hypertension and kidney disease. *Pharmacological reviews* 59(3), pp. 251-287.

Koleganova, N. et al. 2009. A calcimimetic (R-568), but not calcitriol, prevents vascular remodeling in uremia. *Kidney international* 75(1), pp. 60-71.

Komuves, L. et al. 2002. Epidermal expression of the full-length extracellular calcium-sensing receptor is required for normal keratinocyte differentiation. *Journal of cellular physiology* 192(1), pp. 45-54.

Kos, C. H. et al. 2003. The calcium-sensing receptor is required for normal calcium homeostasis independent of parathyroid hormone. *The Journal of clinical investigation* 111(7), pp. 1021-1028.

Krajisnik, T. et al. 2007. Fibroblast growth factor-23 regulates parathyroid hormone and 1alpha-hydroxylase expression in cultured bovine parathyroid cells. *The Journal of endocrinology* 195(1), pp. 125-131.

Kunutsor, S. K. et al. 2013. Vitamin D and risk of future hypertension: meta-analysis of 283,537 participants. *European journal of epidemiology* 28(3), pp. 205-221.

Kuro-o, M. et al. 1997. Mutation of the mouse klotho gene leads to a syndrome resembling ageing. *Nature* 390(6655), pp. 45-51.

Kwak, J. O. et al. 2005. The extracellular calcium sensing receptor is expressed in mouse mesangial cells and modulates cell proliferation. *Experimental & molecular medicine* 37(5), pp. 457-465.

Lahera, V. et al. 1991. Effects of NG-nitro-L-arginine methyl ester on renal function and blood pressure. *The American journal of physiology* 261(6 Pt 2), pp. F1033-1037.

Lau, W. L. et al. 2013. High phosphate feeding promotes mineral and bone abnormalities in mice with chronic kidney disease. *Nephrology, dialysis, transplantation : official publication of the European Dialysis and Transplant Association - European Renal Association* 28(1), pp. 62-69.

Lee, H. J. et al. 2013. Calcium-sensing receptor and apoptosis in parathyroid hyperplasia of patients with secondary hyperparathyroidism. *The Journal of international medical research* 41(1), pp. 97-105.

Lees-Miller, J. P. et al. 1987. Isolation and characterization of an abundant and novel 22-kDa protein (SM22) from chicken gizzard smooth muscle. *The Journal of biological chemistry* 262(7), pp. 2988-2993.

Lepore, J. J. et al. 2005. High-efficiency somatic mutagenesis in smooth muscle cells and cardiac myocytes in SM22alpha-Cre transgenic mice. *Genesis* 41(4), pp. 179-184.

Leroux-Berger, M. et al. 2011. Pathologic calcification of adult vascular smooth muscle cells differs on their crest or mesodermal embryonic origin. *Journal of bone and mineral research : the official journal of the American Society for Bone and Mineral Research* 26(7), pp. 1543-1553.

Li, L. et al. 1996a. SM22 alpha, a marker of adult smooth muscle, is expressed in multiple myogenic lineages during embryogenesis. *Circulation research* 78(2), pp. 188-195.

Li, L. et al. 1996b. Expression of the SM22alpha promoter in transgenic mice provides evidence for distinct transcriptional regulatory programs in vascular and visceral smooth muscle cells. *The Journal of cell biology* 132(5), pp. 849-859.

Li, P. et al. 1999. Circadian blood pressure and heart rate rhythms in mice. *The American journal of physiology* 276(2 Pt 2), pp. R500-504.

Li, Z. et al. 1997. Enhanced proliferation and migration and altered cytoskeletal proteins in early passage smooth muscle cells from young and old rat aortic explants. *Experimental and molecular pathology* 64(1), pp. 1-11.

Liabeuf, S. et al. 2013. Vascular calcification in chronic kidney disease: are biomarkers useful for probing the pathobiology and the health risks of this process in the clinical scenario? *Nephrology, dialysis, transplantation : official publication of the European Dialysis and Transplant Association - European Renal Association*.

Lindberg, K. et al. 2013. Arterial Klotho Expression and FGF23 Effects on Vascular Calcification and Function. *PloS one* 8(4), p. e60658.

Liu, J. et al. 2011. The abnormal phenotypes of cartilage and bone in calcium-sensing receptor deficient mice are dependent on the actions of calcium, phosphorus, and PTH. *PLoS genetics* 7(9), p. e1002294.

Liu, Z. Z. et al. 2012. Iodinated contrast media differentially affect afferent and efferent arteriolar tone and reactivity in mice: a possible explanation for reduced glomerular filtration rate. *Radiology* 265(3), pp. 762-771.

London, G. M. et al. 2008. Association of bone activity, calcium load, aortic stiffness, and calcifications in ESRD. *Journal of the American Society of Nephrology : JASN* 19(9), pp. 1827-1835.

London, G. M. et al. 2005. Arteriosclerosis, vascular calcifications and cardiovascular disease in uremia. *Current opinion in nephrology and hypertension* 14(6), pp. 525-531.

London, G. M. et al. 2013. Vascular calcifications, arterial aging and arterial remodeling in ESRD. *Blood purification* 35(1-3), pp. 16-21.

Loot, A. E. et al. 2013. Ca²⁺ sensing receptor cleavage by calpain partially accounts for altered vascular reactivity in mice fed a high fat diet. *Journal of cardiovascular pharmacology*.

- Luft, F. C. et al. 1979. Cardiovascular and humoral responses to extremes of sodium intake in normal black and white men. *Circulation* 60(3), pp. 697-706.
- Luo, G. et al. 1997. Spontaneous calcification of arteries and cartilage in mice lacking matrix GLA protein. *Nature* 386(6620), pp. 78-81.
- MacLeod, R. J. 2013. Extracellular calcium-sensing receptor/PTH knockout mice colons have increased Wnt/beta-catenin signaling, reduced non-canonical Wnt signaling, and increased susceptibility to azoxymethane-induced aberrant crypt foci. *Laboratory investigation; a journal of technical methods and pathology* 93(5), pp. 520-527.
- Magno, A. L. et al. 2011. The calcium-sensing receptor: a molecular perspective. *Endocrine reviews* 32(1), pp. 3-30.
- Maillard, M. P. et al. 2009. Calcium-sensing receptors modulate renin release in vivo and in vitro in the rat. *Journal of hypertension* 27(10), pp. 1980-1987.
- Makaritsis, K. P. et al. 1999. Role of the alpha2B-adrenergic receptor in the development of salt-induced hypertension. *Hypertension* 33(1), pp. 14-17.
- Maldonado-Perez, D. et al. 2003. Human calcium-sensing receptor can be suppressed by antisense sequences. *Biochemical and biophysical research communications* 311(3), pp. 610-617.
- Malhowski, A. J. et al. 2011. Smooth muscle protein-22-mediated deletion of Tsc1 results in cardiac hypertrophy that is mTORC1-mediated and reversed by rapamycin. *Human molecular genetics* 20(7), pp. 1290-1305.
- Mallya, S. M. et al. 2005. Abnormal parathyroid cell proliferation precedes biochemical abnormalities in a mouse model of primary hyperparathyroidism. *Molecular endocrinology* 19(10), pp. 2603-2609.
- Martinez-Miguel, P. et al. 2013. Regulation of endothelin-converting enzyme-1 (ECE-1) by the calcimimetic R-568. *Pharmacological research : the official journal of the Italian Pharmacological Society* 76, pp. 106-118.
- Mattson, D. L. 2001. Comparison of arterial blood pressure in different strains of mice. *American journal of hypertension* 14(5 Pt 1), pp. 405-408.
- McCarron, D. A. et al. 1982. Dietary calcium in human hypertension. *Science* 217(4556), pp. 267-269.

- McLarnon, S. et al. 2002. Aminoglycoside antibiotics induce pH-sensitive activation of the calcium-sensing receptor. *Biochemical and biophysical research communications* 297(1), pp. 71-77.
- Mendoza, F. J. et al. 2009. Direct upregulation of parathyroid calcium-sensing receptor and vitamin D receptor by calcimimetics in uremic rats. *American journal of physiology. Renal physiology* 296(3), pp. F605-613.
- Mendoza, F. J. et al. 2011. Effect of calcium and the calcimimetic AMG 641 on matrix-Gla protein in vascular smooth muscle cells. *Calcified tissue international* 88(3), pp. 169-178.
- Mizobuchi, M. et al. 2011. Effects of calcimimetic combined with an angiotensin-converting enzyme inhibitor on uremic cardiomyopathy progression. *American journal of nephrology* 34(3), pp. 256-267.
- Moessler, H. et al. 1996. The SM 22 promoter directs tissue-specific expression in arterial but not in venous or visceral smooth muscle cells in transgenic mice. *Development* 122(8), pp. 2415-2425.
- Mohammadi, A. et al. 2013. Spectral Doppler analysis of parathyroid adenoma: correlation between resistive index and serum parathyroid hormone concentration. *AJR. American journal of roentgenology* 201(2), pp. W318-321.
- Molostvov, G. et al. 2008. Extracellular calcium-sensing receptor mediated signalling is involved in human vascular smooth muscle cell proliferation and apoptosis. *Cellular physiology and biochemistry : international journal of experimental cellular physiology, biochemistry, and pharmacology* 22(5-6), pp. 413-422.
- Molostvov, G. et al. 2007. Extracellular calcium-sensing receptor is functionally expressed in human artery. *American journal of physiology. Renal physiology* 293(3), pp. F946-955.
- Moorehead, W. R. and Biggs, H. G. 1974. 2-Amino-2-methyl-1-propanol as the alkalizing agent in an improved continuous-flow cresolphthalein complexone procedure for calcium in serum. *Clinical chemistry* 20(11), pp. 1458-1460.
- Moskalenko, A. V. et al. 2010. Single protein molecule mapping with magnetic atomic force microscopy. *Biophysical journal* 98(3), pp. 478-487.
- Motokura, T. et al. 1991. A novel cyclin encoded by a bcl1-linked candidate oncogene. *Nature* 350(6318), pp. 512-515.

Motoyama, H. I. and Friedman, P. A. 2002. Calcium-sensing receptor regulation of PTH-dependent calcium absorption by mouse cortical ascending limbs. *American journal of physiology. Renal physiology* 283(3), pp. F399-406.

Murakami, T. et al. 1995. Blood vascular bed and pericapillary space in rat parathyroid glands. *Microscopy research and technique* 32(2), pp. 112-119.

Nagao, T. et al. 1992. Heterogeneous distribution of endothelium-dependent relaxations resistant to NG-nitro-L-arginine in rats. *The American journal of physiology* 263(4 Pt 2), pp. H1090-1094.

Nakagawa, K. et al. 2009. Acute cardiovascular effects of the calcimimetic R-568 and its enantiomer S-568 in rats. *Pediatric nephrology* 24(7), pp. 1385-1389.

National Heart, Lung, and Blood Institute. 2013. *What is Hypotension?* [Online]. Available at: <http://www.nhlbi.nih.gov/health/health-topics/topics/hyp/> [Accessed: 20.04.2013].

Naveh-Many, T. et al. 1995. Parathyroid cell proliferation in normal and chronic renal failure rats. The effects of calcium, phosphate, and vitamin D. *The Journal of clinical investigation* 96(4), pp. 1786-1793.

Nemeth, E. F. et al. 1998. Calcimimetics with potent and selective activity on the parathyroid calcium receptor. *Proceedings of the National Academy of Sciences of the United States of America* 95(7), pp. 4040-4045.

Newaz, M. et al. 2005. NAD(P)H oxidase/nitric oxide interactions in peroxisome proliferator activated receptor (PPAR)alpha-mediated cardiovascular effects. *Mutation research* 579(1-2), pp. 163-171.

Nguy, L. et al. 2013. Rats with adenine-induced chronic renal failure develop low-renin, salt-sensitive hypertension and increased aortic stiffness. *American journal of physiology. Regulatory, integrative and comparative physiology* 304(9), pp. R744-752.

Oda, Y. et al. 2000. The calcium sensing receptor and its alternatively spliced form in murine epidermal differentiation. *The Journal of biological chemistry* 275(2), pp. 1183-1190.

Odenwald, T. et al. 2006. Acute blood pressure effects and chronic hypotensive action of calcimimetics in uremic rats. *Journal of the American Society of Nephrology : JASN* 17(3), pp. 655-662.

Ogata, H. et al. 2003. Beneficial effects of calcimimetics on progression of renal failure and cardiovascular risk factors. *Journal of the American Society of Nephrology : JASN* 14(4), pp. 959-967.

Ogata, S. et al. 2006. Ca²⁺ stimulates COX-2 expression through calcium-sensing receptor in fibroblasts. *Biochemical and biophysical research communications* 351(4), pp. 808-814.

Ohanian, J. et al. 2005. Evidence for a functional calcium-sensing receptor that modulates myogenic tone in rat subcutaneous small arteries. *American journal of physiology. Heart and circulatory physiology* 288(4), pp. H1756-1762.

Orban, P. C. et al. 1992. Tissue- and site-specific DNA recombination in transgenic mice. *Proceedings of the National Academy of Sciences of the United States of America* 89(15), pp. 6861-6865.

Ortiz-Capisano, M. C. et al. 2007. Expression and function of the calcium-sensing receptor in juxtaglomerular cells. *Hypertension* 50(4), pp. 737-743.

Otto, A. C. et al. 2003. Enhanced myocardial contractility associated with hypercalcaemia of hyperparathyroidism - a case study in six patients. *Cardiovascular journal of South Africa : official journal for Southern Africa Cardiac Society [and] South African Society of Cardiac Practitioners* 14(3), pp. 141-143.

Pacheco, II and Macleod, R. J. 2008. CaSR stimulates secretion of Wnt5a from colonic myofibroblasts to stimulate CDX2 and sucrase-isomaltase using Ror2 on intestinal epithelia. *American journal of physiology. Gastrointestinal and liver physiology* 295(4), pp. G748-759.

Pai, A. et al. 2011. Elastin degradation and vascular smooth muscle cell phenotype change precede cell loss and arterial medial calcification in a uremic mouse model of chronic kidney disease. *The American journal of pathology* 178(2), pp. 764-773.

Panizo, S. et al. 2009. RANKL increases vascular smooth muscle cell calcification through a RANK-BMP4-dependent pathway. *Circulation research* 104(9), pp. 1041-1048.

Peuler, J. D. et al. 1987. High calcium diet reduces blood pressure in Dahl salt-sensitive rats by neural mechanisms. *Hypertension* 9(6 Pt 2), pp. III159-165.

Phillips, A. A. et al. 2014. Increased central arterial stiffness explains baroreflex dysfunction in spinal cord injury. *Journal of neurotrauma*.

Pi, M. et al. 2000. Sensing of extracellular cations in CasR-deficient osteoblasts. Evidence for a novel cation-sensing mechanism. *The Journal of biological chemistry* 275(5), pp. 3256-3263.

Pi, M. et al. 2002. Calcium-sensing receptor activation of rho involves filamin and rho-guanine nucleotide exchange factor. *Endocrinology* 143(10), pp. 3830-3838.

Pollak, M. R. et al. 1994. Autosomal dominant hypocalcaemia caused by a Ca(2+)-sensing receptor gene mutation. *Nature genetics* 8(3), pp. 303-307.

Pollak, M. R. et al. 1996. Three inherited disorders of calcium sensing. *Medicine* 75(3), pp. 115-123.

Prosdocimo, D. A. et al. 2010. Regulation of vascular smooth muscle cell calcification by extracellular pyrophosphate homeostasis: synergistic modulation by cyclic AMP and hyperphosphatemia. *American journal of physiology. Cell physiology* 298(3), pp. C702-713.

Proudfoot, D. and Shanahan, C. M. 2006. Molecular mechanisms mediating vascular calcification: role of matrix Gla protein. *Nephrology* 11(5), pp. 455-461.

Puchtler, H. et al. 1969. On the history and mechanism of alizarin and alizarin red S stains for calcium. *The journal of histochemistry and cytochemistry : official journal of the Histochemistry Society* 17(2), pp. 110-124.

Qi, H. et al. 2013. Crucial role of calcium-sensing receptor activation in cardiac injury of diabetic rats. *PloS one* 8(5), p. e65147.

Quinn, S. J. et al. 2004. pH Sensing by the calcium-sensing receptor. *The Journal of biological chemistry* 279(36), pp. 37241-37249.

Quinn, S. J. et al. 2013a. CaSR-mediated interactions between calcium and magnesium homeostasis in mice. *American journal of physiology. Endocrinology and metabolism* 304(7), pp. E724-733.

Quinn, S. J. et al. 2013b. Interactions between calcium and phosphorus in the regulation of the production of fibroblast growth factor 23 in vivo. *American journal of physiology. Endocrinology and metabolism* 304(3), pp. E310-320.

Quinn, S. J. et al. 1997. The Ca²⁺-sensing receptor: a target for polyamines. *The American journal of physiology* 273(4 Pt 1), pp. C1315-1323.

Raggi, P. et al. 2011. The ADVANCE study: a randomized study to evaluate the effects of cinacalcet plus low-dose vitamin D on vascular calcification in patients on hemodialysis. *Nephrology, dialysis, transplantation : official publication of the European Dialysis and Transplant Association - European Renal Association* 26(4), pp. 1327-1339.

Rasschaert, J. and Malaisse, W. J. 1999. Expression of the calcium-sensing receptor in pancreatic islet B-cells. *Biochemical and biophysical research communications* 264(3), pp. 615-618.

Ray, K. et al. 1999. Identification of the cysteine residues in the amino-terminal extracellular domain of the human Ca(2+) receptor critical for dimerization. Implications for function of monomeric Ca(2+) receptor. *The Journal of biological chemistry* 274(39), pp. 27642-27650.

Razzaque, M. S. 2009. The FGF23-Klotho axis: endocrine regulation of phosphate homeostasis. *Nature reviews. Endocrinology* 5(11), pp. 611-619.

Renkema, K. Y. et al. 2009. The calcium-sensing receptor promotes urinary acidification to prevent nephrolithiasis. *Journal of the American Society of Nephrology : JASN* 20(8), pp. 1705-1713.

Rey, O. et al. 2012. Negative cross-talk between calcium-sensing receptor and beta-catenin signaling systems in colonic epithelium. *The Journal of biological chemistry* 287(2), pp. 1158-1167.

Rey, O. et al. 2010. Extracellular calcium sensing receptor stimulation in human colonic epithelial cells induces intracellular calcium oscillations and proliferation inhibition. *Journal of cellular physiology* 225(1), pp. 73-83.

Reynolds, J. L. et al. 2004. Human vascular smooth muscle cells undergo vesicle-mediated calcification in response to changes in extracellular calcium and phosphate concentrations: a potential mechanism for accelerated vascular calcification in ESRD. *Journal of the American Society of Nephrology : JASN* 15(11), pp. 2857-2867.

Reynolds, J. L. et al. 2005. Multifunctional roles for serum protein fetuin-a in inhibition of human vascular smooth muscle cell calcification. *Journal of the American Society of Nephrology : JASN* 16(10), pp. 2920-2930.

Riccardi, D. and Brown, E. M. 2010. Physiology and pathophysiology of the calcium-sensing receptor in the kidney. *American journal of physiology. Renal physiology* 298(3), pp. F485-499.

Riccardi, D. et al. 1998. Localization of the extracellular Ca²⁺/polyvalent cation-sensing protein in rat kidney. *The American journal of physiology* 274(3 Pt 2), pp. F611-622.

Riccardi, D. et al. 1995. Cloning and functional expression of a rat kidney extracellular calcium/polyvalent cation-sensing receptor. *Proceedings of the National Academy of Sciences of the United States of America* 92(1), pp. 131-135.

Richard, C. et al. 2010. The calcium-sensing receptor and 25-hydroxyvitamin D-1alpha-hydroxylase interact to modulate skeletal growth and bone turnover. *Journal of bone and mineral research : the official journal of the American Society for Bone and Mineral Research* 25(7), pp. 1627-1636.

Ritter, C. S. et al. 2006. 25-Hydroxyvitamin D(3) suppresses PTH synthesis and secretion by bovine parathyroid cells. *Kidney international* 70(4), pp. 654-659.

Rodriguez, L. et al. 2005. Expression and functional assessment of an alternatively spliced extracellular Ca²⁺-sensing receptor in growth plate chondrocytes. *Endocrinology* 146(12), pp. 5294-5303.

Rodriguez, M. E. et al. 2007. The calcimimetic R-568 increases vitamin D receptor expression in rat parathyroid glands. *American journal of physiology. Renal physiology* 292(5), pp. F1390-1395.

Romero, J. R. et al. 2013. Parathyroid hormone ablation alters erythrocyte parameters that are rescued by calcium-sensing receptor gene deletion. *European journal of haematology* 91(1), pp. 37-45.

Rosenqvist, M. et al. 1992. Cardiac conduction in patients with hypercalcaemia due to primary hyperparathyroidism. *Clinical endocrinology* 37(1), pp. 29-33.

Ross, J. J. et al. 2006. Cytokine-induced differentiation of multipotent adult progenitor cells into functional smooth muscle cells. *The Journal of clinical investigation* 116(12), pp. 3139-3149.

Rostaing, L. et al. 1997. Changes in blood pressure and renal function following subtotal parathyroidectomy in renal transplant patients presenting with persistent hypercalcemic hyperparathyroidism. *Clinical nephrology* 47(4), pp. 248-255.

Ruat, M. et al. 1995. Calcium sensing receptor: molecular cloning in rat and localization to nerve terminals. *Proceedings of the National Academy of Sciences of the United States of America* 92(8), pp. 3161-3165.

Ruiz, A. et al. 2008. The effects of NG-nitro-L-arginine methyl ester on systolic pressure, diastolic pressure and pulse pressure according to the initial level of blood pressure. *Fundamental & clinical pharmacology* 22(1), pp. 45-52.

Rybczynska, A. et al. 2010. Blockade of calcium channels and AT1 receptor prevents the hypertensive effect of calcilytic NPS 2143 in rats. *Journal of physiology and pharmacology : an official journal of the Polish Physiological Society* 61(2), pp. 163-170.

Sabanayagam, C. and Shankar, A. 2011. Serum calcium levels and hypertension among U.S. adults. *Journal of clinical hypertension* 13(10), pp. 716-721.

Sadler, A. M. and Bailey, S. J. 2013. Validation of a refined technique for taking repeated blood samples from juvenile and adult mice. *Laboratory animals* 47(4), pp. 316-319.

Sage, A. P. et al. 2011. Hyperphosphatemia-induced nanocrystals upregulate the expression of bone morphogenetic protein-2 and osteopontin genes in mouse smooth muscle cells in vitro. *Kidney international* 79(4), pp. 414-422.

Sage, A. P. et al. 2010. Regulatory mechanisms in vascular calcification. *Nature reviews. Cardiology* 7(9), pp. 528-536.

Saidak, Z. et al. 2009. Agonists and allosteric modulators of the calcium-sensing receptor and their therapeutic applications. *Molecular pharmacology* 76(6), pp. 1131-1144.

Sandow, S. L. et al. 2002. Involvement of myoendothelial gap junctions in the actions of endothelium-derived hyperpolarizing factor. *Circulation research* 90(10), pp. 1108-1113.

Sansoe, G. et al. 2013. Calcium receptors located in fibrotic septa: a new target to reduce portal pressure in liver cirrhosis. *Clinical science* 125(2), pp. 67-75.

Schiff, H. and Lang, S. M. 2011. Hypertension Secondary to PHPT: Cause or Coincidence? *International journal of endocrinology* 2011, p. 974647.

Schneider, J. E. et al. 2006. How to perform an accurate assessment of cardiac function in mice using high-resolution magnetic resonance imaging. *Journal of cardiovascular magnetic resonance : official journal of the Society for Cardiovascular Magnetic Resonance* 8(5), pp. 693-701.

Schreier, B. et al. 2013. Loss of epidermal growth factor receptor in vascular smooth muscle cells and cardiomyocytes causes arterial hypotension and cardiac hypertrophy. *Hypertension* 61(2), pp. 333-340.

Shanahan, C. M. et al. 1994. High expression of genes for calcification-regulating proteins in human atherosclerotic plaques. *The Journal of clinical investigation* 93(6), pp. 2393-2402.

Shanahan, C. M. et al. 1999. Medial localization of mineralization-regulating proteins in association with Monckeberg's sclerosis: evidence for smooth muscle cell-mediated vascular calcification. *Circulation* 100(21), pp. 2168-2176.

Shanahan, C. M. et al. 2011. Arterial calcification in chronic kidney disease: key roles for calcium and phosphate. *Circulation research* 109(6), pp. 697-711.

Shanahan, C. M. and Weissberg, P. L. 1998. Smooth muscle cell heterogeneity: patterns of gene expression in vascular smooth muscle cells in vitro and in vivo. *Arteriosclerosis, thrombosis, and vascular biology* 18(3), pp. 333-338.

Shanahan, C. M. et al. 1993. Isolation of gene markers of differentiated and proliferating vascular smooth muscle cells. *Circulation research* 73(1), pp. 193-204.

Shen, Z. et al. 2012. Smooth muscle protein 22 alpha-Cre is expressed in myeloid cells in mice. *Biochemical and biophysical research communications* 422(4), pp. 639-642.

Sheriff, D. D. et al. 2000. Does autonomic blockade reveal a potent contribution of nitric oxide to locomotion-induced vasodilation? *American journal of physiology. Heart and circulatory physiology* 279(2), pp. H726-732.

Shimokawa, H. et al. 1996. The importance of the hyperpolarizing mechanism increases as the vessel size decreases in endothelium-dependent relaxations in rat mesenteric circulation. *Journal of cardiovascular pharmacology* 28(5), pp. 703-711.

Shoback, D. M. et al. 2003. The calcimimetic cinacalcet normalizes serum calcium in subjects with primary hyperparathyroidism. *The Journal of clinical endocrinology and metabolism* 88(12), pp. 5644-5649.

Shobeiri, N. et al. 2010. Vascular calcification in animal models of CKD: A review. *American journal of nephrology* 31(6), pp. 471-481.

Shroff, R. et al. 2013. Mechanistic insights into vascular calcification in CKD. *Journal of the American Society of Nephrology : JASN* 24(2), pp. 179-189.

Shroff, R. C. et al. 2008. Dialysis accelerates medial vascular calcification in part by triggering smooth muscle cell apoptosis. *Circulation* 118(17), pp. 1748-1757.

Shu, L. et al. 2011. The calcium-sensing receptor mediates bone turnover induced by dietary calcium and parathyroid hormone in neonates. *Journal of bone and mineral research : the official journal of the American Society for Bone and Mineral Research* 26(5), pp. 1057-1071.

Silve, C. et al. 2005. Delineating a Ca²⁺ binding pocket within the venus flytrap module of the human calcium-sensing receptor. *The Journal of biological chemistry* 280(45), pp. 37917-37923.

Silverberg, S. J. 2000. Editorial: cardiovascular disease in primary hyperparathyroidism. *The Journal of clinical endocrinology and metabolism* 85(10), pp. 3513-3514.

Smajilovic, S. et al. 2006. Extracellular calcium sensing in rat aortic vascular smooth muscle cells. *Biochemical and biophysical research communications* 348(4), pp. 1215-1223.

Smajilovic, S. et al. 2007. Calcimimetic, AMG 073, induces relaxation on isolated rat aorta. *Vascular pharmacology* 47(4), pp. 222-228.

Smajilovic, S. and Tfelt-Hansen, J. 2007. Calcium acts as a first messenger through the calcium-sensing receptor in the cardiovascular system. *Cardiovascular research* 75(3), pp. 457-467.

Smajilovic, S. et al. 2011. The calcium-sensing receptor and calcimimetics in blood pressure modulation. *British journal of pharmacology* 164(3), pp. 884-893.

Somjen, D. et al. 2005. 25-hydroxyvitamin D₃-1 α -hydroxylase is expressed in human vascular smooth muscle cells and is upregulated by parathyroid hormone and estrogenic compounds. *Circulation* 111(13), pp. 1666-1671.

Son, B. K. et al. 2006. Statins protect human aortic smooth muscle cells from inorganic phosphate-induced calcification by restoring Gas6-Axl survival pathway. *Circulation research* 98(8), pp. 1024-1031.

Sricharoenvej, S. et al. 2009. Morphological and microvascular changes of the adrenal glands in streptozotocin-induced long-term diabetic rats. *Italian journal of anatomy and embryology = Archivio italiano di anatomia ed embriologia* 114(1), pp. 1-10.

Stefenelli, T. et al. 1993. Primary hyperparathyroidism: incidence of cardiac abnormalities and partial reversibility after successful parathyroidectomy. *The American journal of medicine* 95(2), pp. 197-202.

Steitz, S. A. et al. 2001. Smooth muscle cell phenotypic transition associated with calcification: upregulation of Cbfa1 and downregulation of smooth muscle lineage markers. *Circulation research* 89(12), pp. 1147-1154.

Sternberg, N. and Hamilton, D. 1981. Bacteriophage P1 site-specific recombination. I. Recombination between loxP sites. *Journal of molecular biology* 150(4), pp. 467-486.

Stuckey, D. J. et al. 2012. In vivo MRI characterization of progressive cardiac dysfunction in the mdx mouse model of muscular dystrophy. *PloS one* 7(1), p. e28569.

Sun, J. and Murphy, E. 2010. Calcium-sensing receptor: a sensor and mediator of ischemic preconditioning in the heart. *American journal of physiology. Heart and circulatory physiology* 299(5), pp. H1309-1317.

Sun, W. et al. 2010. Alterations in phosphorus, calcium and PTHrP contribute to defects in dental and dental alveolar bone formation in calcium-sensing receptor-deficient mice. *Development* 137(6), pp. 985-992.

Sun, Y. et al. 2012. Smooth muscle cell-specific runx2 deficiency inhibits vascular calcification. *Circulation research* 111(5), pp. 543-552.

Sun, Y. et al. 2011. Sudan black B reduces autofluorescence in murine renal tissue. *Archives of pathology & laboratory medicine* 135(10), pp. 1335-1342.

Sun, Y. H. et al. 2006. Calcium-sensing receptor induces rat neonatal ventricular cardiomyocyte apoptosis. *Biochemical and biophysical research communications* 350(4), pp. 942-948.

Tfelt-Hansen, J. et al. 2006. Calcium receptor is functionally expressed in rat neonatal ventricular cardiomyocytes. *American journal of physiology. Heart and circulatory physiology* 290(3), pp. H1165-1171.

Thakore, P. and Ho, W. S. 2011. Vascular actions of calcimimetics: role of Ca(2)(+) -sensing receptors versus Ca(2)(+) influx through L-type Ca(2)(+) channels. *British journal of pharmacology* 162(3), pp. 749-762.

Tharmalingam, S. et al. 2011. Calcium-sensing receptor modulates cell adhesion and migration via integrins. *The Journal of biological chemistry* 286(47), pp. 40922-40933.

Thomsen, A. R. et al. 2012. Biased agonism of the calcium-sensing receptor. *Cell calcium* 51(2), pp. 107-116.

Thorin, E. et al. 1990. Vascular calcium overload produced by administration of vitamin D3 and nicotine in rats. Changes in tissue calcium levels, blood pressure, and pressor responses to electrical stimulation or norepinephrine in vivo. *Journal of cardiovascular pharmacology* 16(2), pp. 257-266.

Toka, H. R. et al. 2012. Deficiency of the calcium-sensing receptor in the kidney causes parathyroid hormone-independent hypocalciuria. *Journal of the American Society of Nephrology : JASN* 23(11), pp. 1879-1890.

Tomazic, B. B. et al. 1987. Nature and properties of cardiovascular deposits. *Scanning microscopy* 1(1), pp. 95-105.

Topala, C. N. et al. 2009. Activation of the Ca²⁺-sensing receptor stimulates the activity of the epithelial Ca²⁺ channel TRPV5. *Cell calcium* 45(4), pp. 331-339.

Tu, Q. et al. 2003. Rescue of the skeletal phenotype in CasR-deficient mice by transfer onto the Gcm2 null background. *The Journal of clinical investigation* 111(7), pp. 1029-1037.

Tyson, K. L. et al. 2003. Osteo/chondrocytic transcription factors and their target genes exhibit distinct patterns of expression in human arterial calcification. *Arteriosclerosis, thrombosis, and vascular biology* 23(3), pp. 489-494.

Urena-Torres, P. A. et al. 2013. Protocol adherence and the progression of cardiovascular calcification in the ADVANCE study. *Nephrology, dialysis, transplantation : official publication of the European Dialysis and Transplant Association - European Renal Association* 28(1), pp. 146-152.

Vargas-Poussou, R. et al. 2002. Functional characterization of a calcium-sensing receptor mutation in severe autosomal dominant hypocalcemia with a Bartter-like syndrome. *Journal of the American Society of Nephrology : JASN* 13(9), pp. 2259-2266.

Vazquez, R. et al. 2010. Accuracy of bedside physical examination in distinguishing categories of shock: a pilot study. *Journal of hospital medicine : an official publication of the Society of Hospital Medicine* 5(8), pp. 471-474.

Viegas, M. S. et al. 2007. An improved and cost-effective methodology for the reduction of autofluorescence in direct immunofluorescence studies on formalin-fixed paraffin-embedded tissues. *European journal of histochemistry : EJH* 51(1), pp. 59-66.

Villa-Bellosta, R. et al. 2011. Role of calcium-phosphate deposition in vascular smooth muscle cell calcification. *American journal of physiology. Cell physiology* 300(1), pp. C210-220.

Villa-Bellosta, R. and Sorribas, V. 2011. Calcium phosphate deposition with normal phosphate concentration. -Role of pyrophosphate. *Circulation journal : official journal of the Japanese Circulation Society* 75(11), pp. 2705-2710.

Vizard, T. N. et al. 2008. Regulation of axonal and dendritic growth by the extracellular calcium-sensing receptor. *Nature neuroscience* 11(3), pp. 285-291.

Walker, M. D. et al. 2010. Cardiac structure and diastolic function in mild primary hyperparathyroidism. *The Journal of clinical endocrinology and metabolism* 95(5), pp. 2172-2179.

Wang, C. C. et al. 2007. Insulin attenuates vascular smooth muscle calcification but increases vascular smooth muscle cell phosphate transport. *Atherosclerosis* 195(1), pp. e65-75.

Wang, Q. et al. 2010. Cardiac hypertrophy, low blood pressure, and low aldosterone levels in mice devoid of the three circadian PAR bZip transcription factors DBP, HLF, and TEF. *American journal of physiology. Regulatory, integrative and comparative physiology* 299(4), pp. R1013-1019.

Wang, R. et al. 2003. Calcium and polyamine regulated calcium-sensing receptors in cardiac tissues. *European journal of biochemistry / FEBS* 270(12), pp. 2680-2688.

Wang, W. et al. 2004. Baroreceptor reflex in heart failure. *Sheng li xue bao : [Acta physiologica Sinica]* 56(3), pp. 269-281.

Ward, B. K. et al. 2012. The role of the calcium-sensing receptor in human disease. *Clinical biochemistry* 45(12), pp. 943-953.

Ward, D. T. et al. 1998. Disulfide bonds in the extracellular calcium-polyvalent cation-sensing receptor correlate with dimer formation and its response to divalent cations in vitro. *The Journal of biological chemistry* 273(23), pp. 14476-14483.

Weston, A. H. et al. 2005. Evidence in favor of a calcium-sensing receptor in arterial endothelial cells: studies with calindol and Calhex 231. *Circulation research* 97(4), pp. 391-398.

White, E. et al. 2009. Pharmacochaperone-mediated rescue of calcium-sensing receptor loss-of-function mutants. *Molecular endocrinology* 23(7), pp. 1115-1123.

Wonneberger, K. et al. 2000. Evidence for a calcium-sensing receptor in the vascular smooth muscle cells of the spiral modiolar artery. *The Journal of membrane biology* 175(3), pp. 203-212.

Xu, R. et al. 2003. Human SM22 alpha BAC encompasses regulatory sequences for expression in vascular and visceral smooth muscles at fetal and adult stages. *American journal of physiology. Heart and circulatory physiology* 284(4), pp. H1398-1407.

Xue, Y. et al. 2012. The calcium-sensing receptor complements parathyroid hormone-induced bone turnover in discrete skeletal compartments in mice. *American journal of physiology. Endocrinology and metabolism* 302(7), pp. E841-851.

Yamamura, A. et al. 2012. Enhanced Ca(2+)-sensing receptor function in idiopathic pulmonary arterial hypertension. *Circulation research* 111(4), pp. 469-481.

Yamashita, T. et al. 2000. Identification of a novel fibroblast growth factor, FGF-23, preferentially expressed in the ventrolateral thalamic nucleus of the brain. *Biochemical and biophysical research communications* 277(2), pp. 494-498.

Yano, S. et al. 2000. Association of decreased calcium-sensing receptor expression with proliferation of parathyroid cells in secondary hyperparathyroidism. *Kidney international* 58(5), pp. 1980-1986.

Yano, S. et al. 2003. Decrease in vitamin D receptor and calcium-sensing receptor in highly proliferative parathyroid adenomas. *European journal of endocrinology / European Federation of Endocrine Societies* 148(4), pp. 403-411.

Yatabe, M. S. et al. 2012. Effects of a high-sodium diet on renal tubule Ca²⁺ transporter and claudin expression in Wistar-Kyoto rats. *BMC nephrology* 13, p. 160.

Yoshida, T. et al. 2002. Mediation of unusually high concentrations of 1,25-dihydroxyvitamin D in homozygous klotho mutant mice by increased expression of renal 1 α -hydroxylase gene. *Endocrinology* 143(2), pp. 683-689.

Yu, Q. et al. 2004. Characterization of high-salt and high-fat diets on cardiac and vascular function in mice. *Cardiovascular toxicology* 4(1), pp. 37-46.

Zhang, J. C. et al. 2001a. Analysis of SM22 α -deficient mice reveals unanticipated insights into smooth muscle cell differentiation and function. *Molecular and cellular biology* 21(4), pp. 1336-1344.

Zhang, X. et al. 2014. Calcium Sensing Receptor Promotes Cardiac Fibroblast Proliferation and Extracellular Matrix Secretion. *Cellular physiology and biochemistry : international journal of experimental cellular physiology, biochemistry, and pharmacology* 33(3), pp. 557-568.

Zhang, Z. et al. 2001b. The extracellular calcium-sensing receptor dimerizes through multiple types of intermolecular interactions. *The Journal of biological chemistry* 276(7), pp. 5316-5322.

Zhu, D. et al. 2011. The appearance and modulation of osteocyte marker expression during calcification of vascular smooth muscle cells. *PloS one* 6(5), p. e19595.

Ziegelstein, R. C. et al. 2006. Expression of a functional extracellular calcium-sensing receptor in human aortic endothelial cells. *Biochemical and biophysical research communications* 342(1), pp. 153-163.

Zitt, E. et al. 2011. Effect of cinacalcet on renal electrolyte handling and systemic arterial blood pressure in kidney transplant patients with persistent hyperparathyroidism. *Transplantation* 92(8), pp. 883-889.

11 Appendix A

In this appendix, the raw data values of the experiments are given in tabularised format.

Table 14: Weights of WT, HET and KO mice. N = number of weighed animals. Mean \pm SEM. 1–6 month data by Thomas Davies (Davies 2013), 12 and 18 month data by MS.

Age	WT			N	HET			N	KO			N
Male												
1	15.65	\pm	0.56	41	15.27	\pm	1.35	9	14.79	\pm	0.76	21
2	25.18	\pm	0.38	37	26.70	\pm	0.70	10	25.72	\pm	0.50	21
3	28.12	\pm	0.35	65	29.52	\pm	0.61	17	27.64	\pm	0.41	27
4	29.78	\pm	0.41	27	29.68	\pm	0.36	7	28.81	\pm	0.38	21
5	31.76	\pm	0.39	42	32.70	\pm	0.97	10	29.96	\pm	0.53	19
6	33.69	\pm	0.56	25	36.45	\pm	1.29	6	32.93	\pm	1.22	8
12	39.57	\pm	1.98	3					37.52	\pm	2.17	3
18	36.30	\pm	2.20	3					35.78	\pm	1.52	3
Female												
1	14.87	\pm	0.40	35	11.34	\pm	1.07	4	12.27	\pm	0.75	21
2	20.99	\pm	0.34	33	21.57	\pm	0.40	5	20.19	\pm	0.54	19
3	23.53	\pm	0.38	36	22.85	\pm	0.50	7	22.37	\pm	0.54	17
4	25.46	\pm	0.61	19	24.65	\pm	0.69	4	23.01	\pm	0.66	13
5	26.90	\pm	0.48	25	25.38	\pm	0.51	7	25.06	\pm	1.04	15
6	30.20	\pm	1.25	8	25.70	\pm	0.35	3	28.70	\pm	2.11	6

Table 15: Results of quantitative immunofluorescence analysis of CaSR expression levels in VSMC preparations of passages 2-6 cultured from WT and KO aortae. CaSR staining intensities were normalised to the SM22 α intensity of the respective cell batch and weighed in respect to the cell number in the respective batch. Staining intensity of KO cells is expressed as fold change compared to WT. Results are shown for all cells present in the preparation (all cells) for either positively stained samples (Positive) or negative controls (Negative) or for the population of VSMC only (VSMC only). All cell group: N = 9 (WT positive), 6 (KO positive), 6 (WT negative), 3 (KO negative), Mean + SEM, * p < 0.05, two-way ANOVA with Bonferroni post-test WT vs KO (p values), VSMC cell only group: N = 9 (WT), 6 (KO), Mean + SEM, ** p < 0.01, two-tailed T-test.

Group	Unit	WT	KO	P
All cells				
Positive	fold	1.000 ± 0.090	0.683 ± 0.075	< 0.05 *
Negative	fold	0.177 ± 0.039	0.091 ± 0.048	> 0.05
VSMC only	fold	1.000 ± 0.081	0.559 ± 0.094	0.0038 **

Table 16: Results of VSMC proliferation studies. Day = days in culture. All data presented as fold-change vs. the data at 1.2 mM Ca²⁺ of the respective first group (Day 5, WT). N = 5 (control VSMC), 1 (WT, KO VSMC), n = 3. All cell batches contained VSMC isolated from 2-3 mice. Mean ± SEM. Two-way ANOVA with Bonferroni post-test (p-values) for Day 10 1.2 mM Ca²⁺ (Day 10) and vs. WT 1.2 mM Ca²⁺ (WT).

Group	Unit	Day 5	Day 10	p
Control cells				
1.2 mM Ca ²⁺	fold	1.00 ± 0.09	3.96 ± 0.72	-
1.8 mM Ca ²⁺	fold	1.21 ± 0.16	6.51 ± 1.27	> 0.05
2.5 mM Ca ²⁺	fold	1.12 ± 0.07	11.95 ± 2.47	< 0.001
WT vs KO VSMC				
1.2 mM Ca ²⁺	fold	1.00 ± 0.07	0.97 ± 0.05	> 0.05
1.8 mM Ca ²⁺	fold	0.98 ± 0.08	0.99 ± 0.09	> 0.05
2.5 mM Ca ²⁺	fold	1.70 ± 0.03	1.11 ± 0.03	< 0.001

Table 17: Results of *ex vivo* aortic ring calcification experiments. All aortic rings were incubated in the presence of 1.8 mM Ca²⁺ and 3 mM Pi. Values in µg Ca²⁺ normalised to explant weight (mg) for 10 days. Mean (± SEM when N > 2), Two-way ANOVA with Bonferroni post-test (for 6 month male group; p-values).

Group	Unit	WT	KO	P
6 month old male mice, N =6				
Endothelium intact				
Vehicle	fold	1.66 ± 0.23	2.81 ± 0.77	> 0.05
10 nM R-568	fold	2.59 ± 0.31	2.19 ± 0.08	> 0.05
Endothelium removed				
Vehicle	fold	2.20 ± 0.34	1.90 ± 0.17	> 0.05
10 nM R-568	fold	2.95 ± 0.62	5.18 ± 1.79	> 0.05

Table 18: Blood pressure measurements via tail cuff. The values for the 3-6 and 10-14 month old animals were obtained with a loan unit (subsequently proven to overestimate its readings, marked “loan” in the table). Since this overestimation applies to the measurements of both WT and KO mice, it was deemed that the values between the two genotypes were still useable for the relative comparisons. Normalised values are averages of all WT and KO values normalised to their respective age group’s mean WT values (mean WT = 1), either including or excluding the overestimated values of the 3-6 and 10-14 month age group measured with the loan unit. Diastolic = diastolic blood pressure, systolic = systolic blood pressure, MAP = mean arterial pressure. Mean \pm SEM, * $p < 0.05$, ** $p < 0.01$, *** $p < 0.001$, two-tailed T-test.

Parameter	Unit	WT		KO		P
3-6 month old animals, N = 8 (WT), 13 (KO) – loan						
Diastolic	mm Hg	145.75	\pm 4.17	103.92	\pm 5.08	< 0.0001 ***
Systolic	mm Hg	187.31	\pm 3.36	157.76	\pm 4.60	0.0002 ***
MAP	mm Hg	159.19	\pm 3.73	121.53	\pm 4.64	< 0.0001 ***
10-14 month old animals, N = 3 (WT), 6 (KO) – loan						
Diastolic	mm Hg	103.06	\pm 4.94	90.65	\pm 6.70	0.2684
Systolic	mm Hg	133.22	\pm 4.41	130.26	\pm 7.60	0.8041
MAP	mm Hg	112.74	\pm 4.76	103.50	\pm 6.52	0.3879
4 month old animals, N = 3 (WT), 9 (KO)						
Diastolic	mm Hg	76.73	\pm 1.23	72.13	\pm 2.54	0.3402
Systolic	mm Hg	108.60	\pm 4.15	104.65	\pm 3.12	0.5242
MAP	mm Hg	86.97	\pm 2.12	82.67	\pm 2.68	0.4028
9 month old animals, N = 7 (WT), 11 (KO)						
Diastolic	mm Hg	80.41	\pm 3.72	70.40	\pm 2.60	0.0475 *
Systolic	mm Hg	109.97	\pm 4.35	101.75	\pm 3.36	0.1781
MAP	mm Hg	89.95	\pm 3.87	80.49	\pm 2.75	0.0717
17 month old animals, N = 3 (WT), 13 (KO)						
Diastolic	mm Hg	78.25	\pm 2.94	70.94	\pm 2.96	0.2765
Systolic	mm Hg	108.18	\pm 1.88	104.07	\pm 3.29	0.5715
MAP	mm Hg	87.88	\pm 2.46	81.61	\pm 3.04	0.3563
Normalised combined values, N = 22 (WT), 52 (KO) – including loan						
Diastolic	fold	1.000	\pm 0.016	0.854	\pm 0.020	< 0.0001 ***
Systolic	fold	1.000	\pm 0.012	0.926	\pm 0.015	0.0045 **
MAP	fold	1.000	\pm 0.014	0.883	\pm 0.018	0.0001 ***
Normalised combined values, N = 11 (WT), 33 (KO) – excluding loan						
Diastolic	fold	1.000	\pm 0.022	0.905	\pm 0.020	0.0159 *
Systolic	fold	1.000	\pm 0.020	0.950	\pm 0.017	0.1293
MAP	fold	1.000	\pm 0.020	0.923	\pm 0.019	0.0331 *

Table 19: Paw temperatures of 3-6 and 10-14 month old male mice. Paw T. = Paw temperature, mean \pm SEM, * $p < 0.05$, two-tailed T-test.

Parameter	Unit	WT	KO	p
3-6 month old animals, N = 10 (WT), 11 (KO)				
Paw T.	°C	17.75 \pm 0.13	17.23 \pm 0.13	0.0106 *
10-14 month old animals, N =3 (WT), 7 (KO)				
Paw T.	°C	17.48 \pm 0.19	17.29 \pm 0.13	0.4625

Table 20: Results of radiotelemetry experiments carried out on 3 month old WT and KO mice, standard diet (1) vs. high salt diet (4 % NaCl diet). Active and resting intervals were globally selected for all mice (active: 20:00-22:00, resting: 8:00-10:00). See Figure 12 for experimental timeline, Figure 18 for selected active and resting time intervals and Table 8 for parameter explanations and abbreviations. * $p < 0.05$, ** $p < 0.01$, *** $p < 0.001$. N = 5, mean \pm SEM, two way ANOVA and Bonferroni post-test. P^a = Bonferroni post-test (WT vs KO), P^b = ANOVA (WT vs KO) within active or resting groups, P^c = ANOVA (diets) within active or resting groups.

Parameter	Unit	WT	KO	P ^a	P ^b	P ^c
Standard diet (1) – Active						
Systolic	mm Hg	133.46 \pm 1.79	126.61 \pm 4.40			
Diastolic	mm Hg	104.05 \pm 1.55	92.37 \pm 3.81	*		
MAP	mm Hg	118.95 \pm 1.34	109.67 \pm 4.18			
PH	mm Hg	29.41 \pm 1.96	34.24 \pm 1.64			
HR	bpm	638.90 \pm 2.34	545.35 \pm 22.82	**		
dp/dt	mm Hg / ms	2412.13 \pm 109.40	2628.54 \pm 300.31			
4 % NaCl diet – Active						
Systolic	mm Hg	133.10 \pm 4.48	123.45 \pm 3.26		*	
Diastolic	mm Hg	103.77 \pm 0.99	90.49 \pm 3.29	**	***	
MAP	mm Hg	118.14 \pm 2.13	107.05 \pm 3.22	*	**	
PH	mm Hg	29.33 \pm 3.94	32.96 \pm 1.05			
HR	bpm	610.53 \pm 19.83	515.24 \pm 24.56	**	***	
dp/dt	mm Hg / ms	2041.84 \pm 104.63	2307.40 \pm 231.43			
Standard diet (1) – Resting						
Systolic	mm Hg	116.04 \pm 3.17	119.39 \pm 3.91			
Diastolic	mm Hg	87.15 \pm 1.60	84.74 \pm 4.09			
MAP	mm Hg	101.65 \pm 2.39	102.02 \pm 4.11			
PH	mm Hg	28.88 \pm 1.75	34.65 \pm 2.34			
HR	bpm	488.98 \pm 13.60	457.74 \pm 32.83			
dp/dt	mm Hg / ms	2181.70 \pm 96.08	2451.37 \pm 245.78			
4 % NaCl diet – Resting						
Systolic	mm Hg	114.04 \pm 2.57	113.59 \pm 1.87			
Diastolic	mm Hg	85.57 \pm 1.39	78.63 \pm 2.28			
MAP	mm Hg	99.68 \pm 1.49	95.78 \pm 1.92			
PH	mm Hg	28.46 \pm 2.54	34.97 \pm 1.92		*	
HR	bpm	469.78 \pm 13.98	382.86 \pm 9.06	*	**	*
dp/dt	mm Hg / ms	2197.51 \pm 127.27	2293.60 \pm 186.32			

Table 21: Results of radiotelemetry experiments carried out on 3 month old WT and KO mice, standard diet (2) vs. 0.5 mg / l L-NAME in drinking water. Active and resting intervals were globally selected for all mice (active: 20:00-22:00, resting: 8:00-10:00). See Figure 12 for experimental timeline, Figure 18 for selected active and resting time intervals and Table 8 for parameter explanations and abbreviations. * p < 0.05, ** p < 0.01, *** p < 0.001. N = 5, mean ± SEM, two way ANOVA and Bonferroni post-test. P^a = Bonferroni post-test (WT vs KO), P^b = ANOVA (WT vs KO) within active or resting groups, P^c = ANOVA (diets) within active or resting groups.

Parameter	Unit	WT	KO	P ^a	P ^b	P ^c
Standard diet (2) – Active						
Systolic	mm Hg	127.25 ± 4.86	112.06 ± 2.61			
Diastolic	mm Hg	101.42 ± 4.93	81.31 ± 2.15	**		
MAP	mm Hg	114.61 ± 4.66	97.27 ± 2.39	**		
PH	mm Hg	25.83 ± 2.46	30.75 ± 1.48			
HR	bpm	621.09 ± 19.69	515.71 ± 16.07	**		
dp/dt	mm Hg / ms	1934.87 ± 162.26	2437.19 ± 244.26			
0.5 mg / l L-NAME – Active						
Systolic	mm Hg	130.00 ± 4.85	127.89 ± 4.65			*
Diastolic	mm Hg	101.79 ± 3.59	89.89 ± 4.11		***	
MAP	mm Hg	115.77 ± 3.40	108.62 ± 4.19		**	
PH	mm Hg	28.22 ± 4.57	38.00 ± 2.07		*	
HR	bpm	537.37 ± 20.03	447.58 ± 13.02	**	***	***
dp/dt	mm Hg / ms	1945.58 ± 293.48	2639.18 ± 241.91		*	
Standard diet (2) – Resting						
Systolic	mm Hg	108.63 ± 2.32	106.62 ± 2.31			
Diastolic	mm Hg	82.67 ± 1.48	76.75 ± 3.36			
MAP	mm Hg	95.98 ± 1.60	92.01 ± 2.80			
PH	mm Hg	25.97 ± 2.04	29.87 ± 1.94			
HR	bpm	482.77 ± 23.93	459.67 ± 19.98			
dp/dt	mm Hg / ms	2008.36 ± 95.08	2399.02 ± 259.70			
0.5 mg / l L-NAME – Resting						
Systolic	mm Hg	122.83 ± 3.69	131.43 ± 5.31			***
Diastolic	mm Hg	95.11 ± 5.74	91.78 ± 5.27			**
MAP	mm Hg	108.84 ± 4.37	111.20 ± 5.23			***
PH	mm Hg	27.72 ± 4.32	39.65 ± 1.44	*	**	*
HR	bpm	472.45 ± 20.85	433.42 ± 18.17			
dp/dt	mm Hg / ms	1943.23 ± 276.62	2722.47 ± 201.67	*	*	

Table 22: Results of cardiac MRI analysis of 12 month old animals. TBW = Total body weight, See Table 9 for abbreviations. LV-EF 3b = left ventricular ejection fraction approximated from third basal MRI slice only. # PFR and PER: one cardiac cycle normalised to 1 second. N = 3, Mean \pm SEM, ** p < 0.01, two-tailed T-test.

Parameter	Unit	WT	KO	P
Raw values				
TBW	g	38.0 \pm 4.2	32.9 \pm 0.2	0.2997
LVM	mg	141.0 \pm 13.5	135.3 \pm 11.4	0.7646
LV-EDV	μ l	60.0 \pm 7.5	68.7 \pm 6.6	0.4360
LV-ESV	μ l	22.0 \pm 4.0	28.3 \pm 8.4	0.5339
LV-SV	μ l	38.0 \pm 3.5	41.0 \pm 4.2	0.6111
LV-EF	%	63.7 \pm 1.9	60.0 \pm 8.5	0.6952
LV-PFR	μ l / s [#]	174.7 \pm 23.9	173.0 \pm 15.5	0.9562
LV-PER	μ l / s [#]	165.3 \pm 12.7	195.7 \pm 38.3	0.4937
DRI	g / μ l	2.4 \pm 0.1	2.0 \pm 0.0	0.0059 **
SRI	g / μ l	6.6 \pm 0.5	5.4 \pm 1.0	0.3207
EDL	mm	8.3 \pm 0.2	9.1 \pm 0.2	0.0503
EDD	mm	6.5 \pm 0.2	6.5 \pm 0.2	0.8203
ESL	mm	7.8 \pm 0.1	8.7 \pm 0.2	0.0093 **
ESD	mm	6.0 \pm 0.2	6.1 \pm 0.1	0.9001
Normalised to TBW				
LVM	mg / g	3.765 \pm 0.343	4.111 \pm 0.349	0.5190
LV-EDV	μ l / g	1.598 \pm 0.166	2.086 \pm 0.201	0.1345
LV-ESV	μ l / g	0.580 \pm 0.075	0.859 \pm 0.253	0.3491
LV-SV	μ l / g	1.017 \pm 0.103	1.247 \pm 0.134	0.2459
EDL	mm / g	0.224 \pm 0.025	0.276 \pm 0.006	0.1096
EDD	mm / g	0.176 \pm 0.017	0.196 \pm 0.006	0.3128
ESL	mm / g	0.210 \pm 0.024	0.265 \pm 0.005	0.0843
ESD	mm / g	0.162 \pm 0.015	0.184 \pm 0.002	0.2249

Table 23: Results of cardiac MRI analysis of 14 month old animals. TBW = Total body weight, See Table 9 for abbreviations, KO (no vis remod): hearts of KO mice which did not show any apparent difference compared to WT control by visual observation, KO (vis remod): hearts of KO mice which showed apparent remodelling compared to WT control by visual observation. # PFR and PER: one cardiac cycle normalised to 1 second. N = 5 (WT), 6 (KO (no rem)), 5 (KO (rem)), Mean \pm SEM, ANOVA with Dunnett post-test vs. WT (p-values).

Parameter	Unit	WT	KO (no vis. remod.)	P
TBW	g	34.6 \pm 3.0	31.6 \pm 1.8	> 0.05
LVM	mg	124.1 \pm 10.5	119.5 \pm 9.9	> 0.05
LV-EDV	μ l	62.0 \pm 9.2	60.3 \pm 6.6	> 0.05
LV-ESV	μ l	22.8 \pm 5.9	20.0 \pm 3.6	> 0.05
LV-SV	μ l	38.8 \pm 3.2	40.3 \pm 3.3	> 0.05
LV-EF	μ l	65.4 \pm 4.2	68.7 \pm 3.8	> 0.05
LV-PFR	μ l / s [#]	178.4 \pm 31.3	220.0 \pm 29.7	> 0.05
LV-PER	μ l / s [#]	215.6 \pm 47.1	200.0 \pm 19.9	> 0.05
DRI	g / μ l	2.1 \pm 0.1	2.0 \pm 0.1	> 0.05
SRI	g / μ l	6.7 \pm 1.3	7.6 \pm 2.0	> 0.05
EDL	mm	8.8 \pm 0.4	8.8 \pm 0.2	> 0.05
EDD	mm	6.1 \pm 0.2	5.9 \pm 0.2	> 0.05
ESL	mm	7.8 \pm 0.3	7.3 \pm 0.3	> 0.05
ESD	mm	5.5 \pm 0.2	5.6 \pm 0.3	> 0.05
RV-EDV	μ l	22.8 \pm 2.9	43.3 \pm 7.6	> 0.05
RV-ESV	μ l	9.0 \pm 2.8	13.0 \pm 3.8	> 0.05
RV-SV	μ l	14.0 \pm 0.6	30.2 \pm 5.1	> 0.05
RV-EF	%	64.6 \pm 7.9	72.0 \pm 6.0	> 0.05

			KO (vis. remod.)	
TBW	g		36.7 \pm 1.5	> 0.05
LVM	mg		124.7 \pm 6.3	> 0.05
LV-EDV	μ l		45.6 \pm 2.9	> 0.05
LV-ESV	μ l		9.4 \pm 2.4	> 0.05
LV-SV	μ l		36.4 \pm 1.1	> 0.05
LV-EF	μ l		80.6 \pm 4.4	< 0.05 *
LV-PFR	μ l / s [#]		137.0 \pm 14.9	> 0.05
LV-PER	μ l / s [#]		206.6 \pm 20.3	> 0.05
DRI	g / μ l		2.8 \pm 0.1	< 0.001 ***
SRI	g / μ l		21.7 \pm 9.5	< 0.01 **
EDL	mm		8.7 \pm 0.2	> 0.05
EDD	mm		5.9 \pm 0.1	> 0.05
ESL	mm		7.4 \pm 0.3	> 0.05
ESD	mm		5.4 \pm 0.1	> 0.05
RV-EDV	μ l		29.8 \pm 8.3	> 0.05
RV-ESV	μ l		15.0 \pm 6.2	> 0.05
RV-SV	μ l		14.8 \pm 3.1	< 0.05 *
RV-EF	%		54.4 \pm 10.8	> 0.05

Table 24: Results of cardiac MRI analysis of 14 month old animals normalised to total body weight. See Table 9 for abbreviations, KO (no vis remod): hearts of KO mice which did not show any apparent difference compared to WT control by visual observation, KO (vis remod): hearts of KO mice which showed apparent remodelling compared to WT control by visual observation. N = 5 (WT), 6 (KO (no rem)), 5 (KO (rem)), Mean \pm SEM, ANOVA with Dunnett post-test vs. WT (p-values).

Parameter	Unit	WT	KO (no vis. remod.)	P
LVM	mg / g	3.607 \pm 0.191	3.765 \pm 0.183	> 0.05
LV-EDV	μ l / g	1.781 \pm 0.206	1.895 \pm 0.176	> 0.05
LV-ESV	μ l / g	0.639 \pm 0.147	0.617 \pm 0.105	> 0.05
LV-SV	μ l / g	1.131 \pm 0.071	1.278 \pm 0.093	> 0.05
EDL	mm / g	0.260 \pm 0.018	0.284 \pm 0.019	> 0.05
EDD	mm / g	0.179 \pm 0.012	0.189 \pm 0.009	> 0.05
ESL	mm / g	0.232 \pm 0.022	0.236 \pm 0.018	> 0.05
ESD	mm / g	0.163 \pm 0.015	0.179 \pm 0.007	> 0.05
RV-EDV	μ l / g	0.661 \pm 0.062	1.367 \pm 0.257	> 0.05
RV-ESV	μ l / g	0.252 \pm 0.069	0.415 \pm 0.129	> 0.05
RV-SV	μ l / g	0.414 \pm 0.032	0.946 \pm 0.160	> 0.05
		KO (vis. remod.)		
LVM	mg / g		3.399 \pm 0.112	> 0.05
LV-EDV	μ l / g		1.243 \pm 0.067	> 0.05
LV-ESV	μ l / g		0.253 \pm 0.064	> 0.05
LV-SV	μ l / g		0.995 \pm 0.031	> 0.05
EDL	mm / g		0.239 \pm 0.014	> 0.05
EDD	mm / g		0.161 \pm 0.005	> 0.05
ESL	mm / g		0.202 \pm 0.010	> 0.05
ESD	mm / g		0.147 \pm 0.004	> 0.05
RV-EDV	μ l / g		0.817 \pm 0.216	> 0.05
RV-ESV	μ l / g		0.406 \pm 0.162	> 0.05
RV-SV	μ l / g		0.411 \pm 0.091	< 0.05 *

Table 25: Results of metabolic cage studies of 12-18 month old WT and KO animals and 3 month old WT and KO animals on standard or high salt (containing 4 % NaCl) diet. Values are normalised against collection period and body weight of the individual animals. ** p < 0.01, mean + SEM, exact p values of two-tail t-tests (12-18 month animal group) and approximations for the Bonferroni post-test of two-way ANOVAs (3 month animal group, WT vs KO) are reported. C. = consumption, e. = excretion

Parameter	Unit	WT	KO	p
12 – 18 month old animals, N = 5-6				
Food c.	(mg / h) / g	1.54 ± 0.30	1.25 ± 0.34	0.6810
Faeces e.	(mg / h) / g	1.84 ± 0.23	2.86 ± 0.30	0.0235 *
Water c.	(mg / h) / g	4.75 ± 0.70	5.71 ± 0.47	0.2794
Urine e.	(mg / h) / g	8.95 ± 1.54	8.97 ± 0.86	0.9927
3 month old animals, N = 5-6				
Standard diet				
Food c.	(mg / h) / g	6.28 ± 0.32	6.36 ± 0.12	> 0.05
Faeces e.	(mg / h) / g	2.65 ± 0.15	2.78 ± 0.14	> 0.05
Water c.	(mg / h) / g	7.91 ± 0.92	9.57 ± 1.64	> 0.05
Urine e.	(mg / h) / g	2.50 ± 0.23	3.24 ± 0.89	> 0.05
4% NaCl diet				
Food c.	(mg / h) / g	6.50 ± 0.12	6.69 ± 0.57	> 0.05
Faeces e.	(mg / h) / g	2.77 ± 0.14	3.13 ± 0.45	> 0.05
Water c.	(mg / h) / g	14.08 ± 1.50	17.15 ± 1.05	> 0.05
Urine e.	(mg / h) / g	5.97 ± 0.89	9.26 ± 0.52	< 0.01 **

Table 26: Clinical chemistry of WT and KO mouse serum and plasma. K⁺ levels of 3 and 18 month old mice were non interpretable due to haemolysis in the samples. * p < 0.05, ** p < 0.01 WT vs. KO, mean ± SEM, two-tailed T-test.

Parameter	Unit	WT	KO	P
3 month old mice, N = 11 (WT), 4-6 (KO)				
Na ⁺	mmol / l	146.4 ± 0.8	147.3 ± 1.1	0.5806
Cl ⁻	mmol / l	110.6 ± 1.0	111.5 ± 3.2	0.7293
Ca ²⁺	mmol / l	2.3 ± 0.1	3.0 ± 0.3	0.0047 **
Mg ²⁺	mmol / l	1.06 ± 0.03	1.14 ± 0.09	0.3107
FGF23	pg / ml	145.0 ± 11.0	384.4 ± 83.5	0.0015 **
3 month old mice, N = 12, 19 (PTH), 11 (WT: 1,25-D3), 9 (KO: 1,25-D3)				
PTH	pg / ml	161.42 ± 32.65	240.05 ± 57.03	0.2636
1,25-D3	pmol / l	188.85 ± 28.87	391.89 ± 65.53	0.0072 **
Aldosterone	pg / ml	508.07 ± 57.45	421.81 ± 59.24	0.3072
Renin	ng / ml	123.82 ± 16.74	115.44 ± 11.65	0.6849
Fetuin A	µg / ml	201.43 ± 11.80	192.98 ± 11.79	0.6171
3 month old mice, metabolic cage studies, N=4-6				
Na ⁺	mmol / l	143.5 6 0.63	140.6 4 0.94	0.0295 *
K ⁺	mmol / l	5.2 3 0.23	5.6 3 0.10	0.2092
Cl ⁻	mmol / l	106.5 6 0.55	106.9 4 1.13	0.7469
Ca ²⁺	mmol / l	2.3 6 0.07	3.5 5 0.24	0.0003 ***
Mg ²⁺	mmol / l	1.2 6 0.04	1.3 5 0.07	0.1263
Pi	mmol / l	2.6 6 0.10	1.9 5 0.33	0.0679
Creatinine	µmol / l	15.4 6 0.66	13.0 5 0.57	0.0265 *
Urea	mmol / l	10.1 6 0.52	10.4 5 0.15	0.6474
Total Protein	mg / ml	54.4 6 1.21	51.2 4 1.32	0.1196
18 month old mice, N = 3				
Na ⁺	mmol / l	149.0 ± 2.1	146.3 ± 1.8	0.3837
Cl ⁻	mmol / l	114.3 ± 0.7	111.0 ± 2.1	0.2020
Ca ²⁺	mmol / l	2.3 ± 0.1	3.0 ± 0.2	0.0401 *
Mg ²⁺	mmol / l	1.65 ± 0.10	2.04 ± 0.19	0.1369
FGF23	pg / ml	131.1 ± 26.3	330.0 ± 28.7	0.0069 **

Table 27: Clinical chemistry of WT and KO mouse urine. ** p < 0.01 WT, *** p < 0.001, mean ± SEM, two-way ANOVA with Bonferroni post-test (3 month old mice, p-values = WT vs KO post-test).

Parameter	Unit	WT	KO	P
Standard diet, N = 5-6, 4 (Mg²⁺ WT), 3 (Mg²⁺ KO)				
Na ⁺ :Cr	fold	38.81 ± 2.90	32.87 ± 3.85	> 0.05
K ⁺ :Cr	fold	50.51 ± 2.95	57.53 ± 2.76	> 0.05
Cl ⁻ :Cr	fold	71.68 ± 3.69	67.62 ± 6.03	> 0.05
Ca ²⁺ :Cr	fold	0.94 ± 0.17	5.52 ± 1.23	< 0.001 ***
Mg ²⁺ :Cr	fold	6.54 ± 0.71	7.87 ± 1.42	> 0.05
Pi:Cr	fold	7.73 ± 0.98	21.43 ± 1.97	< 0.001 ***
Creatinine	µmol / d / g	0.23 ± 0.01	0.22 ± 0.03	> 0.05
Total protein	µg / dl / d / g	1.97 ± 0.33	1.60 ± 0.31	> 0.05
Urea	µmol / d / g	80.23 ± 6.37	80.84 ± 9.91	> 0.05
Uric acid	nmol / d / g	37.33 ± 2.93	32.96 ± 7.29	> 0.05
4 % NaCl diet, N=6				
Na ⁺ :Cr	fold	296.58 ± 20.24	333.04 ± 18.41	> 0.05
K ⁺ :Cr	fold	91.90 ± 3.23	107.57 ± 4.40	< 0.01 **
Cl ⁻ :Cr	fold	358.59 ± 21.97	407.98 ± 23.00	> 0.05
Ca ²⁺ :Cr	fold	1.83 ± 0.15	7.81 ± 0.74	< 0.001 ***
Mg ²⁺ :Cr	fold	7.59 ± 7.59	10.42 ± 10.42	< 0.01 **
Pi:Cr	fold	12.50 ± 1.08	27.05 ± 1.00	< 0.001 ***
Creatinine	µmol / d / g	0.25 ± 0.04	0.21 ± 0.01	> 0.05
Total protein	µg / dl / d / g	1.74 ± 0.19	1.38 ± 0.23	> 0.05
Urea	µmol / d / g	101.80 ± 14.24	91.89 ± 4.73	> 0.05
Uric acid	nmol / d / g	57.95 ± 9.24	50.17 ± 4.01	> 0.05

Table 28: Results of μ CT analysis of 3 month old WT and KO mice. See Table 10 for list of parameter abbreviations. AU = arbitrary units. Mean \pm SEM, * $p < 0.05$, ** $p < 0.01$, two-tailed T-test.

Parameter	Unit	WT (N = 8)		KO (N = 9)		p	
Tb.TV	mm ³	2.13	\pm 0.09	1.88	\pm 0.05	0.0236	*
Tb.BV	mm ³	0.33	\pm 0.02	0.24	\pm 0.01	0.0013	**
Tb.BV/TV	fold	0.16	\pm 0.01	0.13	\pm 0.01	0.0134	*
Tb.CD	mm	369.6	\pm 14.1	285.2	\pm 16.5	0.0016	**
Tb.SMI	AU	2.07	\pm 0.10	2.37	\pm 0.05	0.0123	*
Tb.N	1/mm	5.91	\pm 0.15	5.08	\pm 0.27	0.0189	*
Tb.Th	μ m	39.3	\pm 2.1	37.4	\pm 1.5	0.4827	
Tb.Sp	mm	0.17	\pm 0.00	0.19	\pm 0.01	0.0140	*
Tb.BMD	AU	1165	\pm 3	1139	\pm 8	0.0098	**
Ct.TV	mm ³	0.40	\pm 0.01	0.39	\pm 0.01	0.3707	
Ct.BV	mm ³	0.27	\pm 0.01	0.25	\pm 0.01	0.2036	
Ct.BV/TV	fold	0.66	\pm 0.01	0.66	\pm 0.01	0.5443	
Ct.BMD	AU	1433	\pm 12	1394	\pm 6	0.0069	**
Ct.Th	mm	0.24	\pm 0.01	0.23	\pm 0.00	0.2344	

12 Appendix B

Results and experiments listed here were performed correctly but were either redundant with other results or could not be interpreted due to methodical or other underlying reasons.

12.1 VSMC apoptosis

Apoptosis of cultured VSMC from WT and KO mice was measured by TUNEL staining followed by quantitative immunofluorescence analysis. Prior to the staining, VSMC were cultured in culture medium containing 1.2, 1.8 or 2.5 mM Ca^{2+} and 1 or 3 mM Pi for 48 h to investigate possible effects of extracellular Ca^{2+} and Pi concentration on prevalence of apoptosis in these cells, analogous to the proliferation experiments described before. 3 (WT) and 4 (KO) individual VSMC preparations, each containing VSMC grown from aortae of 2–3 mice, were analysed at different passages and in multiple technical repeats with a total of 91,690 cells in 36 ROIs for WT and 293,651 cells in 48 ROIs for KO.

Analysed VSMC preparations showed a very high degree of heterogeneity in themselves as well as in between each other. Even though VSMC ($\text{SM22}\alpha^+$) could be selected via gating, these differences make a final interpretation impossible.

Apoptotic and non-apoptotic cells were clearly identifiable by the TUNEL staining, as apoptotic nuclei showed strong and immediately recognizable staining (*c.f.* Figure 12). Cells from all different culture conditions combined showed a clear difference in TUNEL staining between apoptotic and non-apoptotic cells, with no differences between cell isolated from WT or KO mice. Apoptotic nuclei were significantly smaller than their non-apoptotic counterparts, again with no differences between genotypes (Figure 100).

The percentage of apoptotic cells of all cells present in the VSMC cultures was about 4-fold higher in cells isolated from WT mice than cells isolated from KO mice, although batch to batch variability was high. No influence of extracellular Ca^{2+} or Pi concentration on apoptosis rate was found (Figure 101). When looking at VSMC ($\text{SM22}\alpha^+$ populations only, see above), both VSMC from WT as well as KO mice showed the same rate of about 1% apoptotic cells (Figure 102), independent of extracellular Ca^{2+} and Pi concentrations. The increased apoptotic rate in observed in WT cells compared to KO when looking at all cells can therefore be limited to non-VSMC. Total cell density (cells / mm^2) showed an about 2-fold increase in KO

cells compared to WT control, independent of extracellular Ca^{2+} or Pi concentration (Figure 103) which is in agreement with the lower rates of apoptosis in KO cells compared to WT when looking at all cells.

All numerical results are listed in Table 29.

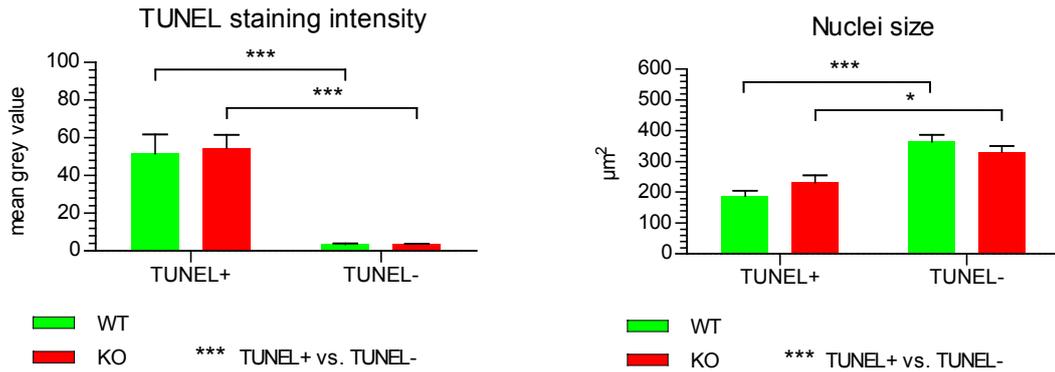


Figure 100: Quantitative fluorescence microscopy of TUNEL stained VSMC preparations showing TUNEL staining intensity and nuclei size of apoptotic (TUNEL+) and non-apoptotic (TUNEL-) cells. Cells from VSMC preparations cultured for 48 h in the presence of 1.2, 1.8 or 2.5 mM Ca^{2+} and 1 or 3 mM Pi were pooled for these analysis. * $p < 0.05$, *** $p < 0.001$. N = 3 (WT), N = 4 (KO), mean + SEM, two way ANOVA with Bonferroni post-test. Preparation, culture maintenance and stainings of VSMC preparations were performed in collaboration with Dr Thomas Davies, quantitative immunofluorescence analysis by MS.

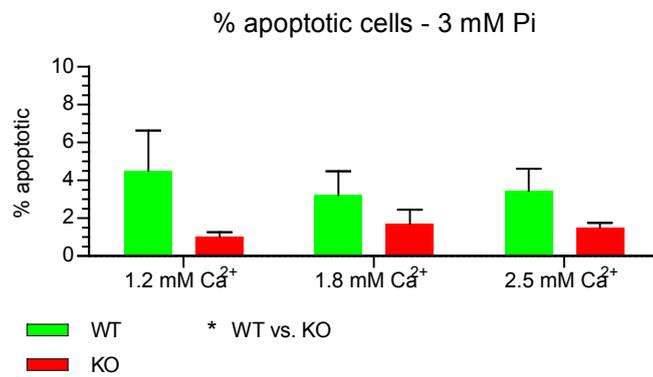
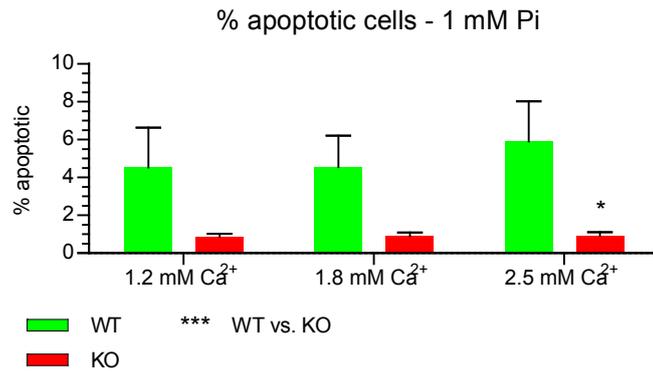


Figure 101: Quantitative fluorescence microscopy of TUNEL stained VSMC preparations showing percentage of apoptotic cells (TUNEL+) in VSMC preparations cultured for 48 h in the presence of 1.2, 1.8 or 2.5 mM Ca²⁺ and 1 or 3 mM Pi. * p < 0.05, *** p < 0.001. N = 3 (WT), N = 4 (KO), mean + SEM, two way ANOVA with Bonferroni post-test. Preparation, culture maintenance and stainings of VSMC preparations were performed in collaboration with Dr Thomas Davies, quantitative immunofluorescence analysis by MS.

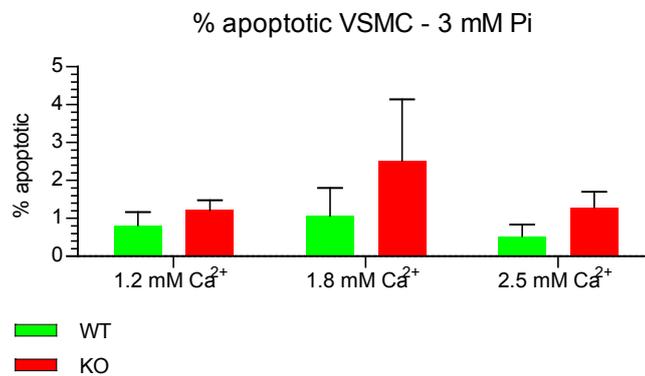
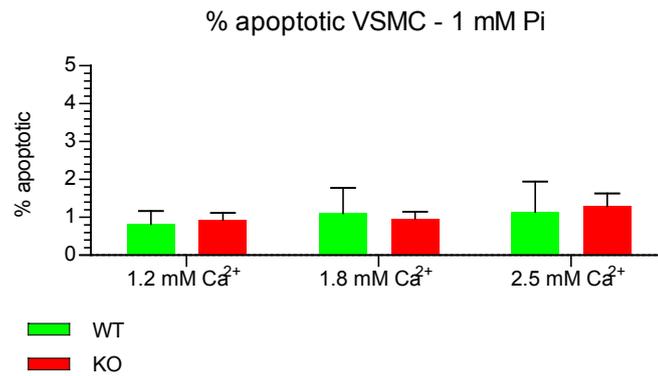


Figure 102: Quantitative fluorescence microscopy of TUNEL stained VSMC preparations showing percentage of apoptotic cells (TUNEL+) of VSMC (SM22 α +) in VSMC preparations cultured for 48 h in the presence of 1.2, 1.8 or 2.5 mM Ca²⁺ and 1 or 3 mM Pi. * $p < 0.05$, *** $p < 0.001$. N = 3 (WT), N = 4 (KO), mean + SEM, two way ANOVA with Bonferroni post-test. Preparation, culture maintenance and stainings of VSMC preparations were performed in collaboration with Dr Thomas Davies, quantitative immunofluorescence analysis by MS.

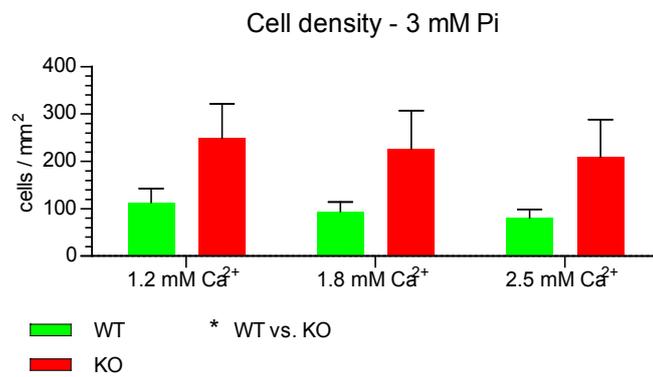
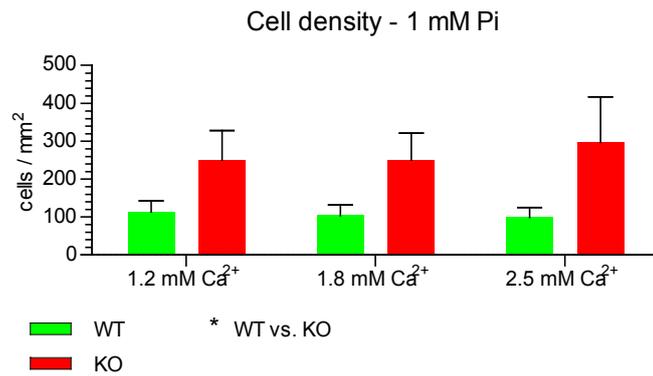


Figure 103: Quantitative fluorescence microscopy of TUNEL stained VSMC preparations showing total cell density in VSMC preparations cultured for 48 h in the presence of 1.2, 1.8 or 2.5 mM Ca²⁺ and 1 or 3 mM Pi. * p < 0.05. N = 3 (WT), N = 4 (KO), mean + SEM, two way ANOVA with Bonferroni post-test. Preparation, culture maintenance and stainings of VSMC preparations were performed in collaboration with Dr Thomas Davies, quantitative immunofluorescence analysis by MS.

Table 29: Results of quantitative fluorescence microscopy of TUNEL stained VSMC preparations. VSMC preparations cultured for 47 h in the presence of 1.2, 1.8 or 2.5 mM Ca²⁺ and 1 or 3 mM Pi. * p < 0.05. N = 3 (WT), N = 4 (KO), mean + SEM, two way ANOVA with Bonferroni post-test. Mgv = mean grey value, c = cells. Preparation, culture maintenance and stainings of VSMC preparations were performed in collaboration with Dr Thomas Davies, quantitative immunofluorescence analysis by MS.

Group	Unit	WT	KO	p
TUNEL intensity				< 0.001 ***
TUNEL+	mgv	51.46 ± 10.25	54.46 ± 7.06	> 0.05
TUNEL-	mgv	3.55 ± 0.38	3.57 ± 0.20	> 0.05
Nuclei size				< 0.001 ***
TUNEL+	µm ²	187.39 ± 18.43	231.14 ± 24.31	> 0.05
TUNEL-	µm ²	364.29 ± 21.96	330.89 ± 20.18	> 0.05
Apoptotic cells – all cells				
1 mM Pi				< 0.001 ***
1.2 mM Ca ²⁺	%	4.53 ± 2.10	0.89 ± 0.13	> 0.05
1.8 mM Ca ²⁺	%	4.54 ± 1.66	0.91 ± 0.18	> 0.05
2.5 mM Ca ²⁺	%	5.90 ± 2.12	0.94 ± 0.17	< 0.05 *
3 mM Pi				< 0.05 *
1.2 mM Ca ²⁺	%	4.53 ± 2.10	1.04 ± 0.22	> 0.05
1.8 mM Ca ²⁺	%	3.22 ± 1.26	1.71 ± 0.74	> 0.05
2.5 mM Ca ²⁺	%	3.44 ± 1.17	1.52 ± 0.23	> 0.05
Apoptotic cells – VSMC				
1 mM Pi				> 0.05
1.2 mM Ca ²⁺	%	0.82 ± 0.34	0.93 ± 0.18	> 0.05
1.8 mM Ca ²⁺	%	1.10 ± 0.67	0.97 ± 0.18	> 0.05
2.5 mM Ca ²⁺	%	1.14 ± 0.80	1.29 ± 0.34	> 0.05
3 mM Pi				> 0.05
1.2 mM Ca ²⁺	%	0.82 ± 0.34	1.21 ± 0.27	> 0.05
1.8 mM Ca ²⁺	%	1.07 ± 0.73	2.52 ± 1.61	> 0.05
2.5 mM Ca ²⁺	%	0.53 ± 0.30	1.29 ± 0.41	> 0.05
Cell density				
1 mM Pi				< 0.05 *
1.2 mM Ca ²⁺	c / mm ²	113.15 ± 29.62	249.74 ± 77.90	> 0.05
1.8 mM Ca ²⁺	c / mm ²	103.62 ± 28.06	250.39 ± 70.64	> 0.05
2.5 mM Ca ²⁺	c / mm ²	98.53 ± 26.04	296.39 ± 120.16	> 0.05
3 mM Pi				< 0.05 *
1.2 mM Ca ²⁺	c / mm ²	113.15 ± 29.62	248.75 ± 72.56	> 0.05
1.8 mM Ca ²⁺	c / mm ²	94.15 ± 19.69	226.39 ± 80.35	> 0.05
2.5 mM Ca ²⁺	c / mm ²	81.05 ± 17.58	209.26 ± 78.47	> 0.05

12.2 Radiotelemetry experiments - Variable time point comparisons based on rolling minimum and maximum detection

Since the circadian rhythms of the individual mice are not perfectly in sync (illustrated in Figure 104), minima and maxima (resting and active period of the mice) in all the individual smoothed curves for MAP of all investigated mice were detected by either a) detecting the minimum and maximum per day (24 h period from 0:00 to 24:00) or b) by using a local minimum and maximum detection approach spanning 17 hours (target hour \pm 8 hours; Figure 105). The time points of the last minima and maximum of the MAP of a given diet regimen was used to select the values of all other parameters from their respective averaged curves. This approach allowed correcting for variations in the mice circadian rhythm, therefore comparing the parameters of the individual mice during their distinct period of highest (maximum MAP) and lowest activity (minimum MAP) as well as incorporating the general trend of the curves due to the use of the averaged values. Data analysis was performed using Microsoft Excel 2010 (Microsoft, Redmond, CA, USA).

Two-way ANOVA showed no significant differences between WT and KO mice in systolic blood pressure, neither during their active nor resting phases, independent of the diet the mice. Mean arterial pressure ($p < 0.05$) and diastolic blood pressure ($p < 0.01$) showed a statistically significant reduction in KO mice compared to WT during the active phase of the mice. During the mice's resting phase, diastolic blood pressure of KO mice was significantly reduced ($p < 0.05$) compared to WT. The diet (standard vs. high salt) had no significant impact on blood pressure (Figure 106).

Pulse height of KO animals was significantly ($p < 0.05$) elevated compared to WT during the active phase of the mice. Heart rate of KO animals was highly significantly ($p < 0.001$) reduced compared to WT during the active phase of the mice when fed standard diet or high salt diet. A highly significant reduction of the heart rate of KO animals was found during active ($p < 0.001$) and resting ($p < 0.01$) phases of the mice; a significant reduction of the heart rate was also seen between diets, where the heart rate of the animals was significantly lower on the high salt diet compared to standard. This reduction was particularly pronounced in KO mice, where post-test showed a significant reduction ($p < 0.05$). Whether this effect is caused by the high salt diet alone or results from the aforementioned incomplete recovery

from surgery is unclear. No difference was found in dp/dt between WT and KO mice (Figure 107).

All numerical results of the variable time point analysis for standard diet vs. 4 % NaCl containing diet are listed in Table 30.

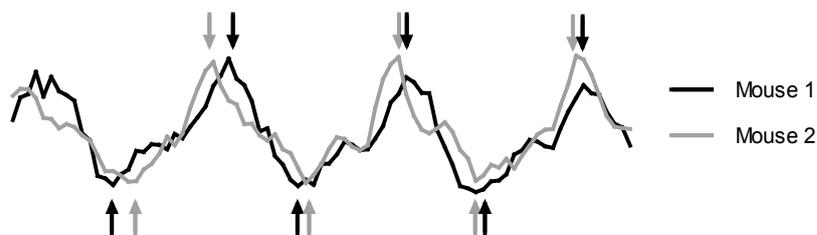


Figure 104: Illustration of small differences in the circadian rhythms of the single mice on a segment of MAP curves from two different mice. Arrows indicate local minima (upward pointing arrows) and maxima (downward pointing arrows).

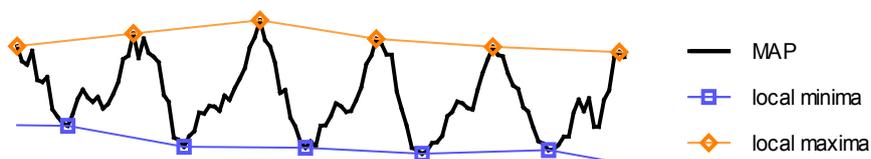


Figure 105: Illustration of local minimum / maximum detection on a segment of a MAP curve (smoothed by rolling average over 4 hours) of a single mouse. Every hour is checked for being the local minimum or maximum value in an interval of ± 8 hours, resulting in detection of daily minima (blue symbols) and maxima (orange symbols) of the MAP of every single mouse. The values of the telemetry parameters pertaining to these detected hours for every mouse were used for comparison of active vs. resting state of the mice and to account for variations in circadian rhythm between the individual mice.

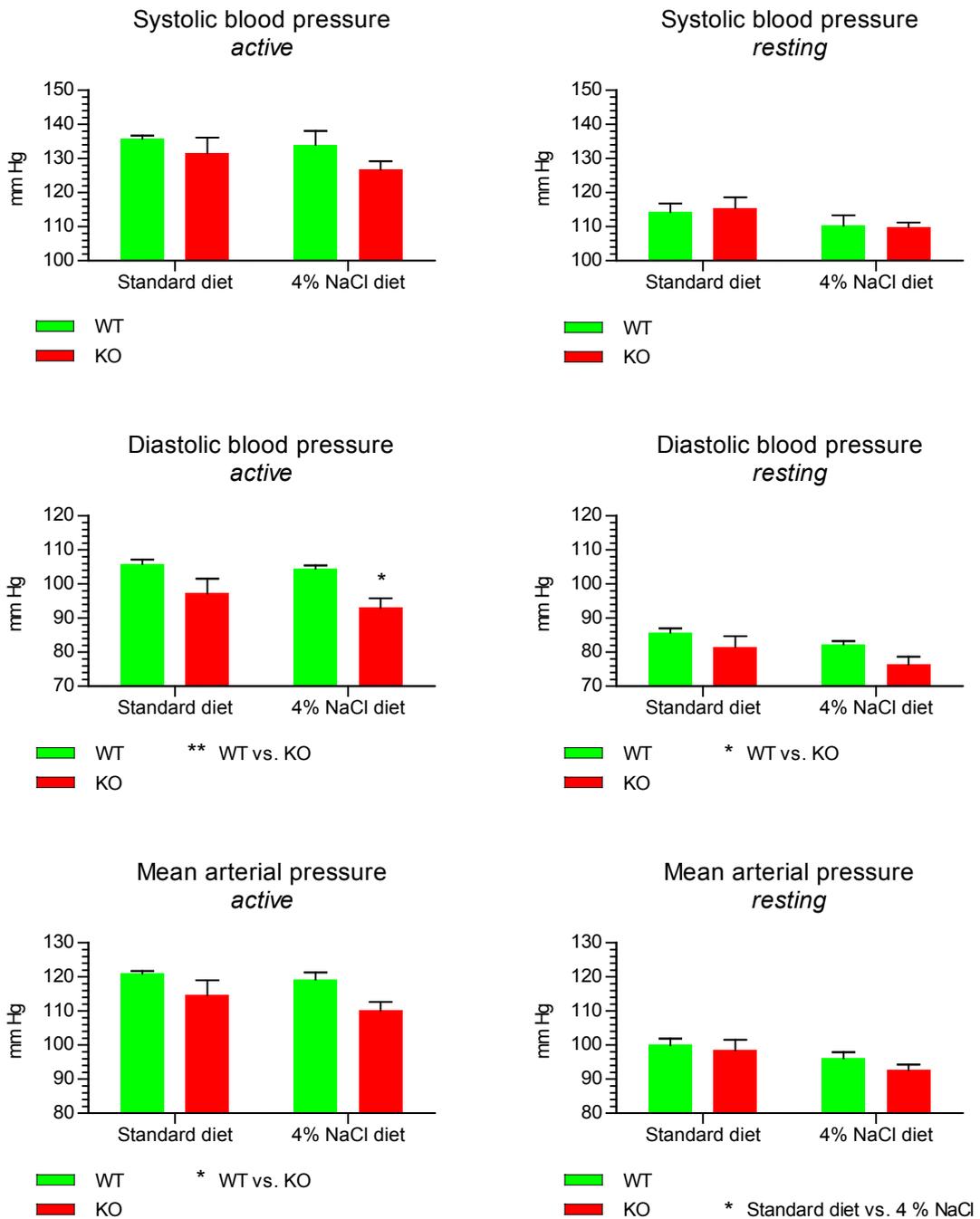


Figure 106: Systolic, diastolic and mean arterial pressure of WT and KO mice during their active and resting times of the day, fed on standard diet or high salt diet as measured by radiotelemetry. Individual active and resting time points were averaged and were detected by rolling maximum (active) and minimum (resting) detection based on MAP curve of each individual mouse. * $p < 0.05$, ** $p < 0.01$, *** $p < 0.001$. $N = 5$, mean + SEM, two way ANOVA and Bonferroni post-test.

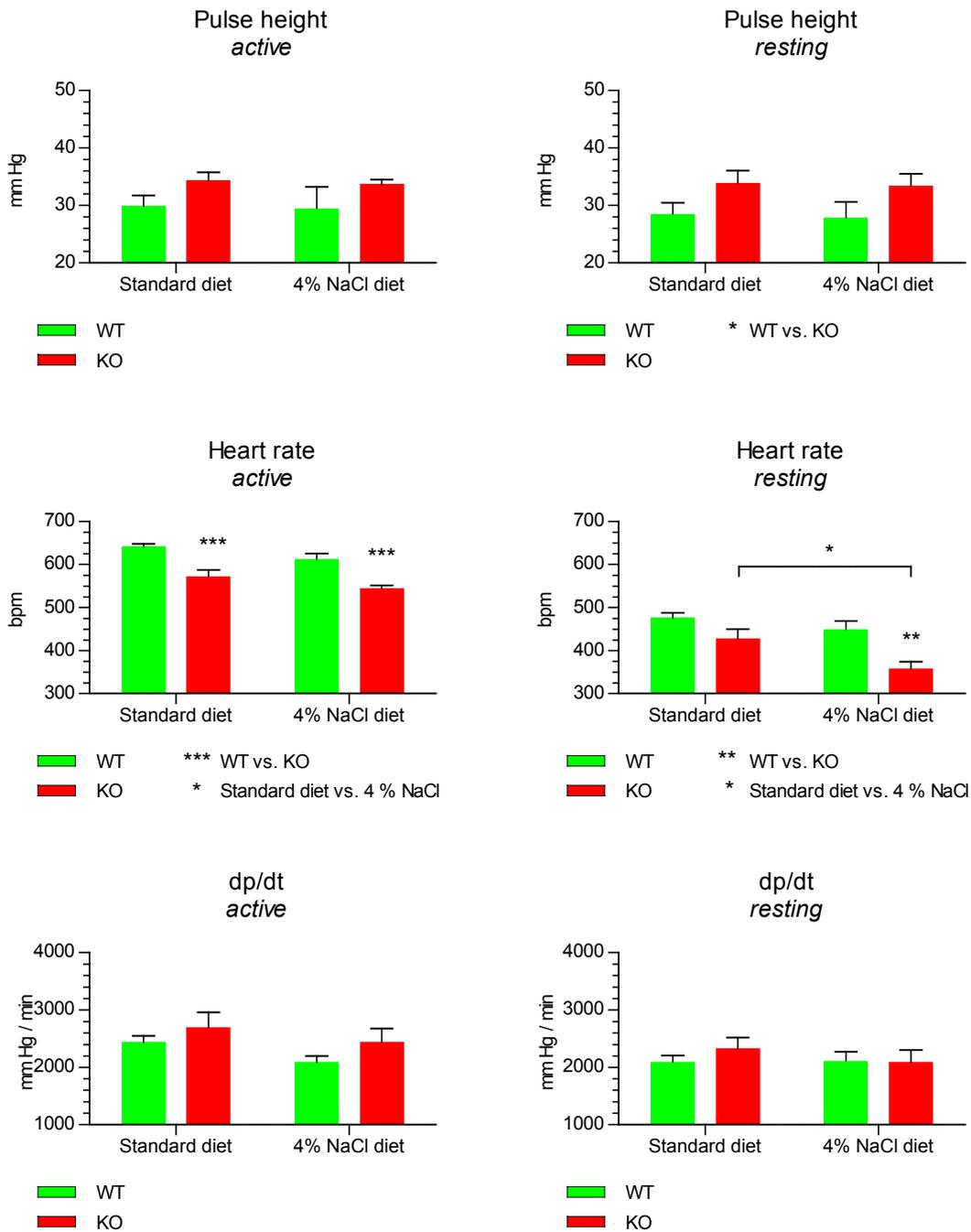


Figure 107: Pulse height, heart rate and dp/dt of WT and KO mice during their active and resting times of the day, fed on standard diet or high salt diet as measured by radiotelemetry. Individual active and resting time points were averaged and were detected by rolling maximum (active) and minimum (resting) detection based on MAP curve of each individual mouse. * $p < 0.05$, ** $p < 0.01$, *** $p < 0.001$. $N = 5$, mean + SEM, two way ANOVA and Bonferroni post-test.

When the mice had been transferred to standard housing cages, diastolic and mean arterial blood pressure showed a significant ($p < 0.01, 0.05$) reduction in KO mice during their active and resting phases compared to WT. this difference was abolished when the drinking water of the mice was supplemented with 0.5 mg / ml L-NAME. Systolic blood pressure did not show a significant difference between WT and KO mice but increased significantly under the influence of the NO synthase inhibitor, especially during the resting phase of the mice ($p < 0.05$), as shown by Bonferroni post-test (Figure 108).

Pulse height was significantly elevated in KO mice compared to WT during the active and resting phases of the mice ($p < 0.05$). As determined by post-test, this elevation was especially pronounced when the mice were administered 0.5 mg/l L-NAME in their drinking water ($p < 0.05$). Heart rates of KO mice during their active phase were highly significantly reduced ($p < 0.001$) compared to WT and dropped significantly further during their active phase as determined by Bonferroni post-test ($p < 0.01$ for WT, $p < 0.05$ for KO) when the mice were given L-NAME. Reduction in heart rate of KO mice compared to WT was smaller when the mice were resting but still significant ($p < 0.05$). dp/dt of KO mice was significantly elevated compared to WT ($p < 0.05$) during active and resting phases, independently of the administration of L-NAME (Figure 109).

All numerical results from the variable time point analysis for standard diet vs. 0.5 mg / ml L-NAME are listen in Table 31.

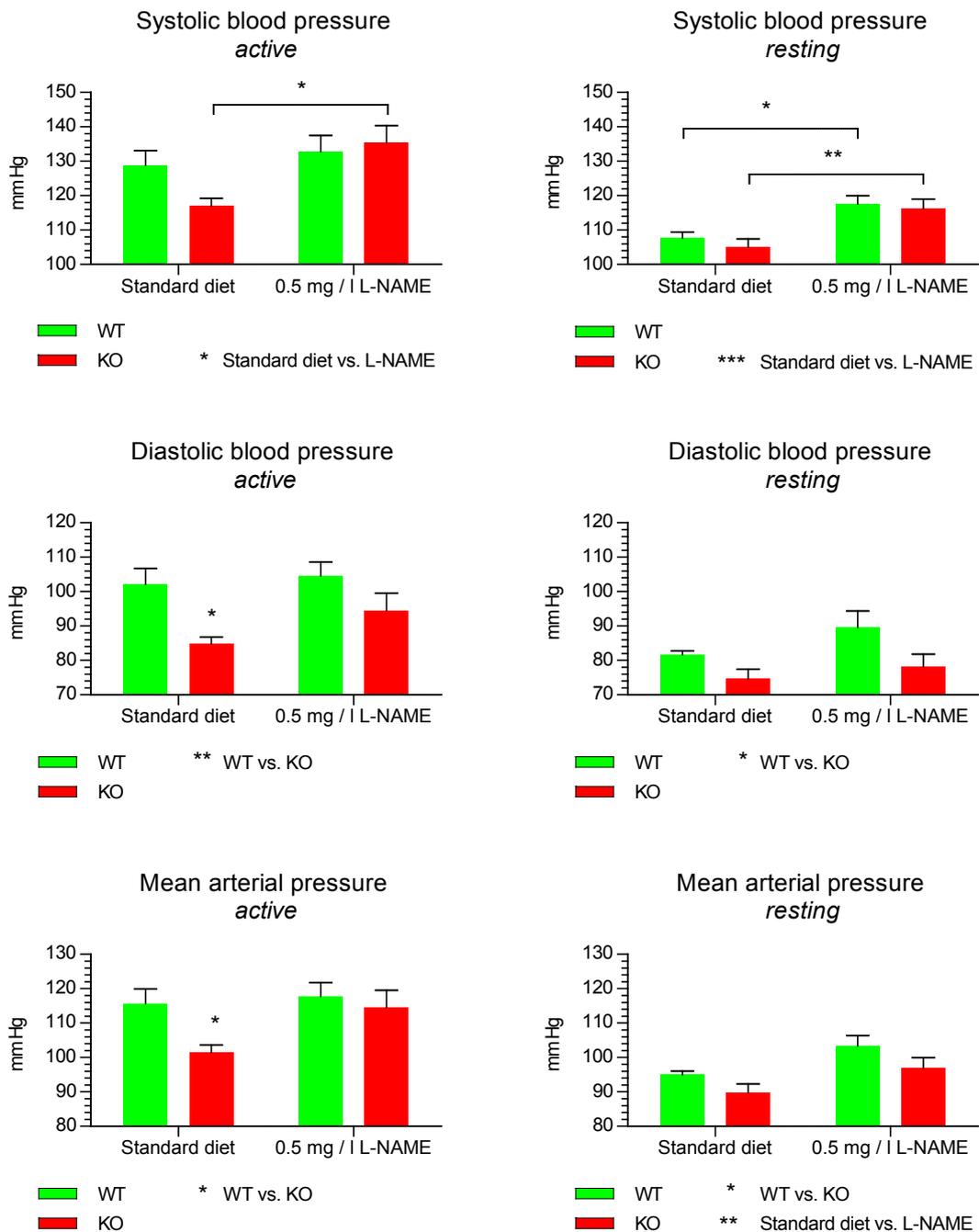


Figure 108: Systolic, diastolic and mean arterial pressure of WT and KO mice during their active and resting times of the day, fed on standard diet or 0.5 mg / ml L-NAME as measured by radiotelemetry. Individual active and resting time points were averaged and were detected by rolling maximum (active) and minimum (resting) detection based on MAP curve of each individual mouse. * $p < 0.05$, ** $p < 0.01$, *** $p < 0.001$. $N = 5$, mean + SEM, two way ANOVA and Bonferroni post-test.

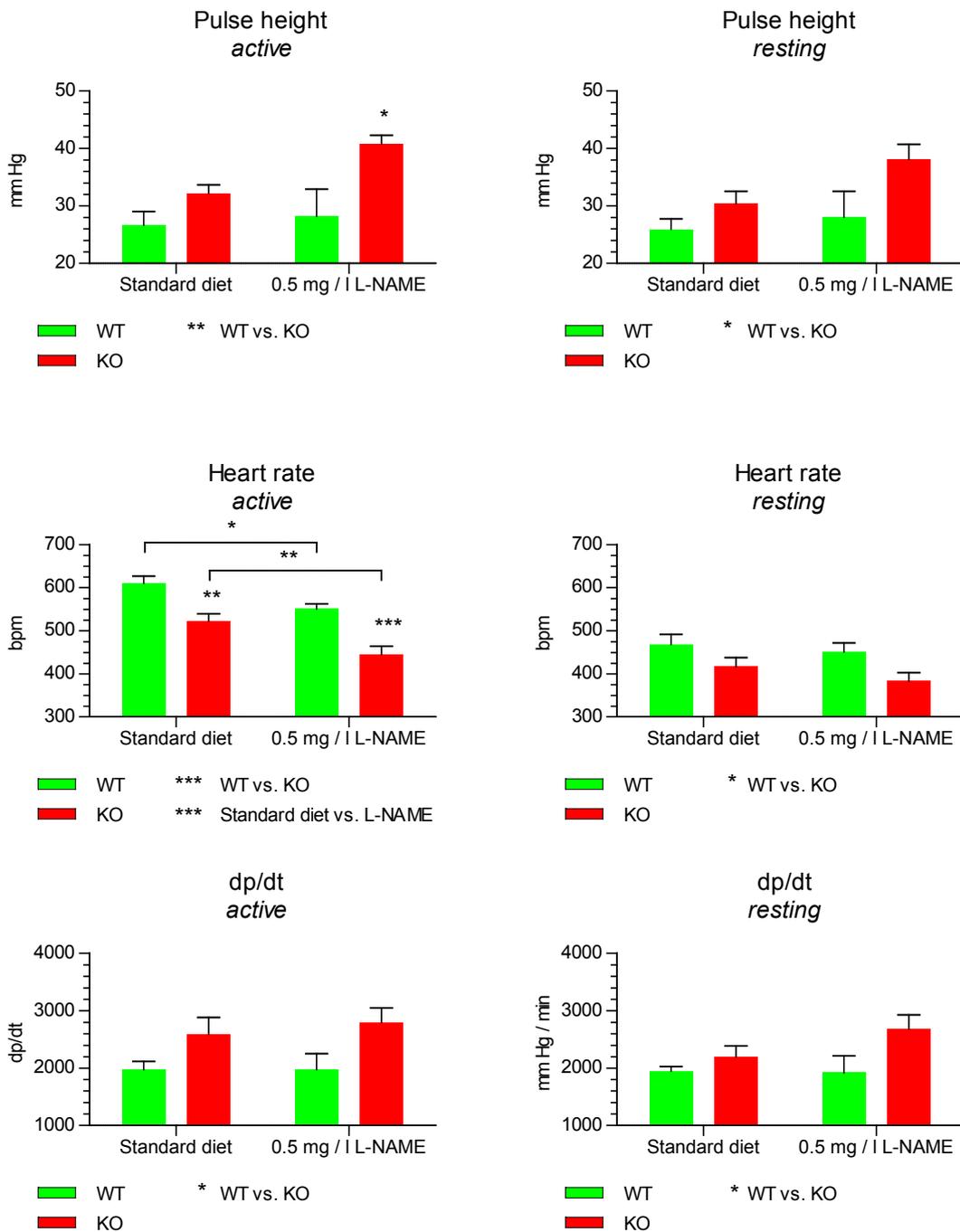


Figure 109: Pulse height, heart rate and dp/dt of WT and KO mice during their active and resting times of the day, fed on standard diet or 0.5 mg / ml L-NAME as measured by radiotelemetry. Individual active and resting time points were averaged and were detected by rolling maximum (active) and minimum (resting) detection based on MAP curve of each individual mouse. * p < 0.05, ** p < 0.01, *** p < 0.001. N = 5, mean + SEM, two way ANOVA and Bonferroni post-test.

Table 30: Results of radiotelemetry experiments carried out on 3 month old WT and KO mice, standard diet (1) vs. high salt diet (4 % NaCl diet). Individual active and resting time points were averaged and were detected by rolling maximum (active) and minimum (resting) detection based on MAP curve of each individual mouse. See Figure 16 for experimental timeline and Table 8 for parameter explanations and abbreviations. * p < 0.05, ** p < 0.01, *** p < 0.001. N = 5, mean ± SEM, two way ANOVA and Bonferroni post-test. P^a = Bonferroni post-test (WT vs KO), P^b = ANOVA (WT vs KO) within active or resting groups, P^c = ANOVA (diets) within active or resting groups.

Parameter	Unit	WT	KO	P ^a	P ^b	P ^c
Standard diet (1) – Active						
Systolic	mm Hg	135.74 ± 0.90	131.55 ± 4.56			
Diastolic	mm Hg	105.79 ± 1.31	97.22 ± 4.32			
MAP	mm Hg	120.91 ± 0.79	114.58 ± 4.41			
PH	mm Hg	29.95 ± 1.80	34.33 ± 1.42			
HR	bpm	641.96 ± ±.46	571.63 ± 15.64	***		
dp/dt	mm Hg / ms	2432.37 ± 113.97	2692.86 ± 262.68			
4 % NaCl diet – Active						
Systolic	mm Hg	133.98 ± 4.08	126.70 ± 2.41			
Diastolic	mm Hg	104.47 ± 0.92	93.01 ± 2.74	*	**	
MAP	mm Hg	119.17 ± 2.04	110.05 ± 2.59		*	
PH	mm Hg	29.51 ± 3.72	33.70 ± 0.81			
HR	bpm	613.29 ± 11.86	544.61 ± 6.58	***	***	*
dp/dt	mm Hg / ms	2089.16 ± 104.38	2441.37 ± 233.39			
Standard diet (1) – Resting						
Systolic	mm Hg	114.22 ± 2.61	115.47 ± 3.11			
Diastolic	mm Hg	85.67 ± 1.30	81.55 ± 3.13			
MAP	mm Hg	99.94 ± 1.90	98.44 ± 3.14			
PH	mm Hg	28.55 ± 1.92	33.92 ± 2.16			
HR	bpm	475.61 ± 11.93	427.34 ± 22.62			
dp/dt	mm Hg / ms	2094.89 ± 110.49	2324.58 ± 189.20			
4 % NaCl diet – Resting						
Systolic	mm Hg	110.28 ± 3.00	109.85 ± 1.39			
Diastolic	mm Hg	82.35 ± 0.92	76.38 ± 2.32		*	
MAP	mm Hg	96.08 ± 1.81	92.68 ± 1.61			*
PH	mm Hg	27.94 ± 2.72	33.47 ± 2.03		*	
HR	bpm	449.90 ± 18.79	357.23 ± 17.00	**	**	*
dp/dt	mm Hg / ms	2112.77 ± 161.26	2090.38 ± 212.17			

Table 31: Results of radiotelemetry experiments carried out on 3 month old WT and KO mice, standard diet (2) vs.0.5 mg / l L-NAME in drinking water. Individual active and resting time points were averaged and were detected by rolling maximum (active) and minimum (resting) detection based on MAP curve of each individual mouse. See Figure 16 for experimental timeline and Table 8 for parameter explanations and abbreviations. * p < 0.05, ** p < 0.01, *** p < 0.001. N = 5, mean ± SEM, two way ANOVA and Bonferroni post-test. P^a = Bonferroni post-test (WT vs KO), P^b = ANOVA (WT vs KO) within active or resting groups, P^c = ANOVA (diets) within active or resting groups.

Parameter	Unit	WT	KO	P ^a	P ^b	P ^c
Standard diet (2) – Active						
Systolic	mm Hg	128.78 ± 4.29	116.95 ± 2.21			
Diastolic	mm Hg	102.10 ± 4.60	84.76 ± 2.04	*		
MAP	mm Hg	115.69 ± 4.21	101.42 ± 2.14	*		
PH	mm Hg	26.68 ± 2.32	32.18 ± 1.51			
HR	bpm	610.37 ± 16.28	522.80 ± 16.70	**		
dp/dt	mm Hg / ms	1972.15 ± 141.65	2593.42 ± 287.34			
0.5 mg / l L-NAME – Active						
Systolic	mm Hg	132.74 ± 4.72	135.35 ± 4.93			*
Diastolic	mm Hg	104.54 ± 3.95	94.51 ± 4.97		**	
MAP	mm Hg	117.66 ± 3.98	114.53 ± 4.90		*	
PH	mm Hg	28.20 ± 4.74	40.84 ± 1.48	*	**	
HR	bpm	550.92 ± 11.68	445.42 ± 18.46	***	***	***
dp/dt	mm Hg / ms	1971.58 ± 280.66	2796.01 ± 252.67		*	
Standard diet (2) – Resting						
Systolic	mm Hg	107.61 ± 1.84	105.03 ± 2.40			
Diastolic	mm Hg	81.64 ± 1.09	74.63 ± 2.79			
MAP	mm Hg	94.89 ± 1.15	89.79 ± 2.49			
PH	mm Hg	25.97 ± 1.79	30.41 ± 2.15			
HR	bpm	467.92 ± 23.89	416.83 ± 20.63			
dp/dt	mm Hg / ms	1944.97 ± 84.79	2194.13 ± 190.33			
0.5 mg / l L-NAME – Resting						
Systolic	mm Hg	117.58 ± 2.33	116.29 ± 2.70			***
Diastolic	mm Hg	89.54 ± 4.74	78.21 ± 3.57		*	
MAP	mm Hg	103.34 ± 2.99	96.89 ± 3.03		*	**
PH	mm Hg	28.04 ± 4.54	38.08 ± 2.65		*	
HR	bpm	450.67 ± 20.97	383.15 ± 19.08		*	
dp/dt	mm Hg / ms	1913.98 ± 298.08	2680.19 ± 247.53		*	

12.3 Cardiac cine MRI - 18 month old animals

3 of the investigated animals died mid-scan under general anaesthesia (1 WT, 2 KO) reducing the number of available completed scans for KO animals to 2. One of the dies KO animals was scanned up to the third basal short axis slice, allowing an approximation of the ejection fraction (see below).

Visual analysis of the long axis (Figure 110) scans as well as the third basal short axis scans (Figure 111; this was the last completed scan for the mice that died during the procedure) did not show any obvious differences between WT and KO hearts. Mean values for the measured parameters (Figure 112), as well as cardiac remodelling indices (Figure 113) from the three completed WT and two completed KO scans did not show any specific trends between 18 month old WT and KO animals.

To allow for some degree of comparison of cardiac parameters, the third basal slice only (instead of the whole heart) was used to approximate the ejection fraction. This method is normally used for ultrasonic observations where heart parameters are extrapolated from the centre of the left ventricle (using the papillary muscle as point of reference) only (Johnson 2008). This analysis was performed on all available WT and KO hearts (N = 3 for both genotypes). No difference between WT and KO hearts was found (Figure 114).

Measurement of heart dimensions from the long axis scans (which were completed on all mice) did not show significant differences between 18 month old WT and KO hearts (Figure 115).

Heart parameters normalised to TBW showed a trend toward increased left ventricular stroke volume, although a statistical comparison was not possible due to the lack of a TBW record for one of the mice (Figure 116).

All numerical results from cardiac cine MRI of 18 month old animals are listed in Table 32.

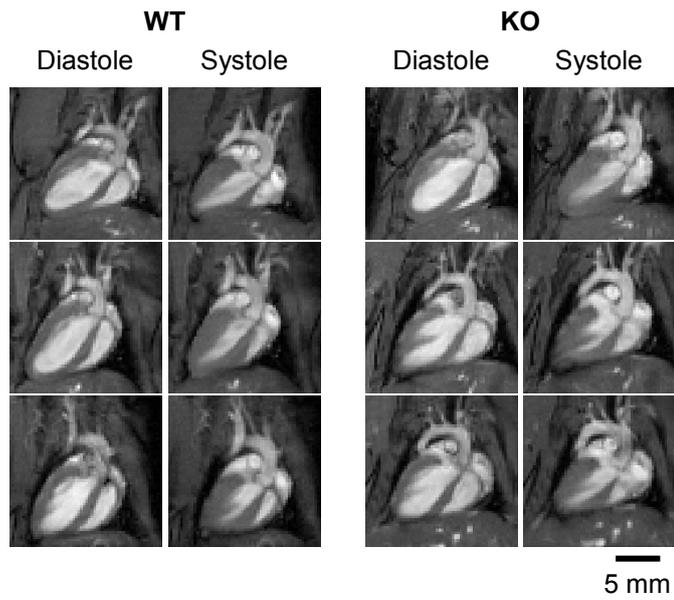


Figure 110: Long axis cardiac MRI scans of hearts from 18 month old WT and KO mice showing diastole and systole.

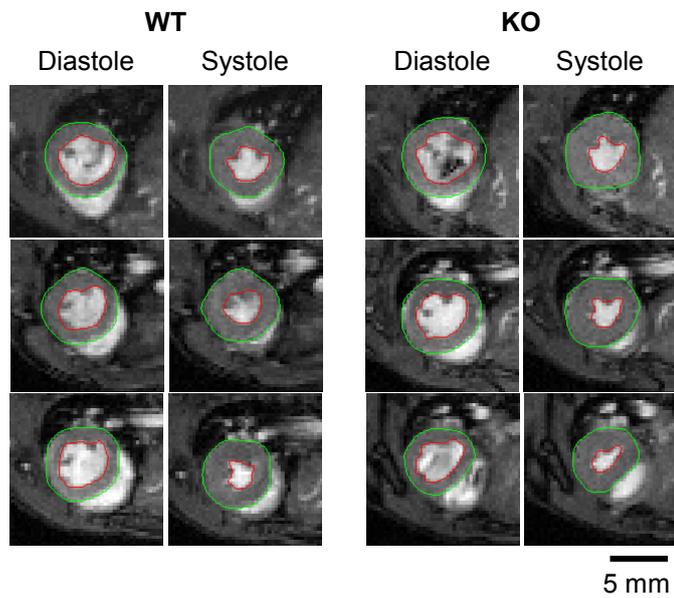


Figure 111: Short axis cardiac MRI scans of the third basal slice of hearts from 18 month old WT and KO mice showing diastole and systole. Green = epicardium, red = endocardium.

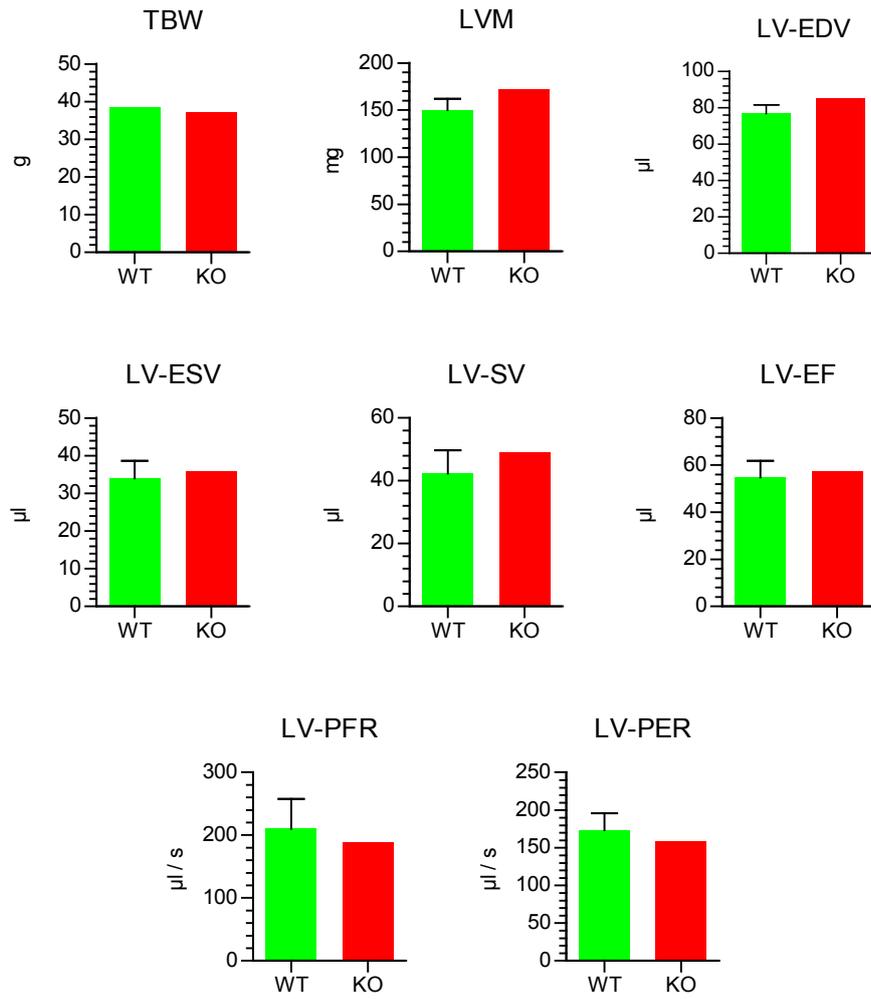


Figure 112: Measured and calculated left-ventricular cardiac parameters from short-axis cardiac cine-MRI scans of 18 month old WT and KO mice. LV = left ventricular, LVM = left ventricular mass, EDV = end diastolic volume, ESV = end systolic volume, SV = stroke volume, EF = ejection fraction, PFR = peak fill rate, PER = peak ejection rate. N = 3 (WT), 2 (KO), mean + SEM (WT), mean (KO).

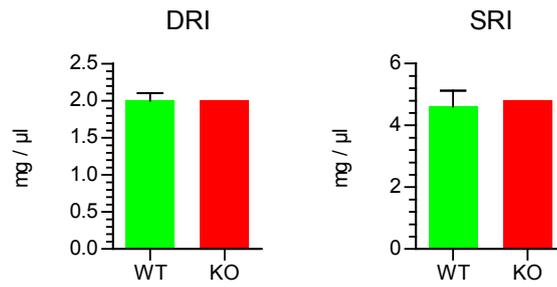


Figure 113: Calculated cardiac remodelling indices of from short-axis cardiac cine-MRI scans of 18 month old WT and KO mice. DRI = end-diastolic remodelling index, SRI = end-systolic remodelling index. N = 3 (WT), 2 (KO), mean + SEM (WT), mean (KO).

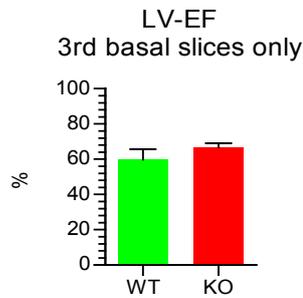


Figure 114: Approximated left ventricular EF from the third basal slice of short axis cine-MRI scans of 18 month old WT and KO mice. LV=EF = left ventricular ejection fraction. N = 3, mean + SEM.

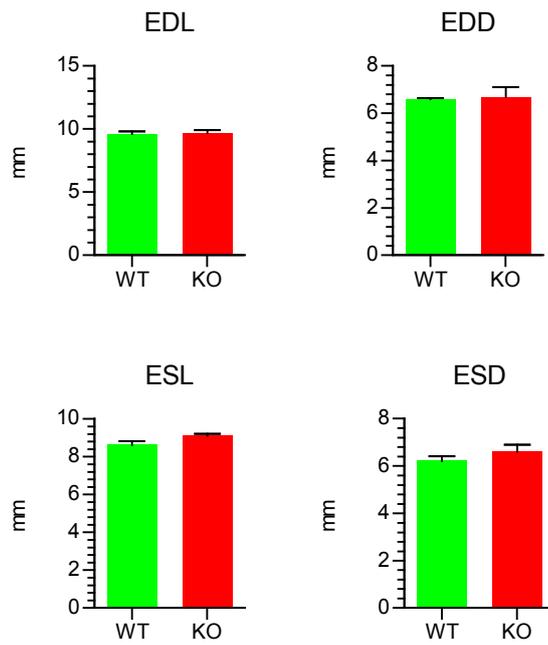


Figure 115: Measured heart dimensions from long-axis cardiac cine-MRI scans of 18 month old WT and KO mice. LV = left ventricular, ESL = end systolic length, ESD = end systolic diameter, EDL = end diastolic length, EDD = end diastolic diameter. N = 3, mean + SEM

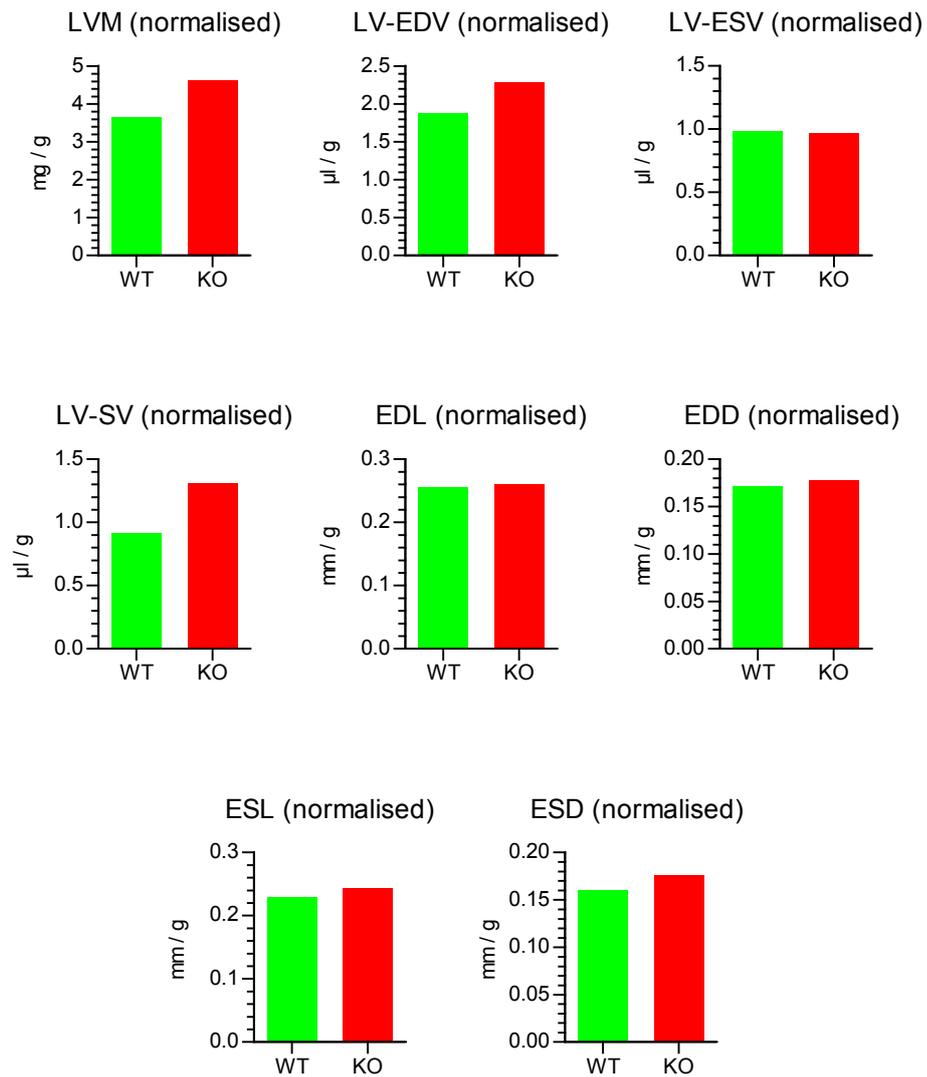


Figure 116: Parameters obtained from cardiac cine-MRI scans of 18 month old mice normalised to TBW. See Table 9 for abbreviations. N = 2 (WT), 2 (KO), mean.

Table 32: Results of cardiac MRI analysis of 18 month old animals. TBW = Total body weight, See Table 9 for abbreviations. LV-EF 3b = left ventricular ejection fraction approximated from third basal MRI slice only. # PFR and PER: one cardiac cycle normalised to 1 second, N = 3 (WT), 2 (KO), 3 (KO: EDL, EDD, ESL, ESD) Mean \pm SEM, two-tailed T-test (where N = 3).

Parameter	Unit	WT	KO	P
Raw values				
TBW	g	38.5 \pm 0.2	37.3 \pm 0.5	
LVM	mg	150.0 \pm 11.9	172.5 \pm 1.5	
LV-EDV	μ l	76.7 \pm 4.8	85.0 \pm 6.0	
LV-ESV	μ l	34.0 \pm 4.6	36.0 \pm 2.0	
LV-SV	μ l	42.3 \pm 7.4	49.0 \pm 5.0	
LV-EF	%	54.7 \pm 7.1	57.5 \pm 1.5	
LV-PFR	μ l / s [#]	209.7 \pm 47.9	188.0 \pm 33.0	
LV-PER	μ l / s [#]	173.3 \pm 22.4	158.0 \pm 16.0	
DRI	g / μ l	2.0 \pm 0.1	2.0 \pm 0.2	
SRI	g / μ l	4.6 \pm 0.9	4.8 \pm 0.3	
EDL	mm	9.6 \pm 0.2	9.5 \pm 0.2	0.7096
EDD	mm	6.6 \pm 0.0	6.5 \pm 0.2	0.8944
ESL	mm	8.6 \pm 0.2	8.7 \pm 0.4	0.9435
ESD	mm	6.2 \pm 0.2	6.2 \pm 0.3	0.8766
LV-EF 3b	%	59.7 \pm 5.9	66.7 \pm 2.3	0.3334
Normalised to TBW				
LVM	mg / g	3.648 \pm 0.306	3.084 \pm 1.543	
LV-EDV	μ l / g	1.870 \pm 0.042	1.518 \pm 0.763	
LV-ESV	μ l / g	0.986 \pm 0.099	0.643 \pm 0.322	
LV-SV	μ l / g	0.909 \pm 0.057	0.875 \pm 0.443	
EDL	mm / g	0.255 \pm 0.009	0.260 \pm 0.009	
EDD	mm / g	0.171 \pm 0.001	0.178 \pm 0.007	
ESL	mm / g	0.229 \pm 0.006	0.243 \pm 0.007	
ESD	mm / g	0.160 \pm 0.010	0.176 \pm 0.004	

13 Curriculum vitae

Personal details

Full name	Martin Wolfgang Schepelmann
Academic degree	Master of Pharmacy (Magister der Pharmazie)
Date and place of birth	November 10 th , 1983; Vienna
Nationality	Austria
Current occupation	Marie Curie Early Stage Researcher / PhD student, Cardiff University, UK

Education and Career

1990–1994	Elementary school (Maria Regina, Vienna, Austria)
1994–2002	Secondary school (Döblinger Gymnasium, Vienna, Austria)
06/2002	School leaving examination (Matura)
2003–2004	Training as paramedic (examination passed with honors) in the context of the Austrian compulsory community service (Zivildienst)
2004–2010	Study of Pharmacy at the University of Vienna, Austria
11/2009–05/2010	Diploma thesis in pharmacy under supervision of Dr. Walter Jäger, Department of Clinical Pharmacy, University of Vienna, Austria and Dr. Isabella Ellinger, Department of Pathophysiology and Allergy Research, Medical University of Vienna, Austria; Title: "Potential mechanisms behind blood pressure modulation by melatonin – Expression analysis of melatonin receptors MT1 and MT2 in the rat aorta"
07/2010	Graduation in pharmacy with first class honors, granted academic degree: Master of Pharmacy (Magister der Pharmazie)
07/2010–06/2011	Research associate in the groups of Dr. Isabella Ellinger and Dr. Theresia Thalhammer at the Department of Pathophysiology and Allergy Research, Medical University of Vienna, Austria; Main focus: <i>in vitro</i> osteoclast cultivation for quantification of influences on osteoclast growth as part of an industry-university spanning research project (FFG Bridge)
07/2011–05/2014	PhD studies in physiology under supervision of Dr. Daniela Riccardi and Dr. Paul Kemp in the course of a Marie Curie Fellowship (employment as a Marie Curie Early Stage Researcher) at Cardiff University, United Kingdom

Supervision- and Teaching-Experience

06/2007	Workshop on plant anatomy in two tenth and one ninth grade biology classes at a secondary school (Billrothgymnasium, Vienna, Austria)
07/2010–08/2010	Supervision of a student summer intern (Medical University Vienna)
09/2010–06/2011	Assistance in supervision of one bachelor and two diploma students (Medical University of Vienna)
2011	Assistance in teaching “statistical seminar for students of medicine”, SSM2 (held by Dr. Isabella Ellinger, Medical University Vienna)
2011 - ongoing	Assistance in supervision of final year project students of medicine and biology (Cardiff University)
2012	Demonstrating: Statistics for 1 st years, Solutions and Molarity (Cardiff University)

Awards

04/1998	1 st place at the Austrian finals of CyberSchool98 (students develop IT-projects; www.cyberschool.at)
05/2001	1 st place at the Austrian finals of Business@School (students develop business plans; initiated by the Boston Consulting Group; www.business-at-school.de)
06/2001	3 rd place at the Austrian-German finals of Business@School (see above) in Munich, Germany
01/2008	Merit scholarship of the University of Vienna (StudFG WS2008) for excellent academic achievements in the year 2007
04/2011	Science2business Award (Team award, 3 rd place) at the LifeScienceSuccess 2011, Techgate, Vienna
06/2011	Travel grant of the Austrian Society for Bone and Mineral Research to attend the ECTS 2011, Athens, Greece
09/2012	Poster prize of the third Retreat of the Center for Pathophysiology, Infectiology and Immunology, Medical University Vienna
12/2012	Travel grant of the Austrian Society for Bone and Mineral Research to attend the International conference on Progress in Bone and Mineral Research 2012, Vienna, Austria

Professional memberships

Member of the Austrian society for Bone and Mineral Research

(<http://www.knochenundmineralstoffwechsel.at/>)

Member of the European Calcified Tissue Society (<http://www.ectsoc.org/>)

Member of the Physiological Society (<http://www.physoc.org/>)

Attended workshops

Conference Organization

E-moderation

Flow Cytometry

Genotyping, predictive testing reporting and genetic counselling

Management Systems and Internal Auditing

Microarrays

Practical Teaching

Pre-/clinical trials

Quality and risk management in the routine diagnostic laboratory

Scientific ethics

Systems biology

General skills

Languages	German (native language), English (fluent)
IT	Microsoft Office (Word, Excel, PowerPoint) Adobe Photoshop, Adobe Illustrator, Adobe Premiere Statistical software (GraphPad Prism, Minitab) Operating systems (DOS, Windows (3.11 – 7)) System assembling and maintenance, computer administration Invitation of offers for IT infrastructure from major companies ECDL (European Computer Driving License)
Driving license	B
Hobbies	Movies, reading, hiking, IT, classical music, microscopy, history

Original publications

M. Schepelmann, L. Molcan, H. Uhrova, M. Zeman, I. Ellinger: The Presence and Localization of Melatonin Receptors in the Rat Aorta. *Cell Mol Neurobiol.* 2011 Nov;31(8):1257-65

A. Heindl, A.K. Seewald, **M. Schepelmann**, R. Rogojanu, G. Bises, T. Thalhammer and I. Ellinger: A novel nucleus-based classifier for discrimination of osteoclasts and mesenchymal precursor cells in mouse bone marrow cultures.

ICMLA Proceedings 2012 NL 70000

A. Heindl, A.K. Seewald, T. Thalhammer, G. Bises, **M. Schepelmann**, H. Uhrova, S. Dekan, I. Mesteri, R. Rogojanu, I. Ellinger: Automated REcognition of tissue-associated erythrocytes (ARETE)-a new tool in tissue cytometry.

Cytometry A. 2013 Apr;83(4):363-74

S. Brennan, T. Davies, **M. Schepelmann**, D. Riccardi: Emerging roles of the extracellular calcium-sensing receptor in nutrient sensing: control of taste modulation and intestinal hormone secretion.

Br J Nutr. 2014 Jan 2:1-7.

Abstracts (1st author only)

M. Schepelmann, A. Heindl, A. Seewald, A. Nussbaumer, M. Pilz, G. Bises, M. Svoboda, P. Pietschmann, I. Ellinger, T. Thalhammer: Influences on murine osteoclast formation and their automated detection by a novel image analysis software. *One minute talk and poster presentation at the 1st Retreat of the Center for Pathophysiology, Immunology and Infectiology, Vienna, September 2010, Austria*

M. Schepelmann, A. Heindl, A. Seewald, A. Nussbaumer, M. Pilz, G. Bises, M. Svoboda, R. Rogojanu, P. Pietschmann, I. Ellinger, T. Thalhammer: Influences on murine osteoclast formation and their automated detection by a novel image analysis software. *Abstract and poster presentation at the Wissenschaftliche Herbsttagung 2010 der Österreichischen Gesellschaft für Knochen und Mineralstoffwechsel, Vienna, November 2010, Austria*

Journal für Mineralstoffwechsel (17) 2010, Sonderheft 2, p.7

M. Schepelmann, A. Heindl, A. Seewald, A. Nussbaumer, G. Bises, R. Rogojanu, P. Pietschmann, I. Ellinger, T. Thalhammer: Influence of melatonin on murine osteoclast formation in culture – automated detection and quantification by a novel image analysis system. 3rd Joint Meeting of ECTS & IBMS, Athens, May 2011, Greece

Bone, 48 (2011), S133-S134, PP0112-S

M. Schepelmann, A. Heindl, H. Uhrova, V. Pohl, R. Rogojanu, A. Seewald, H. Helmer, I. Ellinger: The neonatal IgG Fc-receptor (FcRn) is expressed in the syncytiotrophoblast, fetal endothelial cells and Hofbauer cells of human term placental chorionic villi. *14th IFPA meeting, Geilo, September 2011, Norway*

Placenta, 32 (9): A54, 2011

M. Schepelmann, A. Heindl, A. Seewald, A. Nussbaumer, G. Bises, R. Rogojanu, R. Ecker, P. Pietschmann, I. Ellinger, T. Thalhammer: Automated detection and quantification of multinucleated osteoclasts by a novel image analysis system. Abstract and 2 minute talk. *2nd Retreat of the Center for Pathophysiology, Immunology and Infectiology, Vienna, September 2011, Austria*

M. Schepelmann, T. Davies, S. Brennan, P. Yarova, W. Chang, D. Bikle, M. Krssak, T. Wells, A. Stewart, B. van der Kolk, B. Monk, D. Ward, A. Canfield, D. Edwards, P. Kemp, D. Riccardi: Phenotypic characterisation of a mouse model of targeted gene deletion of the calcium-sensing receptor (CaSR) from vascular smooth muscle cells (SM22 α -Cre x LoxP-CaSR). *6th Mammalian Genes, Development and Disease, Bath, UK, July 2012*

M. Schepelmann, T. Davies, S. Brennan, P. Yarova, W. Chang, D. Bikle, M. Krssak, T. Wells, A. Stewart, D. Ward, A. Canfield, E. Kallay, D. Edwards, P. Kemp, D. Riccardi: A vascular smooth muscle cell (VSMC) specific calcium sensing receptor knock out mouse implicates the CaSR in blood pressure regulation and protection from calcification. *Abstract and 2 minute talk. 3rd Retreat of the Center for Pathophysiology, Immunology and Infectiology, Vienna, September 2012, Austria*

M. Schepelmann, T. Davies, P. Yarova, S. Brennan, W. Chang, D. Bikle, T. Wells, D. Ward, A. Canfield, D. Edwards, P. Kemp, D. Riccardi: Targeted gene deletion of the calcium-sensing receptor (CaSR) from vascular smooth muscle cells shows involvement of the

receptor in proliferation, calcification and modulation of aortic tone. *ISN Nexus, Copenhagen, Denmark, September 2012*

M. Schepelmann, T. Davies, P. Yarova, S. Brennan, W. Chang, D. Bikle, M. Krssak, T. Wells, A. Stewart, B. van der Kolk, B. Monk, D. Ward, A. Canfield, D. Edwards, P. Kemp, D. Riccardi: A mouse model of targeted deletion of the calcium sensing receptor (CaSR) from vascular smooth muscle cells implicates the CaSR in vascular pathophysiology. *Oral communication at the Symposium on the Calcium Sensing Receptor at the International Conference on Progress in Bone and Mineral Research, Vienna, Austria 2012. Bone 2012 Dec; 51(6): S24*

M. Schepelmann, T. Davies, P. Yarova, S. Brennan, J. Graca, W. Chang, D. Bikle, P. Edwards, M. Krssak, A. Stewart, D. Ward, A. Canfield, D. Edwards, S. Price, P. Kemp, D. Riccardi: Holistic characterisation of a vascular smooth muscle cell specific calcium-sensing receptor knock-out mouse. *Oral communication at the 7th Mammalian Genes, Development and Disease, Bath, UK, June 2013*

M. Schepelmann, T. Davies, P. Yarova, S. Brennan, J. Graca, W. Chang, D. Bikle, P. Edwards, M. Krssak, A. Stewart, D. Ward, A. Canfield, D. Edwards, S. Price, P. Kemp, D. Riccardi: Targeted deletion of the extracellular calcium-sensing receptor (CaSR) from vascular smooth muscle cells reveals roles for the receptor in blood pressure regulation and protection against vascular calcification. *IUPS, Birmingham, UK, July 2013*

M. Schepelmann, P. Yarova, T. Davies, S. Brennan, J. Graca, W. Chang, D. Bikle, D. Ward, A. Canfield, W. Richards, D. Edwards, S. Price, P. Kemp, D. Riccardi: The vascular smooth muscle cell Calcium-sensing Receptor (CaSR) is involved in blood pressure regulation, Ca²⁺ homeostasis and protection from calcification. *ASN kidney week 2013, Atlanta, USA, November 2013*

Book chapter

A. Heindl, **M. Schepelmann**, R. Ecker, P. Pietschmann, I. Ellinger, A. Seewald, T. Thalhammer: Towards the automated detection and characterization of osteoclasts in microscopic images

In: Principles of Osteoimmunology. Molecular Mechanisms and Clinical Applications; Ed. P. Pietschmann, Wien: Springer-Verlag

Invited talks

26.9.2011 Invited talk at the institute of Pathophysiology and Allergy Research, Medical University Vienna, Austria: "Perspectives on investigating the Calcium sensing receptor's role in vascular calcification". Invitation by Dr. Isabella Ellinger

11.5.2012 Invited talk at the institute of Pathophysiology and Allergy Research, Medical University Vienna, Austria: "Investigating the role of the CaSR in the vasculature using targeted gene deletion". Invitation by Dr. Enikő Kallay